A CRYOGENICALLY-COOLED FABRY-PEROT INTERFEROMETER FOR BALLOON INFRARED ASTRONOMY

by

Martin Francis Kessler B.Sc., A.R.C.S.

A thesis submitted for the degree

of

Doctor of Philosophy of the University of London

and

for the Diploma of Imperial College

Astronomy Group

Blackett Laboratory

Imperial College

London S.W.7.

December 1980

Abstract

Far-infrared astronomical spectroscopy has developed rapidly since its birth in 1975. The emission lines in this region arise mainly from atomic and ionic fine structure transitions and from molecular vibration-rotation and pure rotation transitions. The astrophysics, deducible from observations of the intensities and profiles of these lines, was examined. Candidate lines for a programme of far-infrared spectroscopy were chosen after considering their predicted intensities, instrumental constraints, expected atmospheric contamination and previous detections.

The relative merits of various spectroscopic techniques (prism and grating spectrometers, Michelson, lamellar grating and Fabry-Perot interferometers and heterodyning) were compared before it was decided to build a mechanically scanned Fabry-Perot Interferometer. The design adopted is a novel variation of a parallel spring hinge arrangement. The etalon plates are mounted perpendicularly to the springs rather than parallel as in previous designs. Capacitance micrometry is used to monitor the change in etalon gap.

An ambient temperature prototype instrument was designed and built for work in the 10μm atmospheric window. It performed well in the laboratory and was taken to the 1.5m Infrared Flux Collector in Tenerife on several occasions. Telluric absorption features were seen in scans of Mars and the Moon. The 12.8μm neon emission line was detected in G.29.9-0.0.

Several design changes resulting from experiences in Tenerife were made before the liquid nitrogen-cooled far-infrared version was constructed. This uses stretched metal mesh for the mirrors, which are also the capacitors for the gap sensing electronics. Both the Fabry-Perot and a new photometer, containing the order-sorting filters, were fitted into a standard liquid helium dewar. After laboratory testing, the interferometer was flown with the Imperial College Balloon Telescope in December, 1979. Stabilisation problems precluded any astronomical observations during the flight but the mechanical performance was shown to be adequate.

In addition, an electromechanically resonant focal plane chopper was designed and built. Near-infrared observations of the dust formation phase of Nova Cygni 1978 were made and interpreted.

to

my Mother

d. 30 September 1977

Preface

Most of the work described in this thesis was carried out during my four years as an SRC-supported research student from October 1975 - October 1979.

Chapter one considers the astrophysical justification for infrared line astronomy. The processes that give rise to emission lines in this wavelength region are briefly summarised, before the astrophysics contained in these lines is examined in detail. The achievements of infrared line astronomy are reviewed and the chapter concludes with a brief account of the development of infrared astronomy in general.

Chapter two outlines the difficulty of making astronomical observations in the infrared through the terrestrial atmosphere. A model atmosphere is described and used to compute transmission and emission spectra at high resolving powers around the wavelengths of interesting astrophysical lines.

Chapter three describes the selection of candidate lines for a programme of infrared spectroscopy. Some theoretical work on estimating line intensities is briefly reviewed.

Chapter four gives the reasons for choosing to build a Fabry-Pérot Spectrometer (F-P), with which to attempt observations of astronomical emission lines. The theory of this instrument is given, before relevant design criteria are discussed. Previous Fabry-Pérot designs are summarised and the general features of the IC design explained.

Chapter five discusses the design details and laboratory testing of a near-infrared F-P. This instrument operates at ambient temperature and pressure and is used in the 10μm atmospheric window. Its performance during three observing trips is described and some astronomical results are presented.

Chapter six begins with a description of a liquid-nitrogen-cooled far-infrared F-P for balloon-borne applications. The auxiliary filtering and the design of a new two-channel photometer are discussed before results from laboratory tests on the F-P and its sub-systems are given. This interferometer formed part of the IC infrared payload for a balloon flight in 1979 December. The chapter closes with a brief analysis of the mech-

anical performance of the F-P during this flight.

Chapter seven summarises the previous chapters and briefly discusses some of the conclusions. Some recommendations are made for future work.

Appendix A contains details of a focal-plane chopper that was used with the IC telescope in the 1976 flight campaign. Appendix B presents some 1μm - 5μm observations of Nova Cygni 1978 and Appendix C contains two publications arising from the work described in this thesis.

Acknowledgements

I would like to express my gratitude to the many people who helped me during the course of the work described in this thesis.

First and foremost, my thanks go to my supervisor, Dr Bob Joseph, who suggested the project and has provided much help and encouragement. His broad knowledge of both astronomy and physics combined with his astute assessment of important areas of research, has been a constant source of inspiration for the last five years. Secondly, I wish to thank Dr Peter Meikle and Mr Jim Allen for all their advice and guidance; the former for his assistance with practical problems, for many stimulating discussions and for his consistent ability to ask embarrassingly-relevant questions, and the latter not only for the interferometer electronics but also for his mechanical expertise and his friendly cynicism.

The help of many other members of Imperial College has been invaluable and is gratefully acknowledged; Dr Mike Selby for the loan of much equipment; Steve Morris and David Rosen for computing assistance; Jack Crabtree, Bill Stannard and Brian Willey for mechanical advice and construction; Richard Chater of the Analytical Services Laboratory for taking many far-infrared spectra of the interferometer optics; Charlie Cooper for initiating me into the mysteries of glass-working; and Nic Jackson and Ian Clark for their photographic skills.

I thank Mrs Yvonne Masson for her speedy production of this excellent typescript. The Science Research Council funds the IC balloon astronomy programme and also supported me as a research student for four years. The hard work expended by the members of the Appleton Laboratory Stabilised Balloon Platform team in preparing the SBP for flight is greatly appreciated.

Lastly, but by no means least, I want to thank my parents, Dietrich and Georgie Kessler, both for their interest and encouragement and also for providing a haven, where astronomy could be temporarily forgotten.

Contents

List of Tables

List of Figures

Chapter 1

Infrared Line Astronomy

1.1 Potential of Infrared Line Astronomy

The infrared wavelength region is rich in spectral lines. These arise from atomic and ionic fine structure transitions, from molecular pure rotational and rotational-vibrational transitions and from recombinations. The fine structure lines are the infrared counterparts of the well known optical forbidden lines and are ideal tools for diagnosing astrophysical plasmas. Measurement of the intensities of fine structure lines in gaseous nebulae permits a very accurate determination of relative ionic abundances and of electron number densities. Other uses of fine structure lines include elucidation of the structure of galaxies and observations of star formation regions. The distribution of interstellar dust may be examined using fine structure and recombination lines. The molecular transitions carry information about the cool, dense part of the interstellar medium. Observations of molecular lines aid understanding of the heating mechanism of the interstellar medium, permit investigation of the dynamics of molecular clouds and may even place constraints upon big-bang cosmological models.

Far-infrared (wavelengths from about 20μm-300μm) line astronomy is a brand new branch of astrophysics. The first far-infrared line to be detected was the 88μm fine structure line of [OIII] (Ward et al., 1975). Even more recently, the first far-infrared molecular line, a transition between high rotational lines of carbon monoxide, was found by Watson et al. (1980a).

The potential of far-infrared line astronomy is enormous. This wavelength region contains information on both the hot and cold components of the interstellar gas in our galaxy, on the dynamics of other galaxies and even on conditions soon after the Big Bang. The field is ready and waiting to be explored.

Before proceeding to a more detailed examination of the science contained in infrared lines, some spectroscopic groundwork must be laid.

1.2 Spectroscopic Terminology

In the next two sections, the terminology used to denote fine structure and molecular energy levels is briefly summarised. Also, the types of transitions giving rise to astrophysical infrared lines are examined. For a more detailed account of atomic spectra, the reader is referred to Kuhn (1962) and for molecular spectra to Herzberg (1971).

1.2.1 Atomic Spectra

In the hydrogen atom, the electron moves in a potential which is a function of radial distance only. This permits an explicit of Schrödinger's time-independent equation and leads to the Bohr energy levels. The state of the electron is described by four quantum numbers, namely: n, the principal quantum number; ℓ, the orbital angular momentum, which may take integer values between 0 and n-1; m_ℓ, the z-component of the angular momentum, which has integer values between $-\ell$ and $+\ell$; and m_s, the z-component of the intrinsic angular momentum (spin, $s\hbar$) of the electron, where $m_s = \pm\frac{1}{2}$. Electrons with $\ell = 0,1,2,3$ etc are referred to as s,p,d,f etc. electrons. In the absence of an external magnetic field, the energy of a level ONLY depends on n and thus, each level is $2n^2$-fold degenerate.

It is impossible to solve Schrödinger's equation analytically for an atom with two or more valence electrons because the potential now contains cross terms from interactions between the electrons. Approximations have to be made. These will be examined by considering the energy level diagram for an atom with two p electrons in its valence shell. By neglecting the inter-electron forces, the so-called central field approximation, a single energy level is expected (figure 1.1). The classical Coulomb repulsion between the valence electrons depends on the relative orientation of their individual orbital angular momenta. These couple together to give a resultant orbital angular momentum, $\underline{L}$, which is a new quantum number and can take any integer value between $\ell_1+\ell_2$ and $|\ell_1-\ell_2|$. (For 3 or more electrons, $\underline{L} = \sum_i \underline{\ell}_i$ and ranges from 0 to $\sum_i |\ell_i|$). This effect splits the single energy level into three levels. These are designated S, P and D according to whether the value of L is 0, 1 or 2 respectively and are shown in figure 1.1. Quantum mechanically, the orbital wave function must have definite symmetry under exchange of the electrons. This exchange interaction energy splits the level into 2S+1 levels (2L + 1 if L < S), where S is the total spin angular momentum

Figure 1.1

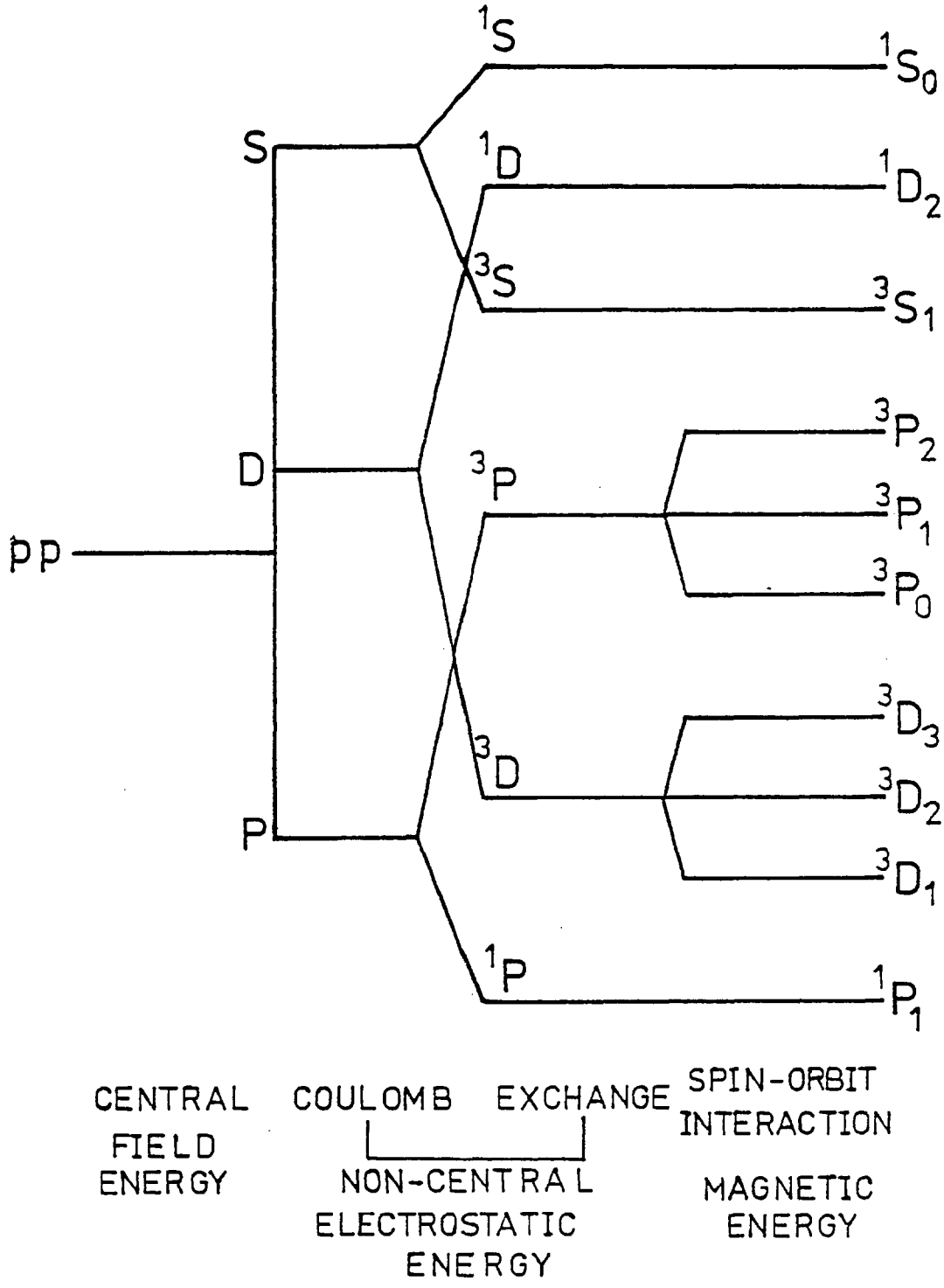

Schematic Illustration of the Principle of Energy Level Splitting.

given by $\underline{S} = \sum_i \underline{s}_i$. (Refer to figure 1.1).

The electron has an intrinsic magnetic moment due to its charge and spin. As a result of moving in the central electric field, it experiences a magnetic field proportional to its orbital angular momentum. This magnetic energy, or spin-orbit interaction, further splits the energy levels and causes the fine structure. Transitions between these levels produce the fine structure lines of interest in this work. Effectively, the spin and orbital angular momenta have been coupled together to form the total angular momentum vector, $\underline{J}$, where $\underline{J}$ is given by the vector sum of $\underline{L}$ and $\underline{S}$ (for Russell-Saunders coupling). The magnitude of $\underline{J}$ is $\sqrt{j(j+1)}\hbar$ and its z-component is given by $J_z = m_j h$ where j and m_j are new quantum numbers replacing m_l and m_s, which are rendered meaningless by spin-orbit coupling. J takes integral and half-integral values from (L+S) to |L-S| and, thus, the multiplicity of a term is 2S+1. The different fine structure levels are labelled by their J and L values with the multiplicity written as a superscript on the left e.g. $^4D_{5/2}$ where L = 2, J = 5/2 and S = 3/2. If the magnetic moment of the nucleus is also considered, a further splitting of levels occurs, leading to hyperfine structure.

The size of fine structure splitting depends on the atomic charge, Z, of the element involved and on the quantum numbers of the relevant energy level. As an example, the fine structure energy, E_{fs}, arising between the interaction of the L and S of a hydrogen-like atom is given by,

$$E_{fs} = \alpha^2 \frac{hcRZ^4}{n^3} \left[\frac{J(J+1) - L(L+1) - S(S+1)}{L(L+1)(2L+1)} \right], \qquad 1.1$$

where α, the fine structure constant, and R, the Rydberg constant, are given by,

$$\alpha = \frac{2\pi e^2}{hc} \qquad \text{and} \qquad R = \frac{2\pi^2 \mu Z^2 e^4}{ch^3}. \qquad 1.2$$

μ is the reduced mass of the electron. For the 2P term in the ground state of the hydrogen atom, the fine structure splitting is 5×10^{-5}eV (Harwit, 1973, p.261) and as Z increases so does the splitting e.g. 2×10^{-3}eV (i.e. $\lambda \sim 600\mu$m) for sodium compared to 7×10^{-2}eV (18μm) for Caesium (Thorne, 1974). The hyperfine levels of the hydrogen atom are separated

by 6×10^{-6}eV, leading to the important 21cm line.

In order to explain why these fine structure transitions are not seen in the laboratory, the restriction (if any) on radiative transitions must be examined. The electromagnetic field of the emitted or absorbed photon is treated as a small perturbation to the atom. After unit time, there is a certain probability, the transition probability, that the electron will have changed its state. The transition probability may be expanded as a power series. The first term of the expansion is proportional to the electric dipole moment of the two states involved; higher terms correspond to magnetic dipole and electric quadrupole transitions. By examination of the conditions under which the first term is non-zero, selection rules, governing electric dipole transitions, are deduced. These rules forbid electric dipole transitions between fine structure levels but allow magnetic dipole transitions. The latter have very small transition probabilities, i.e. the lifetime of the electron in the upper state is very long, and so, at normal laboratory densities, the levels are collisionally de-excited. However, in regimes of very low density, e.g. the interstellar medium, radiative de-excitation occurs with the emission of a "forbidden" photon.

1.2.2 Molecular Spectra

The total energy of a molecule can be approximated to the sum of three parts; electronic, vibrational and rotational, each about 100 times smaller than the last. The spectra of polyatomic molecules are very complex, owing to their large number of degrees of freedom. There follows a brief outline of the spectrum of a diatomic molecule in order to give the 'flavour' of molecular spectroscopic terminology. The electronic energy levels are calculated by studying the motion of the electrons around the nuclei and comparing the results to the motion in the "united" atom. Transitions between electronic energy levels lead to lines in the UV and visible spectral regions and so further discussion is inappropriate here.

The vibrational energy levels are found by firstly treating the diatomic molecule as a quantum harmonic oscillator and then by slightly modifying the potential to a more realistic form, the Morse potential, V, given by,

$$V = D_e\left[1-e^{-\beta x}\right]^2 \quad , \qquad 1.3$$

where D_e is the dissociation energy of the molecule, β is a constant and x is the displacement of the nuclei from their equilibrium separation. The energy levels, E(v), expressed in term values, G(v), where $G(v) = E(v)/hc$, are,

$$G(v) = \omega(v+\tfrac{1}{2}) - \omega x(v+\tfrac{1}{2})^2 + \omega y(v+\tfrac{1}{2})^3 + \ldots . \qquad 1.4$$

where v is the vibrational quantum number, x and y are anharmonicity constants and are in general quite small, and ω is the vibrational constant, given by,

$$\omega = \frac{\sqrt{hc}}{2\pi c}\sqrt{\frac{2D_e}{\mu}}\,.\,\beta \qquad 1.5$$

The values taken by v may be 0, 1, 2 ..... As v increases, the gap between successive levels decreases.

A rotating diatomic molecule may be considered as a system of two masses separated by a fixed distance, rotating about an axis perpendicular to the line joining the masses. This system is easy to solve and leads to energy levels, E(J), expressed in term form, where, $F(J) = E(J)/hc$ are,

$$E(J) = BJ(J+1) \quad , \qquad 1.6$$

where J is the rotational quantum number. The rotational constant, B, is given by

$$B = \frac{h}{8\pi^2 cI} \quad , \qquad 1.7$$

where I is the moment of inertia of the molecule about the axis of rotation. However, in general, the distance between the masses is not constant because a) the molecule is not rigid and thus centrifugal force will cause the internuclear distance to increase slightly and b) the molecule may be vibrating. The result of these two effects is that higher terms have to be included in the energy level expression and also the rotational constant, B, becomes dependent on the vibrational quantum number, v. The energy levels, in term form, where $F(J) = E(J)/hc$, are,

$$F_v(J) = B_v J(J+1) - D_v J^2(J+1)^2 + \ldots\ldots \quad , \qquad 1.8$$

where D is a small constant. Before leaving rotational spectra, the idea of branches must be introduced. The O,P,Q,R,S branches correspond to $\Delta J = -2,-1,0,1,2$ respectively. Transitions may be labelled by a branch and the lower of the two rotational quantum numbers. Figure 1.2 (from Herzberg, 1971) shows schematically the vibrational and rotational levels of two electronic states of a molecule.

Three kinds of spectra can be distinguished. Firstly, transitions between the rotational levels of a given vibrational and electronic state form the pure rotation spectrum and give rise to lines in the far-infrared, milli- and centimetric regions. Secondly, rotation-vibration spectra arise from transitions between the rotational levels of one vibrational state and the rotational levels of another vibrational state of the same electronic level, causing lines throughout the infrared region. Thirdly, there is the electronic spectrum. Transitions of these three kinds are indicated on figure 1.2.

A homonuclear molecule, e.g. H_2, cannot have any electric dipole rotational or vibration spectrum because it lacks a permanent dipole moment. Transitions in such molecules must occur by electric quadrupole radiation and are therefore relatively weak. A heteronuclear molecule, e.g. CO, has the following electric dipole spectra. The pure rotation spectrum is a series of lines almost equally spaced in wavenumber (cf. eqn. 1.8). The vibrational spectrum is split into bands because of the rotational fine structure of each vibration level. Each electronic energy level has rotational and vibrational structure, so the electronic spectrum consists of series of bands.

1.3 Astrophysics in Infrared Lines

It has been shown in the preceding sections that infrared lines are produced by atomic and ionic fine structure transitions, and by molecular vibrational-rotational and pure rotational transitions. In addition to these mechanisms, infrared lines are also produced by recombinations. These processes give rise also to lines in the optical and radio regions. In some cases, the information derived from infrared lines complements that from other wavelengths, while in other cases, it is superior.

Figure 1.2

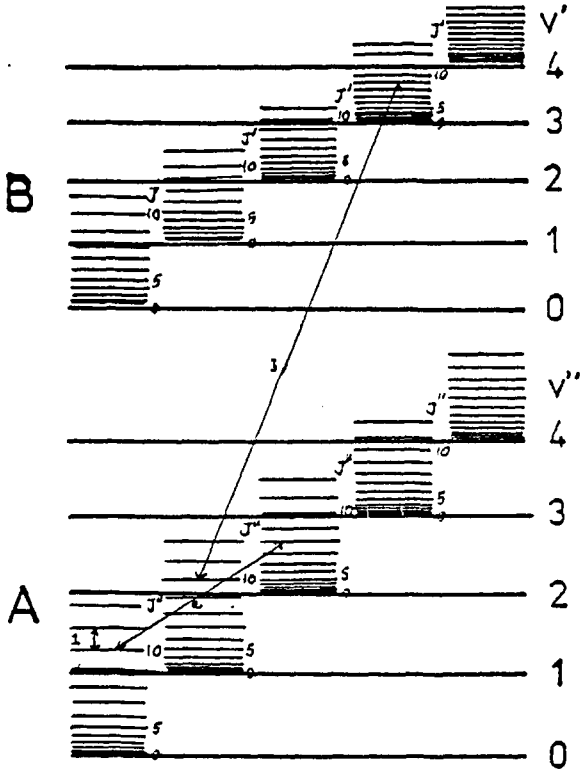

Vibrational and Rotational Levels of Two Electronic States A and B of a Diatomic Molecule. (From Herzberg, 1971).

Generally, infrared observations have the advantage over the radio work of comparatively small beam sizes. This is particularly important when there is a suspicion of non-uniform density, or "clumping", in the object. Compared to the optical, the extinction by dust of the infrared is nearly negligible. For a B-V colour excess of 1.0, there is an optical (B) absorption by dust of 4 magnitudes (Schild, 1977). At 5μm, this figure has dropped to less than a quarter of a magnitude; the wavelengths of the lines under discussion here are ∿10 times longer and thus dust extinction will be even less. This insensitivity to dust can be of advantage in two ways. Firstly, the numbers obtained from infrared measurements are better than those from optical because they are not subject to uncertain corrections for interstellar reddening. Secondly, dust-enshrouded regions may be observed and information, inaccessible to optical astronomers, extracted, e.g. the dynamics at the centre of our galaxy.

Obviously ionic fine structure and molecular lines must, in general, come from different types of astronomical object. For molecules to exist, they must be protected from the dissociating and ionising ultraviolet radiation. This shielding may be achieved either by interstellar dust or by having very dense molecular clumps, so that the centre is self-shielded. Thus, molecular far-infrared lines carry information about the cool dense part of the interstellar medium. On the other hand, ionic fine structure lines come from ions and thus, these lines are useful for diagnosing astrophysical plasmas. Since the ionic and molecular lines come from such different regions, they are now discussed separately to investigate what astrophysical information can be extracted. Atomic fine structure lines come from both types of sources, hot and cold, and are mentioned where relevant.

1.3.1 Fine Structure Lines

Fine structure lines are the infrared counterparts of the well-known optical forbidden lines that have been used for years by optical astronomers in the study of gaseous nebulae. The fine structure levels are populated by electron-ion collisions and thus the transitions radiate away the kinetic energy of the nebula. These lines are the most important cooling mechanisms for interstellar plasmas, despite the low abundances of the species producing them.

Many species of interest have between one and five p electrons in their outer shell. Figure 1.3 (adapted from Simpson, 1975) shows the fine structure for these configurations. Ions with either two or four valence electrons have a pair of infrared lines as well as optical transitions, e.g. [OIII]. Configurations with either one or five electrons have a doublet in the ground state leading to a single infrared transition, e.g. [NeII]. Observation of this line is the only way to see these ionisation stages. There is no fine structure in the ground state of p^3 configurations; due to the higher excitation energy, fine structure lines from the higher levels of p^3 configurations are very weak.

As discussed by Watson and Storey (1980), fine structure lines have simple observational properties that make it easy to extract information. The nebulae are generally optically thin in these lines (this is also true for optical forbidden lines), so no radiative transfer analysis is needed. The excitation temperatures for the fine structure levels are low compared to the average nebular temperature, thus causing the line strengths to be almost independent of the nebular temperature. Also, the Einstein spontaneous transition probability is so small that even at low densities some lines are "saturated". This last point is discussed further in the next paragraph. Table 1.1 is a list of interesting fine structure lines, arranged in order of increasing wavelength for each electronic configuration.

The most important use of infrared fine structure lines is in the determination of very accurate relative ionic abundances and electron number densities. These can be calculated in the following way. The intensity of a particular fine structure line depends on the number of ions in the line of sight that are in the upper level of the two fine structure levels involved in the transition, i.e. the fractional level population. In general this depends on the electron number density, n_e, because the levels are populated by electron-ion collisions. However, if the spontaneous transition rate is very small, the fine structure levels can come into thermal equilibrium with the electrons. Due to the high electron temperature, this results in the fine structure levels being populated according to their statistical weights. Thus the line intensity is now proportional to the total ionic column density, $n_{ion}\iota$, where n_{ion} is the ionic number density and ι, the depth of the nebula along the line of sight. The point at which the line intensity becomes independent of n_e, i.e. "saturated", may be calculated by applying the

Figure 1.3

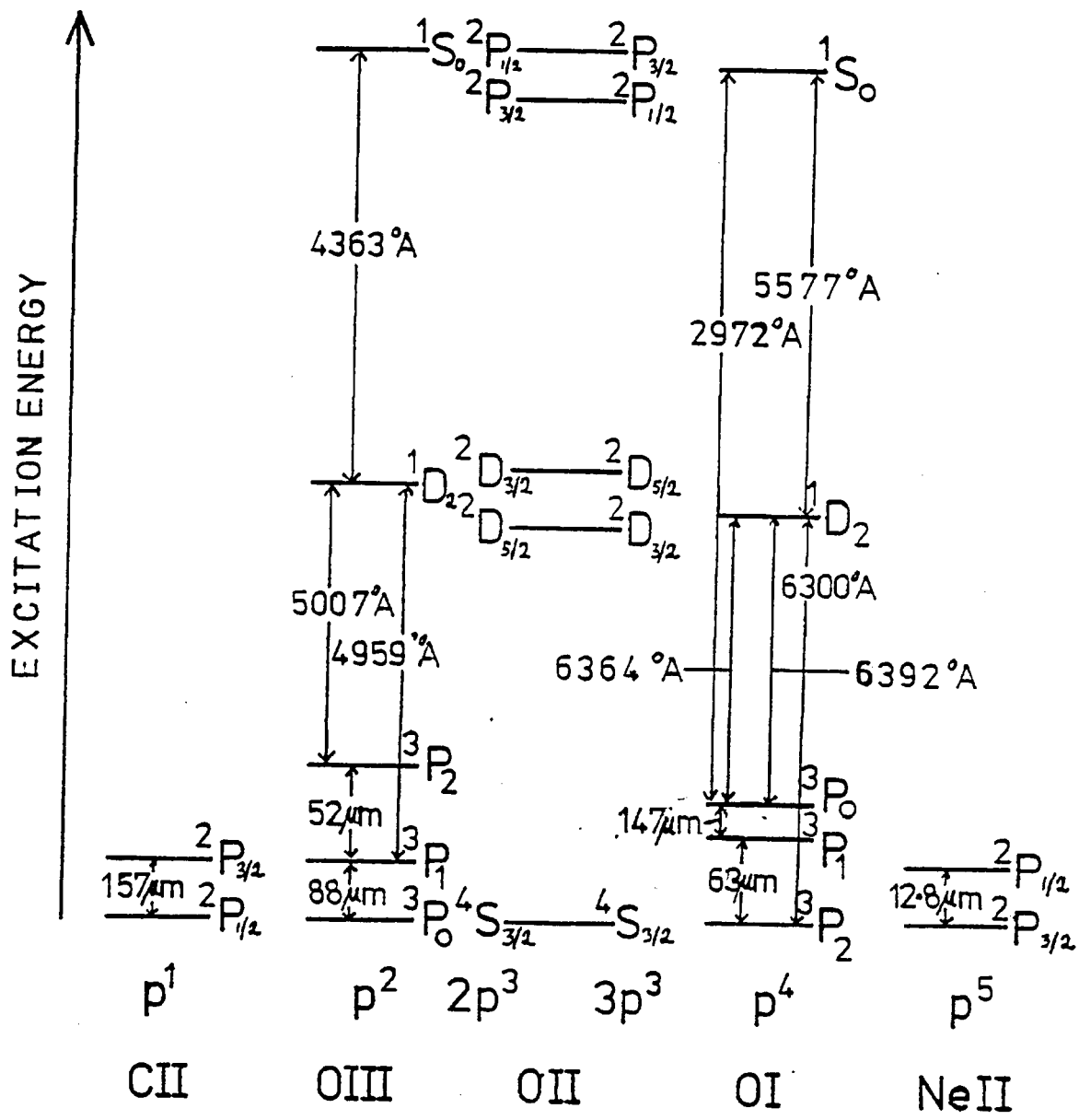

Schematic Energy Level Diagram for $2p^n$ and $3p^n$ Configurations.
(Adapted fron Simpson, 1975).

Table 1.1

Configuration	Transition	Species	Wavelength (μm)
p^1	$^2P_{3/2} - {}^2P_{1/2}$	SIV	10.52
		PIII	19.7
		OIV	25.91
		SiII	34.8
		NIII	57.3
		CII	157.4
p^2	$^3P_2 - {}^3P_1$	ArV	7.9
			13.1
		Cl IV	11.8
			20.4
		NeV	14.3
			24.2
		SIII	18.71
			33.44
	$^3P_1 - {}^3P_o$	PII	32.9
			60.0
		OIII	51.82
			88.36
		SiI	68.5
			129.7
		NII	121.7
			203.9
		CI	370.4
			609.1
p^4	$^3P_1 - {}^3P_2$	ArIII	8.99
			21.84
		Cl II	14.34
			33.4
	$^3P_o - {}^3P_1$	NeIII	15.55
			36.04
		SI	25.2
			56.3
		OI	63.17
			145.5
p^5	$^2P_{1/2} - {}^2P_{3/2}$	CaIV	3.21
		MgIV	4.5
		ArII	6.99
		NaIII	7.33
		NeII	12.81

Some Important Fine Structure Lines.

principle of detailed balance to the level population. Figure 1.4 from Watson and Storey (1980) is the result of such a calculation. This shows level population ratios for the ground state of OIII. For electron number densities above $10^4 cm^{-3}$, the 88μm [OIII] line is saturated. To get accurate relative ionic abundances, the intensities of two saturated fine structure lines, one from each ion, must be measured. Since both these intensities are proportional to $n_{ion}\iota$, their ratio gives the relative abundance of the two ions without needing to know the depth of the nebula. This abundance ratio will be more accurate than one derived from optical measurements; the infrared measurements also have greater applicability since the infrared lines saturate at much lower densities than the optical. Figure 1.4 also demonstrates the insensitivity of the level populations to temperature.

The electron number density may be calculated, again without needing to know ι, if the intensities of a pair of fine structure lines from the same ion are measured in the same beam. Figure 1.4 shows that the ratio of the 52μm [OIII] line to the 88μm one is a function of n_e, as long as one of the lines remains unsaturated. Comparison of the value of n_e, obtained from infrared measurements using small beam sizes, with that obtained by measurement of the radio free-free emission using relatively large beam sizes will aid in estimating the 'clumpiness' of the source. Once n_e is known, ionic abundances relative to hydrogen may be calculated if assumptions about the depth and shape of the nebula are made. Watson and Storey (1980), referring to Osterbrock (1974), discuss how to use n_e to investigate general elemental abundances, the ionisation structure of nebulae and also how to determine the effective temperature of the ionising star.

The advantage in the infrared of great insensitivity to dust extinction has previously been mentioned. In this paragraph, the use of infrared observations to probe the dust is discussed. Many ions have pairs of far-infrared lines. If conditions in a source can be deduced from other observations, then predictions of the ratio of the intensities of the two fine structure lines may be made. Comparison of the predicted ratio with a measured ratio may help to estimate the wavelength dependence of interstellar dust in the far-infrared region. At the moment, there is some doubt as to whether this follows a $1/\lambda$ or a $1/\lambda^2$ law. This problem is not insignificant, for even at 100μm, the optical depth to the galactic centre is 1.6 (Erickson et al., 1977). Doubly-ionised sulphur is partic-

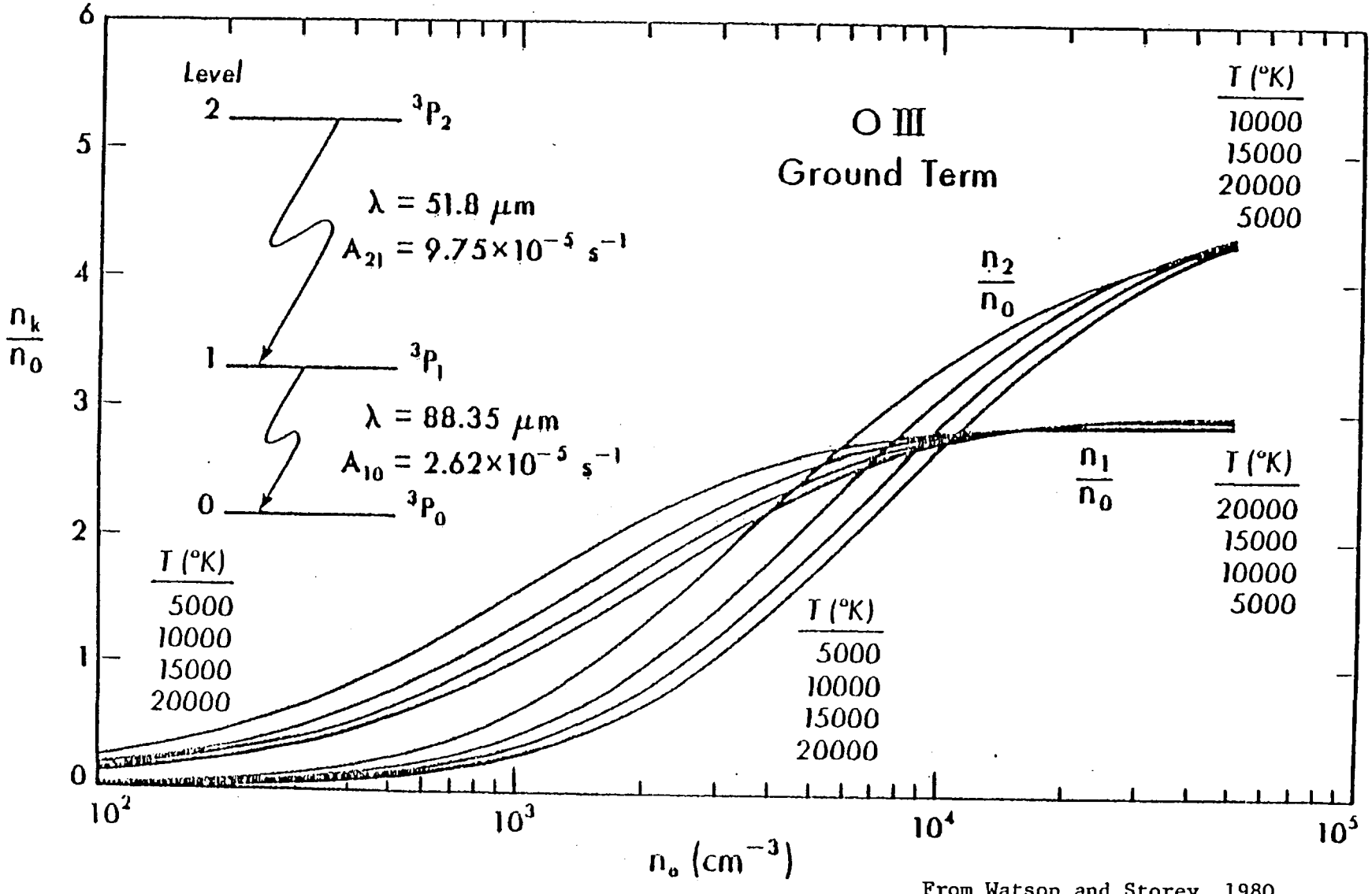

From Watson and Storey, 1980.

Figure 1.4

OIII Fine Structure Level Population Ratios.

ularly important in this context for one of its two fine structure lines is at a wavelength of 18.7μm, right in the middle of the 20μm silicate absorption feature. This line is very bright in HII regions and should be an ideal probe of the properties of interstellar silicate grains. Another method of detecting dust and measuring interstellar absorption is to compare the intensities of infrared recombination lines with their optical and radio counterparts, many of which have already been detected.

Elucidation of the structure and dynamics of galaxies by high spectral and spatial resolution measurements of emission lines is complicated in the optical by obscuration and dust scattering and in the radio by possible interstellar stimulated emission amplification. Thus, when possible, it is preferable to work in the infrared. The [NeII] line at 12.8μm has been used for this purpose for M82 (Beck et al., 1978), NGC 253 (Beck et al., 1979) and for our own galaxy by several authors (cf. section 1.5.2).

Infrared observations are particularly important in the study of star formation and young HII regions, as these are still deeply embedded in dust. Infrared lines are easily excited by collisions because of their low excitation energies. The mass flux around a protostar which has not yet started thermonuclear burning may be enough to excite these levels (Andriesse et al., 1979) and for this reason, they suggest making high spectral resolution observations of objects such as the Becklin-Neugebauer object to determine their nature.

In addition to the main uses of fine structure lines described above, there are many others. For example, neutral oxygen is a very interesting species because its first ionisation potential is only slightly higher than that of hydrogen and so it is found on the edges of HII regions, where it is excited by collisions with hydrogen atoms. Thus observations of [OI] fine structure transitions will give information on the structure of the HI/HII transition zone, the ionisation front.

As the ability to detect far-infrared fine structure lines increases, so will the number of uses for them. However, at present, their most important use is in determining relative ionic abundances.

1.3.2 Molecular Lines

Infrared molecular lines are of interest in many areas. Their use in the study of star formation regions, the study of the heating mechanism

of the interstellar medium and in determining the deuterium-to-hydrogen ratio are outlined in the following few paragraphs.

Hill and Hollenbach (1978) have examined what happens when a compact HII region, powered by a young massive star, expands into its surrounding molecular cloud. A dissociation front and shock wave travel out through the cloud, heating the gas. Eventually, the gas cools by infrared line radiation. They conclude that the strongest lines are the molecular hydrogen quadrupole transitions, the fine structure transitions of OI and later the rotational transitions of carbon monoxide.

The heating mechanism for the interstellar medium is not well understood. Possible sources of energy include ionisation by cosmic rays and the interstellar radiation field as well as photoelectric emission from dust. Since, in equilibrium, the cooling rate is equal to the heating rate, the former deserves attention. The main mechanism for energy loss is collisional excitation of atoms, ions and molecules followed by radiation in the infrared. The cool dense part of the interstellar medium has a rich far-infrared spectrum, for the excitation conditions are such that the majority of the energy lost through molecular transitions falls in this wavelength region. Molecules such as CO (the most important tracer of dense molecular gas), H_2, HD, together with CI and CII, provide important cooling mechanisms for these regions. Even trace molecules, such as HCl (Dalgarno et al., 1974) may contribute significantly to the cooling because above a critical density, the cooling is independent of molecular abundance and roughly proportional to the rotational constant, B (cf. equation 1.7) of the molecule. In cases of low temperatures (10-100K) and densities (10^2-$10^6 cm^{-3}$), the clouds will not be in thermodynamic equilibrium. This both complicates the interpretation of the observations in terms of physical conditions and also leads to exotic phenomena such as SiO, H_2O and OH masers. Measurements of molecular intensities gives information on the galactic history of the elements, while detailed mapping and fitting of observed line profiles to models allows a determination of density distributions and velocity fields in dense interstellar clouds.

The excited rotational levels of H_2 and HD are long-lived and, thus, collisions maintain the level populations in thermal equilibrium. Dalgarno and Wright (1972) suggest that measurements of the relative intensities of these lines would give the HD/H_2 and ortho-H_2/para-H_2

abundance ratios as well as the kinetic temperatures. The H/D ratio is of cosmological significance, because the amount of deuterium in the universe at present is a sensitive indicator of the density in the very early universe.

Far-infrared molecular line astronomy only began in 1980 (Watson et al.). There is certain to be a rapid exansion of work in this field and the next few years should see some of the potential, described above, fulfilled.

1.4 Line Astronomy in Context

Line astronomy has made vast contributions to astrophysics in all bands of the electromagnetic spectrum. Before discussing the achievements of infrared line astronomy, some of these other contributions are summarised.

One of the foundations of modern astrophysics was laid in 1859 when Bunsen and Kirchoff discovered that each element had characteristic spectral lines. This discovery was used to interpret the dark lines in the solar spectrum that Frauenhofer had reported 45 years earlier. Shortly afterwards, Jansen discovered helium in the sun through its spectral lines, some 27 years before Ramsay isolated it on the earth (1895). In the next few decades, with the development of the quantum theory, Saha's theory of thermal ionisation and excitation and theories of atomic structure, the theoretical interpretation of stellar spectra became possible. Since then, observations of line intensities, profiles, central frequencies and splittings have enabled astronomers to deduce the physical conditions in many sources.

For the early 'line astronomers' the optical window was the only information channel open to them. In 1904, Hartmann discovered interstellar matter through its calcium absorption lines. The first interstellar molecules, CH^+, CH and CN, were identified in the late thirties by their optical absorption spectra. McKellar (1941), using data from the rotational excitation of CN, deduced a rotational temperature of 2.3K for the interstellar medium many years before the discovery of the 3K background.

More recently, advances in technology have opened up other spectral windows. An important example is the 21cm spin-flip line, which radio

astronomers have used to map the galactic distribution of atomic hydrogen. There are, at present, over fifty known interstellar molecules; most of these were first detected by radio frequency transitions. One notable exception is molecular hydrogen, which was found by its ultraviolet absorption spectrum (Carruthers, 1970) and later seen in the infrared (Gautier et al., 1976). Other molecules detected in the UV are CO, HD and OH and in the IR, C_2(0.8μm) and CO(870μm, 124μm and 119cm). Lines have also been detected in the X-ray and γ-ray spectral regions.

Thus, line astronomy continues to provide astronomers with information in all wavelength regions. The contribution from infrared lines is now discussed.

1.5 Achievements of Infrared Line Astronomy

The next two sections look firstly at the landmarks in the subject and then at the scientific results of infrared line astronomy. Both sections are heavily biassed towards the far-infrared work but some mention is made of relevant observations in the short-wavelength atmospheric windows.

1.5.1 Landmarks

In the short wavelength region, the first fine structure line to be detected was that of [NeII] at 12.8μm in the planetary nebula, IC418, by Gillett and Stein (1969). This line has subsequently been widely observed. On the molecular side, Gautier et al. (1976) first detected emission from H_2 in the Orion nebula. Thompson et al. (1978) were the first to detect H_2 emission in an extragalactic object, NGC 1068.

The pioneering work in the far-infrared was done by Ward et al. (1975) who found the 88μm [OIII] line in the Omega nebula. Its companion line, at 52μm, was also discovered by the Cornell group (Melnick et al., 1978). Thus, the first pair of infrared lines from one species had been found. The Cornell group followed up with the detection of fine structure emission from a neutral species, [OI] at 63μm in M42 (Melnick et al., 1979a). Far-infrared fine structure line studies may be considered to have come of age with the maps by Storey et al. (1979) of several HII regions in 88μm [OIII] emission. This group at Berkeley have also opened up a new field with two detections of far-infrared molecular lines. Watson et al. (1980a) saw emission from rotational transition of carbon

monoxide at 119μm and 124μm in the Orion Nebula; while Storey et al. (1980a) observed two absorption lines of OH (119.23μm and 119.44μm) in the direction of Sgr B2. The paper by Moorwood et al. (1980) is a good example of the use of fine structure lines to derive physical conditions in astronomical objects.

1.5.2 Results

The problem of interstellar iron abundances is mentioned in section 3.1.2. In the absence of far-infrared data, the best approach is to examine the very-near-infrared $^4P_{21/2} - {}^4F_{41/2}$ transition of FeII at 8617Å, because this will be less sensitive to electron temperature than the optical lines. Cosmovici et al. (1980) report the first high spectral resolution observations of this line. They find the abundance of iron in Orion to be x35 less than in the sun and x3.6 higher than in the interstellar medium.

In the 1μm - 5μm region, hydrogen recombination lines are used to derive extinction to various objects e.g. Willner et al. (1977). Emission from molecular hydrogen at 2.1μm in planetary nebulae has been observed by Beckwith et al. (1978a) to be correlated with [OI] (λ6300Å) clumps. They consider it likely that the hydrogen molecules are inside the dense clumps and protected from dissociation by dust.

The use of the three bright fine structure lines which fall in the 10μm atmospheric window to determine abundances, the nature of exciting sources, and composition of radiating material, has become commonplace. An interesting use of the [NeII] line, that of mapping galactic dynamics, was mentioned in section 1.3.1. Wollman et al. (1976, 1977) found both red- and blue-shifted [NeII] emission in Sgr A West from a region about 40" across and roughly co-incident with the thermal radio source of the same size. They conclude that the observed motion of NeII was representative of the velocity distribution of the ionised gas as a whole. From the velocity dispersion, they put a limit of $4 \times 10^6 M_\odot$ upon the mass within 0.8 pc of the galactic centre.

The Orion Molecular Cloud has been the focus of much work. Gautier et al. (1976) discovered several molecular hydrogen vibration-rotation emission lines here, and identified the strongest as the v = 1-0 S(1) line at 2.1μm. Joyce et al. (1978) tested the suggestion that the emission came from a shock front by using high spatial resolution. They conclude

that the emission arises from collisionally-excited H_2 in a thin shock-heated layer inside the cool molecular cloud. For spherical (planar) geometry, the shock velocity is limited to 15(30) km s^{-1}. Beckwith et al. (1978) mapped the 2.1μm emission and used line intensities and ratios to derive a vibrational temperature of 2200K and a rotational temperature of 1100K. They consider the energy sources present and conclude that none of them has sufficient energy density to produce shock excitation of the H_2. Thus, if the H_2 is shock-excited, the shock must have arisen from a cataclysmic event, e.g. a supernova. Rapid shock heating, followed by slower cooling, would also produce 12.3μm pure rotational H_2 emission from the cooler gas downstream. Beck et al. (1979) have found this line and their results are consistent with the 2μm data. The 63μm [OI] line is also expected to be an important coolant of past shock gas and was found in M42 by Melnick et al. (1979a) but with low spatial resolution. Storey et al. (1979) made a partial map of M42 in [OI] 63μm emission and say that the line emission comes from the HII/neutral material transition zone and not from the region of molecular hydrogen emission. Rotational transitions from another expected coolant, CO, were detected in the shocked region by Watson et al. (1980a).

Table 1.2 lists all the far-infrared lines detected to date (October 1980). The earlier papers only report fluxes and, apart from comparing the measured intensities with prediction - e.g. Baluteau et al. (1976) - do not use the results further. The rest of the literature in this field, excluding papers fully discussed above, are now briefly summarised in chronological order.

Greenberg et al. (1977) observed [SIII] 18.7μm emission in three nebulae, and obtained the first direct measurement of an ionic column density, namely S^{++} in NGC 7027 and BD 30^{o}+3639. Dain et al. (1978) find agreement between their observed 88μm [OIII] emission in HII regions and the predictions of Simpson (1975). However, their fluxes from Sgr A and Sgr B2 (upper limit) are very low. Radio observations of these sources (Churchwell et al., 1974) may be interpreted to infer an underabundance of HeII. These two facts, together, could be explained by a lack of hard UV photons. The good agreement between predictions (from radio observations) and observed 51.8μm [OIII] emission in Orion led Melnick et al. (1978) to conclude that M42 is not very clumpy. Moorwood et al. (1978) detected [OIII] 88μm and [SIII] 18.7μm emission in the Orion nebula, with intensities in good agreement with the predictions of Simpson

Table 1.2

Species	Wavelength (μm)	Objects	Reference
SIII	18.7	HII regions and P.N.'s	b,c,f,j,l.
NeV	24.3	Only NGC 7027	p.
OIV	25.9	Only NGC 7027	p.
SIII	33.4	Only M17	l.
OIII	52	GC, HII regions and P.N.'s	e,h,k,l.
NIII	57.3	M17, W51	l.
OI	63	HII regions and a P.N.	g,i.q.
OIII	88	GC, HII regions	a,b,d,f,i,l.
CO	118.6	M42	o.
OH	119.2	Towards SgrB2 in Absorption	n.
OH	119.4	Towards SgrB2 in Absorption	n.
CO	124.2	M42	o.
CII	157	M42 and NGC 2024	m.

References

a. Ward et al., 1975.
b. Baluteau et al., 1976.
c. Greenberg et al., 1977.
d. Dain et al., 1978.
e. Melnick et al., 1978.
f. Moorwood et al., 1978.
g. Melnick et al., 1979a.
h. Melnick et al., 1979b.
i. Storey et al., 1979.
j. McCarthy et al., 1979.
k. Watson et al., 1980b.
l. Moorwood et al., 1980.
m. Russell et al., 1980.
n. Storey et al., 1980a.
o. Watson et al., 1980a.
p. Forrest et al., 1980.
q. Melnick et al., 1980.

Notes

The author knows of three other papers in preparation in this field:

Baluteau et al., 1980. 18.7μm [SIII] and 52μm [OIII].
Moorwood et al., 1980b. 52μm [OIII], 57μm [NIII] and 88μm [OIII].
Watson et al., 1980c. 52μm [OIII] and 57μm [NIII].

Detected Far-Infrared Lines (October 1980).

(1975). They use these results, in conjunction with optical data, to examine the density, temperature and ionisation equilibrium of the source. The peak emission in each line comes from the maximum density region; the [SIII] emission is localised to high density clumps while the [OIII] line is emitted throughout the entire cloud. From their upper limit on the [SIII] 33μm line, Moorwood et al. also propose an alteration to the density structure of the model of Simpson (1973). More accurate measurements of 52μm [OIII] in galactic HII regions are reported by Melnick et al. (1979b). They find reasonable agreement between the observed and predicted 52μm/radio continuum ratios but not such a good match for the 52μm/88μm [OIII] ratios. They ascribe this to clumpiness in the sources and also suggest doubling the OIII abundance of Simpson (1975). The same authors (1979a) observed very bright [OI] 63μm emission from M42 and M17. For both objects, the flux in the line is about 0.3% of the total energy radiated by the nebula! Emission from [SIII] 18.7μm was mapped in M17 and detected in three other HII regions by McCarthy et al. (1979). They develop a simple theory to predict [SIII] fluxes from radio data and find good agreement for two of their four sources. For the other two, it is necessary to include silicate dust extinction and/or lower SIII abundances. Storey et al. (1979) detected [OIII] 88μm emission in many sources and find that in each case the peaks of the fine structure and radio continuum emission are co-incident. They map three sources in both 88μm [OIII] emission and 88μm continuum emission and find two distinct peaks. This shows that spherical models which have the dust uniformly mixed with the ionised material will not give realistic predictions for the properties of the source. Storey et al. (1979) also derive OIII column densities and estimate OIII fractional abundances but conclude that these will not be reliable until better electron densities are known. The NeII clouds at the galactic centre emit 52μm [OIII] flux (Watson et al., 1980b). An effective temperature of 32000-40000K is deduced for the radiation field ionising these clouds. The 157μm [CII] was detected by Russell et al. (1980) in NGC 2024 and M42, and approximate gas temperatures are deduced.

In summary, far-infrared molecular line astronomy has barely begun. Two transitions of each of two molecules have been detected this year by the Cornell Group. However, this work is very promising, because the detected CO intensities are such that many more CO transitions ought to be detectable. From these, rotational temperatures and CO column densities are calculable. The OH lines are equally exciting for any method of studying the excitation processes for OH masers is to be welcomed. As

the results above show, far-infrared fine structure line astronomy is developing rapidly and fulfilling the potential, expressed for it in section 1.3.1, by deriving abundances and electron number densities. A pointer for the future of fine structure work may well be the comprehensive nature of the recent paper by Moorwood et al. (1980). They measure simultaneously (and therefore in the same beam) two pairs of infrared lines, [SIII] (18.7μm and 33μm) and [OIII] (52μm and 88μm), and also [NIII] (57μm) in M17. They derive ionic abundances and electron number densities, and investigate the ionisation structure of the nebula.

Many new discoveries are still to be made in far-infrared line astronomy. Much exciting follow-up work awaits observers. This field is certain to blossom in the next few years and to provide a rich harvest.

1.6 Development of Infrared Astronomy

In order to gain some perspective on the rôle and difficulties of infrared line astronomy, the historical development of infrared astronomy, as a whole, is now sketched.

Infrared astronomy began almost 200 years ago with the very discovery of infrared radiation by Herschel (1800). He was using a thermometer to investigate the heat content of different colours in the solar spectrum when he found energy beyond the red end of the spectrum. The next astronomical object to be detected was the full moon by Piazzi Smyth (1859) using an "excellent thermo-multiplier". The ruins of Piazzi Smyth's observatory in Tenerife are shown in figure 1.5. A few years later, the 4th Earl of Rosse measured the moon through its phases and deduced a surface temperature that agrees with the modern value to within 10%.

After the pioneering work in the early 19th century, there was a long pause in the development of infrared astronomy. This was due to the low sensitivity of available detectors, compounded by the atmosphere's opacity throughout most of this spectral region (cf. Chapter 2). In the first half of the 20th century, the main planets and some bright stars were added to the list of known infrared objects. (Refs. listed in Allen, 1975, Ch.1). Pettit and Nicholson (1930), using thermocouples and a water cell, observed 124 stars and presented bolometric corrections for them. Their lunar data was used by Wesselink (1948) to show that the moon must be covered with dust.

Figure 1.5

The Ruins of Piazzi Smyth's Observatory on the Peak of Guajara.

In the 1950's improved detectors began to become available. Fellgett (1951) used a cooled lead sulphide photoconductor to look at 51 stars between 1-2.5μm. He noted that there was some evidence for excess infrared emission from Be stars. However, despite encouraging results with the PbS detector he concluded that it was important "to use every resource to increase cell sensitivity". Lead sulphide cells cannot be used beyond about 3μm and so mercury- and copper-doped germanium photoconductive detectors were developed for use between 5μm and 15μm. Since all these photoconductors are only sensitive over a limited wavelength range, it was a great step forward when Low (1961) invented the liquid-helium-cooled gallium-doped germanium bolometer. Not only does the Low bolometer have a large wavelength range but it is also very sensitive even in the 5-15μm range and it is therefore not surprising that this type of detector has been so widely used for the past 15 years. For applications with a low radiation background, the Low bolometer is, now, gradually being replaced by new photoconductors, e.g. arsenic-doped silicon for 10μm and gallium-doped germanium for 100μm.

When better detectors became available, infrared astronomers began to make astronomical observations at the few wavelengths where the sea-level atmospheric transmission is relatively high. These are the so-called atmospheric "windows" and without them, ground-based infrared astronomy would be impossible. H.L. Johnson was one of the earliest and busiest workers in this field. In 1962, he defined four photometric bands between 1μm and 5μm and observed many stars at K(2.2μm) and L(3.6μm), providing revised effective temperatures and bolometric corrections. He followed this with the first observations of stars at 5μm, (Johnson and Mitchell, 1963), the first detection of an extragalactic object (3C273) in the infrared (Johnson, 1964) and the first observations through the 20μm atmospheric window (Johnson, Low and Steinmetz, 1965). The 10μm atmospheric window was opened by Murray and Wildey (1963), who detected the Moon, Jupiter and α Ori. The two atmospheric windows longwards of 20μm, i.e. at 35μm and 350μm, are both very poor and it is only recently that ground-based observations have been attempted at these wavelengths. Low, Rieke and Armstrong (1973) observed planets, stars and galactic nebulae between 28-40μm; Joyce, Gezari and Simon (1972) made the first reported 345μm observations (M17, M82 and Venus) although Low, Hoffmann and Harper have some earlier (1970) unpublished observations. To sum up, ground-based observations through the 1-14μm atmospheric windows are now commonplace, while those using the longer wavelength windows are still

relatively rare.

There are no atmospheric windows between 30μm and 300μm. Thus far-infrared observations have had to await the development of techniques for observing from above most of the atmosphere. At an altitude of 14km, the atmosphere has become fairly transparent (Traub and Stier, 1976) and so astronomical observations are possible from high flying aircraft. The telescopes used in aircraft have steadily increased in size from the 30cm telescope of Low, Aumann and Gillespie (1970) to the 90cm telescope in the Kuiper Airborne Observatory (Cameron, Bader and Mobley, 1971). Observations from still higher altitudes are possible by using balloon-borne instruments. These telescopes and their associated pointing systems have also grown in size and complexity from the pioneering 1" refracting telescope of Hoffmann and Frederick (1969), through medium size reflectors e.g. the 40cm system of Furniss, Jennings and Moorwood (1972) to the now routinely-flown telescopes larger than 1m (Fazio et al., 1974; Joseph et al., 1977; Drapatz, 1980.). A new concept in balloon-borne telescopes is to cool the entire telescope with liquid helium (Campbell, 1979). In the late sixties and early seventies, far-infrared and sub-millimetre observations were made from above the atmosphere with rocket borne telescopes e.g. the work on the cosmic background of Houck et al. (1972) and Williamson et al. (1973). The observing time on rocket flights is very short, about five minutes maximum. To date, no non-military observations have been made from telescopes in orbit, but missions planned include an Infrared Astronomical Satellite (IRAS), which has a liquid-helium-cooled 60cm telescope.

Needless to say, the first far-infrared astronomical object to be discovered was the sun. Its long wavelength spectrum was measured by Beer (1966) from a balloon and by Eddy et al. (1969) from an aeroplane. The moon was the only object detected by Hoffmann, Woolf and Frederick (1967) during their 350μm partial sky survey. Aumann, Gillespie and Low (1969) measured the far-infrared flux from three planets, Mars, Jupiter and Saturn. In the same year, the first 100μm extra-solar system object, the galactic centre, was discovered (Hoffmann and Frederick, 1969). The galactic HII regions, M17 and M42, were shown to have large far-infrared fluxes by Low and Aumann (1970), who also claimed the detection of a Seyfert galaxy, NGC 1068. This detection was not confirmed by Harper and Low (1973), but NGC 1068 was eventually found by Telesco, Harper and Loewenstein (1976). Thus, the credit for the detection of the first gal-

axies in this wavelength range must go to Harper and Low (1973) for finding NGC 253 and M82. In 1971 Hoffmann, Frederick and Emery published firstly, a 100μm map of the galactic centre region showing five peaks and secondly, a 100μm survey of the galactic plane, in which they found 72 sources and identified most of them with continuum radio sources, bright and dark nebulae and infrared stars.

During the rest of the seventies, many new groups, e.g. Furniss, Jennings and Moorwood (1972), Friedlander, Goebel and Joseph (1974) and Fazio et al. (1974) entered the field of far-infrared astronomy, and the number of sources known grew steadily. It is perhaps surprising that the first far-infrared detection of a planetary nebula occurred as late as 1977 (Telesco and Harper) and that it was a year later that extragalactic HII regions were first extensively studied (Werner et al., 1978).

Infrared astronomy has only been pursued during the last 15 or so years and far-infrared astronomy for just over half that time. It is a measure of the extreme youth of the latter subject that its entire observational literature prior to October 1979 can be contained in a single box file. Yet, even in this short period, infrared astronomy has established itself as a dynamic and productive discipline. Observations in its several octaves of the electromagnetic spectrum have ranged in distance from the solar system to other galaxies and in time from the origin of the universe to currently proceeding star formation. Jupiter and Saturn have been shown to radiate more energy than they receive (Aumann, Gillespie and Low, 1969); stellar infrared excesses in the near-infrared have been found and attributed to free-free emission or thermal re-radiation from circumstellar dust grains; planetary nebulae, HII regions and galaxies have been shown to radiate large amounts of energy in the far-infrared; and the spectrum of the cosmic microwave background has been measured in the far-infrared and millimetre regions (Woody and Richards, 1979).

As with all new fields, the initial rush was to detect as many new objects as possible, but now, techniques and sensitivities have improved sufficiently that more sophisticated observations can be made. Accurate photometry is being done on very faint sources, and polarimetric and spectroscopic observations are being made of many objects.

Chapter 2

Atmospheric Transmission and Emission

The aim of this chapter is to examine the behaviour of the atmosphere around the wavelengths of interesting astrophysical lines. A model of the atmosphere is described and transmission and emission spectra, calculated from this model, are presented.

2.1 General Problem

At sea level, the earth's atmosphere is opaque throughout most of the infrared region. The absorption is due to vibrational and rotational transitions of several different molecules, especially water and carbon dioxide. The few gaps, that exist between the molecular bands, lead to regions of relatively high transmission. These so-called 'atmospheric windows' (Table 2.1) permit some infrared astronomical observations to be made from the ground.

At low altitudes, the far-infrared (30μm - 300μm) region of the spectrum is totally obscured by the atmosphere, because all the absorption lines are very intense and so pressure-broadened that they overlap. However, the transmission through the residual atmosphere improves with height above the surface of the earth. In fact, the transmission around 100μm increases by an order of magnitude for each 15km. increase in altitude (Traub and Stier, 1976). Thus, at typical aircraft altitudes (13km.), the transmission over broad bands of the far-infrared region is adequate to permit astronomical observations, even though there are still a large number of deep absorption features.

These absorption lines must be examined in detail before attempting narrow-band spectroscopic observations with balloon- or aircraft-borne instruments. It is not sufficient for an astrophysical line to fall in a wavelength region where the overall atmospheric transmission is good, for there could be a telluric absorption feature at the same wavelength as the astronomical line, thus rendering its detection more difficult, if not impossible. When this is the case the severity of the absorption as a function of altitude must be calculated. The case of the 28μm line of molecular hydrogen is an interesting example of the value of this approach. Originally, this line was thought to be co-incident with an

Table 2.1

Designation	Mean Wavelength (μm)	Waveband (μm)	Quality of Window
J	1.25	1.1 - 1.4	Good
H	1.65	1.5 - 1.8	Good
K	2.2	2.0 - 2.4	Good
L	3.5	3.0 - 4.0	Lower Half, Fair Upper Half, Good
M	4.8	4.6 - 5.0	Poor
N	10	7.5 - 14	Fair except for Ozone at 9.6μm
(Q)	20	17 - 25	Very Poor
(Z)	35	28 - 40	Very Poor
-	350	330 - 370	Very Poor

(from Allen, 1975)

Atmospheric Windows.

atmospheric line, but subsequent calculations showed that, at high altitudes, the telluric feature split into two distinct lines, bracketing but not obliterating the hydrogen line (Drapatz and Michel, 1974).

The emission from the atmosphere is also of interest. As the absorption of the atmosphere varies with wavelength, so, by Kirchoff's law, does the emissivity. Thus, as the bandpass of the spectrometer is altered, the atmospheric radiation incident on the detector varies. This could cause uncertainty either in the detection of an astrophysical line or in measurement of its intensity with respect to the continuum of the astronomical source. Chopping should, in theory, eliminate this effect but, in practice, the cancellation will not be perfect due to inequalities in the two infrared beams. Therefore, the magnitude of the variations of emitted atmospheric flux with wavelength must be investigated.

Telluric absorption lines have one redeeming aspect. If detected and uniquely identified, they provide a wavelength calibration scale for the spectrometer (cf. section 5.3.4).

2.2 Objectives

The object of this chapter is to determine the atmospheric confusion around interesting astrophysical lines. In the absence of sufficient experimental data, it is necessary to compute theoretical spectra using model atmospheres.

In his work in this field, the author has been extensively guided by Kyle and Goldman (1975) and Traub and Stier (1976). Both of these papers present calculated transmission spectra for various altitudes at diverse spectral resolutions, and also give limited data on emitted atmospheric flux. The two sets of transmission spectra are very similar. The main difference is that, at balloon altitudes, the absorption lines of Traub and Stier (1976) are narrower and in general deeper than those of Kyle and Goldman (1975). This is because the lower resolution of the latter authors' output causes their lines to be artificially broadened. The transmission data from these two papers is of sufficient spectral resolution to be used for examining telluric-astronomical line co-incidences and for wavelength calibration. On the other hand, the flux data is too broad-band to investigate variations in atmospheric emission over small wavelength ranges. It was thus decided to calculate transmission and emission spectra at very high resolution over narrow spectral regions.

2.3 Computer Modelling of the Atmosphere

2.3.1 The Model

Firstly, the transmission through a homogeneous slab of atmosphere is calculated and then a simple modification is made so that the homogeneous transmission case becomes a good approximation to transmission through a real exponential atmosphere.

Following Traub and Stier (1976), consider radiation of intensity, I, passing through a slab of air of thickness, dh. The amount absorbed, dI, is given by

$$\frac{dI}{I} = -\eta\, k\, dh = -d\tau \quad , \tag{2.1}$$

where η is the air mass (related to the angle at which the radiation passes through the atmosphere) and τ is the optical depth. The absorption coefficient, k, can be rewritten as,

$$k = S\, F(\nu)\, n \quad , \tag{2.2}$$

where S is the line intensity in cm^{-1}/molecule cm^{-2}, $F(\nu)$ is a normalised line shape and n is the molecular number density. Equation 2.1 may be integrated over a homogeneous path of total length, H, to give

$$\tau = \int_0^H \eta\, S\, F(\nu)\, n\, dh = \eta\, S\, F(\nu)\, N \quad , \tag{2.3}$$

where N is the column density in molecules cm^{-2}. The other half of equation 2.1 may also be integrated to yield the transmission, T_υ,

$$T_\upsilon = \frac{I}{I_o} = e^{-\tau}. \tag{2.4}$$

Thus, by combining equations 2.3 and 2.4, a final expression for the transmission of the slab at a particular wavelength is obtained,

$$T_\upsilon = \exp(-\eta\, S\, F(\nu)\, N). \tag{2.5}$$

From here, it is only a small step to the flux, E_υ, emitted at a particular wavelength, assuming that the atmosphere is in thermal equilibrium,

$$E_\upsilon = (1-T)\ B_\upsilon \quad , \qquad 2.6$$

where B_υ is the Planck function, evaluated at the relevant wavelength and for the temperature of the isothermal slab of atmosphere. The line shape adopted for these calculations is the Lorentzian profile,

$$F_L(\nu) = \frac{\alpha/\pi}{\alpha^2+(\upsilon-\nu_o)^2} \qquad 2.7$$

where ν_o is the frequency of the transition and α the Lorentzian half-width. The validity of this assumption is discussed in section 2.3.4.

Both α and S are normally quoted at a standard temperature, T_o, and pressure, p_o, and thus a a correction must be applied if they are used in other circumstances. The half-width varies with temperature, T, and pressure (by definition) p as

$$\alpha = \alpha_o \frac{p}{p_o} \left(\frac{T_o}{T}\right)^{\frac{1}{2}} . \qquad 2.8$$

According to McClatchey et al. (1973), the line intensity is pressure independent but varies with temperature,

$$S(T) = S(T_o) \frac{Q_v(T_o)}{Q_v(T)} \cdot \frac{Q_r(T_o)}{Q_r(T)} \cdot \exp + \left[\frac{hc\ E(T-T_o)}{k\ T\ T_o}\right]. \qquad 2.9$$

where Q_v and Q_r are the vibrational and rotational partition functions respectively, E is the energy of the lower state of the transition and h, c and k have their normal meanings. The temperature dependence of the rotational partition function is given by $\left(\frac{T}{T_o}\right)^n$ where n is either 1.0 or 1.5 depending on the molecule. McClatchey et al. (1973) also tabulate the vibrational partition function at various temperatures. As this never deviates significantly from unity, it is not considered in the computations.

Up to this point, only a constant pressure atmospheric path has been considered. Traub and Stier (1976) compare the optical depth (i.e. transmission, eqn. 2.4) calculated for this case to that for an exponential

atmosphere above a base pressure, p_b. They find that the two average optical depths agree to within 1% for $(\nu-\nu_o) \gtrsim 5\alpha$, if an effective pressure, p_{eff}, equal to

$$p_{eff} = \tfrac{1}{2} p_b \qquad 2.10$$

is adopted for use in the Lorentzian line-broadening formulae.

Moreover, the real atmosphere is not isothermal. Nevertheless, adoption of a constant temperature - that which occurs at an altitude of p_{eff} - should be adequate for transmission calculations (Traub and Stier, 1976) although it would be desirable to use a variable temperature for computing atmospheric emission.

To use this model to calculate transmission and emission spectra, it is necessary to know what molecular species are responsible for the absorption, where their transitions are, how intense and wide these lines are, and how many molecules of each species are present. The next two sections of this chapter deal with evaluating these parameters.

2.3.2 The AFCRL Tape

Data on the transitions of important infrared-absorbing molecules in the terrestrial atmosphere have been collated by McClatchey *et al*. (1973) and made available in the form of a computer magnetic tape entitled "The Air Force Cambridge Research Laboratories Atmospheric Absorption Line Parameters Compilation". The tape contains information on over 100,000 transitions of seven molecules (water vapour, carbon dioxide, ozone, nitrous oxide, carbon monoxide, methane and oxygen) covering a spectral range from 1μm to beyond 3mm. The following data is given for each line: the resonant frequency, ν_o; the line intensity, S_o at a temperature of 296K; the Lorentz line width, α_o, at a temperature of 296K and a pressure of 1013mb; the energy, E, of the lower state of the transition; the rotational and vibrational quantum numbers of the upper and lower states; and molecular and isotopic identifications.

Both Kyle and Goldman (1975) and Traub and Stier (1976) point out omissions in the AFCRL compilation. However, none of these missing lines fall in spectral regions where calculations are made and they are therefore ignored.

2.3.3 Molecular Abundances

In order to calculate the atmospheric transmission from equation 2.5, the column densities, N, of the relevant molecules must be known. In most references, however, abundances are quoted in parts per million (ppmv) or, more rarely, by mass (ppmm). The volume mixing ratio, fv, can easily be converted to molecules cm^{-2} because,

$$fv = \frac{N}{N_T} \quad , \qquad 2.11$$

where N_T is the total column density. If the atmosphere is assumed to be in static equilibrium, then the pressure, p_b, at any level is due to the weight of molecules in the column above that level, i.e.,

$$p_b = N_T \, \overline{m} \, g \quad , \qquad 2.12$$

where $\overline{m}$ is the atmospheric mean molecular weight (constant at 28.964 below 80km., U.S. Standard Atmospheres Supplement, 1966) and g is the local acceleration due to gravity. Thus, N_T can be evaluated from p_b. Values for p_b and g were obtained from the U.S. Standard Atmosphere (1962) and are listed in table 2.2 together with the calculated values for N_T.

There is disagreement in the literature concerning both the amount of 'trace' gases in the atmosphere and also their variation in concentration with altitude. Thus, there must be a degree of arbitrariness in choosing molecular abundances. The references in Traub and Stier (1976) were used as the starting point in the search for abundances.

The adopted volume mixing ratios for carbon dioxide, carbon monoxide and oxygen are essentially the same (to within, at worst, 25%) as those quoted by Traub and Stier (1976) and Kyle and Goldman (1975). All the measurements of the abundance of water vapour quoted by Traub and Stier (1976) have large errors and show no definite trend with altitude. So, a rough average of 2.6 ppmv is adopted, even though this is just outside the range of 3-10 ppmv reported by Ehhalt (1974) and a factor of ten less than that used by Kyle and Goldman (1975), who quote no source for their value. The ozone volume mixing ratio comes from table 4.17 in the U.S. Standard Atmosphere (1962). The column densities derived from this are overestimates, probably by up to a factor of two, because the ozone

Table 2.2

Atmospheric Parameters Used for Computer Model.

ALTITUDE Km	P_b mb.	P_{eff} mb.	T_{eff} K	g cms^{-2}	N_T cm^{-2}	MOLECULAR ABUNDANCES													
						H_2O		CO_2		O_3		N_2O		CO		CH_4		O_2	
						fv	N	fv	N	fv	N	fv	N	fv	N	fv	N	fv	N
30	11.97	5.99	235.7	971.5	2.542×10^{23}	2.6	6.61×10^{17}	325	8.26×10^{19}	6.81	1.73×10^{18}	0.12	3.05×10^{16}	0.06	1.53×10^{16}	0.7	1.78×10^{17}	209470	5.32×10^{22}
35	5.75	2.88	250.4	970.0	1.223×10^{23}	2.6	3.18×10^{17}	325	3.97×10^{19}	7.86	9.61×10^{17}	0.09	1.10×10^{16}	0.06	7.34×10^{15}	0.6	7.34×10^{16}	209470	2.56×10^{22}
40	2.87	1.44	265.0	968.4	6.115×10^{22}	2.6	1.59×10^{17}	325	1.99×10^{19}	7.64	4.67×10^{17}	0.07	4.28×10^{15}	0.06	3.67×10^{15}	0.4	2.45×10^{16}	209470	1.28×10^{22}

Units of f_v are ppmm.
Units of N are cm^{-2}.

mixing ratio peaks at 35km and then falls rapidly with further increase in altitude. For nitrous oxide, data from Goldman et al. (1970, 1973), Farmer (1974), Ehhalt (1974), Harries (1973) and Schütz et al. (1970) were examined. No absolutely clear picture emerged and a slow decline in the concentration of nitrous oxide with altitude (unlike Traub and Stier, 1976) is used. The concentration of methane is assumed to decrease with height after comparing Allen (1976), Lowe and McKinnon (1972), Farmer (1974), Ackerman and Muller (1972) and Ehhalt (1974). The adopted molecular abundances and column densities of all these species at different altitudes are listed in table 2.2.

2.3.4 Computational Details

The computer programme used to calculate atmospheric transmission and emission is a very slightly modified version of that given in appendix B of McClatchey et al. (1973). In essence, the programme calculates the transmission at a series of closely-spaced frequencies and then convolves these values with a triangular slit function before printing out the averaged results.

In slightly more detail, the programme decodes the AFCRL tape, supplies any line half-widths that are missing from the tape and then modifies the line intensity and half-width for the relevant pressure and temperature according to equations 2.8 and 2.9. The user defines a spectral band for the calculations; the programme then searches for all absorption features, whose line centres fall within a given distance of the initial frequency of this band. The absorption per molecule due to each relevant line of each molecule is calculated (eqn. 2.2) and then, after multiplying by the correct abundance, the individual absorptions are summed over all lines to give the integrated optical depth at that frequency (eqn. 2.3). From this, the transmission is calculated by equation 2.4. This process is repeated again and again, each time at a slightly higher frequency until the end of the desired spectral band is reached. The frequency increment is specified by the user at the start of the programme. These monochromatic transmissions are then convolved with a triangular slit function of user-defined half-width, before the atmospheric emission is calculated using equation 2.6. Next, both the transmission and emission spectra are written onto a magnetic tape, which is later processed, using the Interactive Graphics Facility of the Imperial College Computer Centre, to yield the plots shown in section 2.4.

A Lorentzian profile is used for all the absorption lines. This means that both the inaccuracies of the Lorentzian shape in the wings and also any contribution from Doppler broadening are neglected. Originally, it was planned to replace the Lorentz profile with a Voigt profile (a convolution of the Doppler and Lorentz shapes) when the rest of the programme was working but time prevented this. At balloon altitudes, Doppler broadening dominates over pressure for wavelengths less than 100μm. Thus, usage of a Lorentzian profile will introduce some uncertainty into the results.

2.3.5 Brief comparison with other models

This is not a full comparison of different models. Rather, various points about the models used by Traub and Stier (1976) and Kyle and Goldman (1975) are mentioned so that a more meaningful comparison of their results with those presented in the next section may be made.

Traub and Stier (1976) use a very similar model with a single layer, constant temperature and pressure atmosphere, but they use a Voigt line shape where necessary and also correct the line intensity for a stimulated emission term. For species that are not well-mixed, i.e. those whose concentration varies with height, they use different effective temperatures and pressures. The model of Kyle and Goldman (1975) is more sophisticated, splitting the atmosphere into seven homogeneous layers and adopting the Voigt profile for all lines.

2.4 Results

Atmospheric transmission and emission spectra have been calculated at three different balloon altitudes for nine astrophysical lines. The results, presented in figures 2.1 to 2.8, are plotted at a resolving power of around 5000; the wavelength range covered for each line is approximately equivalent to a resolving power of 12. The abscissa in the emission plots is the energy (in Watts) collected from the atmosphere by a 41-inch aperture telescope with a 3 arc minute field of view and a one micron spectral bandpass. It is assumed that the detector optics are well-matched to the telescope and thus no allowance is made for any atmosphere seen around the edge of the secondary mirror.

The transmission spectra show clearly that at balloon altitudes all of these nine lines are free from serious atmospheric confusion. The

Figure 2.1

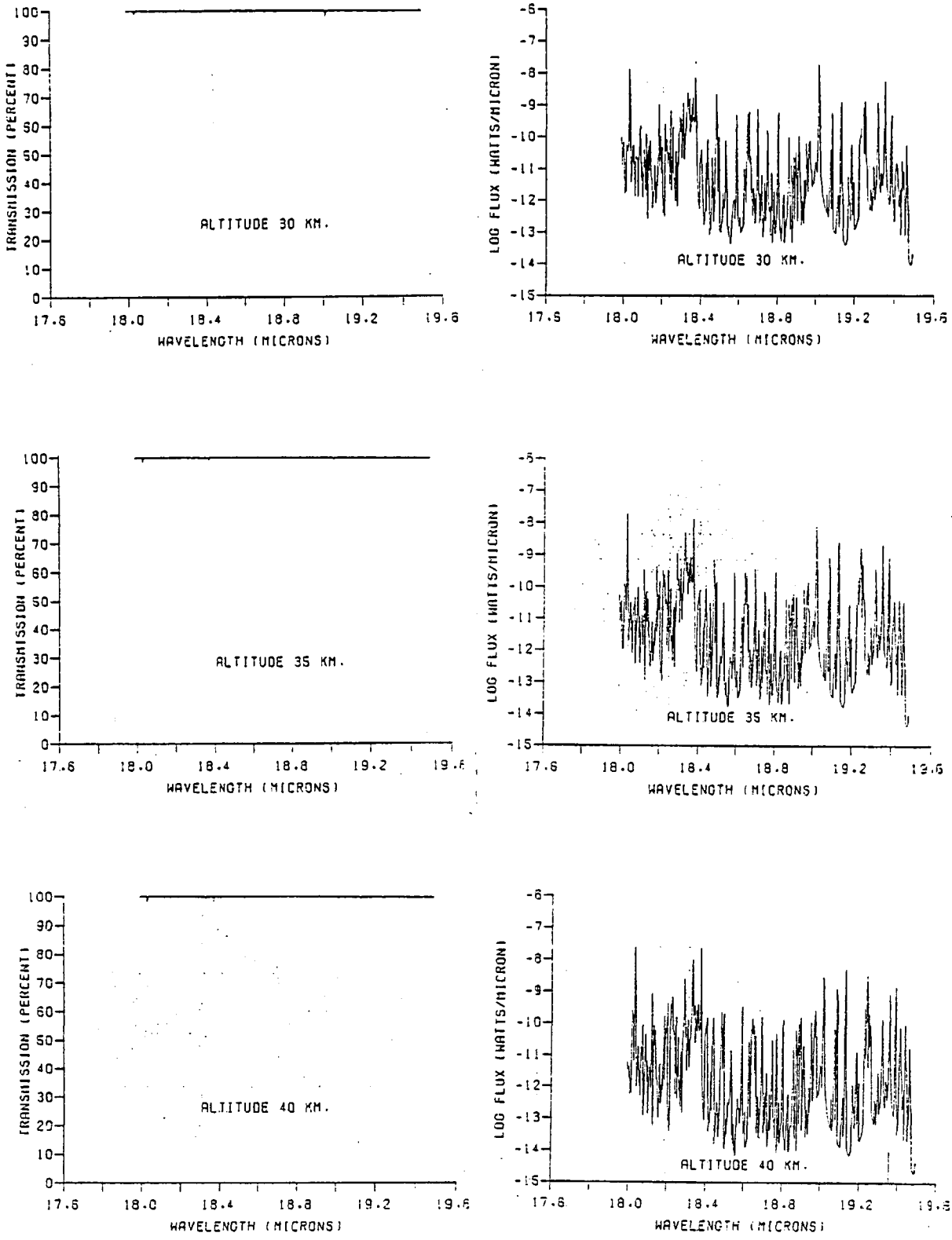

Atmospheric Transmission and Emission near the 18.71μm [SIII] line.

Figure 2.2

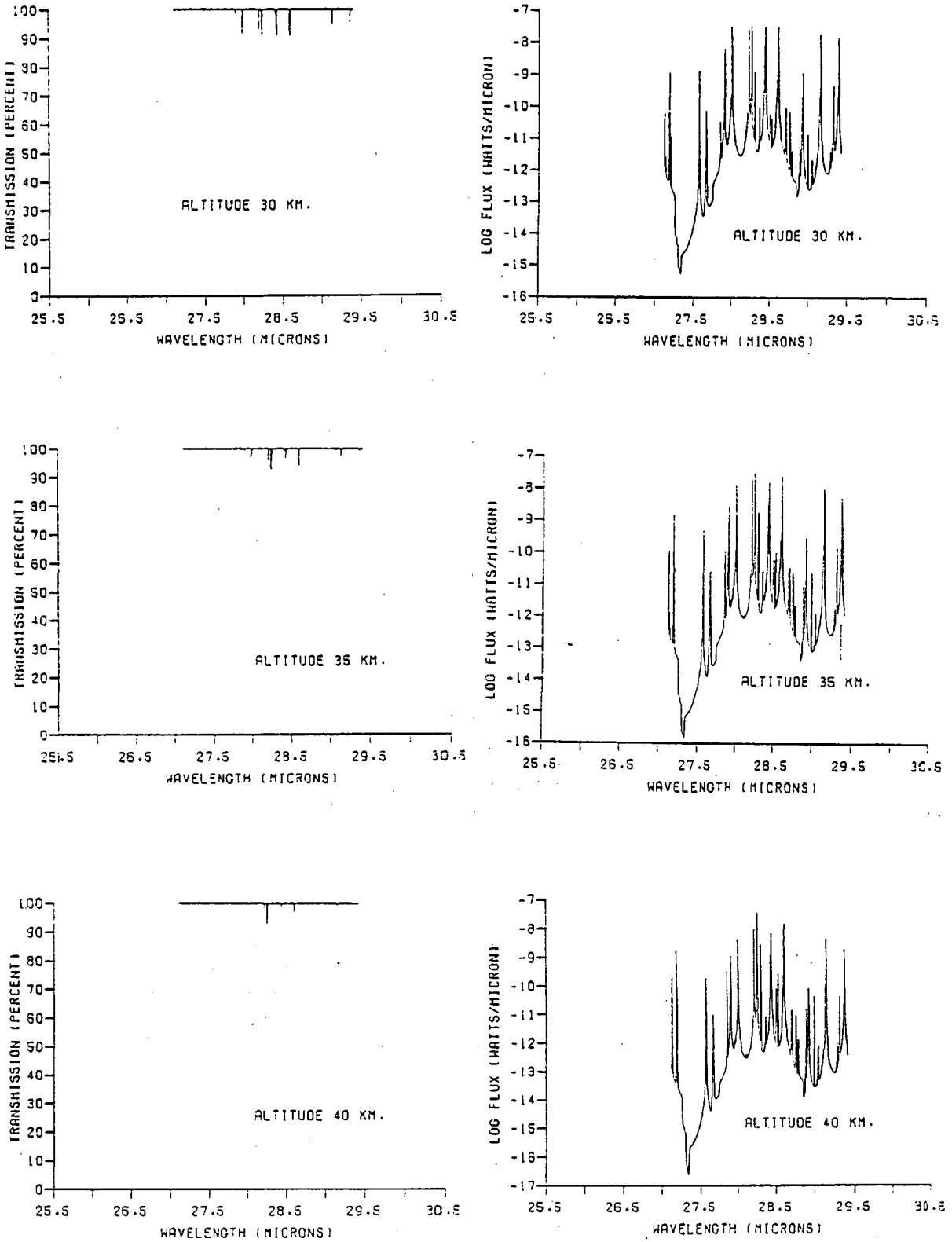

Atmospheric Transmission and Emission near the 28.22μm H_2 line.

Figure 2.3

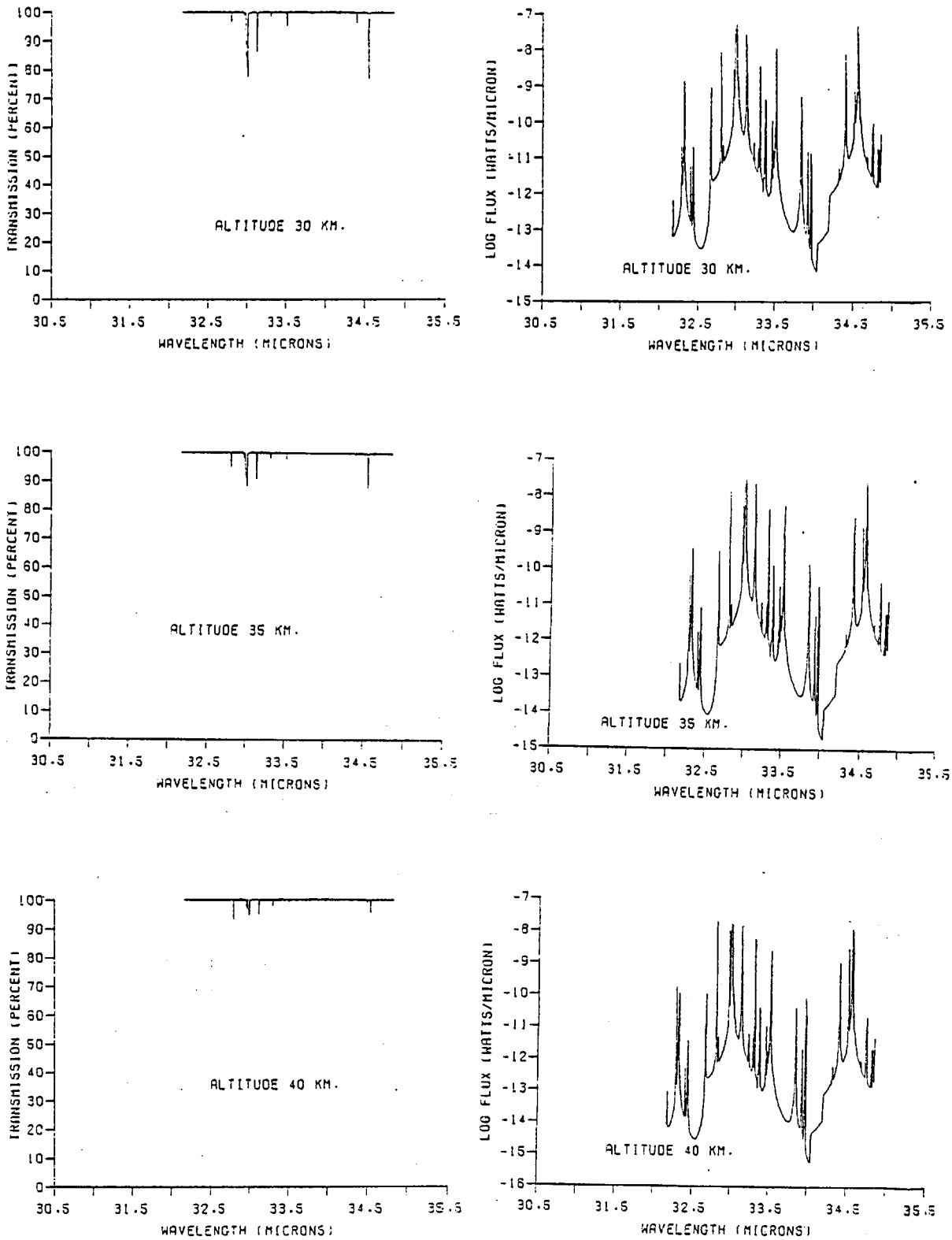

Atmospheric Transmission and Emission near the 33.44μm [SIII] line.

Figure 2.4

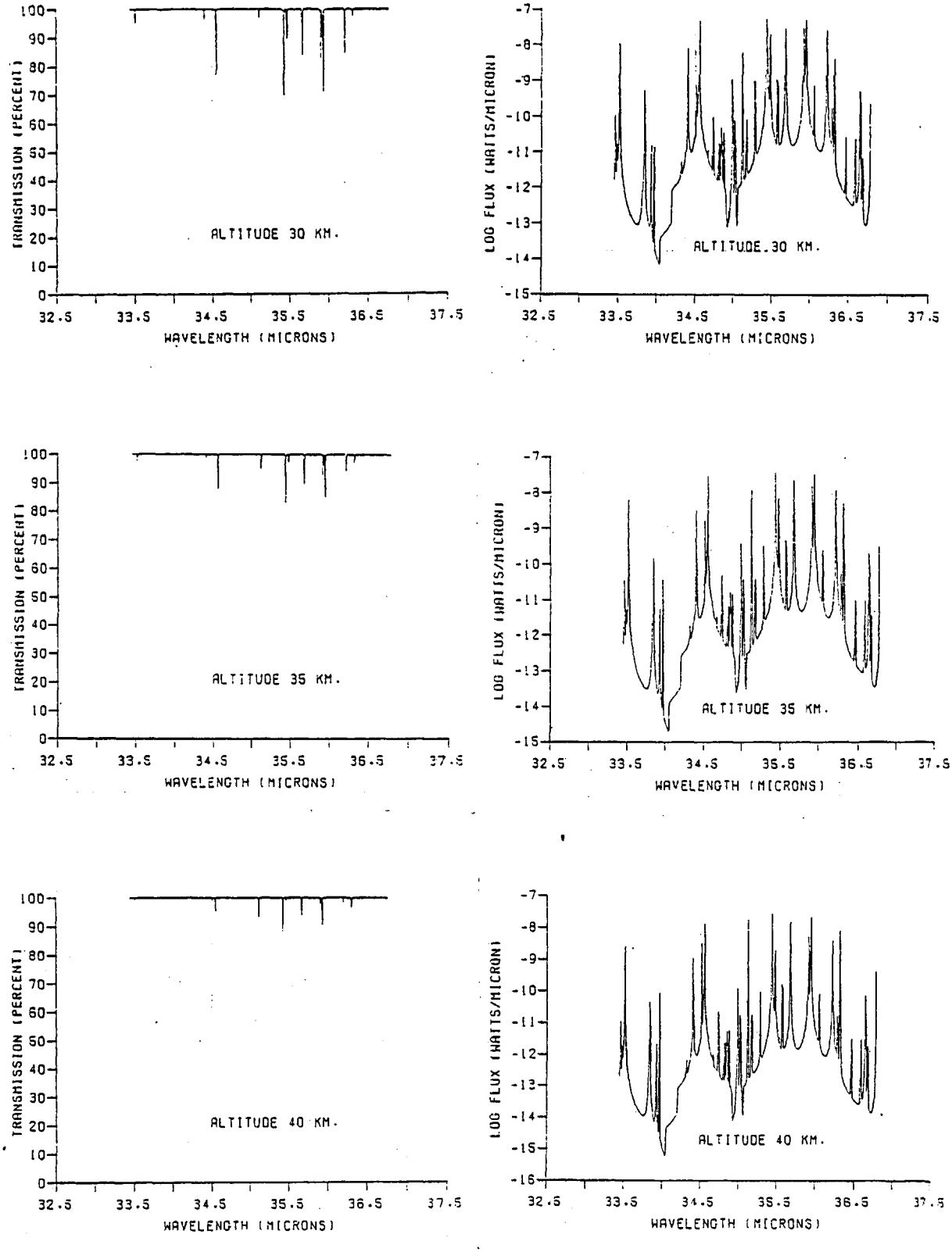

Atmospheric Transmission and Emission near the 34.80μm [SiII] and 35.3μm [FeII] lines.

Figure 2.5

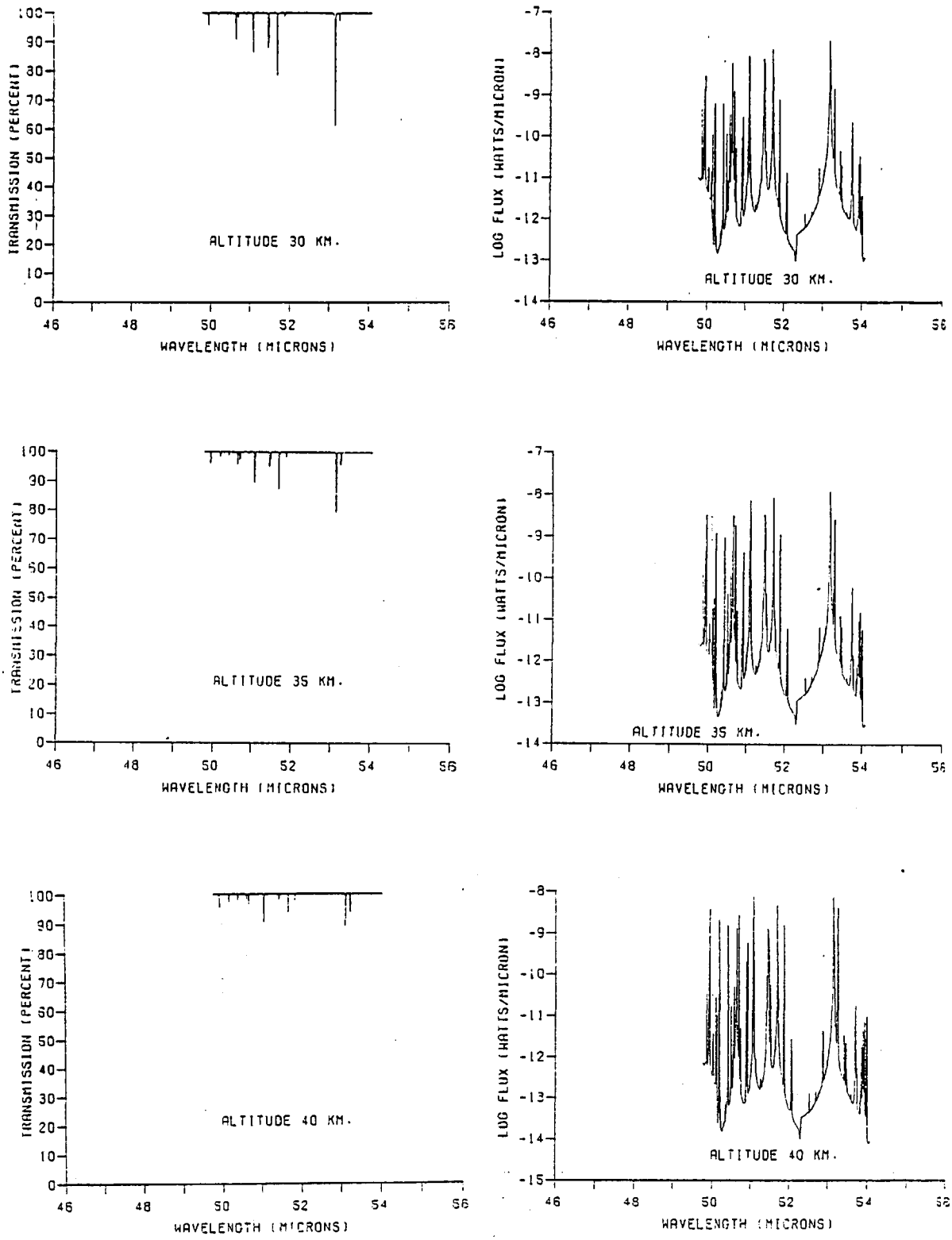

Atmospheric Transmission and Emission near the 51.82μm [OIII] line.

Figure 2.6

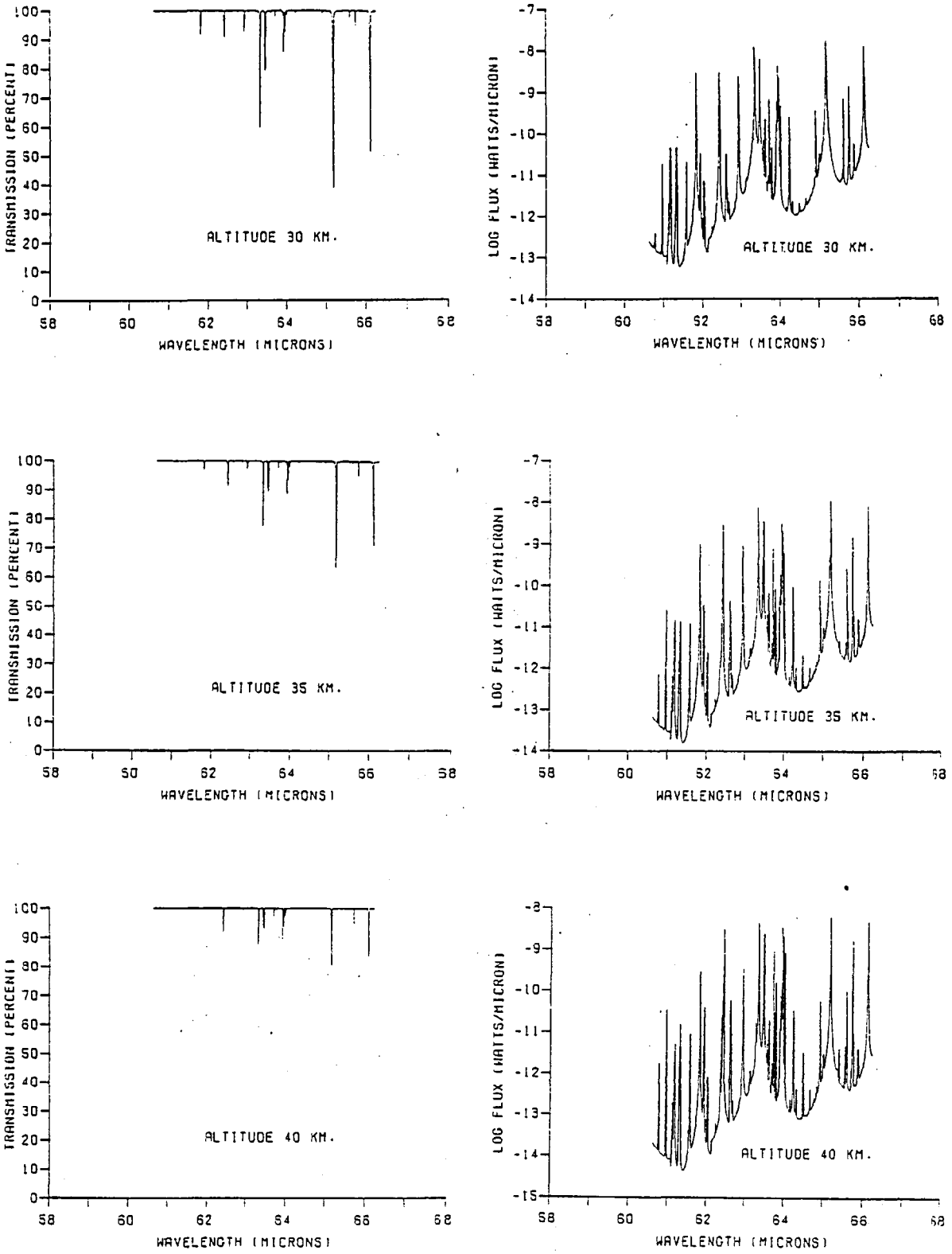

Atmospheric Transmission and Emission near the 63.17μm [OI] line.

Figure 2.7

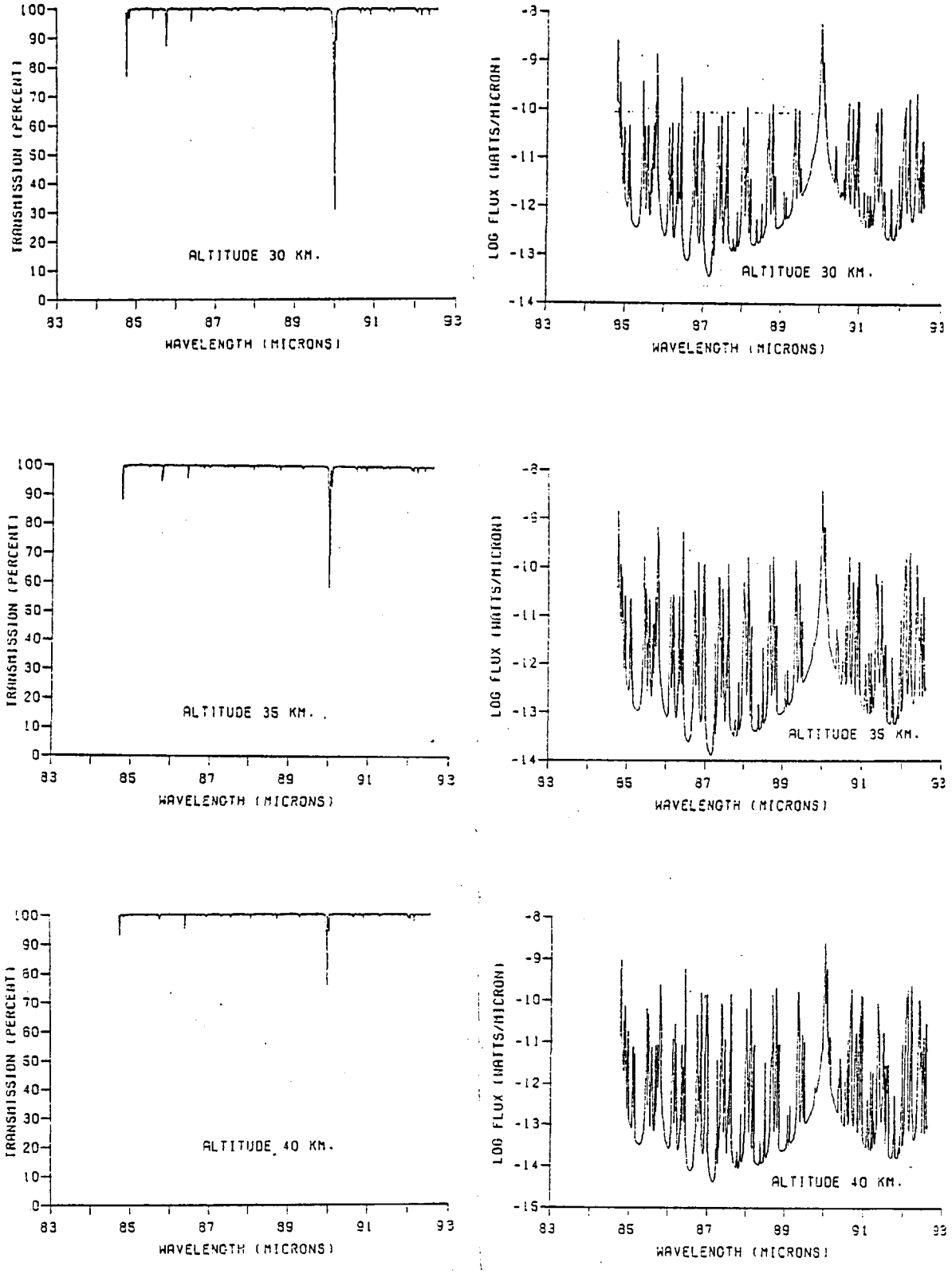

Atmospheric Transmission and Emission near the 88.37μm [OIII] line.

Figure 2.8

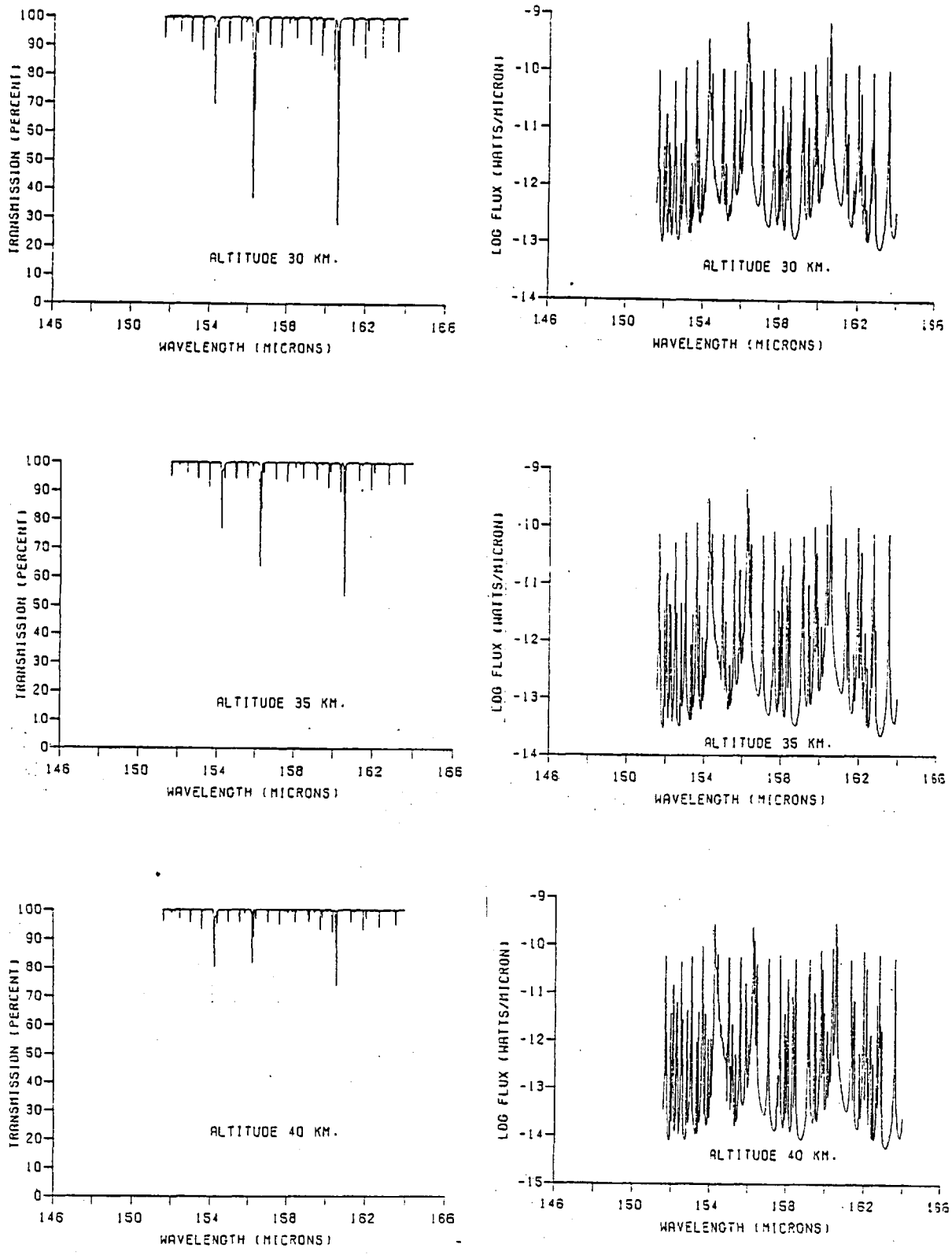

Atmospheric Transmission and Emission near the 157.2μm [CII] line.

worst case is the molecular hydrogen line which, as expected, is bracketed by two atmospheric features (cf. section 2.1). A resolution in excess of 2000 is needed to separate the 28μm line from the telluric absorption lines. Of the remaining astrophysical lines, those of [OIII] at 52μm and [OI] are the closest to atmospheric lines. However, even these two only need a resolving power of 400 to be discerned from the atmosphere. At balloon altitudes the atmosphere is almost totally transparent for the 18.7μm [SIII] line; this is not surprising as this line has been successfully detected from the ground (Greenberg et al., 1977). The 88μm [OIII] line is also very free of atmospheric contamination, needing a resolution of only 45 for unambiguous detection.

The emission spectra of the atmosphere near each of the nine lines are very similar. At an altitude of 30km, the flux collected by the telescope varies rapidly from $\sim 10^{-13}$W μm^{-1} to $\sim 10^{-8}$W μm^{-1}; ten kilometres higher, this has fallen by a factor of ten. The general shape of the emission spectra is roughly the inverse of that of the transmission curves with an additional fast modulation. This variation arises because as the transmission of the atmosphere changes from e.g. 0.9990 to 0.9999, the emission, as calculated by equation 2.6, varies by an order of magnitude! Thus, the emission is very sensitive to the accuracy of the atmospheric model. In view of the simplicity of the latter, the emission spectra should be used as a guide to the behaviour of the atmosphere, rather than as hard data.

The transmission spectra of figures 2.1 to 2.8 were compared with those of Kyle and Goldman (1975) and Traub and Stier (1976) for both the wavelengths of absorption lines and also the atmospheric transmission at the line centre. The three sets of spectra agree on the positions of all absorption features, bar one. The exception is a line at 86.7μm in figure 2.7. However, since the depth of this feature does not change with altitude, it is presumed to be a computer artifact. The atmospheric transmissions at the line centres, as calculated in this work, are substantially higher than those of Kyle and Goldman (1975) and Traub and Stier (1976), which agree reasonably well with each other. The discrepancy is worst at short wavelengths. The reason for the difference should not take too much additional work to locate (cf. chapter 7). Possible causes include adoption of different molecular abundances and over-simplifications in the model.

2.5 Conclusions

A very simple atmospheric model has led to results similar to those obtained by other authors using more sophisticated models. Further work is needed, firstly, to determine why the absorption features calculated in section 2.4 are less intense than those calculated by other authors, and secondly, to examine the accuracy of the emission spectra. However, from the work described in this chapter, it is clear that the atmosphere does not rule out detection of any of these astrophysical lines. The easiest lines to discriminate are those of [SIII] at 18.7μm, [OIII] at 88μm and [CII] at 157μm.

Chapter 3

Choosing Target Lines

The purpose of this chapter is to describe the selection of candidate lines for the IC programme of infrared spectroscopy. Some recent theoretical work on estimating intensities of infrared lines is examined under the headings of gaseous nebulae (i.e. HII regions and planetary nebulae) and the cool interstellar medium. Several lines are chosen for study on the basis of predicted intensities, freedom from atmospheric contamination and technical feasibility.

3.1 Gaseous Nebulae

Before examining the predicted line intensities, the general features of the models used to make these estimates are presented.

3.1.1 Atomic Processes

The intensity of a certain fine structure line from a particular ion depends upon the population of the relevant excited energy level of the relevant stage of ionisation. Thus, both the ionisation structure of the nebula and also the relative populations of the energy levels need to be known. Ionisation equilibrium is established by a balance between photoionisation and radiative recombination. The level populations are determined by competing excitation and de-excitation processes. In cases of interest to the present work, these are dominated, respectively, by electron-ion collisions and by spontaneous radiative decay.

An outline of the formal method used to deduce the ionisation equilibrium of a nebula is now given. If the processes of photoionisation and radiative recombination are in equilibrium, then the ionisation balance equation is,

$$n(X^{+m}) \int_{\nu_o}^{\infty} 4\pi J_\nu \, a_\nu(X^{+m}) \, d\nu = n_e \, n(X^{+m+1}) \, \alpha(X^{+m}) \quad , \qquad 3.1$$

where $n(X^{+m})$ is the number density at a point of element X, m-times ion-

ised; ν_o, the threshold frequency for ionisation; J_ν, the mean intensity of the radiation field; $a_\nu(X^{+m})$, the photoionisation cross-section for X^{+m} in the ground state; n_e, the electron number density; and $\alpha(X^{+m})$, the radiative recombination coefficient. Following Flower (1969), it is seen that in order to specify fully the ionisation structure, equation 3.1 must be solved together with the equation of radiative transfer,

$$\frac{dI_\nu}{ds} = j_\nu - \kappa_\nu I_\nu \quad , \qquad 3.2$$

where I_ν is the specific intensity at a point, j_ν, the photon emission coefficient (or emissivity) at the point; κ_ν, the opacity, and ds, a path length element, for each and every ion present. These two equations are coupled together by the opacity,

$$\kappa_\nu = \sum_{X^{+m}} n(X^{+m})\, a_\nu(X^{+m}) \quad , \qquad 3.3$$

and by the mean intensity,

$$J_\nu = \frac{1}{4\pi} \iint I_\nu d\Omega . \qquad 3.4$$

By making suitable approximations for I_ν and neglecting the contribution to equation 3.3 of all elements heavier than helium, J_ν is found at all points in the nebula. Then, using known values for a_ν and α, equation 3.1 is solved to give a ratio, R_m, between the number of ions in successive ionisation stages for each ion, where,

$$R_m = \frac{n(X^{+m})}{n(X^{+m-1})} \quad . \qquad 3.5$$

The number density of m-times-ionised element X, obtained from equation 3.5 and the conservation equation, $n(X) = \sum_m n(X^{+m})$, is,

$$n(X^{+m}) = \frac{R_1 R_2 \ldots\ldots\ldots R_m}{(1+R_1+R_1R_2+\ldots.)} \quad \frac{n(X)}{n(H)} \quad n(H) \quad , \qquad 3.6$$

where n(H) is the hydrogen number density. Thus, the population of any ionisation stage can be found if the total abundance relative to hydrogen is known. This is a major source of error in predictions of line intensities because it is inferred from measurement of observable ionisation stages. Simpson (1975) estimates that it may be uncertain by factors of at least x2 to x3.

However, most of the authors who have made fine structure line intensity predictions do not use the formal approach described above. Instead, they use either model or observed ionisation structure for one element, and apportion similarly the other elements among their ionisation stages according to their ionisation potentials e.g. Delmer, Gould and Ramsay (1967). This semi-empirical determination of ionisation structure is throught to introduce errors of around 25% (Simpson, 1975).

Once the distribution of an element among its various ionisation stages is known, the next step, in the calculation of fine structure intensities, is the determination of the level populations. In the steady state, the population, n_i, of a given level, i, may be found by applying the principle of detailed balance to that level,

$$n_i \sum_k P_{ik} = \sum_k n_k P_{ki} \quad , \qquad 3.7$$

where n_k is the population of level k; P_{ik}, the transition probability per unit time for depopulating level i to any other level, k; and P_{ki} the transition probability per unit time of populating level i from any other level k. In general, P_{ik} contains terms for depopulating level i by spontaneous decay, stimulated emission and collisional de-excitation to lower levels and by collisional excitation and stimulated absorption to higher levels. In the same way, P_{ki} contains contributions to populating level i via spontaneous decay, stimulated emission and collisional de-excitation from higher levels and via collisional excitation and stimulated absorption from lower levels. The collisions referred to above are between electrons and ions. There are other processes for populating levels e.g. proton-ion collisions, photo-ionisations, radiative recombinations, but these are usually assumed to be negligible. Even the direct photon (de)excitations are normally ignored unless the nebula has a large J at the line frequency. Solving equation 3.7 together with the conservation equation, $n(\text{total}) = \sum_i n_i$, gives the level populations.

From here, it is only a small step to calculate the line intensity for the transition i→j. The equation of radiative transfer (equation 3.2) must be solved around the line frequency, υ. The emissivity in the line is given by,

$$j_\nu = \frac{h\nu}{4\pi} A_{ij} n_i \quad , \qquad 3.8$$

where A_{ij} is the Einstein spontaneous transition probability for the transition. The opacity is no longer given by equation 3.3 but rather by,

$$\kappa_\nu = \frac{d\tau_\nu}{ds} = \frac{h\nu}{4\pi} \phi_\nu (B_{ji} n_j - B_{ij} n_i) \quad , \qquad 3.9$$

where τ_ν is the optical depth; ϕ_ν, a profile function; B_{ji} and B_{ij}, the Einstein stimulated absorption and emission coefficients respectively, and n_j, the population of the lower level. The solution to equation 3.2 is now,

$$I_\nu = \int_0^\ell j_\nu \, \phi_\nu \, e^{-\tau_\nu} \, ds \, , \qquad 3.10$$

where ℓ is the depth of the nebula along the line of sight, and negligible incident radiation at the line frequency has been assumed. The line intensity from the entire nebula is found by integrating equation 3.10 firstly over the line profile and then over the surface of the nebula.

3.1.2 Predictions

Burbidge, Gould and Pottasch (1963) first showed that the cooling process in nebulae, with electron temperatures less than 10^4K, was dominated by infrared fine structure lines. Since then, other authors, using variations and approximations to the scheme described in section 3.1.1, have made predictions about the fluxes from planetary nebulae and HII regions. Planetary nebulae are considered first.

Delmer, Gould and Ramsay (1967), using optical line data, estimate the intensities for lines falling in the 10μm and 20μm atmospheric windows from nine bright planetary nebulae. In general, these fluxes are too

high by a factor of approximately x15. Flower (1970) applies his previously-developed computer models (Flower, 1968) to three planetary nebulae and calculates fine structure intensities relative to absolute Hβ fluxes. He also calculates the expected intensity ratio for several pairs of lines arising from p^2 and p^4 configurations as a function of electron number density. The variation of the emission and absorption coefficients with n_e is calculated by Simpson (1975) for many forbidden lines. She discusses the effect of self-absorption, defining density parameters at which collisional de-excitation and stimulated absorption and emission become important. Observed line strengths are used by her to calculate ionic abundances for SIV, NeII and ArIII. She then reverses the procedure, and using a model for ionisation structure, predicts line intensities from many planetary nebulae. Table 3.1 compares these three sets of predictions with experimental results for various lines from a low-excitation nebula (IC418), a high excitation one (NGC 7662) and one (NGC 7027) which shows both low and high ionisation stages, thus indicating density clumping. The later predictions are generally lower than those of Delmer, Gould and Ramsay (1967) and are closer to observed values.

Petrosian (1970) notes that the lower density of HII regions makes them more suitable for observations of the longer wavelength lines. He assumes that the electron temperature is high enough to neglect its effect on collisional excitation rates and calculates line intensities and intensity ratios for the Orion Nebula. A method is also given for scaling the Orion intensities to other HII regions. Simpson (1975) uses her model (Simpson, 1973) to estimate the infrared line spectrum of M42. Her predictions are compared with those of Petrosian (1970) and also, with measured values in table 3.2. Although the estimates of Simpson (1975) are the more accurate, they are usually still too high. Zeilik (1977) comments that M42 is the only HII region for which detailed calculations had been made (at the time). He developed a model, which contains both graphite and silicate dust, to match the observed radio and near-infrared emission. This model is used to calculate emissivities of many lines from four compact HII regions. He predicts very strong iron lines (e.g. 2×10^{-16} W cm^{-2} at the earth in the 35μm [FeII] line from G45.5-0.0), but points out that this may be due to adoption of solar, rather than interstellar, iron abundances. The latter could be up to x100 less (cf. section 1.5.2). For the 10μm atmospheric window lines, the predictions of Zeilik (1977), where tested, are too low (cf. table

Table 3.1

Line	Nebula	Intensity (in units of 10^{-18} W cm^{-2})			
		Delmer, Gould & Ramsay	Flower	Simpson	Measured
8.99 ArIII	IC418	10	[a]0.2	3.7	<4.6[c]
	NGC7662	4	0.05	1.9	<90[c]
	NGC7027	70	-	-	10[d],4.3[e]
10.5 SIV	IC418	<1	[a]2.4	2.9	<1.5[c]
	NGC7662	~100	[b]0.5	-	9[b]
	NGC7027	~100	-	-	36[c],35[f],51[g]
12.8 NeII	IC418	~300	[a]35	6.8	21[h]
	NGC7662	<1	[b]0.2	2.5	<180[c]
	NGC7027	4	-	23	<18[c]
18.7 SIII	IC418	10	[a]8	11	-
	NGC7662	3	[b]0.05	0.16	-
	NGC7027	50	-	14	15[i]
33 SIII	IC418	-	[a]8	2.6	-
	NGC7662	-	[b]0.05	0.08	-
	NGC7027	-	-	5.3	-
52 OIII	IC418	-	[a]8	5.3	-
	NGC7662	-	[b]6.8	20	-
	NGC7027	-	-	120	-
88 OIII	IC418	-	[a]1.1	0.72	-
	NGC7662	-	[b]1.1	4	-
	NGC7027	-	-	21	<20[j]

Notes

a. Hβ flux is 8×10^{-17} W cm^{-2} (Allen, 1976).
b. Hβ flux is 25×10^{-17} W cm^{-2} (Allen, 1976).
c. Holtz, Geballe and Rank, 1971.
d. Geballe and Rank, 1973.
e. Bregman, 1978.
f. Gillett, Merrill & Stein, 1972.
g. Aitken and Jones, 1973.
h. Gillett and Stein, 1969.
i. Greenberg, Dyal & Geballe, 1977.
j. Watson, Storey & Townes, 1979.

Predicted Fine Structure Line Intensities from Planetary Nebulae

Table 3.2

Line	Intensity (in W cm^{-2})		
	Petrosian	Simpson	Observed
8.99 ArIII	$3x10^{-15}$	$3.65x10^{-16}$	[a] $1.77x10^{-17}$
10.5 SIV	$1x10^{-13}$	$1.39x10^{-14}$	[a] $2.44x10^{-17}$
12.8 NeII	$4x10^{-14}$	$2.92x10^{-15}$	[a] $8.1x10^{-18}$
18.7 SIII	$2.1x10^{-14}$	$1.19x10^{-14}$	[b] $1.4\text{-}2.4x10^{-15}$ [c] $5.2\text{-}7.9x10^{-15}$
33 SIII	$1.7x10^{-14}$	$1.12x10^{-14}$	[c] $<1.6x10^{-15}$
52 OIII	$1.5x10^{-14}$	$5.84x10^{-15}$	[d] $7x10^{-15}$
88 OIII	$3.9x10^{-15}$	$2.71x10^{-15}$	[e] $1.2x10^{-16}$ [f] 1×10^{-15}

Notes

a. Lester, Dinerstein and Rank, 1979.
b. McCarthy, Forrest and Houck, 1979.
c. Moorwood et al., 1978 (Size of Nebula taken from Simpson, 1975).
d. Melnick et al., 1979b.
e. Storey et al., 1979.
f. Dain et al., 1978.

Predicted Fine Structure Line Intensities from the Orion Nebula

3.4) but for longer wavelengths they are reasonably consistent with observations.

In the course of modelling the effects of young, expanding HII regions upon the surrounding molecular clouds, Hill and Hollenbach (1978) examine the expected infrared line radiation. They find that the lines cooling the shock front come from quadrupole transitions of molecular hydrogen and fine structure transitions of OI, CII, SiII and FeII. The majority of the energy removed by the last three species comes from the HII region itself (Zeilik, 1977), and not from the shock front, which is primarily cooled by OI lines at 63μm and 147μm. There is also some [OI] emission from the following ionisation front. The shocked molecular emission is weak; the 2μm 1-0 S(1) molecular hydrogen line from the shock is about 100 times less intense than the [OI] lines. Molecular hydrogen emission can also be caused by UV pumping of the molecule. The emission produced in this way from the v=0 rotational states is expected to be similar to that from the shock front, while the UV pumped 2μm S(1) line may be about 100 times stronger than the corresponding shocked emission. When carbon monoxide is added to their models, Hill and Hollenbach (1978) find that cooling via its rotational transitions is dominant, although the 63μm [OI] line remains the most important single transition. For an integration time of 400s per resolution element, they conclude that "the 63μm and 147μm lines of OI, S(2) - S(7) v=0 lines of H_2 and the 1-0 S(1) line of H_2 are predicted to be of observable strength".

3.2 The cool interstellar medium

Pottasch (1968) estimates the infrared line fluxes from both normal and also small, dense HI regions. For normal HI regions, he assumes that the general interstellar radiation field ionises all elements with ionisation potentials less than 13eV and that cosmic rays cause about 5% of each element to be further ionised. He considers clouds at different temperatures and chooses their sizes to give a specific 21cm brightness temperature. By assuming that the dominant excitation and de-excitation processes are electron collisions and spontaneous decay, he predicts the intensity at the earth for many transitions. The strong lines include the 156μm (now 157μm) transition of [CII] ($4\text{-}8\times10^{-13}$ W cm^{-2}) for clouds of temperature 100K to 2000K), the 35μm [SiII] line ($1\text{-}14\times10^{-13}$ W cm^{-2}), the 63μm [OI] line ($1.6\text{-}4.6\times10^{-13}$ W cm^{-2}) and the 28μm H_2 line

$(1.6\text{-}42 \frac{n(H_2)}{n(H)} \times 10^{-13}$ W cm^{-2}) if $n(H_2)/n(H) \gtrsim 0.1$. For the dense regions, cosmic ray ionisation is negligible and the general radiation field is unable to penetrate the entire cloud. Thus, there are more neutral species. The consequent lack of electrons means that the collisional excitation process is now dominated by collisions with hydrogen atoms. Under these conditions, the strongest lines from a cloud of specified size are from [FeI] at 24μm ($1\text{-}109 \times 10^{-14}$W cm^{-2}) and [OI] at 63μm ($4\text{-}24 \times 10^{-14}$W cm^{-2}) with the 28μm H_2 line being very weak. In a later paper (Pottasch, 1973), he uses ultraviolet measurements of absorption from the upper energy level of the [CII] 157μm line (among others) to obtain more accurate level populations. Predicted intensities per square degree for transition of [CII], [OI], [SiII] and [CI] (369μm) in the directions of Zeta Oph and, for CII, towards δ Sco. These fluxes are larger than the earlier ones by up to a factor of 10. Pottasch (1973) considers the [SiII] line to be observable with the detector sensitivities then current.

Dalgarno and Wright (1972) calculate emissivities for the rotational lines of H_2 and HD. They use these to predict the fluxes in some lines from Sgr B2 (Table 3.3). Because HD has a permanent dipole moment, its transitions are by electric dipole radiation and hence, have much higher transition probabilities than the electric quadrupole transitions of H_2. This is why HD is a significant coolant, despite being much less abundant than the lighter molecule. Drapatz and Michel (1974) point out that the intensities of lines from rotational transitions of H_2 and HD are reduced firstly, by absorption by concommitant dust and secondly, at certain densities and temperatures, the collisional excitation rate may become uncompetitive with spontaneous decay. They conclude that the dust permits study only of the cool, outer shell of the cloud. Table 3.3 lists their predicted line intensities, which are much lower than earlier work. Bussoletti and Stasinska (1975) predict fluxes from some molecular clouds (in front of Sgr A and Sgr B2, and the HCN cloud in Orion), from globules related to HII regions, and from presumed protostars (including the B-N source and W3-IRS5). They take account of radiative de-excitation and dust absorption and find that the S(0), R(0), R(1) and R(2) lines in Sgr B2 and Orion HCN have intensities above 10^{-18}W cm^{-2}. These transitions ought, therefore, to be detectable.

Of some relevance, due to the slightly longer wavelengths considered, are papers by de Jong (1974) and Cosmovici et al. (1979). The former presents expected intensities from ^{12}CO, ^{13}CO, HCl and HD in collapsing

Predicted H_2 and HD Line Intensities

Table 3.3

Species	Transition	Wavelength(μm)	Predicted Intensity in W cm^{-2}		
			Dalgarno and Wright	Bussoletti and Stasinska	Drapatz and Michel
H_2	S(0)	28.2	[a] 4.5×10^{-16}	[a,b] 1.69×10^{-15}	100K [f] 1.1×10^{-18} 200K [f] 7.4×10^{-18}
	S(1)	17.03	[a] 2×10^{-15}	[a,c] 4.06×10^{-16}	100K [f] 7.8×10^{-20} 200K [f] 2.3×10^{-17}
	S(2)	12.28	[a] 7×10^{-17}	[a,b] 5.20×10^{-18}	100K [f] 2.5×10^{-22} 200K [f] 4.8×10^{-18}
HD	R(0)	112	[a] 1.2×10^{-16}	[a,d] 2.28×10^{-16}	-
	R(1)	56.2	[a] 6.3×10^{-16}	[a,d] 5.55×10^{-16}	-
	R(2)	37.7	[a] 3.7×10^{-16}	[a,d] 9.05×10^{-17}	-
	R(3)	28.5	[a] 6×10^{-17}	[a,e] 2.37×10^{-18}	[f,g] 1.0×10^{-24} [f,g] 2.0×10^{-20}

Notes

a. Fluxes from molecular cloud near Sgr B2.
b. Reduce this figure by x9 to allow for dust absorption.
c. Reduce this figure by ∿ x100 to allow for dust absorption.
d. Reduce this figure by ∿ x1.4 to allow for dust absorption.
e. Dust absorption makes this line undetectable.
f. Flux with a 1 arc minute field of view from dense clouds at temperatures of 100K and 200K.
g. Assumes $n_{HD} = 1.4\times10^{-5}$.

interstellar clouds at 20K and 50K. For wavelengths less than ∿ 300μm, he finds no lines standing out above the continuum. The latter group, from the Max Planck Institute in Garching, present relative intensities for rotational lines from CO, HCN, CN, CS and SiO at temperatures of 10K, 20K and 30K between 150μm and 3mm.

The early predictions of line fluxes from the cool interstellar medium were high, but, as for fine structure lines, subsequent work has revised these intensities downwards. No detections of lines from these regions have been made and so there is no experimental evidence for the quality of the predictions. For the initial work with a new instrument, it is important to know that the lines are present and detectable in order that the instrumental performance may be assessed. For this reason, it was decided not to attempt to observe lines from the dense cool interstellar medium but to concentrate on the gaseous nebulae.

3.3 The Imperial College Line Astronomy Programme

The work described in this thesis is the beginning of the Imperial College line astronomy programme. Originally it was planned to work at wavelengths longer than 20μm. However, fairly early on, it became obvious that the rebuilding of the Marconi Stabilised Balloon Platform, following its disastrous failure in 1976 (Sugden, 1978), was going to take much longer than initially expected. Thus, it was decided to build a short wavelength prototype of the balloon instrument and to use it in the 10μm atmospheric window with the 1.5m Infrared Flux Collector at Tenerife. This work is reported in chapter 5.

The brightest lines between 8μm and 13μm are [ArIII] at 9.0μm, [SIV] at 10.5μm and [NeII] at 12.8μm. All of these have been detected in many objects. A Fabry-Pérot (F-P) Interferometer was built (cf. chapter 4) to make observation of these lines. However, the limited wavelength coverage of this instrument means that a particular line must be chosen for study. All these 3 lines are very interesting, but, eventually, the neon line was selected because it has the additional advantage of proximity in wavelength to the (then undetected) S(2) rotational line of molecular hydrogen. It was hoped that, given sufficient sensitivity at 12.8μm, only very minor changes in filters would be needed before a search for the 12.3μm line could be undertaken.

A candidate line for the first flights of the balloon-borne F-P must be strong, free from undue atmospheric confusion and technically feasible with the proposed instrumentation. In general, the estimated fluxes of Simpson (1975) for planetary nebulae are less than for HII regions and thus the predictions of Zeilik (1977) for the latter objects were carefully examined. Table 3.4 lists those of his predictions which, to the author's knowledge, had been tested by January 1979. Apart from his underestimate of the flux in the short wavelength lines, the predictions are not inconsistent with observations. His strongest lines are shown in table 3.5, which also gives a rough estimate of the spectral resolution (column 3) needed to separate the line from the nearest atmospheric feature present at an altitude of 30 km. An idea of the severity of the problem is obtained from column 4, which shows the atmospheric transmission at the centre of the feature. The two iron lines were ruled out because the upper limit for the 35μm [FeII] line, obtained by Moorwood et al. (1978) lends support to the suspicion of Zeilik (1977) that interstellar and not solar iron abundances are appropriate here (cf. sections 1.5.2 and 3.1.2). The [NeIII] was considered to require a spectral resolution too high to attempt a detection on the first campaign with a new instrument. The balance between the two oxygen lines was tipped in favour of that at 88μm because of the technical problems with a metal mesh F-P etalon at the shorter wavelength.

The last question to be answered here is the integration time required per resolution element to detect the time. This is obtained from,

$$\tau = \tfrac{1}{2}\left[\frac{(SNR)(NEP)}{FtA}\right]^2 \quad , \qquad 3.11$$

where SNR is the desired signal to noise ratio; NEP, the noise equivalent power in flight; F, the flux in the line; t, the transmission, or rather efficiency of the telescope system; and A the collecting area of the telescope. Dain et al. (1978) report an 88μm [OIII] line flux from M42 of 1×10^{-15} W cm^{-2}. If an NEP of 3×10^{-13} W Hz$^{-1/2}$, a transmission of 7% and an area of 7500cm^2 (for the IC 1m telescope) are assumed, then a SNR of 5 in one resolution element is achieved after 8 secs observation. The observation time is roughly twice the integration time to allow for the effects of chopping. The fluxes predicted by Zeilik for compact HII

Table 3.4

Species	Wavelength(μm)	Source	Zeilik(W cm^{-2})	Detected(W cm^{-2})
Ar III	8.99	W3A-IRS1	2×10^{-17}	[a] 3.2×10^{-16}
		G29.9-0.0	1.5×10^{-18}	[b] $1-6\times10^{-18}$
		S88B	3.1×10^{-20}	[c] 1.6×10^{-17}
S IV	10.52	W3A-IRS1	3.6×10^{-17}	[a] 4.5×10^{-16}
		S88B	1.2×10^{-20}	[c] 1.1×10^{-17}
Ne II	12.8	W3A-IRS1	9.5×10^{-18}	[a] 2.1×10^{-16}
		G29.9-0.0	8.1×10^{-18}	[b] $9-22\times10^{-17}$
		S88B	1.5×10^{-18}	[c] 1.7×10^{-17}
S III	33.4	W3A-IRS1	1.6×10^{-17} $\equiv 5.5\times10^{-10}$ W cm^{-2}sr^{-1}	< [d] 9×10^{-10} W cm^{-2}sr^{-1}
Si II	34.8	W3A-IRS1	7.2×10^{-18} $\equiv 2.5\times10^{-}$ W cm^{-2}sr^{-1}	< [d] 7×10^{-10} W cm^{-2}sr^{-1}
Fe II	35.3	W3A-IRS1	6.1×10^{-16} $\equiv 2.1\times10^{-8}$ W cm^{-2}sr^{-1}	< [d] 8×10^{-10} W cm^{-2}sr^{-1}
Ne III	36.0	W3A-IRS1	4.4×10^{-17} $\equiv 1.5\times10^{-9}$ W cm^{-2}sr^{-1}	< [d] 7×10^{-10} W cm^{-2}sr^{-1}
O III	51.8	W3A-IRS1	7.2×10^{-16}	-
O III	88.4	W3A-IRS1	1.2×10^{-16}	[e] 1.0×10^{-16} [f] 3.1×10^{-16}
C II	157.4	W3A-IRS1	5×10^{-20}	-

Notes

a. Willner, 1977.
b. Soifer & Pipher, 1975.
c. Pipher et al., 1977.
d. Moorwood et al., 1978.
e. Storey et al., 1979.
f. Dain et al., 1978.

Experimental Tests of Fine Structure Intensities Predicted by Zeilik(1977)

Table 3.5

Species	Wavelength(μm)	Resolution	Transmission (%)
Fe II	35.2	180	40
Fe II	25.99	3600	80
O III	51.7	400	80[a] 70
Ne III	15.38	500	20
O III	88.35	45	30[a] 30

Notes

a. These figures from chapter 2. All others from Kyle and Goldman(1975).

The Strongest Lines Predicted by Zeilik (1977)
(In decending order of intensity)

regions are up to a factor of 10 less than that reported by Dain et al. (1978). This increases the observation time to 14 minutes per element. This is rather longer than would be liked but is not unacceptable.

Thus, it was decided to make the 88μm [OIII] line the prime target for detection, with the 52μm [OIII] and 35μm [FeII] lines as second campaign objectives.

Chapter 4

Choosing a Fabry-Pérot Spectrometer

The aim of this chapter is to choose a spectroscopic technique suitable for making balloon-borne observations of far-infrared astrophysical emission lines. Various 'sequential' and 'multiplex' methods are compared and the reasons for choosing a Fabry-Pérot (F-P) Interferometer given. The theory of the F-P is summarised and previous designs examined. The chapter concludes with a description of the general features of a novel F-P design.

4.1 Introduction

An ideal spectrometer can be characterised by two fundamental quantities, its luminosity, L, and its resolving power, R. The luminosity is a measure of the light-gathering power of the instrument and is related to the amount of energy from the source that passes through the device and into the detector. L is an invariant of the system and is defined by the product of the area of the field stop and the solid angle subtended by the aperture stop at the field stop. The resolving power is given by $\lambda/\delta\lambda$ where λ is the wavelength at which the spectrometer is operating and $\delta\lambda$ is the minimum wavelength separation that can be distinguished without prior knowledge of the response of the instrument to perfectly monochromatic light, the instrumental profile. Jacquinot (1954, 1960) has shown that L and R may be directly related and that, in many spectrometers, their product is a constant. The potential luminosity-resolution product, $(LR)_{pot}$, is solely a function of the particular spectrometer and, as such, can be used to compare different instruments. The actual luminosity-resolution product obtained depends on the application and may be much less than $(LR)_{pot}$ - e.g. if the source does not fill the acceptance cone of the device. A high throughput is particularly important for work in the infrared, where measurements are often "energy-limited" by a low signal-to-noise ratio at the detector, rather than by optical considerations.

Infrared detectors have, in general, a very broad spectral response. Thus, to prevent any spectral ambiguity, it is vital that a longwavelength spectrometer adequately rejects the vast amount of energy present at the shorter wavelengths.

4.2 Choice of Instrument

Various spectroscopic techniques will be surveyed in the next few sections with a view to selecting the one most applicable to balloon-borne detection of far-infrared emission lines. In the first three sections, methods of sequential spectroscopy are compared. Heterodyning is mentioned in section 4.2.4. Two Fourier Transform Instruments are then discussed. The conditions necessary to obtain a multiplex advantage with these instruments are explained in section 4.2.6., and, in the next section, the Imperial College Balloon Telescope is examined to see if these conditions can be satisfied.

4.2.1 Spectrophotometry

The simplest method of obtaining a low resolution spectrum is to use a filter wheel, consisting of a set of narrow band filters with slightly different peak wavelengths. This technique is known as spectrophotometry and has been used extensively in the 1-5μm atmospheric region, ever since Johnson (1962) defined the JKLM photometric bands. Resolving powers of up to 50, depending on the parameters of the dielectric multilayers, may be achieved. As the resolution is increased, the actual energy throughput of the system drops, not only because of the smaller spectral bandpass but also because very narrow-bandwidth filters have lower peak transmissions than their wider-bandpass counterparts. A refinement of this technique is to deposit the dielectric coatings in such a way that their thickness increases uniformly around the circumference of a circle. Thus, the wavelength transmitted varies with position. These 'Circular Variable Filters' are commercially available (e.g. from OCLI, High Wycombe, Bucks) out to 20μm wavelength with resolving powers of up to 100 (Yen, 1969). At present, neither of these two methods can be used longwards of about 25μm, since the quarter-wavelength coatings become so thick that they lack uniformity and adhesion.

4.2.2 Prism and Grating Spectrometers

Jacquinot (1954) in his classic paper on the luminosity of spectrometers emphasises that, when comparing various instruments, it is vital to ensure that they are being used at the same resolution. In this case, the luminosity of the prism and grating spectrometers is proportional to the product of the angular dispersion, D, and the normal area of the emergent beam. Using the well-known expressions (e.g. Longhurst, 1967)

for the dispersions of these instruments, he finds, for the prism,

$$L_{Prism} \propto A\frac{dn}{d\lambda} \quad , \qquad 4.1$$

where A is the base area of the prism and n is the refractive index. For the grating, used at the maximum of the blaze angle, ψ,

$$L_{Grating} \propto A\frac{2\sin\psi}{\lambda} \quad , \qquad 4.2$$

where A is the area of the grating. The ratio, P, of the luminosities of these two instruments is given by,

$$P = \frac{L_{Prism}}{L_{Grating}} = \lambda\frac{dn}{d\lambda} \quad , \qquad 4.3$$

where a typical blaze angle of 30^{o} has been assumed. Jacquinot (1954) showed that for many materials P was always less than 1 and usually below 0.2 in the wavelength range from 0.25μm to 32μm. Moreover, as a general point, n changes most rapidly in regions where the imaginary part of the refractive index, the absorption, is substantial. Thus, the conclusion is that, under similar conditions, the grating spectrometer is superior to the prism.

Several grating instruments have been used for infrared astronomy. Aitken and Jones (1973) have produced N-band spectra of planetary nebulae and the galactic centre with such an instrument and the liquid-helium-cooled grating spectrometer, described by Houck and Ward (1979), was used for the first detection of a far-infrared emission line.

4.2.3 The Fabry-Pérot Interferometer

The ideal Fabry-Pérot (F-P) etalon consists of a pair of perfect optical flats arranged parallel to each other with their inner faces highly reflecting. The radiation undergoes many reflections inside the gap. At each reflection a little of the energy leaks out, leading to many transmitted beams. These interfere, either constructively or destructively, to produce a transmission spectrum that consists of a series of narrow passbands. Thus, to get unique spectral information, additional filtering is required. The F-P has the advantage of a two-

dimensional circular aperture as compared to the one-dimensional slit geometry of the prism and grating instruments. This leads to a dramatic increase in throughput. Jacquinot (1954) has shown that, as for the prism and grating, the luminosity of the F-P is inversely proportional to its resolving power. Comparing the F-P to a grating, with a blaze angle of 30^{o}, used in the maximum of the blaze, he finds that

$$\frac{L_{F-P}}{L_{Grating}} = \frac{3.4}{\beta} \quad , \qquad 4.4$$

where β, the angular height of the slit of the grating spectrometer, is usually between 0.01 and 0.1. He concludes that the F-P can be superior to the grating spectrometer by up to two orders of magnitude.

4.2.4 Heterodyne Spectroscopy

Heterodyne spectroscopy consists of mixing the incoming radiation with single-frequency local oscillator radiations and then detecting the beat frequency. This technique needs not only a stable local oscillator tunable over a certain spectral region with high enough power to overcome detector noise, but also detectors that respond at the beat frequency. The method is capable of very high resolving powers, up to about 10^{8}. Suitable detectors exist but longwards of the solid state diode lasers at around 30μm, there is difficulty in finding suitable local oscillators.

4.2.5 Fourier Transform Instruments

The lamellar grating spectrometer is a development of the conventional grating instrument. The diffracted radiation in the zero-th order is modulated as $\cos^{2}(\frac{\pi\Delta}{\lambda})$ as the path difference, Δ, between the two sets of lamellae is changed (Richards, 1964). The spectrum is recovered by a Fourier transform. Hoffman, Drapatz and Michel (1977) have built such an interferometer and report a resolution of 0.05 cm^{-1} over the 20μm to 200μm spectral region.

The other well-known Fourier transform spectrometer is the Michelson Interferometer. This divides the incoming wavefront into two beams and then recombines them after they have travelled different distances. By altering the path difference, a wavelength-dependent modulation is imposed on the radiation and, once again, the spectrum is obtained by a Fourier transform. As with the F-P, the Michelson has

the advantage of a large luminosity due to its circular symmetry. The Michelson is smaller and easier to build for the short wavelengths than the lamellar grating. However, due to multiple beam effects in the beam splitter, it is not possible to obtain constant modulation over a wide wavelength range. Figure 4.1 (adapted from Hoffmann et al, 1977) shows the modulation efficiency of the two instruments and highlights the need for several beamsplitters if a Michelson is to cover the range from 20-300μm. A Michelson interferometer for balloon work has recently been described by Anderegg et al. (1980). To obviate the need for different beamsplitters, a polarising Michelson was developed by Martin and Puplett (1969). Instruments of this design have been used by Robson et al. (1974) and Mather et al. (1974) for work on the cosmic microwave background.

4.2.6 The Multiplex Advantage

The term 'multiplex' is used when all the spectral elements are observed simultaneously, as in the Michelson Interferometer, rather than sequentially, as in the grating spectrometer. It was first realised by Fellgett (1951) that, under the right conditions, multiplexing permits the reaching of a certain signal-to-noise ratio (SNR) for each and every spectral element more quickly than in conventional sequential spectroscopy.

The conditions under which this advantage is realised are now examined. As the observing time on a source increases, the integrated signal increases linearly with time, while the noise only increases as the square root of time. Thus the SNR is proportional to $(\text{time})^{\frac{1}{2}}$. Consider, firstly a system limited by detector noise. If a total time, T, is available for the measurement of N spectral intervals, then, in the multiplex case, a SNR per element proportional to $T^{\frac{1}{2}}$ is achieved compared to $(T/N)^{\frac{1}{2}}$ for the sequential method. The gain of $N^{\frac{1}{2}}$ in SNR is the theoretical limit; the advantage realised by the Michelson, in practice, will be discussed in a later paragraph. A simple way of thinking about this improvement is that when multiplexing, the detector noise is 'shared out' among all the resolution elements, whereas working sequentially, each element receives all the detector noise.

Now consider what happens when the system is background noise limited, rather than detector noise limited. Observing many elements simultaneously is equivalent to increasing the spectral bandwidth of the instrument and allowing more background radiation to reach the detector. In this case, the noise is proportional to the square root of the back-

Figure 4.1

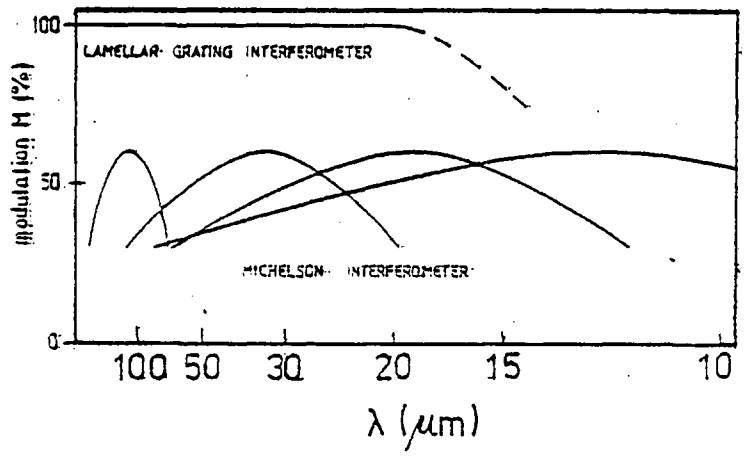

Comparison of the Modulation Efficiencies of the Lamellar Grating and Typical Michelson Interferometers with Mylar Beamsplitters. Adapted from Hoffmann et al. (1977).

ground or, to the square root of the number of spectral elements observed at once and thus, the multiplex advantage is exactly cancelled.

Under certain conditions, it is actually possible to be worse off when multiplexing. Suppose it is desired to observe a weak emission line in the presence of a strong one. If limited by photon noise in the signal, then observing these simultaneously means that the noise from the latter will be present on the former and may even swamp it.

Treffers (1979) re-examined the problem of SNR in Fourier transform spectroscopy. He concluded that although a perfect multiplex spectrometer would have an advantage of $N^{\frac{1}{2}}$ over a scanning instrument, a realiseable device (e.g. a Michelson) only has a gain of $(N/8)^{\frac{1}{2}}$. Following Tai and Harwit (1976) he explains that the discrepancy of $2\sqrt{2}$ arises for two reasons. Firstly, a real instrument imposes a $\cos^2$ modulation and does not perform a full complex Fourier transform, thus leading to a loss of $x\ \sqrt{2}$. Secondly, the modulation in a true Fourier transform instrument would go negative and the inability of detectors to respond to negative power causes a further loss of x2.

In summary, it has been shown that a multiplex gain will only be realised if the system is detector noise limited. In the next section, the Imperial College 41" Balloon-Borne Telescope is examined to see under what conditions, if any, the system becomes background noise limited.

4.2.7 Photon Shot Noise with IC Telescope

The IC Balloon Telescope is of a conventional Cassegrain design with a chopping secondary mirror. All objects warmer than 4.2K in the telescope beam contribute significant thermal radiation towards the total radiation background loading the detector; the fluctuations in this background cause the background noise that is being investigated in this section. The radiating objects in a simple telescope system are the liquid-nitrogen-cooled quartz scatter filter, the polyethylene vacuum window of the dewar, the primary and secondary mirrors and the atmosphere. The secondary mirror is undersized and thus, the atmospheric contribution can be split into two parts; the first is due to the atmosphere in the telescope beam and the second to the atmosphere 'seen' by the detector around the edge of the secondary mirror.

Equation 105 of Smith, Jones and Chasmar (1968, Ch.5) gives the mean square power fluctuations, $\overline{\Delta F}^2$, in a post-detection bandwidth, Δf hertz, from a body in thermal equilibrium at a temperature, T, as,

$$\overline{\Delta F}^2 = \Delta f \; 4 \; \varepsilon \; A \; \Omega \; t \; \frac{h^2}{c^2} \int_{\nu_1}^{\nu_2} \frac{\nu^4 \exp(h\nu/kT)}{(\exp(h\nu/kT)-1)^2} \, d\nu \quad W^2, \qquad 4.5$$

where ε is the emissivity of the body; t, the transmission of the optics; A and Ω, the area and solid angle respectively over which the radiation is collected; ν_1 and ν_2, the ends of the spectral passband in hertz and h, c, and k have their usual meanings. Using equation 4.5, the expected background photon shot noise for five different spectral bandpasses was calculated. Table 4.1 lists the adopted values for T, ε, A and Ω for each optical element and the contributions to the noise from each of these are detailed in table 4.2. The individual contributions were summed in quadrature to give the expected background noise assuming an overall transmission for the optics of 0.4 and a detector efficiency of 0.3.

The best Ga:Ge bolometers have noise equivalent powers of just under $10^{-14} W/\sqrt{Hz}$ while a typical value would be a few times $10^{-14} W/\sqrt{Hz}$. Comparison of these numbers with the background noises given in table 4.2 shows that, even without an interferometer, the system must be narrow-banded to some extent in order to remain detector noise limited. This problem will become even more acute when more sensitive detectors are incorporated. If an ambient temperature interferometer is used, the photon noise will significantly increase, because its optical elements will each contribute noise of similar magnitude to the dominant source, namely the polyethylene window.

4.2.8 Conclusions

Spectrophotometry and heterodyning can be eliminated as suitable techniques almost immediately. The former, because it is not capable of high enough resolving powers and the latter, a technique of the future, both because of its present technical difficulties and also because such high resolving powers are not needed to merely detect lines. On the grounds of luminosity, the F-P has been shown to be superior to both the prism and grating spectrometers. Of the Fourier transform instruments,

Table 4.1

Optical Element	Temperature(K)	Emissivity	Area(m^2)	Solid Angle(sr)
[a]Atmosphere	240	[c]0.04	[d]0.75	[f]$6x10^{-7}$
[b]Atmosphere	240	[c]0.04	[e]$2.8x10^{-5}$	[g]$8.46x10^{-2}$
Primary Mirror	240	0.05	[e]$2.8x10^{-5}$	[h]$1.54x10^{-2}$
Secondary Mirror	240	0.05	[e]$2.8x10^{-5}$	[h]$1.54x10^{-2}$
Dewar Window	240	0.08	[e]$2.8x10^{-5}$	[i]0.1
Quartz Window	77	0.1	[e]$2.8x10^{-5}$	[i]0.1

Notes

a. Atmosphere in telescope beam.
b. Atmosphere 'seen' around edge of secondary mirror.
c. Rough average from Traub and Stier (1976).
d. Area of primary mirror.
e. Area of Fabry lens.
f. Three arc minute field of view.
g. $(0.1-1.54x10^{-2})$ sr.
h. Convergence angle of IC 41" telescope.
i. Acceptance angle of IC far-infrared photometer.

Parameters for Telescope.

Table 4.2

Optical Element	[c]Photon Shot Noise in Various Spectral Passbands				
	10-13μm	25-40μm	40-80μm	50-100μm	10-100μm
[a]Atmosphere	7.7×10^{-14}	5.2×10^{-14}	3.1×10^{-14}	2.3×10^{-14}	1.4×10^{-13}
[b]Atmosphere	1.8×10^{-13}	1.2×10^{-13}	7.1×10^{-14}	5.2×10^{-14}	3.3×10^{-13}
Primary Mirror	8.5×10^{-14}	5.7×10^{-14}	3.4×10^{-14}	2.5×10^{-14}	1.6×10^{-13}
Secondary Mirror	8.5×10^{-14}	5.7×10^{-14}	3.4×10^{-14}	2.5×10^{-14}	1.6×10^{-13}
Dewar Window	2.7×10^{-13}	1.8×10^{-13}	1.1×10^{-13}	8.0×10^{-14}	5.1×10^{-13}
Quartz Window	1.3×10^{-15}	2.3×10^{-14}	2.5×10^{-14}	2.1×10^{-14}	3.9×10^{-14}
Total	3.6×10^{-13}	2.4×10^{-13}	1.4×10^{-13}	1.1×10^{-13}	6.6×10^{-13}
∴ [d] Photon Shot Noise	1.2×10^{-13}	8.4×10^{-14}	5.0×10^{-14}	3.7×10^{-14}	2.3×10^{-13}

Notes

a,b Atmosphere as defined in table 4.1.
c Units are W $Hz^{-\frac{1}{2}}$.
d Assuming a detector efficiency of 0.3 and an overall optical transmission of 0.4.

Background Photon Shot Noise.

the Michelson is preferred to the lamellar grating firstly, because of its compactness for a balloon-borne instrument and secondly, because its moving mirror only needs one-dimensional stabilisation compared to the two-dimensional requirement of the lamellae. Thus the choice rests between the F-P and the Michelson.

Factors influencing this choice include the effects of changes in background, ease of construction and the value of multiplexing. These will now be examined in turn. In a Michelson, changes in background will be recorded as spectral features; an F-P will also be affected if it is being used in a slow scan or a stop-and-integrate mode, but to a lesser extent, and the effects should be easier to discover and remove.

The argument that a Michelson is mechanically more complex than an F-P has been countered in the past by pointing to the auxiliary filtering requirements of the latter. At high resolution, the only suitable order-sorting filters are other F-P's and since these must be scanned in unison with the main F-P, the system is mechanically complex. However, if intensity rather than profile measurements of the lines are desired, the overall resolution can be kept down to the point where a fixed gap F-P (or other means) may be used for auxiliary filtering and then, the mechanical complexity of the instrument is considerably diminished.

Multiplex instruments are at their best when there is no pre-knowledge of the spectrum, i.e. all elements have equal importance. For emission line work, however, only a few spectral intervals around each line are relevant. A sequential device can 'jump' from line to line, ignoring the 'uninteresting' space between them, while an encoding instrument must go through it.

Auxiliary filtering constraints mean that it is difficult to use an F-P for more than one line. However, photon shot noise considerations mean that the Michelson must be narrowbanded to such an extent that only one or two astrophysical lines fall into its reduced range (the 30μm - 40μm region excepted). Thus, forthis work, there is very little advantage in using a multiplex instrument.

In summary, the Michelson is larger and more complex than the F-P and it also needs sophisticated data processing to recover a spectrum. Its main virtue, that of being multiplex, is of little value for this present application. Taking all these factors into account, it was decided to build a Fabry-Pérot Interferometer.

4.3 Fabry-Perot Considerations

4.3.1 Fabry-Perot Theory

The theory of the F-P can be found in many standard texts (e.g. Hadni, 1967 or Longhurst, 1967). Most of these assume that the spectrometer will be operated in high order and therefore neglect the phase change, $\phi(\lambda)$, on reflection at each surface. An F-P, built to operate in 1st order, is described in chapter 6. Thus, in the following, a summary of the general F-P equations, complete with wavelength-dependent phase shifts, is presented.

Figure 4.2(a) is a schematic diagram of an F-P and defines some of the variables. The reflecting face of each plate has intensity reflection, transmission and loss (due to absorption and diffraction) coefficients, R, T and A respectively. The intensity transmission, $\mathcal{T}$, of the interferometer is given by the Airy function,

$$\mathcal{T} = \frac{\text{Transmitted Intensity}}{\text{Incident Intensity}} = \left(1 - \frac{A}{1-R}\right)^2 \left[1 + \frac{4R}{(1-R)^2} \sin^2(2\pi\mu d\cos\theta/\lambda - \phi(\lambda)\right]^{-1} . \qquad 4.6$$

This is plotted in figure 4.2(b) for various values of R. The maximum transmission, $\mathcal{T}_m$, is given by,

$$\mathcal{T}_m = \left(1 - \frac{A}{1-R}\right)^2 = \left(\frac{T}{1-R}\right)^2 = \left(\frac{1-R-A}{1-R}\right)^2 , \qquad 4.7$$

and occurs whenever,

$$2\pi\mu d \cos\theta/\lambda - \phi(\lambda) = n\pi , \qquad 4.8$$

where n is the order of interference. The maxima are equally spaced in wavenumber $(1/\lambda)$ if ϕ is <u>not</u> wavelength dependent. The distance between the maxima, the so-called free spectral range, $\Delta\lambda$, can be obtained by differentiating equation 4.8 to get,

$$\Delta\lambda = \frac{\lambda^2}{2\mu d\cos\theta + \frac{\lambda^2}{\pi}\frac{d\phi}{d\lambda}} = \frac{\lambda}{\left(n + \frac{\phi}{\pi} + \frac{\lambda}{\pi}\frac{d\phi}{d\lambda}\right)} . \qquad 4.9(a)$$

Figure 4.2

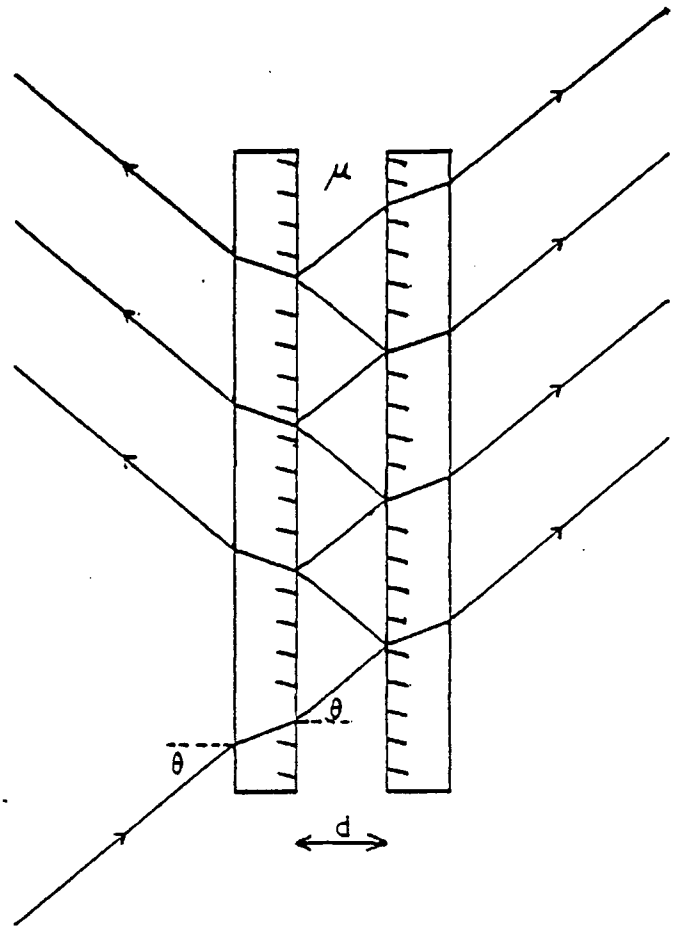

(a). The Fabry-Perot Etalon.

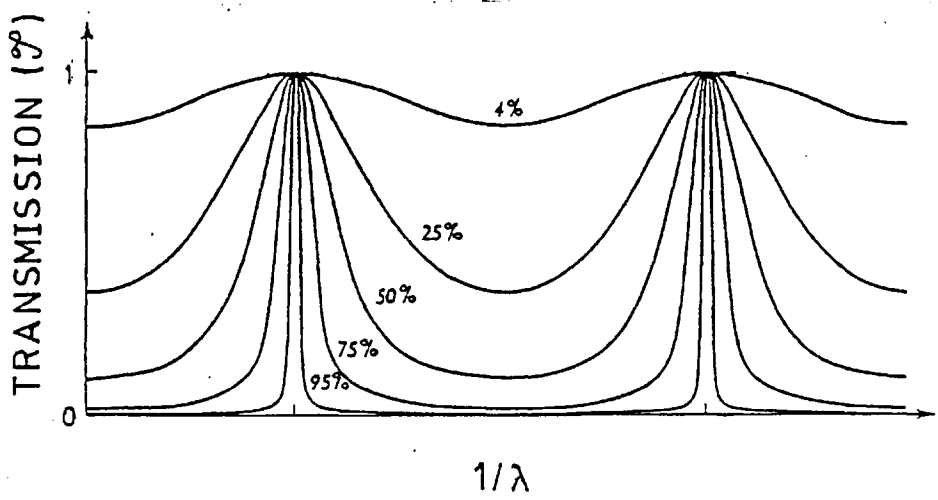

(b). The Airy Function.

If ϕ is independent of λ, equation 4.9(a) reduced to,

$$\Delta\lambda = \frac{\lambda^2}{2\mu d\cos\theta} = \frac{\lambda}{(n + \frac{\phi}{\pi})} \quad , \qquad 4.9(b)$$

which for high order operation ($n >> \phi/\pi$) further reduced to the familiar expression,

$$\Delta\lambda = \lambda/n \quad . \qquad 4.9(c)$$

The full-width half-height, $\delta\lambda$, of the Airy function is,

$$\delta\lambda = \frac{2\lambda^2 \sin^{-1}(\frac{1-R}{2\sqrt{R}})}{\pi(2\mu d\cos\theta + \frac{\lambda^2}{\pi}\frac{d\phi}{d\lambda})} = \frac{2\lambda \sin^{-1}(\frac{1-R}{2\sqrt{R}})}{\pi(n + \frac{\phi}{\pi} + \frac{\lambda}{\pi}\frac{d\phi}{d\lambda})} \quad . \qquad 4.10$$

This is the minimum width of a transmission peak for the ideal F-P and can be expressed as a finesse, $\mathcal{F}_R$, defined as,

$$\mathcal{F}_R = \frac{\Delta\lambda}{\delta\lambda} = \pi\left[2 \sin^{-1}(\frac{1-R}{2\sqrt{R}})\right]^{-1} \quad . \qquad 4.11(a)$$

The above is the maximum possible finesse and is referred to as the 'reflective finesse'. If the reflectivity of the plates is $\gtrsim 0.6$, equation 4.11(a) takes on its usual form,

$$\mathcal{F}_R = \frac{\pi\sqrt{R}}{1-R} \quad . \qquad 4.11(b)$$

Instrumentaldefects, e.g. lack of either parallelism or flatness of the plates, degrade the overall instrumental finesse, $\mathcal{F}_I$, which affects the resolving power, $\mathcal{R}$, of the instrument because,

$$\mathcal{R} = \frac{\lambda}{\delta\lambda} = (n + \frac{\phi}{\pi} + \frac{d\phi}{d\lambda})\mathcal{F}_I \quad . \qquad 4.12(a)$$

The more familiar form of equation 4.12(a),

$$\mathcal{R} = n\mathcal{F}_I \quad , \qquad 4.12(b)$$

is obtained under the same conditions which reduce equation 4.9(a) to 4.9(c). Chabbal (1953, 1958) has distinguished between three different types of defects: macroscopic distortion, e.g. spherical bowing of the plate with maximum error, d_1; microscopic irregularities with a Gaussian distribution and r.m.s. deviation, $\sqrt{d_2^2}$; and lack of parallelism, with total error across the plates of d_3 (see figure 4.3). In each case, a defect finesse, $\mathcal{F}_d$, can be assigned, if the plate error, d, is expressed as a fraction, m, of a wavelength. The total defect finesse, $\mathcal{F}_D$, is given by,

$$\mathcal{F}_D^{-2} = \mathcal{F}_{d_1}^{-2} + \mathcal{F}_{d_2}^{-2} + \mathcal{F}_{d_3}^{-2} \quad . \qquad 4.13$$

When an F-P is used with a telescope, its resolving power may be further limited if all the rays do not pass through it at the same angle. The Jacquinot criterion,

$$\mathcal{R}_c = \frac{2\pi}{\Omega} \quad , \qquad 4.14$$

defines the convergence-limited resolving power, $\mathcal{R}_c$, for an F-P accepting a beam of solid angle, Ω. This limit, expressed as an aperture finesse, $\mathcal{F}_{ap}$, for a telescope of focal ratio, F, is,

$$\mathcal{F}_{ap} = \frac{8F^2}{n} \quad . \qquad 4.15$$

The overall finesse of the interferometer, as used for the effective resolving powerin equation 4.12 is obtained by summing all the contributory finesses (reflective, defect, aperture) in reciprocal quadrature,

$$\mathcal{F}_I^{-2} = \sum_i \mathcal{F}_i^{-2} \quad . \qquad 4.16$$

$\mathcal{F}_I$ may be considered to be the effective number of interfering beams.

Figure 4.3

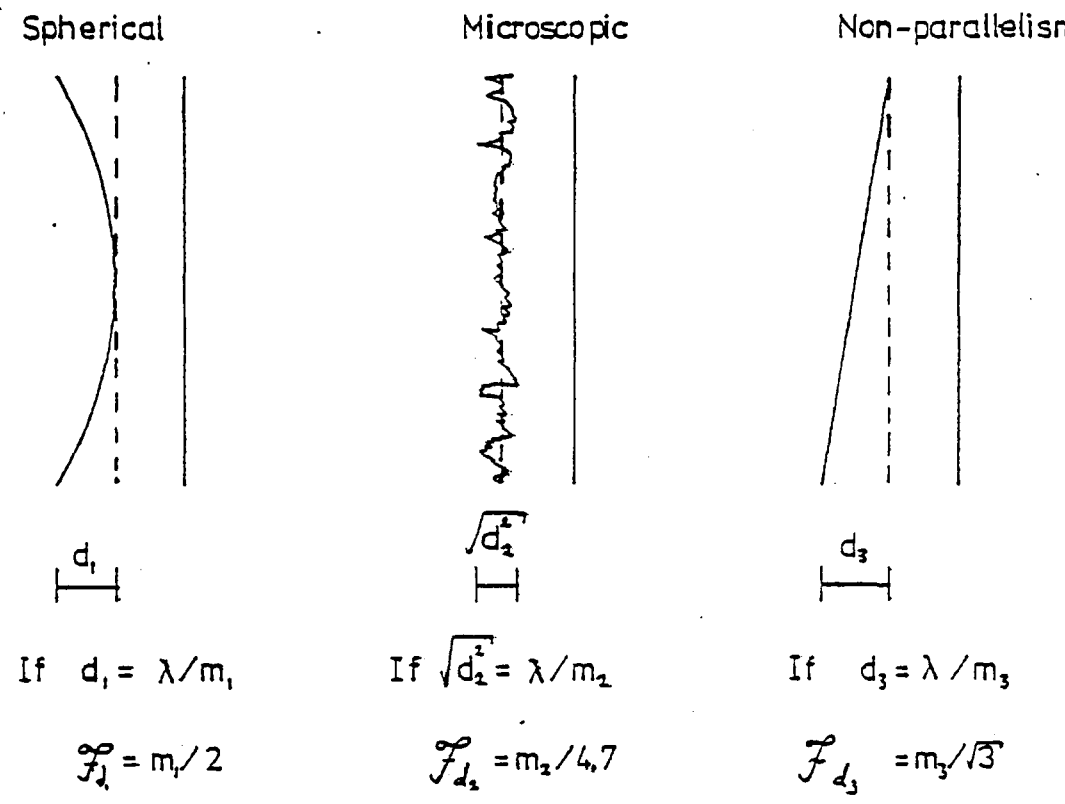

Different Types of Defects.

4.3.2 Design Criteria

The resolving power of an F-P is determined by the product of the order in which it is operated and the overall finesse (eqn. 4.12). As n is increased, the free spectral range decreases (eqn. 4.9) making the auxiliary, order-sorting, filtering progressively more difficult. The reflective finesse can be improved by increasing the reflectivity of the plates. However, if this is done, the absorption becomes more significant and the maximum transmission (eqn. 4.7) drops as shown in figure 4.4(a). There is very little point in increasing $\mathcal{F}_R$ beyond $\mathcal{F}_D$, because as demonstrated in figure 4.4(b), $\mathcal{F}_I$ (and, hence, the resolving power) only increases very slowly after $\mathcal{F}_R = \mathcal{F}_D$. The defects also degrade the transmission (figure 4.4(c)) because they make the etalon act as a large number of little etalons, each with a different gap, and so, only a small fraction of the total area transmits the desired wavelength. Thus, for maximum transmission and resolution, it is necessary to maximise the defect finesse and then match R to it, while keeping A to a minimum.

To use the full luminosity-resolution product of any spectrometer, the source must fill the acceptance cone, of solid angle Ω, of the device. In astronomical applications, a telescope (collecting area, A) is used to transfer Ω onto the sky as a smaller angle, ω, to match the object size. In order not to lose luminosity, the area, a, of the spectrometer entrance aperture must be large enough so that,

$$a\Omega \gtrsim A\omega \quad . \qquad 4.17$$

Thus for higher resolution (smaller Ω, cf. eqn. 4.14), a must be increased. An ideal case is to have an F-P the size of the primary mirror and just above the telescope, for this minimises the spread of angles through the instrument! For practical reasons (cf. chapters 5 and 6), it was decided initially to operate the IC F-P in the convergent telescope beam and to accept the resolution limitation. In this case, equation 4.17 is satisfied if the area of the F-P is larger than the beam at the position of the F-P.

4.3.3 Scanning Techniques

In the foregoing description the F-P has been presented as a multiple narrow-bandpass filter with ancillary optics to select one bandpass. The use of an F-P as a spectrometer depends on being able to move this chosen

Figure 4.4 (a)

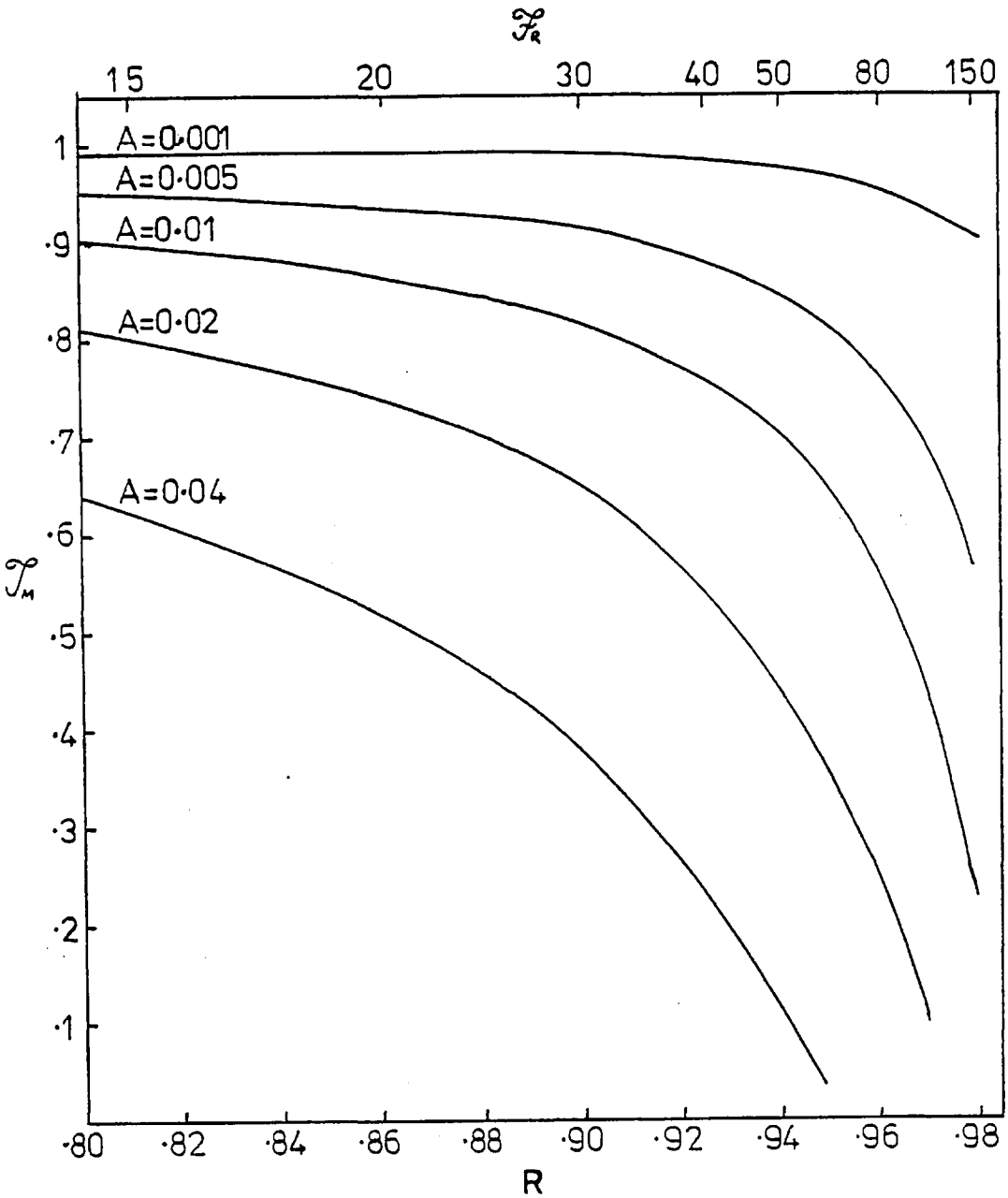

The Effect of Absorption upon Transmission.

Figure 4.4

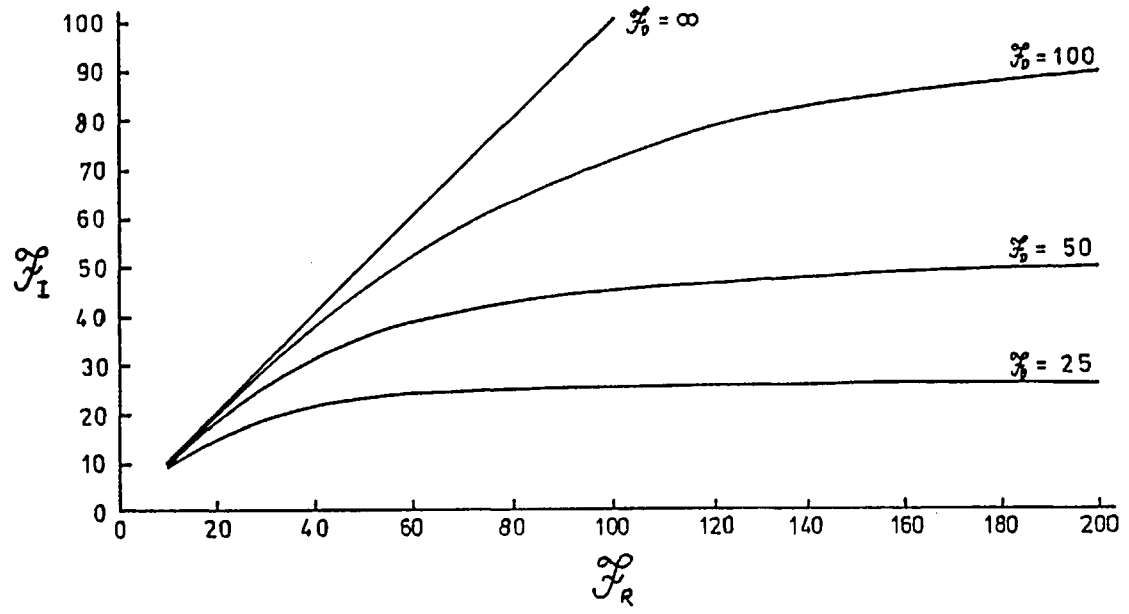

(b). Variation of Overall Finesse with Reflective and Defect Finesses.

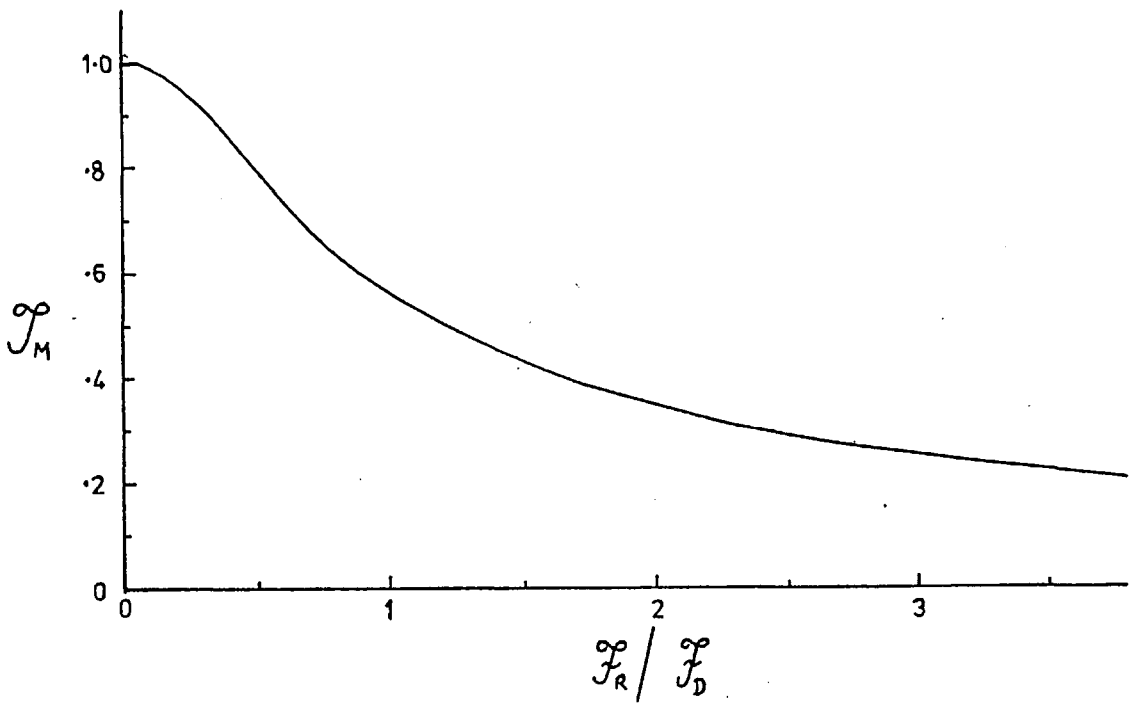

(c). Transmission as a Function of the Ratio of Reflective to Defect Finesse. (The exact shape of the curve depends upon the type of defect).

bandpass in wavelength. This is referred to as 'scanning' the instrument. If the F-P is illuminated with an extended source of radiation, a ring system is produced at infinity. When the rings are brought to a focus on a screen, different wavelengths produce rings of different radii. Thus, by choosing a ring, some wavelengths are selected for transmission while the rest are rejected. For a single detector, it is usual to put a circular aperture on axis in order to isolate the central ring or spot. Equation 4.8 shows that three variables are available in practice for altering the wavelength of the radiation passing through the aperture. These are the angle of incidence, the refractive index of the material between the reflecting layers and the etalon gap.

The effective angle of incidence may be altered by either moving the circular aperture off-axis or by tilting the entire etalon. The disadvantage of this method is that, for an F-P, the angular dispersion ($d\lambda/d\theta$) is not constant. it increases as the sine of the angle of incidence. Thus, if the aperture size is optimised for on-axis work, the resolving power will diminish as the tilt increases. If the size is chosen for off-axis conditions to avoid this problem, there will be a loss of luminosity for small angles of incidence.

The refractive index of a gas is proportional to its pressure over a wide range and, so, by altering the pressure of the gas between the plates, the optical thickness, μd, will be changed and the F-P will be scanned in wavelength. This technique is limited in range by the magnitude of the constant of proportionality between μ and the pressure.

The third method involves physically changing the gap between the plates and is loosely referred to as 'mechanically scanning'. This is the technique that was chosen for the instrument described in this thesis. The difficulty in this approach is to maintain the parallelism of the etalon while changing its separation. All three of these scanning methods have been used in the past and a few of these instruments will now be reviewed.

4.4 Some previous Fabry-Pérot Designs

The original interferometer, described by Fabry and Pérot (1899) was a delightfully ingenious construction. To achieve fine parallelism adjustment and scanning motion, water-filled rubber bags were placed next to and in contact with thin steel rods. The bags were connected to barrels full of water. As the water level in the barrels was altered, the water pressure inside the bags changed, the bags then expanded or contracted thus distorting the steel rods and movement occurred! A 12mm change in water level adjusted the parallelism by one arc second while a 1m change in another barrel scanned the plates 5μm. Since then, much effort and cunning have been expended upon new and improved techniques. To illustrate the wide diversity of approach, some designs will be reviewed here. The concentration on mechanical scanning reflects the prejudice of the author and not the relative attention received by each method.

4.4.1 Scanning by change of refractive index

Two approaches to altering the refractive index of the medium between the reflecting surfaces have been employed. Pressure scanning has been widely used. Geake, Ring and Woolf (1959) describe the astronomical use of a pressure-scanned F-P which covered about 20Å of the visible spectrum for a pressure change of 5 atmospheres. Auth (1969) exploits the change in refractive index and etalon gap with temperature to build a solid F-P of fused quartz capable of scanning 10 visible orders with high resolution (finesse $\gtrsim$ 60) and high transmission for a temperature change of 20°C.

4.4.2 Scanning by change of angle of incidence

Geake and Wilcock (1957) tilt-scan their air-gap F-P, part of a stellar spectrophotometer, by using a synchronous motor and cam to make $\cos\theta$ vary linearly with time. More recently, Roche (1976) emphasises that tilt-scanning a solid F-P produces a physically compact and stable system which does not require stringent tolerances on mechanical mounting, optical alignment or angular scan control. He reports the technical feasibility of making etalons with $\mathcal{F}_I \sim 50$ and $\mathcal{T}_M > 65\%$ in the wavelength range 1μm - 15μm, with bandwidths, limited by pre-filtering requirements, of $< 0.2\ cm^{-1}$. A prototype instrument, using a sapphire

etalon (at 3.8μm), tilted via a stepping motor and reduction drive and with scan rate and range controlled digitally is described by Roche (1976).

4.4.3 Scanning by changing etalon gap

Chabbal and Soulet (1958) and Shepherd (1960) both mount one of their flats at the centre of an annular flexible membrane (figure 4.5(a)). When an axially symmetric force, F, is used to distort the membrane, the circular symmetry of the system constrains the suspended plate to move parallel to itself. The membrane was stretched, in the former case, by effectively pushing at the centre of the flat; and, in the latter case, by altering the gas pressure on one side of the membrane. Roig (1958) adjusts the parallelism of his system by moving a weight along a rod, thereby changing the degree of flexure of the plate's support. The other plate is suspended from brass rods. These are heated and their thermal expansion provides the mechanical scanning.

Parallel spring hinges, as described in appendix A, are used by many authors. Greenler (1958) working in the 5μm - 20μm region, and Bradley (1962) both mount one plate on a spring hinge carriage, which is displaced sideways for scanning. The only difference is in the position of the plates (figure 4.5(b)). The former has his plates outside the spring arrangement, while Bradley has his between the base and carriage. Terhune and Peters (1961) put their mirrors on and above two identical spring hinge carriages and drive these apart magnetically.

Slater, Betz and Henderson (1965) developed a magnetostrictively-tuned F-P which operates at a resolving power of $\sim 10^5$ in the visible after a rocket launch. One of the plates in the instrument described by Clarke, Norman and Borsay (1975) is mounted on a piston, which is moved inside an invar cylinder to set the initial gap. Micrometers are used for coarse parallelism adjustment and piezoelectric stacks for fine alignment and scanning.

4.4.4 Modern Developments

One of the more recent developments in Fabry-Perot techniques has been the use of multipass instruments. The advantage of multipassing is that it gives a very high fringe contrast over a wide range of finesses without significant reduction in transmission. The technique has been used for high resolution spectroscopy of scattered light and is described

Figure 4.5

(a) FLEXIBLE MEMBRANE

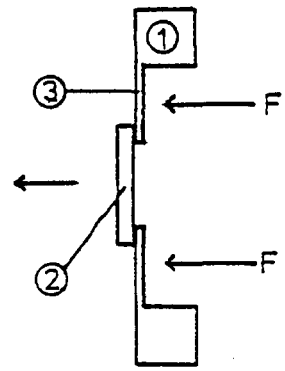

(b) PARALLEL SPRING HINGES

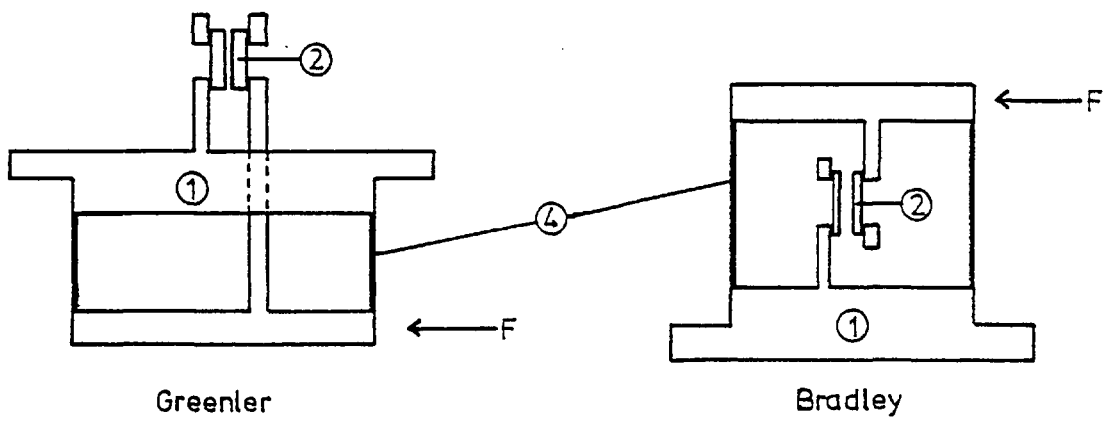

Mechanical Scanning Techniques.

by Lindsay and Shepherd (1977), Roychoidhuri and Hercher (1977) and references therein.

Another advance has been the development of servo-stabilised etalons. Rather than design a mechanical arrangement to keep the plates parallel for long periods and also during scanning, Ramsay (1962) constructed a system in which the flats were continually and automatically maintained parallel. He monitors the parallelism by sending a collimated beam of white light through a small area on the edge of the etalon. The light returns through a second small area, diametrically opposed to the first and falls onto a photomultiplier (figure 4.6(a)). Maximum transmission occurs when AB=CD; piezoelectric transducers, driven by error signals from the photomultiplier, maintain this condition. A second light beam, passing through an orthogonal diameter completes the parallelism control. The etalon is scanned by driving all the piezo's in unison. The disadvantage of this method is that if the source is very faint, scattered light from the monitor becomes significant.

To overcome this problem of scattered light, Hicks, Reay and Scaddan (1974) and Atherton, Hicks, Reay and Wells (1978) have developed servo-controlled etalons using capacitance micrometry for monitoring the parallelism. Four parallel plate capacitors (figure 4.6(b)) are formed at the ends of two perpendicular diameters by evaporating conducting surfaces onto the faces of the F-P plates. Deviations from parallelism cause the capacitance ratios X_1/X_2 and Y_1/Y_2 to alter. These error signals are used to drive piezoelectric transducers to correct the alignment. A fifth capacitor, Z, is compared with a fixed reference capacitor to monitor the etalon gap.

4.4.5 Fabry-Pérots for Infrared Astronomy

Most F-P's for infrared astronomy have been mechanically scanned. Two examples, one low and one high resolution, of instruments for the 10μm atmospheric window are described. Then, both the F-P's, known to the author, designed for the far-infrared are mentioned.

Selby, Jorden and MacGregor (1976) describe a liquid-helium-cooled instrument with a resolving power of about 100. The plates are of barium fluoride, dielectrically coated, and mounted inside a parallel spring assembly (cf. Bradley, 1960). A superconducting coil is used to scan the device and the position of the moving plate is servo-controlled with

Figure 4.6

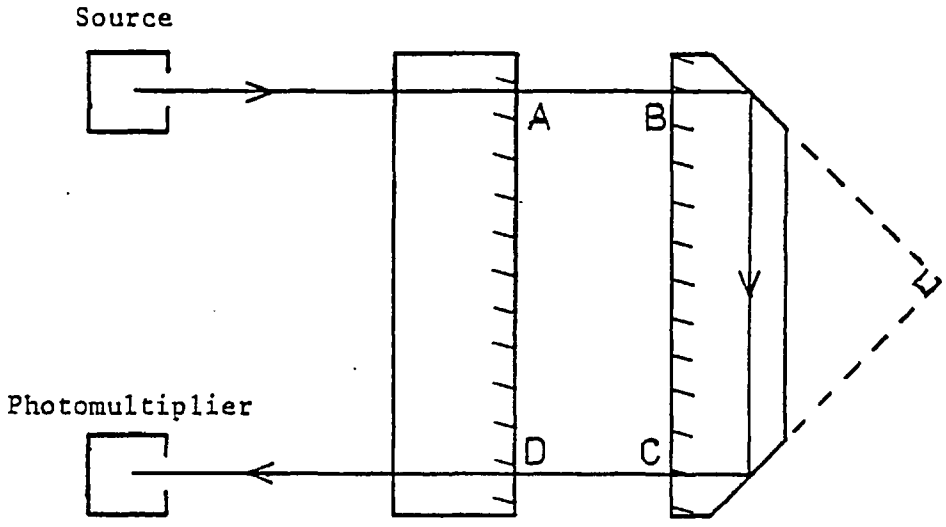

(a) Ramsay (1962).

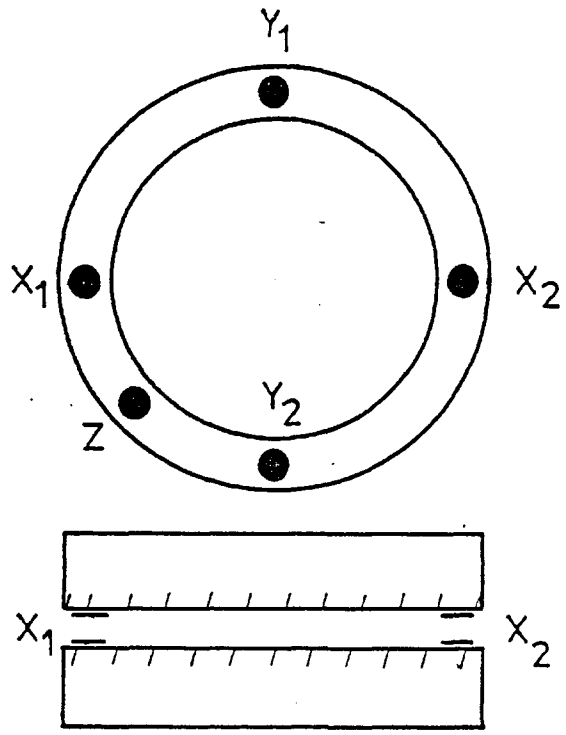

(b) Hicks et al. (1974) and Atherton et al. (1978).

Servo-stabilised Fabry-Perot Etalons.

respect to that of the fixed one by capacitance micrometry. Van der Wal and Slingerland (1979) use a low-resolution, liquid-helium-cooled, grating spectrometer, a medium-resolution liquid-nitrogen-cooled F-P and an ambient temperature high-resolution F-P to obtain a resolving power of 10^5 at 10μm. The F-P's are based on piezo-electrically scanned models in the Burleigh Instruments range and have coated zinc selenide plates. The medium-resolution etalon can be adjusted when cold. To assist in finding astronomical objects, both etalons can be easily removed from, and replaced in, the optical beam without disturbing any of the other components.

Chanin and Lecullier (1978) have developed a far-infrared F-P to work at the temperature and pressure encountered at balloon altitudes. A stepping motor and optical table drive assembly are used to mechanically scan the etalon. This consists of stretched, electroformed, metal mesh, in a piston/cylinder arrangement which obviates the need for parallelism adjustments. The position of the moveable grid is measured with a co-axial capacitor displacement gauge. Changes in spacing of 0.01μm are detectable. Storey, Watson and Townes (1980) use an ambient temperature scanning F-P and a fixed-gap, liquid-helium-cooled, order-sorting F-P to achieve a resolving power of $\sim 10^3$ between 50μm and 200μm from the Kuiper Airborne Observatory. The etalon mirrors are made from gold-plated, electroformed, nickel mesh and are attached to two hollow piezoelectric tubes. The etalon gap can be set between 0mm and 5mm; the piezoes, which are also used for parallelism adjustment, can change this by about 18μm. The high voltages necessary to drive the transducers mean that the F-P must be inside the vacuum jacket of the cryostat, to prevent corona discharge. A filter wheel inside the dewar contains three different order-sorting F-P's, which are made by clamping a photo-etched and electropolished spacer between two stretched grids.

4.5 General Features of the IC F-P Design

The choice of scanning method for the F-P, described in this thesis, was dictated by the need to keep a balloon-borne instrument simple, compact, reliable and low in power consumption. Pressure scanning was never seriously considered due to the problems of generating and containing pressures of up to 40 atmospheres (cf. the 1-8μm pressure scanned instrument of Beer and Ring, 1961). Tilt-scanning suffers from a change in

instrumental profile width, typically of up to 25%, with angle. This would cause different spectral elements to contain different amounts of continuum signal. This difference could be larger than the line flux and so, scanning by varying θ was not used, despite its mechanical attractions. Once the decision to tune the etalon by varying the gap had been taken, many previous methods (cf. section 4.4.3) of doing this were considered. Parallel spring hinges (cf. Appendix A) are very attractive for a balloon-borne instrument because, in addition to being simple, robust, and compact, they also provide parallel motion automatically. Thus, it was eventually decided to use a spring hinge arrangement, but in a novel form. Only the general feature of the design will be described here; points specific to either the long- or short-wavelength instrument will be left to chapters 5 and 6.

In appendix A, it is noted that as the platform or carriage of a parallel spring arrangement is displaced sideways, it also falls towards the base. Mr J. Allen of this group realised that this latter motion could be used to scan an F-P. To achieve this, the etalon plates were mounted perpendicularly to the springs (fig. 4.7(a)) and not parallel as previously done. Now, as the carriage is pushed a given distance sideways, the gap between the plates diminishes by a much smaller amount. The magnitude ofthis demagnification permits the carriage to be directly driven with a motorised micrometer. The etalon gap is monitored using capacitance micrometry (cf. section 5.1.4) because of the considerable expertise (e.g. Hicks, Reay & Scaddan 1974) in this field within the IC Astronomy Group.

The main disadvantage of this method is that the relationship between the x and y displacements is non-linear. Using the approximation and notation shown in figure 4.7(b), the demagnification, D, is given by,

$$D = \frac{y}{\delta x} \approx \frac{2\ell}{y} \quad . \qquad 4.18$$

This problem can be minimised by giving the carriage an initial displacement to take it into the region where D is only slowly varying with y and then, operating the instrument in a small range about this point.

The questim of the accuracy of the parallel motion now arises. For an F-P of this design, working at a wavelength of 100μm, it is necessary to move the carriage by about 1½ mm to scan one free spectral range.

Figure 4.7

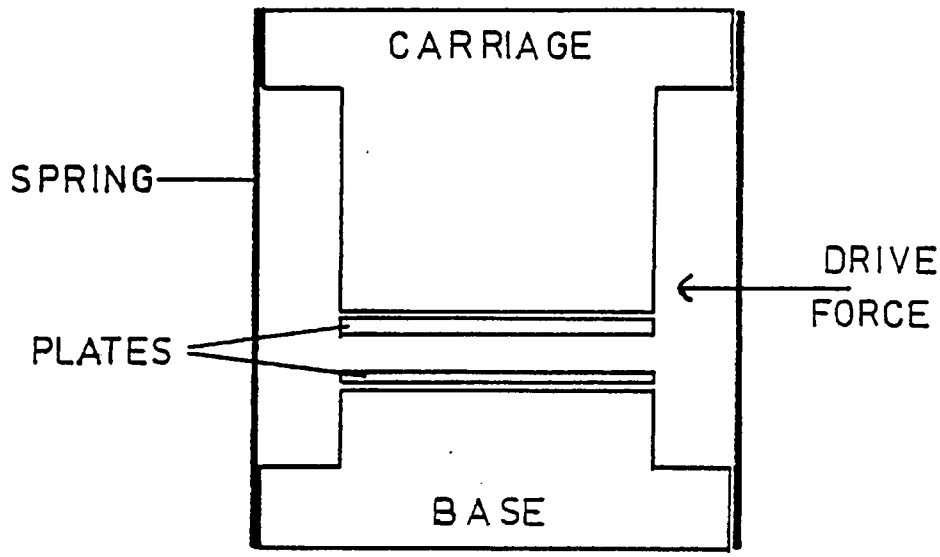

(a). Design.

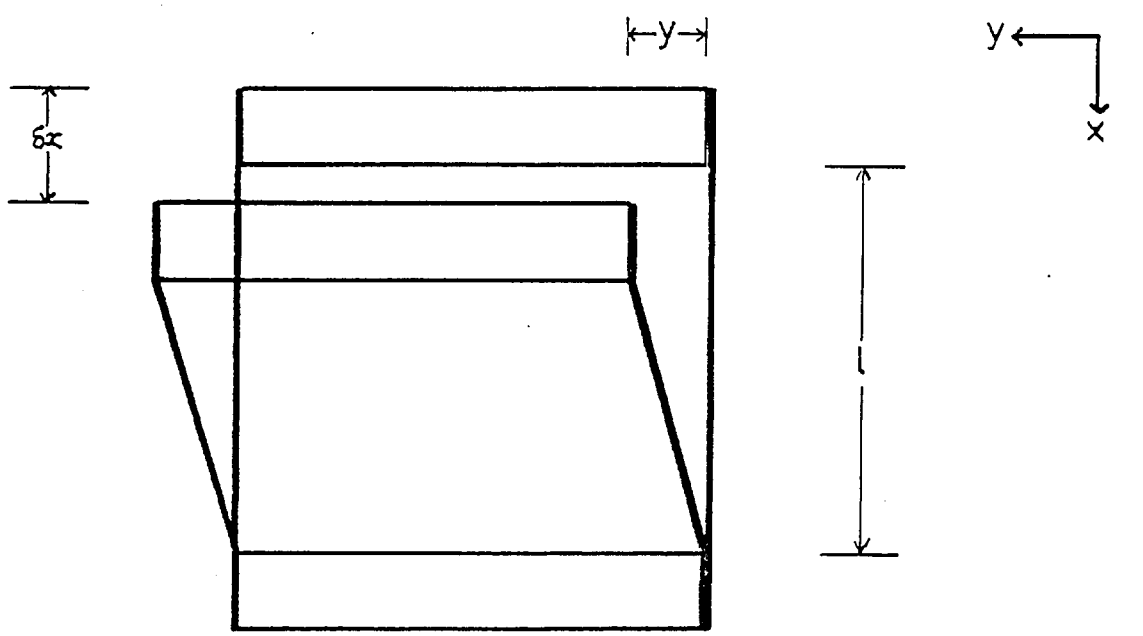

(b). Notation Used.

General Features of the IC F-P.

Jones (1962) reports that it is easy to reduce deviations from parallelism in spring hinge assemblies to less than $10^{\mathring{A}}$ for displacements of several millimetres and that, with care, NPL had achieved parallelism of better than $1^{\mathring{A}}$ over 10mm movement. For etalon plates of 30mm diameter, the easily obtainable parallelism corresponds to a parallelism finesse in excess of 40 at 100μm. This is more than adequate for the planned F-P.

Chapter 5

Near-Infrared Fabry-Pérot Interferometer

This chapter begins by describing the design considerations of a short (12.8μm) wavelength version of the balloon-borne Fabry-Pérot Interferometer. The laboratory performance of the instrument is then discussed. Finally, details of its use with the 60" Infrared Flux Collector (IRFC) in Tenerife in 1977 December, 1978 May and 1978 October are presented.

5.1 Design Details

The next four sections describe the design of the near-infrared interferometer. Firstly, the rationale for operating both the F-P and its order-sorting filter at ambient rather than cryogenic temperature is given because this choice obviously affects other aspects of the instrument. Then, details of the mechanical, optical and electrical design are discussed in turn.

5.1.1 Evironmental Considerations

The choice between warm and cold operation of the interferometer and its order-sorting filter depends upon three factors, namely ease of use, ability to find astronomical objects and background photon shot noise. It was decided to operate the F-P, itself, at ambient temperature and pressure so that alterations and adjustments could easily be made. The narrow bandwidth of the F-P and order sorter is expected to make finding objects difficult; this problem may be eliminated by making both the F-P and order sorter removeable from the beam, while searching for the object. This is easily accomplished for the ambient temperature F-P but would be difficult for the order sorter, if the latter were inside the dewar. Thus the position of the order-sorting filter must be decided by photon shot noise considerations. Figure 5.1 shows the optical elements that would be present for both a warm and a cold order sorter. The number above each element is its reflection, R, transmission, T, or efficiency, E. The noise contribution for each component in each case is calculated from equation 4.5 and is detailed in table 5.1. The conclusion is that an ambient temperature order sorter increases the background photon shot noise by a factor of x8 compared to cold operation. However

Figure 5.1

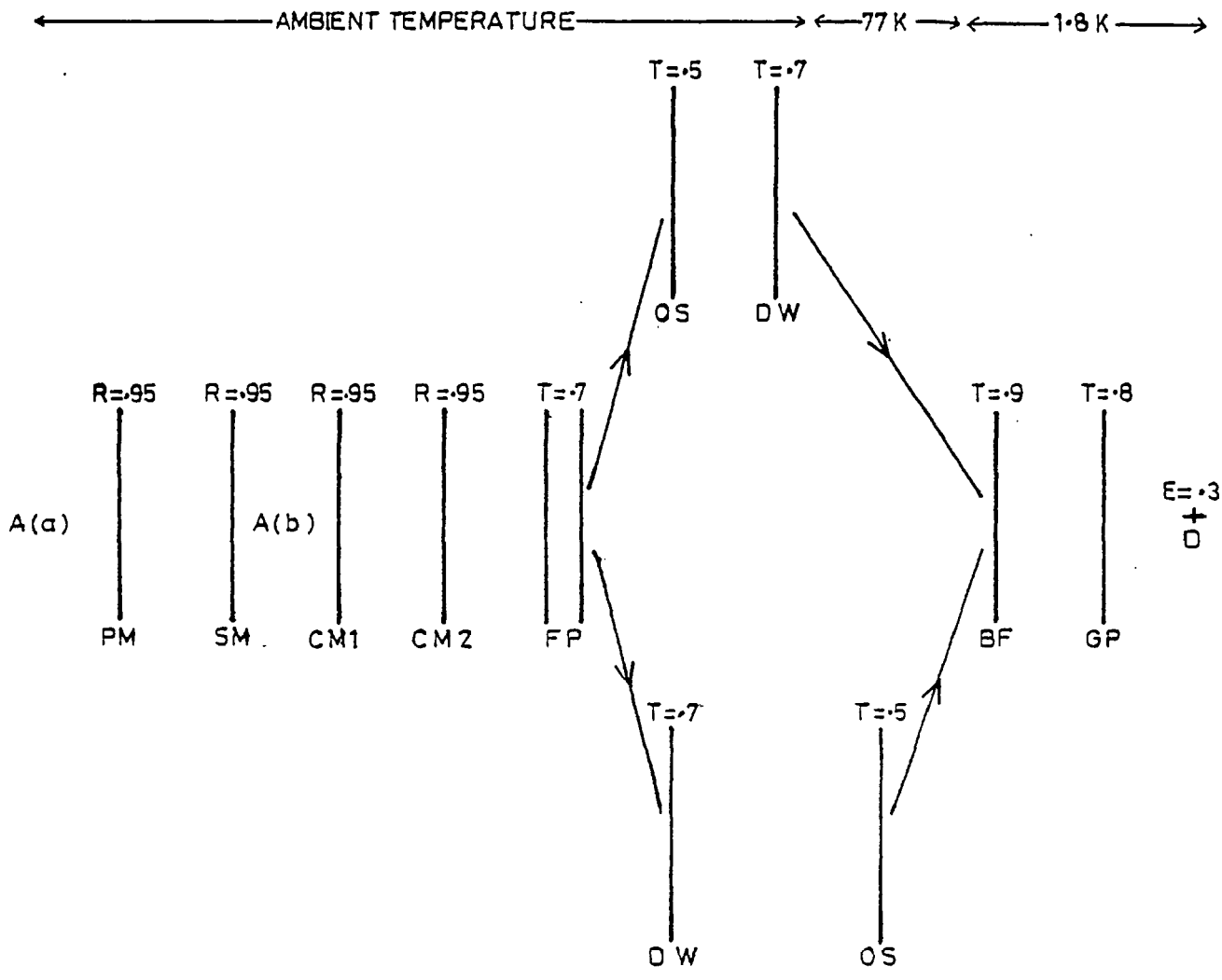

A(a) Atmosphere in Beam.
A(b) Atmosphere around SM.
PM Primary Mirror
SM Secondary Mirror.
CM1 Chopper Mirror.
CM2 Chopper Mirror.
OS Order-Sorting Filter.
DW Dewar Window.
BF Barium Fluoride Lens.
GP Grubb Parsons Filter.
D Detector.

Elements in Optical Train for 'Hot' and 'Cold' Order Sorter.

Table 5.1

	Optical Element	Temperature (K)	Emission Bandpass (μm)	Solid Angle (sr)	Area (m^2)	Emissivity	[i]Transmission	Noise ($W\,Hz^{-\frac{1}{2}}$)
Elements common to warm and cold cases	[a]Atmosphere	280	12.78-12.82	[c]1.8×10^{-9}	[g]1.64	0.08	0.04	2.8×10^{-16}
	[b]Atmosphere	280	12.78-12.82	[e]1.2×10^{-2}	[h]7.9×10^{-7}	0.08	0.05	1.4×10^{-15}
	Primary Mirror	280	12.78-12.82	[d]4.2×10^{-3}	[h]7.9×10^{-7}	0.05	0.05	2.4×10^{-16}
	Secondary Mirror	280	12.78-12.82	[d]4.2×10^{-3}	[h]7.9×10^{-7}	0.05	0.05	2.5×10^{-16}
	Chopper Mirror 1	280	12.78-12.82	[f]1.6×10^{-2}	[h]7.9×10^{-7}	0.05	0.05	5.1×10^{-16}
	Chopper Mirror 2	280	12.78-12.82	[f]1.6×10^{-2}	[h]7.9×10^{-7}	0.05	0.05	5.2×10^{-16}
	F-P Plate 1	280	12.78-12.82	[f]1.6×10^{-2}	[h]7.9×10^{-7}	0.10	0.08	8.7×10^{-16}
	F-P Plate 2	280	12.7 -12.9		[h]7.9×10^{-7}	0.10	0.08	2.0×10^{-15}
Warm order sorter	Order-Sorter	280	10-13	[f]1.6×10^{-2}	[h]7.9×10^{-7}	0.5	0.15	2.6×10^{-14}
	Dewar Window	280	10-13	[f]1.6×10^{-2}	[h]7.9×10^{-7}	0.1	0.22	1.4×10^{-14}
Cold order sorter	Dewar Window	280	12.7-12.9	[f]1.6×10^{-2}	[h]7.9×10^{-7}	0.1	0.11	2.3×10^{-15}
	Order Sorter	77	10-13	[f]1.6×10^{-2}	[h]7.9×10^{-7}	0.5	0.22	9.4×10^{-17}

$\therefore$ Background photon shot noise = 3.0×10^{-14} W $Hz^{-\frac{1}{2}}$ for a warm order sorter
3.6×10^{-15} W $Hz^{-\frac{1}{2}}$ for a cold order sorter

Notes

a. Atmosphere in a 10 arc second beam. b. Atmosphere 'seen' around edge of secondary. c. 10 arc second beam.
d. f/13.6 telescope. e. $(1.6\times10^{-2}-4.2\times10^{-3})$sr. f. IC 10μm photometer has f/7 beam.
g. Collecting area of IRFC. h. Area of Fabry lens. i. Transmission of downstream optics including detector efficiency.

this is still less than the expected detector noise on the telescope and the order sorter is, therefore, used at ambient temperature.

5.1.2 Mechanical Design

The mechanical design of the F-P is shown schematically in figure 5.2(a). An aluminium carriage, 1, is supported above an aluminium base, 2, by two 0"01-thick strips of phosphor bronze, 3. The two mirrors, 4, are glued (using GE7031 varnish) into aluminium mounting rings, 5, which are kinematically spring-loaded (not shown) against adjustment mechanisms in the carriage and base respectively. Three ball-ended 6BA screws, 6, through the upper carriage are used for coarse parallelism adjustment (to about 1 arc minute) and for setting the etalon gap. The lower plate holder, 5, has three glass blocks, 7, each with a $\frac{1}{2}^{o}$ taper and a V-shaped groove (figure 5.2(b)), glued (using a beeswax and resin mixture) onto its underside. Three other glass blocks are let into the base and spring-loaded ball-bearings, 8, running between these blocks and the tapered V-grooves, give fine parallelism control to about 1 arc second, matched to the overall flatness of the etalon mirrors. Irregularities in the threads of the standard screws, 9, used to push the ball-bearings are not important due to the demagnification of the motion by the tapered grooves. The faces of the glass blocks, that are in contact with the ball-bearings, are polished to an optical finish to prevent them introducing irregularities into the adjustment mechanism. The pushing screws, 9, are also spring-loaded (not shown in figure 5.2(a)) to take out backlash. In order to prevent the lower plate rotating about the beam axis, two of the three glass blocks let into the base are themselves V-grooves but not tapered. These are shown in figure 5.3(a), which is a photograph of part of the F-P base.

The capacitor for gap measurement consists of two gold-coated glass pillars, 10, glued onto the two plate holders. The lower capacitor pad is the larger of the two to allow for the sideways scanning movement; both pads have slightly bevelled rims. The height of the pillars is chosen so that the capacitor gap is much smaller than the etalon spacing. (Two separate pairs of capacitor pads can be seen on figure 5.3(b).) The upper carriage is displaced sideways with a ball-ended micrometer, 11, pushing on a glass flat, 12, on the side of the carriage. A heavily-geared-down d.c. motor is used to turn the micrometer through an extendable coupling, as shown in figure 5.4(a). This coupling can also cope with angular mis-alignments of several degrees. Figure 5.4(b) is a

Figure 5.2

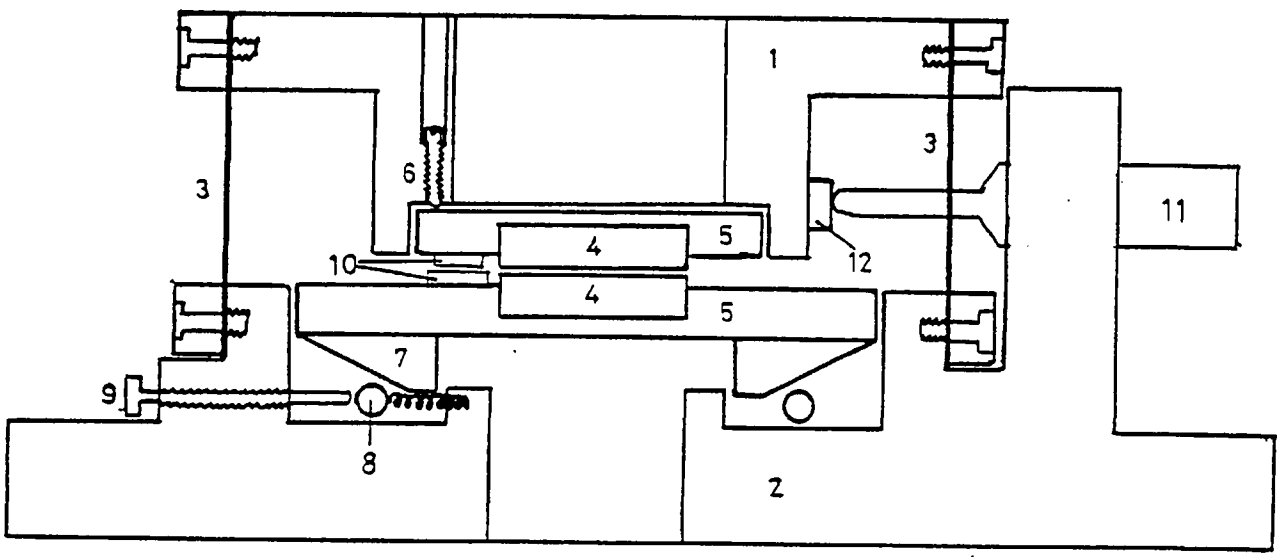

(a). Mechanical.

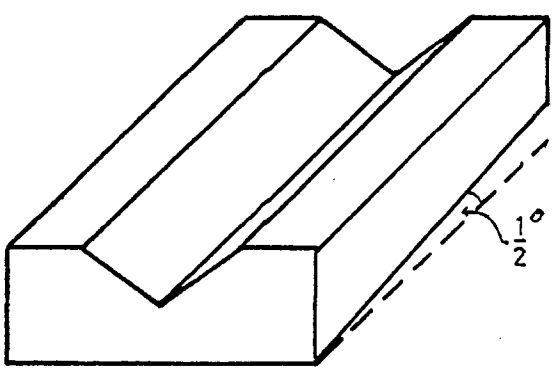

(b). Tapered V-Groove.

Near-Infrared Fabry-Perot Interferometer Design.

Figure 5.3

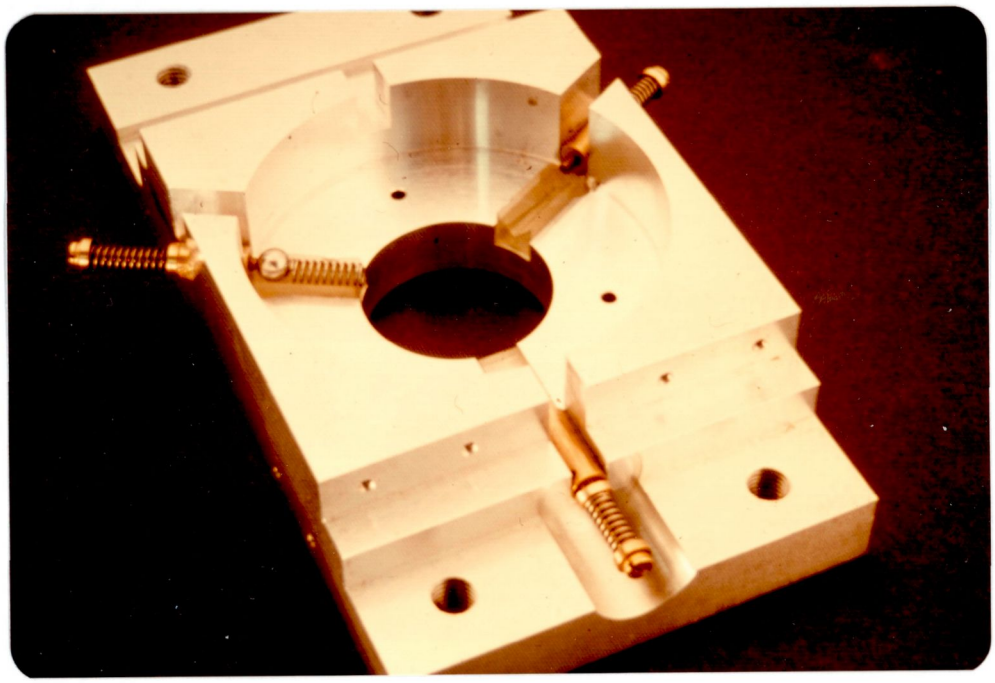

(a). Base with part of Ball-Bearing Adjustment Mechanism.

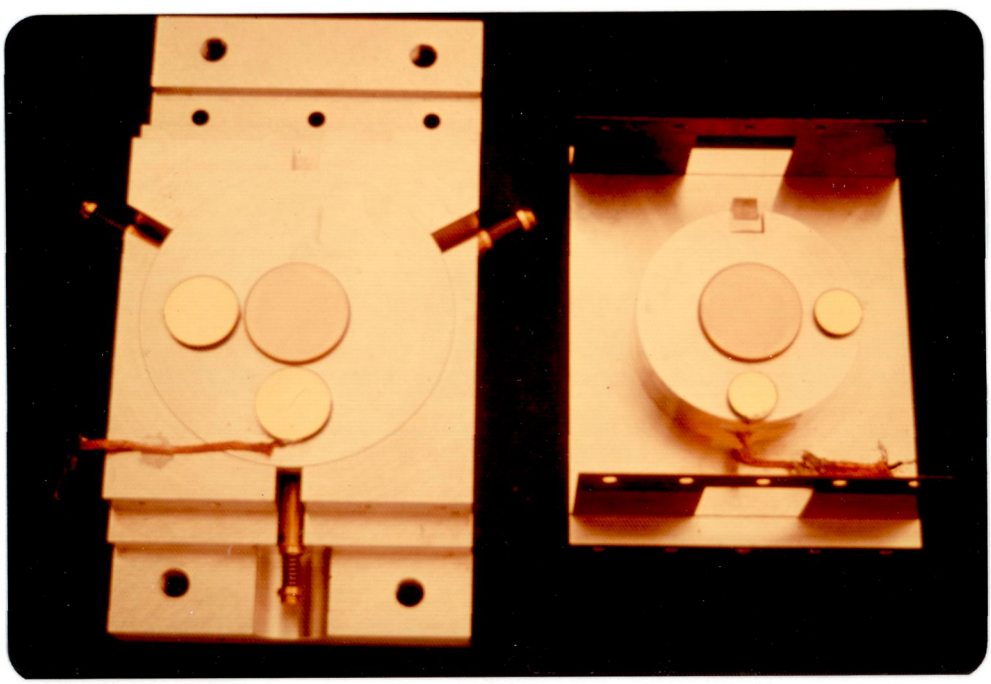

(b). Base and Carriage prior to Assembly.

The Disassembled Near-Infrared Fabry-Perot Interferometer.

Figure 5.4

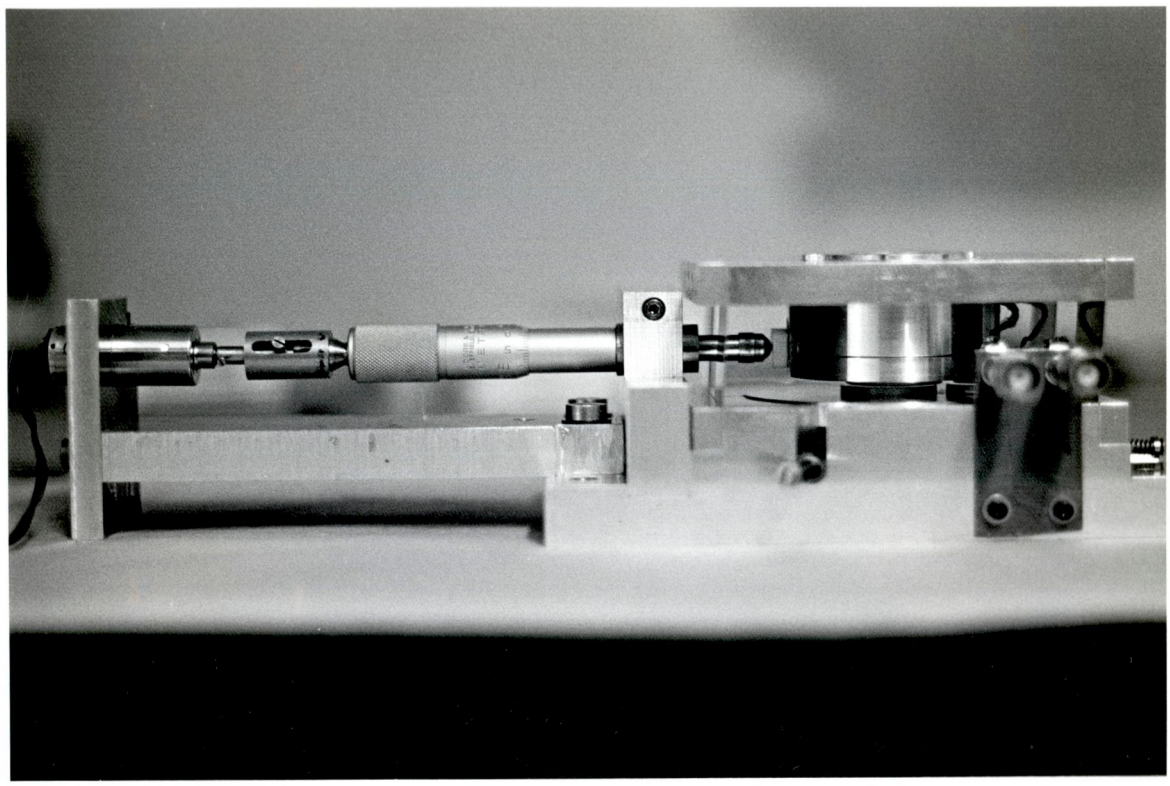

(a). The Extendable Coupling.

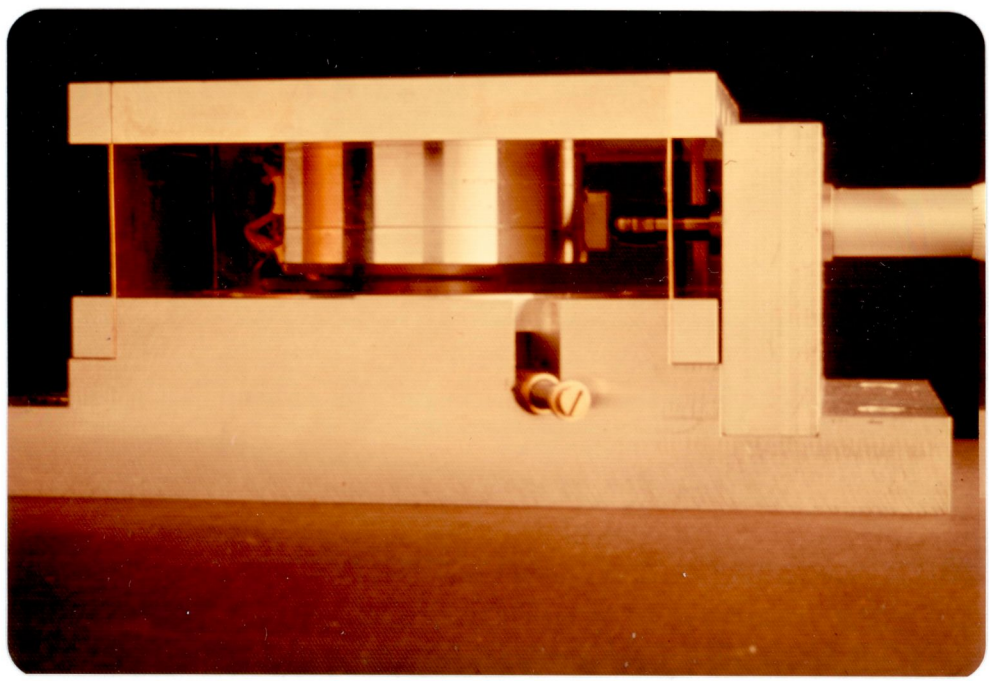

(b). Close-up of Instrument.

The Complete Near-Infrared Fabry-Perot Interferometer.

close-up of the assembled instrument. The F-P is electrically insulated from the telescope and attached thereto inside the adjustable dewar mount (cf. figure B.1) underneath the cryostat.

5.1.4 Optical Design

The optical design is governed by the desired resolving power. In order to resolve the 12.8μm [Ne II] line, a resolving power, $\mathcal{R}$, in excess of 2000 is needed (Wollman et al., 1976) but the line has been detected at $\mathcal{R}$ = 50 (Gillett et al., 1975). For simplicity, the telescope beam is not re-collimated for passage through the F-P, which therefore operates in the converging (f/13.6) beam. This limits the resolution of the instrument to 1500 (equations 4.14 and 4.15) and thus resolving the line is ruled out. The next limiting factor is the mechanical scanning assembly, which was originally designed to work at wavelengths almost ten times longer. To scan a free spectral range at 12.8μm, the carriage must be moved just over 0.1mm. Over this distance, the parallelism of the motion should be good to better than a few seconds of arc (cf. section 4.5), yielding a parallelism finesse in excess of 30 for plates 25mm in diameter. It is likely to be easy to improve the parallelism of the scan and therefore, a design value of 50 was adopted for each of the individual finesses. This leads to an overall finesse of 20-30 and permits resolving powers of several hundred to be achieved in relatively low orders, thus reducing the pre-filtering problem.

From equation 4.9, it is seen that as the order (or gap between plates) is increased, the free spectral range decreases and the auxiliary filtering must have a smaller bandwidth. Figure 5.5 shows the relationship between these two quantities. It is used to visualise the operating conditions of the F-P and to help select the order-sorting filter. This plot shows the resolving power (or instrumental width) attained with various combinations of overall finesse and plate separation. On the right hand side is the reflectivity needed to obtain a reflective finesse equal to the overall finesse on the left hand side. Due to the large cost (∿ £1000 at 1977 prices) of having a narrow bandpass filter specially made, a stock filter was purchased from the Optical Coating Laboratory Inc. This multi-layer dielectric-coated filter has peak transmission at 12.88μm, a half-power bandwidth of 0.2μm and its 2% transmission points are 0.49μm apart (figure 5.6). From figure 5.5, it is seen that using this filter requires the F-P gap to be less than 160μm and that for an overall finesse of 30, the resolving power is 700.

Figure 5.5

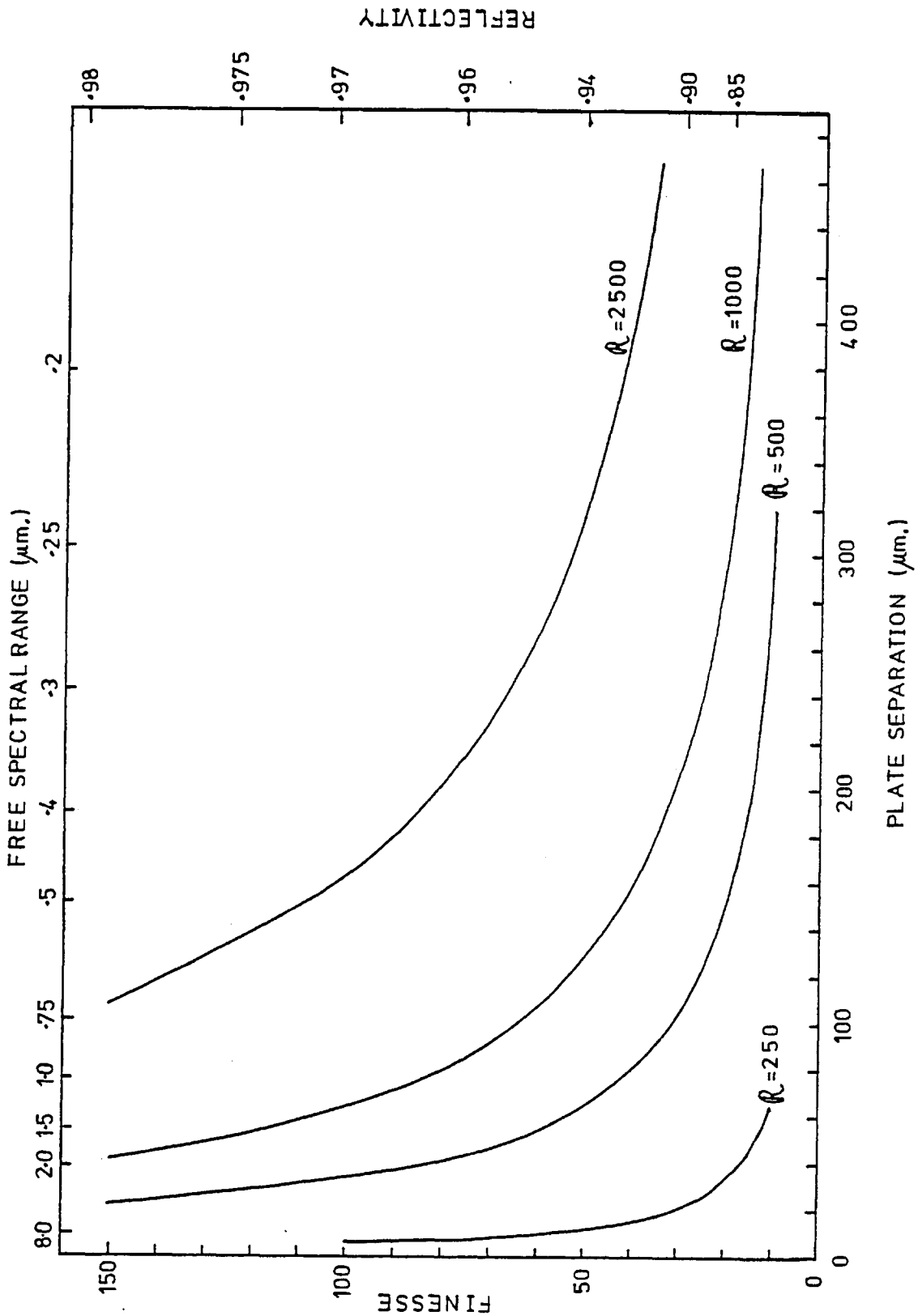

Design Curves for 12.8μm. F-P.

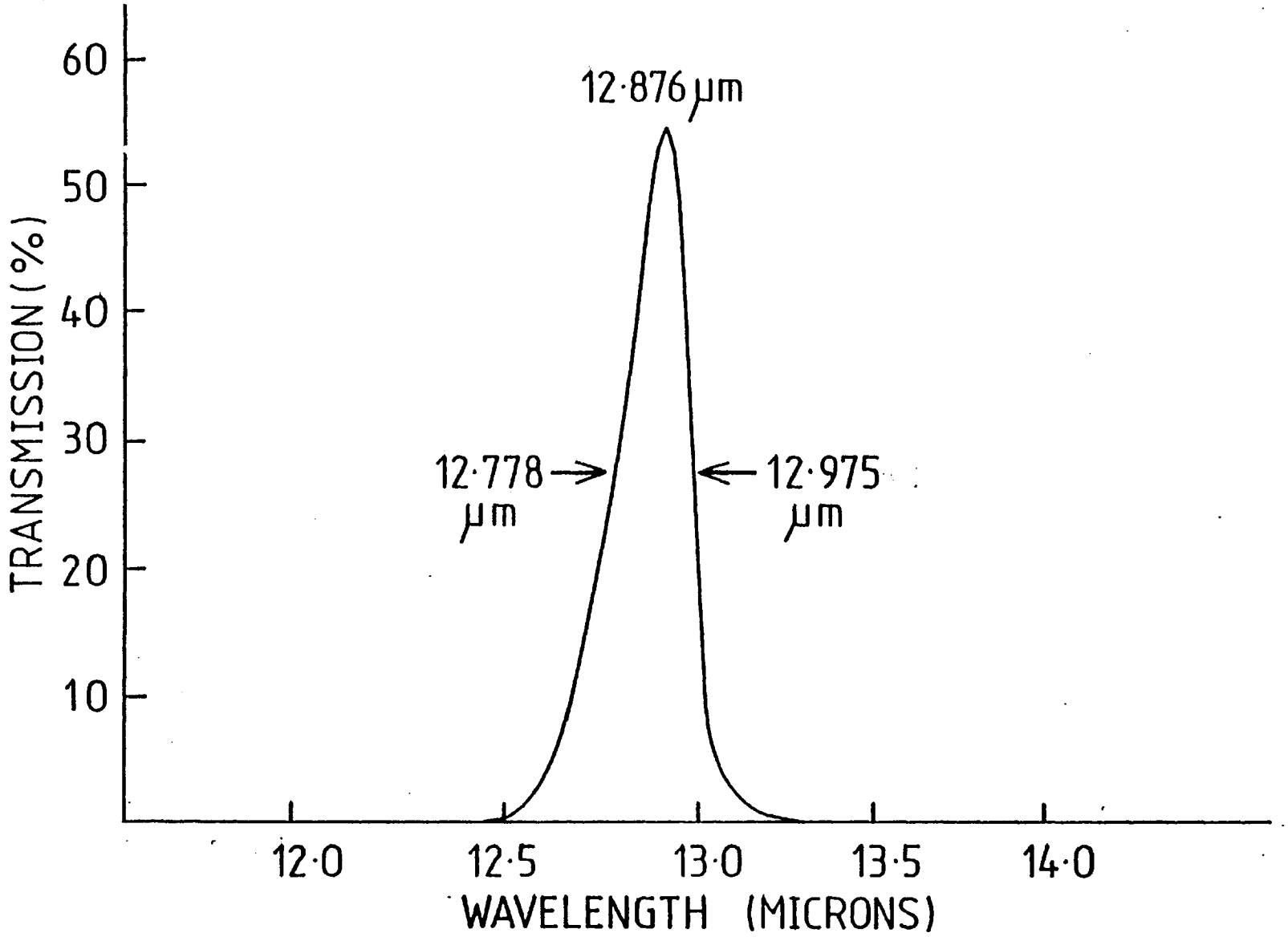

Figure 5.6

The Order-Sorting Filter

In the 10μm wavelength region, F-P mirrors still consists of a partially reflecting coating on a suitable substrate, i.e. optical rather than millimetre wave technology. An easy method of adjusting the etalon to parallelism is to view any visible light fringes that can be formed. This means that both the coating and the substrate must have some transmission at visible wavelengths. The criteria for selecting the material for the plates are that it is transparent from 0.5μm to at least 15μm, is capable of taking an optical polish, allows a reflecting coating to adhere, has minimal absorption and is relatively stable and inert. Many materials have the required transmission but have other disadvantages. Silver bromide and chloride are phototropic. Caesium and potassium halides are hygroscopic to varying degrees, leading to degradation of highly polished surfaces. Thallous bromide-iodide (KRS-5) suffers from cold flow and is also poisonous. Zinc selenide fills all the requirements and was therefore chosen; its only disadvantage is a high refractive index (2.4 at 10.6μm), causing high reflection loss unless anti-reflection coated. To obtain a defect finesse of 50, the plates must be flat to $\lambda/100$ at 12.8μm, i.e. about $\lambda_{visible}/15$. The Spectroscopic Accessory Company (Specac, St. Mary Cray, Kent), who make the plates, recommend that a 6mm thickness of zinc selenide is necessary to hold this figure.

The reflectivity of the plates must be 94% (from equation 4.11) to get a reflective finesse of 50. This can be obtained by depositing either a thin metallic layer or a dielectric stack on a substrate. A thin gold coating is very attractive because its reflectivity is constant across a wide wavelength range in the infrared, thereby allowing the same plates to be used for observations of different spectral lines. In constrast, a dielectric coating only has a nominally flat reflectivity over a wavelength region of 10% of the central region, e.g. a 95% reflectivity will have dropped to $\sim$ 92% at the ends of the 10% region.

The absorption in the coating must be minimised (cf. section 4.3.2) to keep the transmission of the F-P high. Results from a computer programme, developed by Dr P.R. Jorden, show that a 0.01μm thick film of gold on zinc selenide has a 10μm-13μm reflectivity of just over 96% and an absorption of 0.2%, which is acceptable. However, Mike Taylor of ITT (private communication, 1977) says that the values of the real and imaginary parts of the refractive index vary by up to x10 depending on the speed at which the gold is deposited. His estimates for the absorption range from 1.5% to 4%. Two pairs of mirrors were thus made; the first

with a thin layer of gold and the other with dielectric coatings. The latter plates are designed to have an infrared reflectivity of 94% between 12.3μm and 12.8μm. The other face is anti-reflection coated. All the plates are circular with a diameter of 25mm and are slightly wedged to prevent multiple reflection inside each plate.

The photometer (figure 5.7) used with the F-P was designed by W.P.S. Meikle and is described here for completeness. It is made from oxygen-free high-conductivity copper and is contained in a bottom-entry liquid-helium dewar (IR Labs. Model HD-3) with a KRS-5 entrance window. A gallium-doped germanium Low bolometer, 7, is directly beneath a detector stop, 5, and a Grubb Parsons 10μm-13μm bandpass filter, 6. The aperture in the detector stop is matched to the circle of least confusion produced by the barium fluoride Fabry lens, 8, which re-images the primary mirror onto the detector. The telescope focal plane is arranged to be at the Fabry lens; the field of view on the sky is defined by a field stop, 3, placed here. A forward stop, 1, at the end of a chimney, 2, limits the acceptance cone of the photometer to about f/7. The chimney is made as long as the dewar will allow to minimise the background radiation seen by the detector. Throughout the design, it is attempted to minimise the number of interfaces between any component and the cold surface, so as to improve the thermal sinking of that component.

5.1.4 Electrical Design

The only cooled parts of the electronics are the wirewound load resistors which, like the bolometer, are operated at $\sim$ 1.8K. A slightly modified version of the pre-amplifier described by Low and Rieke (1974) is mounted directly on the side of the dewar to minimise pick-up. The pre-amplifier has a J-FET input to provide both a very large ($\sim 10^9\Omega$) input impedance and also sufficient gain to take the detector output above the noise level of a micropower operational amplifier, which is the next stage. The complete amplifier has a feedback-stabilised voltage gain of about one thousand, a bandwidth of 0.1 Hz - 300 Hz and a noise at $\sim$ 10 Hz of 8-12 n V $Hz^{-\frac{1}{2}}$.

The computer system at the IRFC on Tenerife includes a NOVA mini-computer with a CAMAC interface. To enable the F-P to be operated under computer control, the I.C. group supply a CAMAC Input/Output (I/O) register. The state (high or low) of each of the 24 output lines from this unit can be controlled from the software by standard CAMAC calls. A

Figure 5.7

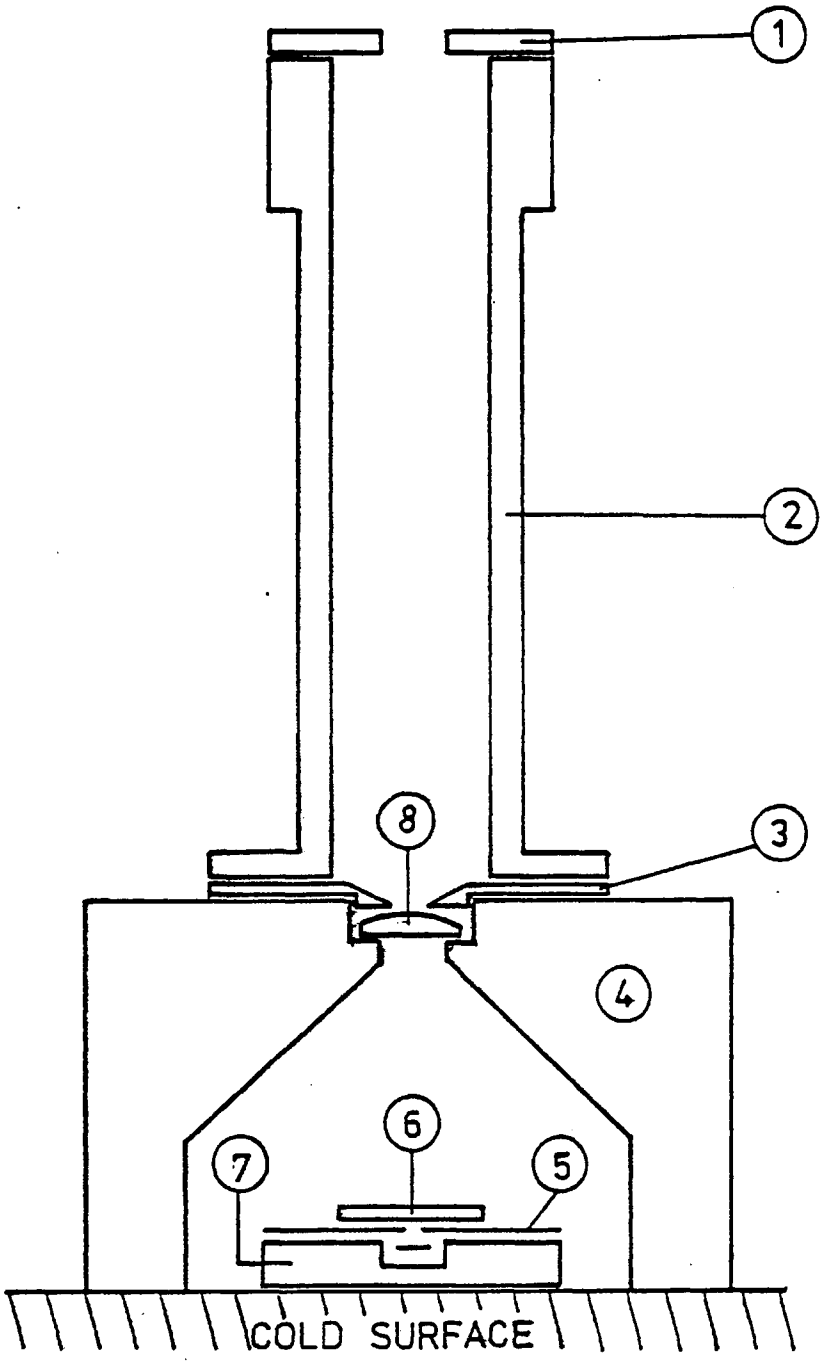

The WPSM Photometer.

"computer interface" was built which uses three of these lines to control the scanning of the instrument. One line starts and stops the scanning motor, another controls the scan direction and the third selects either fast or slow motion. The slow speed is manually adjustable and is used for scanning while the fast speed is used to minimise the time wasted in taking up the backlash in the gearbox and coupling when the scan direction is altered. The same interface also provides manual control of these 3 functions and this is how the F-P is operated in laboratory tests.

Electrical contact to the F-P capacitor pads (section 5.1.2) is made by extending the gold coating in a narrow stripe down one side of the glass pillar (almost but not quite) to the bottom and affixing one end of a piece of gold foil to this with conducting epoxy. The centre of the strip is attached to the aluminium plate holder over an insulating layer. To the other end of the strip is soldered the conductor of a co-axial cable, which connects the capacitor to the gap-sensing electronics.

The etalon gap is monitored using the technique of capacitance micrometry. Jones and Richards (1973) describe a system in which a displacement, of between 10^{-2}mm and 10^{-11}mm, is made to alter the value of one, e.g. C_1, of a pair, C_1 and C_2, of nominally equal capacitors, arranged in a transformer ratio bridge (figure 5.8). If the voltage across the centre-tapped secondary is $2\nu \sin \omega t$, the output current, i_D, is given by,

$$i_D = \nu(C_1-C_2)\omega \cos \omega t. \qquad 5.1$$

Changes in i_D are proportional to changes in C_1, which in turn are proportional to the displacement for small displacements. In practice, C_1 and C_2 are not equal so a balance control is provided to remove both this effect and also any differential stray capacitance. Also, equation 5.1 does not tell the full story for the real world. Due to finite cable and connector resistances and to the resistivity of the gold coating on the pads, equation 5.1 must be modified by the inclusion of a term varying as $\sin\omega t$, i.e. in phase with ν and therefore a 'resistive' component(R). This term may be large enough to saturate the downstream electronics and thus, the balance control also has a resistive offset, which is added in to reduce the R component.

The general form of the capacitance micrometer electronics is shown in figure 5.9. An oscillator provides two outputs of equal amplitude but

Figure 5.8

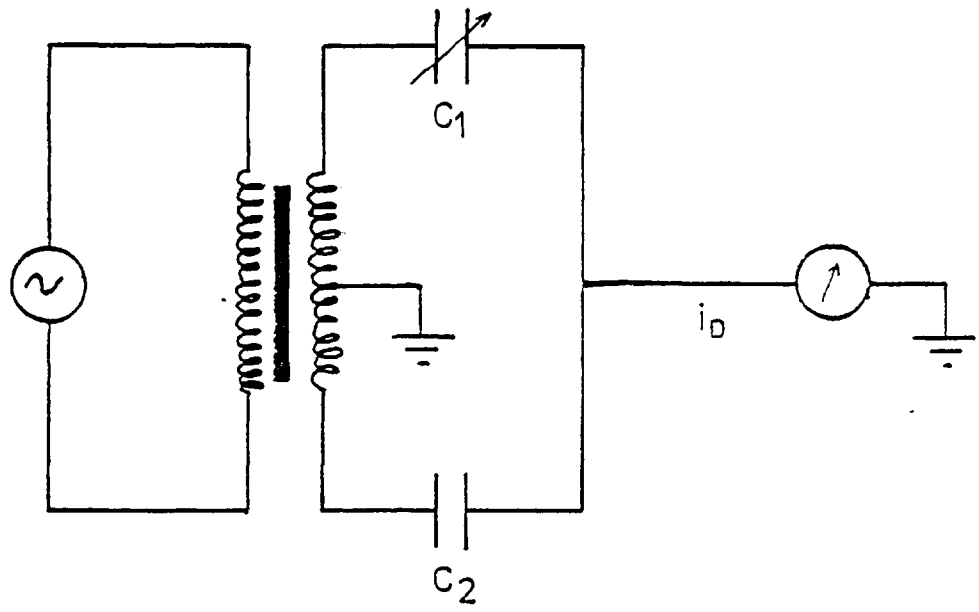

Transformer Ratio Bridge.

Figure 5.9

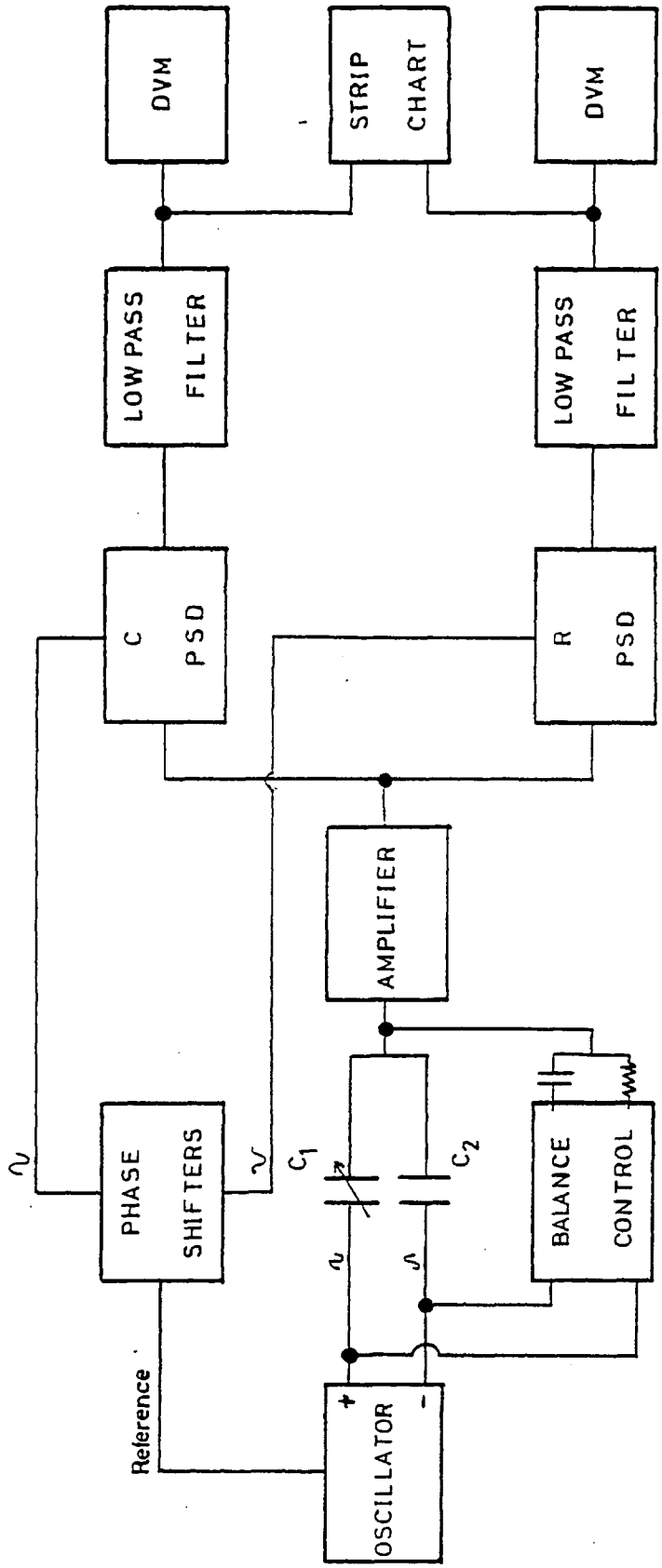

Block Diagram of Capacitance Micrometer Electronics.

in antiphase. These drive the two capacitors to be compared. The F-P capacitor is C_1, and C_2 is a fixed value reference capacitor, which should be close to and physically similar to C_1 in order to minimise differential drifts. The sensitivity of the bridge increases linearly with frequency,ω, (cf. equation 5.1) but the tolerance to variations in the stray capacitance between the cables and ground and between the pads and F-P structure decreases as ω^2. Therefore, the oscillator is operated at a frequency of approximately 16 kHz, as a reasonable compromise. The outputs from the two capacitors are summed, together with the capacitative and resistive offsets, at the input of a charge amplifier with a gain of several hundred. Two phase-sensitive detectors, using phase-shifted reference signals 90° out of phase with each other, are used to extract the capacitative, C, and resistive, R, components of the signal. The C output gives the change in plate spacing while R is used to monitor any resistive drifts in the system. The two phase-sensitive detectors have a 12 dB per octave roll-off and their outputs are further smoothed by low-pass filters with bandwidths of 0-2 Hz. Both the R and C outputs are usually displayed on digital voltmeters (DVM's) and strip charts.

The last two paragraphs outline the general features of capacitance micrometry. In this paragraph, some specific features of the electronics used to monitor the etalon gap of the near-infrared F-P are briefly described. All the design work and the majority of the construction of this electronics was carried out by Mr J. Allen. A standard Wien bridge LC oscillator is used to drive the primary windings of a transformer, whose secondary is multiply tapped (figure 5.10) to provide coarse and fine capacitative offsets and a fine resistive offset. The reference capacitor, of silver mica, is contained in a die-cast box next to the F-P on the telescope. Three long cables are taken up onto the flux collector; two for the bridge drives and one return for the summed outputs from the F-P and reference capacitors. The F-P assembly is earthed through the capacitance micrometer electronics to keep stray capacitances to the etalon metalwork constant. It is insulated from the telescope to prevent ground loops. All cables are held firmly in place to prevent, firstly, movement causing variations in stray capacitance and secondly, flexure causing changes in the capacitance of the cables. To aid data processing and to enable the computer to scan the F-P to a particular wavelength, the C output is converted to digital form by the DVM and enters the computer via the input lines of the CAMAC I/O register. The conversion in the DVM is controlled in software by another of the output lines of the I/O register.

Figure 5.10

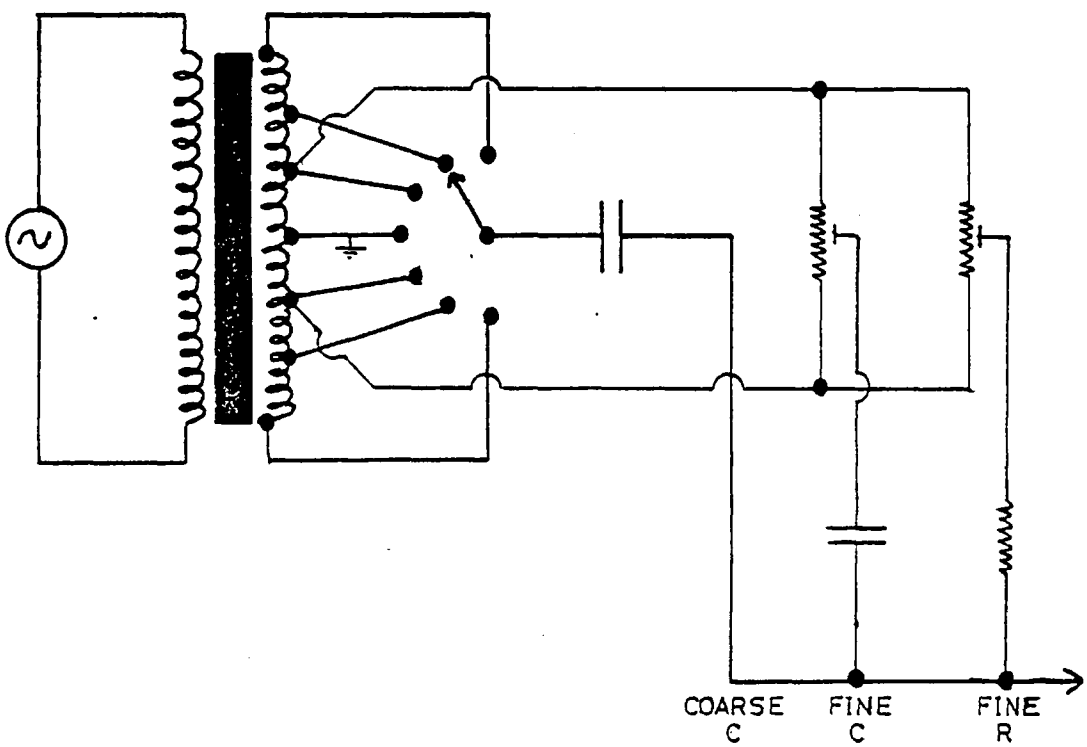

Balance Box.

5.2 Laboratory Performance

The results of measurements of the laboratory performance of the near-infrared F-P are presented in the next four sections under the headings of mechanical, capacitance micrometer, etalon plate and F-P tests.

5.2.1 Mechanical Tests

In order to align the etalon plates parallel to each other, a miniature mercury discharge lamp is viewed through the assembled F-P. The coarse parallelism of the mirrors is then adjusted until all the multiple images of the electrodes of the lamp are superposed. After this has been done, closely spaced, apparently straight fringes are seen across the entire etalon. To improve the contrast of these high order F-P fringes, a diffusing screen and a Kodak Wratten gelatin filter (usually green but occasionally orange and isolating one line in the mercury spectrum) are inserted into the optical train. The 6BA adjusting screws are then used to move the "straight" fringes around, increasing their separation all the time (i.e. decreasing the order) until the centre of the F-P ring pattern appears. Next, the ball bearings are moved in their tapered V-grooves, firstly, to make the pattern as symmetrical as possible and secondly, to minimise the change in the pattern as the eye is moved across the etalon. The best alignment achievable leads to the following condition: If the centre spot is dark when the eye is above the centre of the etalon, then as the eye, travelling out along any radius of the etalon, reaches the edge, the centre spot is just starting to turn bright, i.e. a change of less than half a visible order. As the eye moves across a diameter, the direction of movement of the rings (i.e. expanding or contracting) alters. This indicates that the residual misalignment is of the form shown in figure 5.11(a) and therefore must be due to the plates themselves. Since the distance y-x is less than $\lambda_{vis}/4$, the parallelism finesse obtained is in excess of 50 at 12.8μm. Thus, this alignment technique allows the plates to be set parallel to better than the design goal.

The parallelism of the scanning motion is measured by observing visible fringes. The instrument is aligned as described in the above paragraph and then scanned in steps of 5 visible fringes. After each stop, the fringe pattern seen, as the eye moves across a diameter, is compared with the initial one to calculate the deviation from parallel motion. At first, the phosphor-bronze springs were located only by the clamping screws (cf. figure 5.2(a)) passing through them. However this was found

Figure 5.11

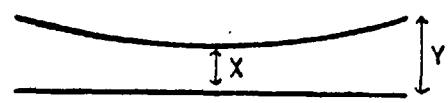

(a). Residual Misalignment.

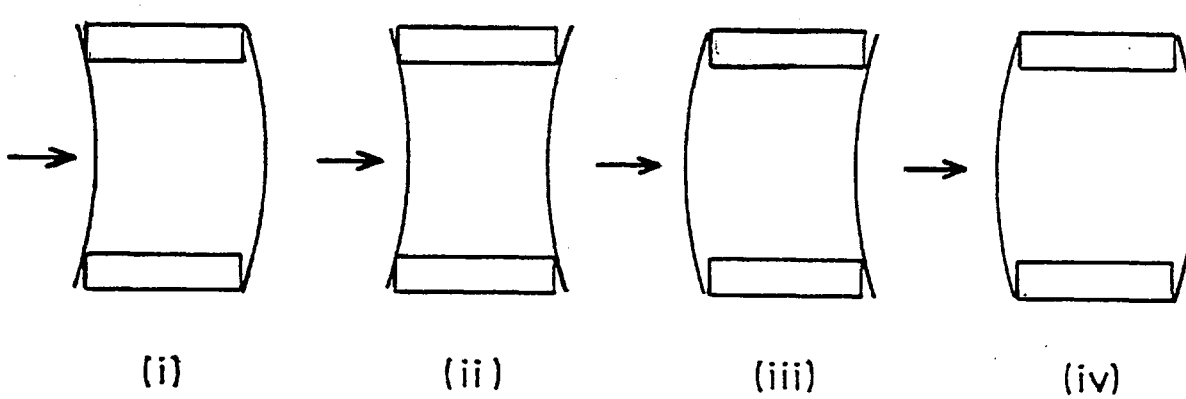

(b). Possible Spring Configurations.

to be inadequate, because it allows the free length of the spring to vary by up to half a millimetre both across one spring and also from the one to the other, thus leading to degraded parallel motion. Dowels are not used as the holes through the thin springs would wear and rapidly become oversized. The adopted solution is to hold the base and carriage a fixed distance apart during assembly by a pair of accurately machined aluminium parallels between the clamping blocks. After all the screws have been tightened, the parallels are removed. Both of the springs have a slight set to them and so, the scan parallelism attained with each of the four possible configurations (figure 5.11(b)) was checked. The evidence is not totally conclusive but arrangement (ii) seems best and is, therefore, used. The variation of scan parallelism with initial deflection from vertical was briefly examined. It was found that deviations from parallel motion are larger when operating around an initial deflection of 0.5mm than when in the region 0.9-1.3mm. Thus, it was decided to operate the F-P with an initial displacement of 1mm for this reason and also two others. Firstly, at larger deflections, the demagnification only varies slowly with displacement (cf. section 4.5) and secondly, this pretensions the carriage against the micrometer, thereby increasing the resistance of the instrument to 'sag' caused by changes in orientation. The deviations from parallel motion are due to tilting of the carriage and not to any form of mechanical slippage because when the scan is reversed, the original pattern is re-obtained. Over a change of 25 visible fringes (approximately equivalent to scanning one free spectral range at 12.8μm) the scan parallelism achieved corresponds to no discernable tilt in a direction perpendicular to the micrometer axis and to a tilt along the direction of motion of about 1.5 arc seconds, i.e. a parallelism finesse at 12.8μm of 50. This performance is therefore fully up to the design requirement. The limiting factor now is probably inequalities in the inter-spring lengths of the base and carriage respectively (cf. Jones and Young, 1956).

Using the same fringe counting technique, the demagnification of the micrometer motion as a function of the average displacement was measured. The F-P is set to some initial displacement and then the micrometer movement needed to scan 20 visible orders (i.e. an etalon gap change of about $5\frac{1}{2}$μm) is noted. The results are presented in figure 5.12. There is some scatter because each point represents the demagnification at an arithmetic average of the initial and final displacements. Additional scatter is due to inability to identify and then stop at the exact centre of a fringe.

Figure 5.12

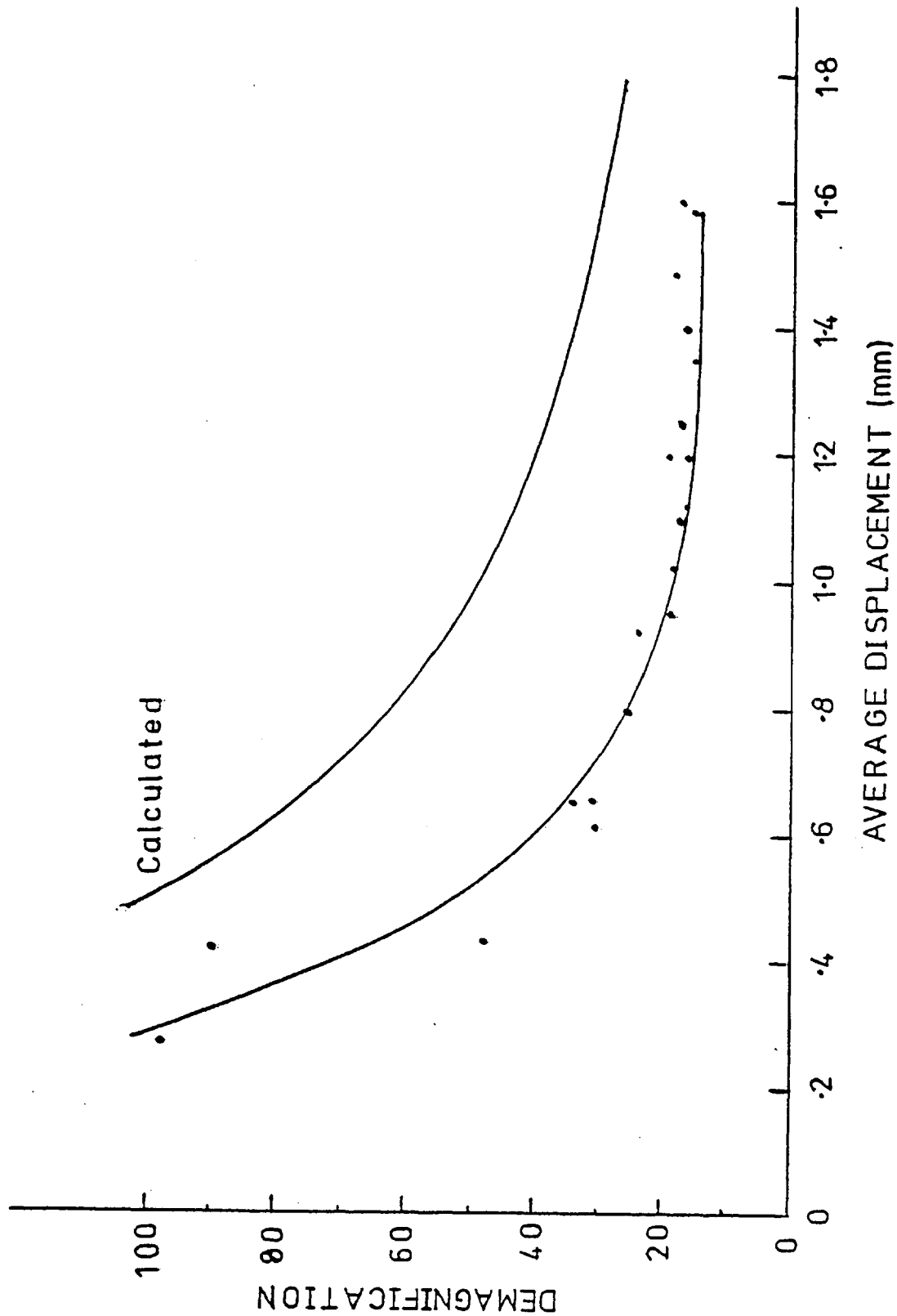

Demagnification of Scanning Motion as a Function of Initial Displacement.

However, comparison of figure 5.12 with the curve obtained from equation 4.18 shows that the approximation of figure 4.7(b) is never very good.

After aligning the F-P it can be picked up and moved around without disturbing the parallelism. However, sometimes when it is sharply struck, there is a sudden jump in the pattern, leaving a severe misalignment. This is caused by movement of the ball bearings in their V-grooves. Two of the three ball bearings are held between two V-grooves (cf. section 5.1.2). If the grooves of these blocks are not perfectly parallel, the ball rides up the walls of the grooves as it is pushed by the adjusting screws; thus, a sharp blow will cause it to move. This problem may be minimised by very carefully lining up the two grooves but, nevertheless, this was one of the reasons for abandoning this technique for the far-infrared version (cf. section 6.1.1). To check on the drift of the F-P, it was carefully aligned and allowed to stand overnight in the laboratory. Twelve hours later, it was misaligned by one visible fringe, i.e. an infrared parallelism finesse of 30. Using optical techniques no changes in the ring pattern are seen as the instrument is tilted over a range of angles from -40° to $+40^{\circ}$ in all directions. However, the capacitance micrometer indicates a sensitivity to tilt of 0.001μm per degree (equivalent to a parallelism finesse of 200 for a change of 0° to $+40^{\circ}$), but not much weight is to be given to this lower limit because the capacitance micrometer is neither designed nor calibrated to measure tilts. No detailed temperature testing has been done, but the instrument takes about 2 hours to settle down after a 25° temperature change.

5.2.2 Capacitance Micrometer Tests

Equation 5.1 shows that, in the capacitance micrometer (CM) electronics, the current which flows into the charge amplifier is proportional not only to the difference in capacitance but also to the frequency and amplitude of the oscillator. Thus, the stability of the frequency and amplitude is of obvious interest. The frequency stability was measured roughly by taking spot readings with a Counter/Timer while the oscillator was driving the electronics. Over a period of one hour, it is stable to one part in 50,000 and over 18 hours, 1 in 9000. To get some idea of the amplitude stability, the output from the balance box was amplified and phase-sensitivity detected using the normal reference signal from the oscillator. The drift per hour in this configuration is a factor of 15 less than the output drift obtained by comparing two nominally identical reference capacitors. Thus, both the amplitude and frequency stability

of the oscillator are easily adequate.

The next point of concern with the capacitance micrometer is its calibration. Firstly, the variation of the CM output for a given change in etalon gap at a given electronic gain (i.e. sensitivity) with drastic changes in F-P order was investigated using the following technique. The F-P is given a certain initial displacement from vertical, the three coarse adjusting screws are used to set a certain etalon gap, d, [corresponding to a capacitor pad gap, z, where d - z = constant and thus, $\delta z = \delta d$], and then the instrument is optically aligned. Next, the F-P is scanned a certain number (usually 20) of visible fringes, i.e. d and therefore z are changed by a given amount and the corresponding change in CM output noted. This enables the sensitivity in millivolts of CM output per micron gap change to be evaluated at a particular average etalon gap. No attempt is made to measure the absolute gap; rather, it is recorded in terms of the value of the reference capacitor, C_2 needed to zero the CM output. This capacitance is unique to one gap as long as all other variables are held constant. The above process is then repeated at different gaps (i.e. different reference capacitors). Figure 5.13 plots the results, which show that S is proportional to C_2^2. This is expected since the charge amplifier and psd 'convert' the current i_D of equation 5.1 to an output voltage, V, given by

$$V = X(C_1 - C_2) \quad , \tag{5.2}$$

where X is the electronics' transfer function. If C_1, the F-P capacitor, varies by δC, the output changes by

$$\delta V = X\varepsilon_o A \frac{\delta z}{z^2} \quad , \tag{5.3}$$

where A is the area of the F-P capacitor pads. Thus the sensitivity is given by

$$S = \frac{\delta V}{\delta z} = X\varepsilon_o A \, {}^1/_{z}{}^2 = \frac{X}{\varepsilon_o A} C^2 \quad . \tag{5.4}$$

Secondly, since S varies quadratically with etalon gap over large discrete changes in order, it is necessary to see how approximately linear it is

Figure 5.13

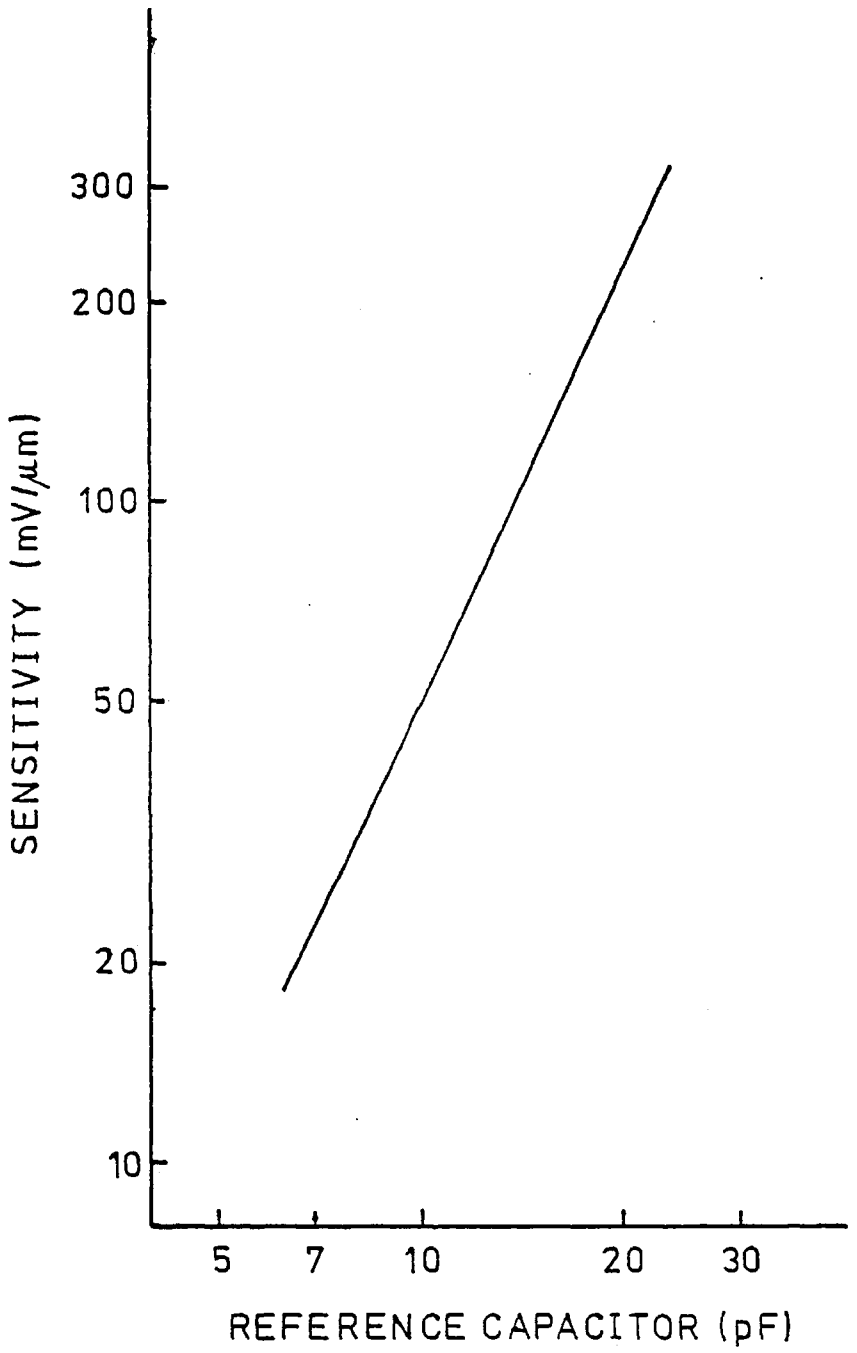

Sensitivity of Capacitance Micrometer as a Function of Etalon Gap.

when scanning over successive orders. To do this, the coarse adjustment screws are used to set a certain gap and then left alone. The F-P is given an initial displacement and, after being optically aligned, is scanned through 20 visible orders and S obtained, as above, for an average deflection. The instrument is then scanned to another initial displacement, re-aligned optically (if necessary) and the above process repeated to obtain another value of S. Figure 5.14 shows these results and demonstrates that S is non-linear even over the limited change in z involved in the scanning mode. However, at an initial deflection of around 1mm, the chosen operating point for the F-P, the carriage need only be moved about 0.1mm sideways to scan an entire infrared free spectral range. Over this short distance, the CM is linear to within a few percent.

In early trials of the CM system, severe short-term ($\sim$ few minutes) drifts in output were observed. These were eliminated by isolating the F-P from atmospheric draughts. The cause of the drifts is, thus, presumed to be variations of the dielectric constant of the air in the capacitor gap with temperature, pressure and relative humidity. With the F-P enclosed, there is a steady residual drift of about 0.02μm/hour or, to put it another way, in ten hours the drift is equivalent to one F-P resolution element (assuming a finesse of 30), a figure which is only just acceptable.

The peak-to-peak noise in the capacitance output in a noise bandwidth of 2 Hz is equivalent to gap changes of 0.02μm. This is four times smaller than the minimum change in plate spacing to be measured and so, the noise performance of the system is easily adequate. By shorting the input to the CM amplifier, it was established that this noise is associated with the F-P rather than with the electronics and is probably caused by the same mechanisms responsible for the drift.

5.2.3 Etalon Tests

As discussed in Section 5.1.3, two etalons were constructed, one having a thin gold film as a reflecting layer and the other a multi-layer dielectric coating. The thickness of the gold layer was monitored during deposition by measuring the change in the visible transmission of the mirror; calculations show that a 0.01μm thick layer (to give an infrared reflectivity of just over 96%) of gold on zinc selenide has a visible transmission of 61%. The dielectric coatings were deposited upon the other pair of plates by ITT (Harlow, Essex) and consist of seven layers

Figure 5.14

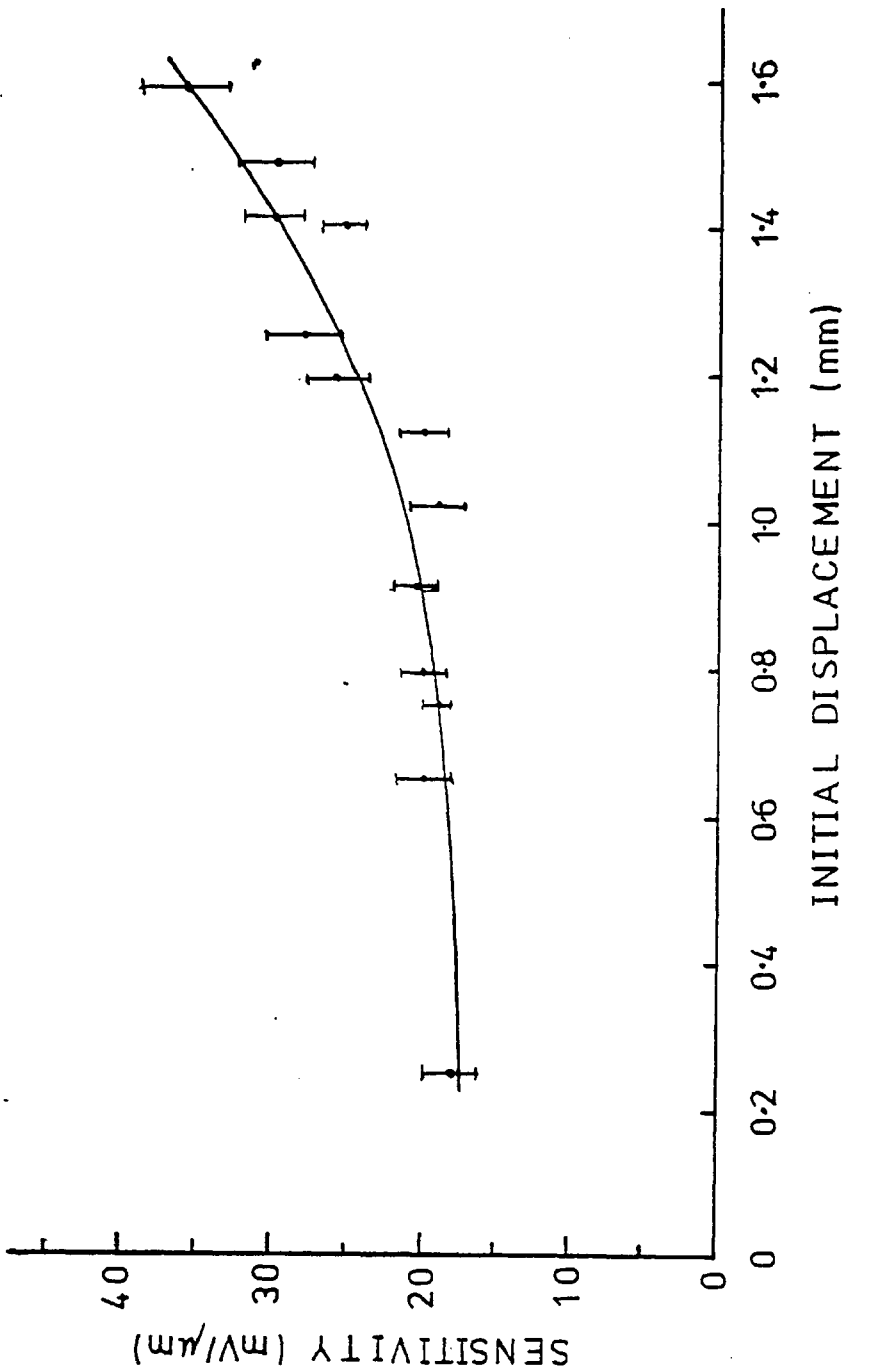

Sensitivity of Capacitance Micrometer over Small Gap Changes.

of zinc sulphide and thorium fluoride. The stack is designed to have a reflectivity of 94% (for a better match to the defect finesse than obtained with the metallic coatings) centred at a wavelength of 12.5μm, and an absorption always under 1% but expected to be nearer 0.5%. The anti-reflection coating on the other side of the dielectric-coated plates is a λ/4 layer of thorium fluoride with design reflectivity of 1% at 12.4μm rising to about 3% at wavelengths 20% away from the centre wavelength.

Due to the small size of the sample chambers of the infrared spectrometers easily available, it was not possible to measure the reflectivity, R, of the plates. However, the transmission, T, as a function of wavelength, was measured using a Perkin-Elmer grating spectrometer. The results are displayed in figure 5.15. For the dielectric-coated plate, the three regions of high reflectivity (low transmission), where the thicknesses of the layers are respectively 5λ/4, 3λ/4 and λ/4, are immediately obvious; the faster variation is due to interference between the individual layers comprising the stack. As expected, the gold layer shows a nearly constant high reflectivity throughout this spectral region. Because of the inaccuracy of the grating instrument when operating at low signal levels, it is not possible to obtain reliable quantitative information (e.g. summing design R and measured T to evaluate the absorption) from these data. They serve, however, to indicate the useable wavelength range of the etalons.

The specifications on the zinc selenide plates call for one side to leave an overall figure of $\lambda_{vis}/5$ and the other $\lambda_{vis}/1$. The flatness of all the plates was checked in a Twyman-Green (TG) Interferometer and, despite figure errors ranging from spherical to cylindrical, all eight faces are within the specification. Figure 5.16 is a photograph of the TG fringe pattern of the good side of one plate. Since the surface is better than $\lambda_{vis}/2$, it is necessary to tilt the reference wavefront and to estimate the figure error in the plate from the distortions in the wedge fringe pattern. Apart from the region around the edge, the flatness of the plate in figure 5.16 is better than $\lambda_{vis}/10$.

5.2.4 F-P Tests

The absorption, A, in the plates' coatings was estimated by measuring the maximum transmission, $\mathcal{T}_M$, of the F-P and using equation 4.7 re-arranged as follows:

Figure 5.15

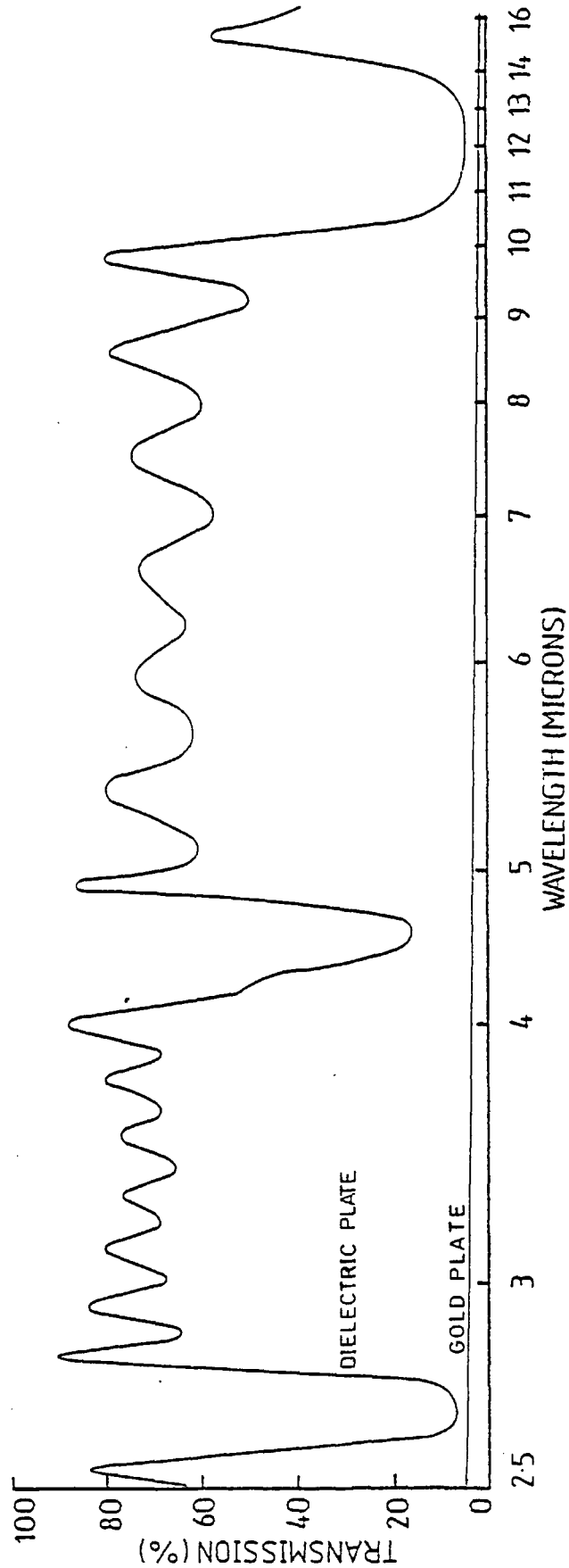

Note: Wavelength scale expands by x2 after 5μm.

Transmission Spectra for Gold- and Dielectric-Coated Zinc Selenide Fabry-Perot Plates.

Figure 5.16

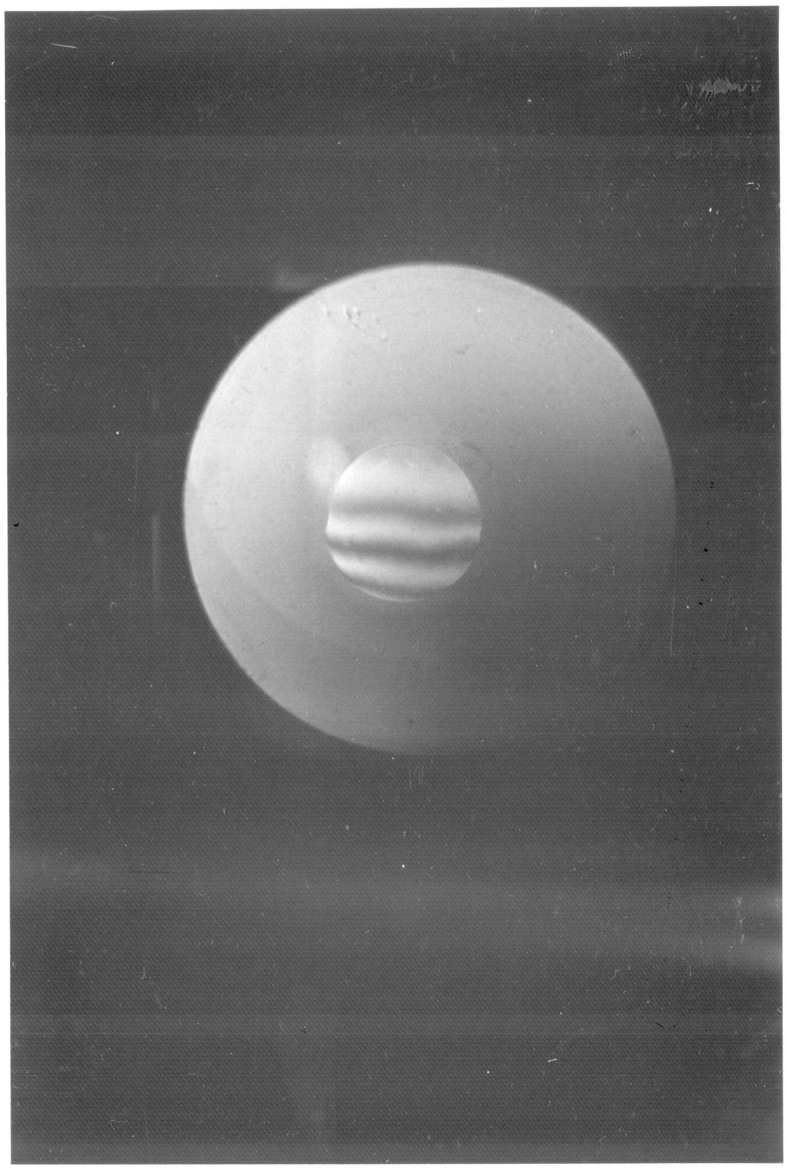

Twyman-Green Interferogram for a Zinc Selenide Plate.

$$A = (1-R)(1-\mathcal{F}_M^{\frac{1}{2}}) \quad . \qquad 5.5$$

The F-P was optically aligned and its insertion loss measured by putting it into an infrared beam. This loss, after correction for spectral bandwidth factors, is a measure of the peak transmission of the instrument. For the gold-coated etalon, it was difficult to get any energy through the F-P and an upper limit to the ratio $F\text{-}P_{in}/F\text{-}P_{out}$ of 1/1000 was measured. After correcting by a factor of x20 for bandwidth (3.5μm bandwidth of G-P filter in photometer compared to ∿ 10 F-P orders each assumed to be 0.02μm wide), this gives a peak transmission of <2% leading to an absorption in excess of 3%. This is too high to allow an F-P to work and so the gold coated plates were abandoned. All further near-infrared work was, therefore, carried out using the dielectric coated plates.

To see if the instrument were actually working as an F-P in the infrared, it was optically aligned and put into the sample chamber of an infrared grating spectrometer. The latter was then scanned in wavelength and the variation in the transmission through the F-P observed. The results are shown in figure 5.17. This trace is the square of that for a single plate (cf. figure 5.15) with a faster modulation superposed. This modulation is definitely due to Fabry-Pérot action for two reasons. Firstly, the peaks move in wavelength as the F-P is scanned and secondly, their separation (∿ $11cm^{-1}$) corresponds to an etalon gap of about 450μm. A direct measurement of the plate spacing yields a similar value.

The last point to be discussed in figure 5.17 is the low peak transmission in the region of interest around 12μm. The grating spectrometer passes an f/5 beam through the F-P in its sample chamber. This equivalent to an aperture finesse of 3 (equation 4.15). Thus, the overall finesse, $\mathcal{F}_I$, of the F-P is limited to a similar value. The maximum transmission, $\mathcal{T}_M$, is given by

$$\mathcal{T}_M = \mathcal{F}_I/\mathcal{F}_R \quad , \qquad 5.6$$

where $\mathcal{F}_R$ is the reflective finesse (50 in this case). This gives a $\mathcal{T}_M$ of 6%, which agrees reasonably well with that measured. The reduction of $\mathcal{T}_M$ with range of angles incident, i.e. aperture finesse, can be thought of in two very physical ways. Firstly, consider a perfectly monochromatic cone of light passing through the F-P. It is obvious that only the rad-

Figure 5.17

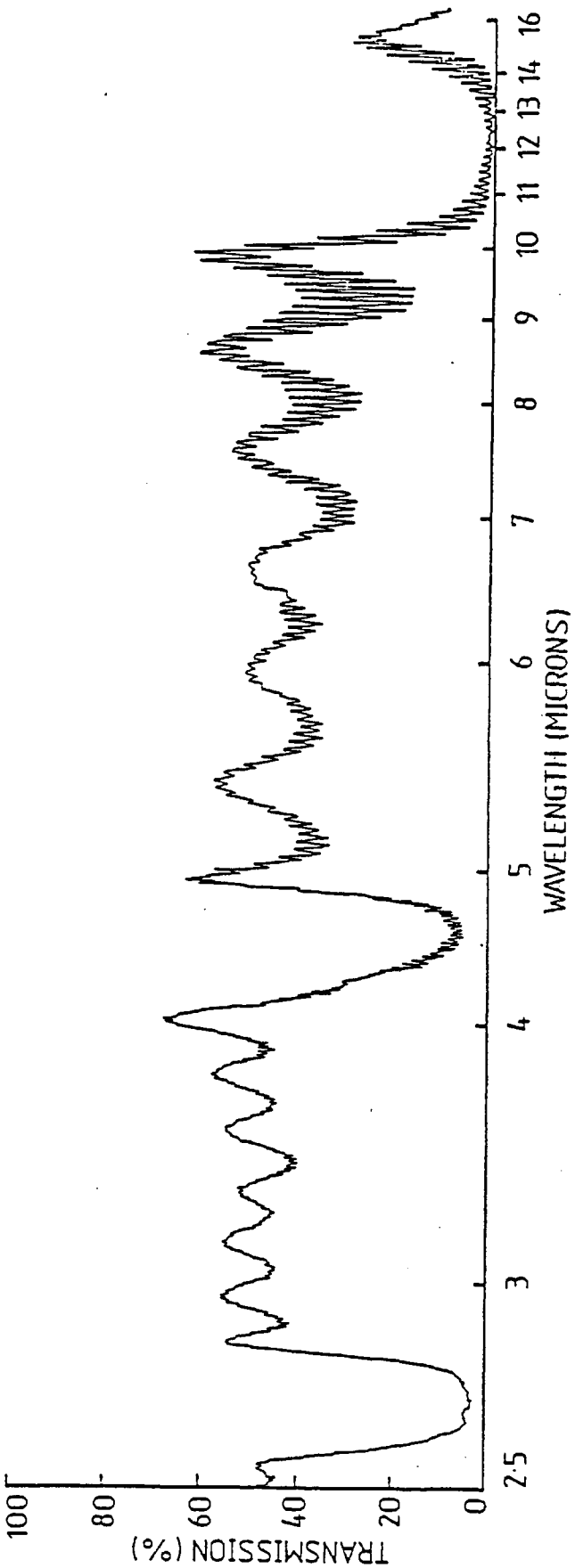

Note: Wavelength scale expands by x2 after 5μm.

Transmission Spectrum of Near-Infrared Fabry-Perot Interferometer.

iation incident at a particular angle finds the correct F-P gap for transmission. Radiation at all other angles (the majority of the cone) is rejected, causing a large drop in energy throughput. Secondly, the F-P plates individually have high reflectivity and can only, jointly, have high transmission, by interacting with each other via multiple reflections of the radiation. If the number of interfering beams (the overall finesse) is only 3, the amount of interaction possible is severely limited. Therefore, the two plates tend to act individually, each reflecting most of the incident energy.

The above argument depends on the overall finesse of the F-P being limited to 3. This value was confirmed by comparing the resolution obtained with that expected if $\mathcal{F}_I$ were indeed 3. The order of the F-P was calculated, from the etalon gap and equation 4.8, to be about 70, thus leading to an expected resolution of $\sim$ 200 (equation 4.12), which agrees with that obtained in figure 5.17. The resolution of the grating spectrometer at 13μm is nearly 400 and so this was not a limiting factor. Thus, this test conclusively shows that the instrument is working as a Fabry-Pérot Interferometer.

The next series of tests in the laboratory was designed to get some idea of the resolution and maximum transmission of the F-P. The following experimental procedure was used. The interferometer is optically aligned and the capacitance micrometer calibrated by counting visible fringes (cf. section 5.2.2). After the etalon gap has been measured using a travelling microscope, the instrument is placed underneath a dewar containing the 10μm photometer (cf. section 5.1.3). Radiation from a chopped black body is directed into the dewar through the F-P by a 45° mirror as shown in figure 5.18. An Oriel grating monochromator can be inserted into the optical train as necessary. The bolometer output, after passage through the preamplifier (cf. section 5.1.4), is phase-sensitively detected using an Ithaco lock-in amplifier and the result displayed on a strip chart. All optical components are aligned for maximum signal and the standard detector noise checks made before starting upon the test programme.

Firstly, the F-P without an order-sorting filter was left at a fixed gap as the monochromator was scanned in wavelength. A series of peaks was seen on the chart record as the passband of the monochromator co-incided with different orders of the F-P. From the spacing of these peaks in wavelength, the etalon gap was calculated. This value agrees

Figure 5.18

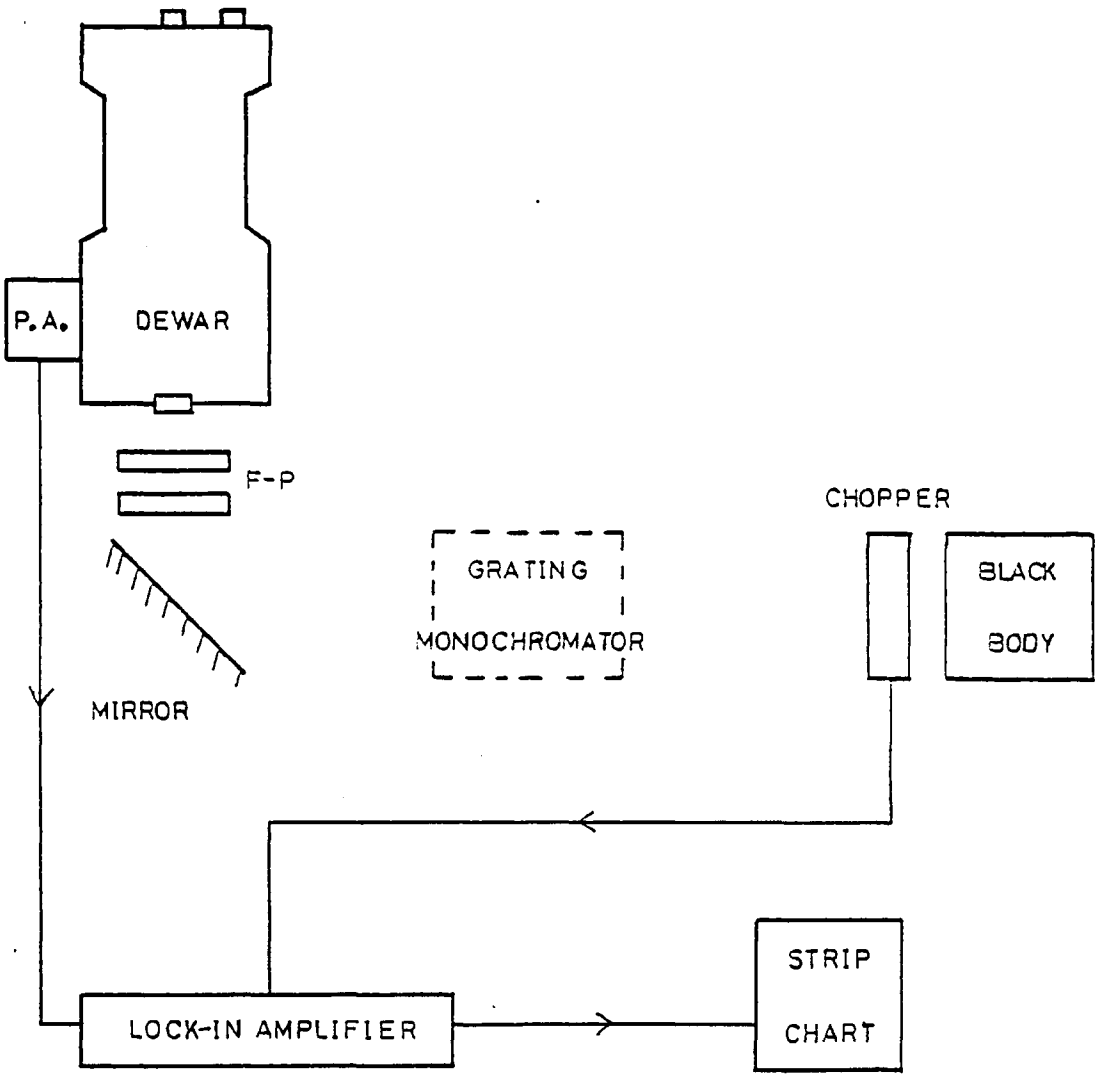

P.A. = Pre-Amplifier.

Laboratory Arrangement for F-P Tests.

with that obtained by the travelling microscope.

Next, the monochromator was removed and replaced by the narrow-band order-sorting filter. The F-P was then scanned and figure 5.19 shows the profile of the order sorter (O/S) being mapped out by successive F-P orders. This trace is definitely of the O/S's profile for it shows a lop-sided triangle with a slow short-wavelength fall-off matching the O/S profile (cf. figure 5.6). Since the gap change needed to scan one free spectral range is known (half the mean wavelength) this test provides an infrared check on the optical measurements of the demagnification of the micrometer's motion and of the sensitivity of the capacitance micrometer. No discrepancies were found. The chart record also shows that the modulation is only 50%. This could be due either to the detector seeing several orders (F-P rings) simultaneously or to the free spectral range of the F-P being smaller than the bandwidth of the O/S. The depth of modulation did not increase when the aperture of the F-P was stopped down but it did when the F-P was operated (later) at a smaller gap. Thus the second explanation is probably the correct one.

The small scale variations in figure 5.19 looked to be more than just noise and so these scans were repeated at a much slower F-P scan rate and a longer time constant on the lock-in amplifier. The features are genuine and repeatable (figure 5.20) and are associated with the 10-13μm filter in the photometer, for, when this was removed in a later run, the features also vanished. All of these little peaks have approximately the same width and so it seems reasonable to take their width as a lower limit to the resolution of the F-P. There are about 20 peaks in one scan of the O/S which has a 5% bandwidth of 0.4μm. This gives an upper limit to the bandwidth of the F-P of 0.02μm, i.e. a resolution in excess of 600. Knowing the gap, the overall finesse may be calculated and is found to be 15.

The monochromator was then replaced in the optical path. The width of its spectral passband is controlled by the width of its entrance and exit slits. The latter were progressively reduced and at each setting, the F-P was used to scan the passband of the monochromator. Despite a very low signal-to-noise ratio, a monochromator bandwidth of 0.05μm was successfully detected. This confirms that the bandwidth of the F-P is less than 0.05μm.

Figure 5.19

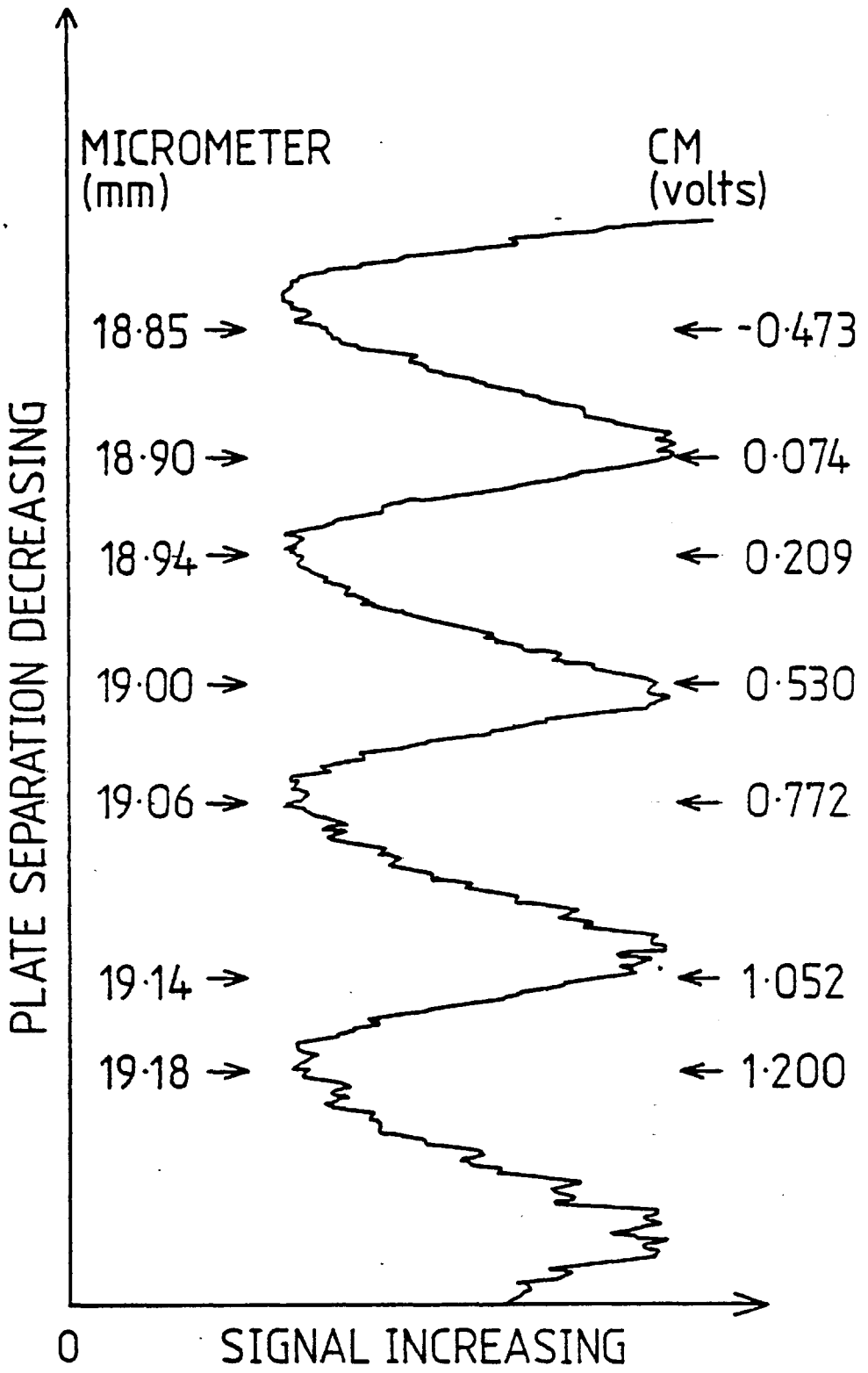

F-P Scans of Profile of Order-Sorting Filter.

Figure 5.20

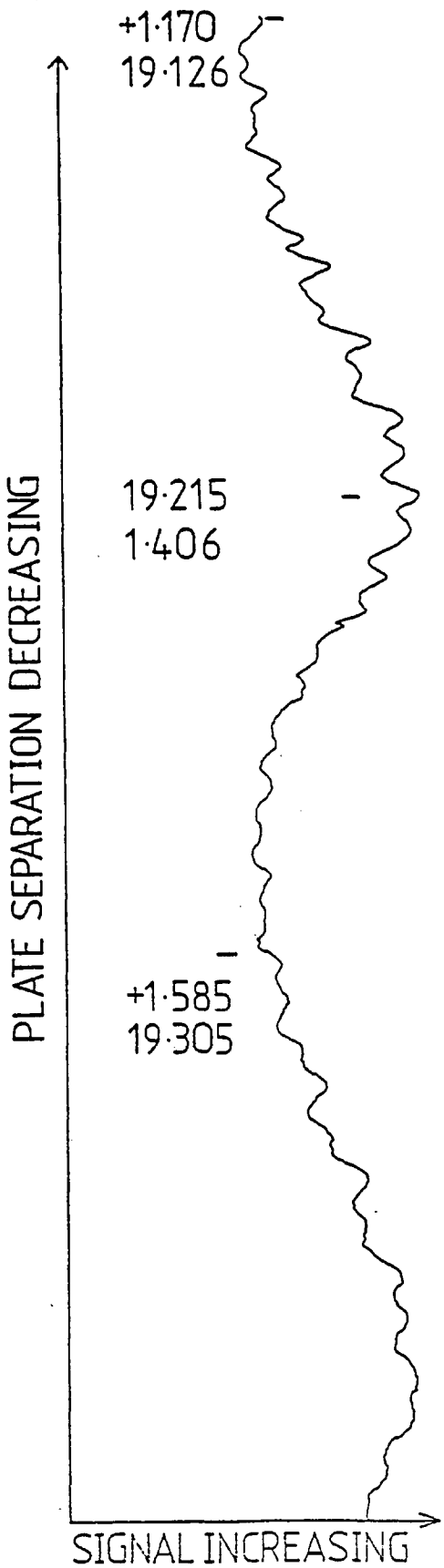

Details of Scans of Order-Sorter by F-P.

In order to get a rough idea of the transmission of the F-P, it was scanned until the signal passing through it was a maximum. Then, the slits of the monochromator were narrowed until its bandwidth matched that of the F-P. When the latter was removed from the optical train, the signal increased by a factor of 13. This technique is very crude and there are many possible sources of error, so the strongest conclusion that can be drawn from this measurement is that the transmission of the F-P is in excess of 8%.

Finally, the F-P was replaced in and the monochromator removed from the beam. The interferometer was then moved around slightly in order to ascertain the precision to which it has to be located on the telescope. The size of the signal passing through the F-P is unaltered if the instrument is moved by up to several millimetres in any direction or tilted by up to $1\frac{1}{2}^{o}$.

The conclusions from these laboratory runs are that the instrument is operating as a Fabry-Pérot Interferometer with overall finesse in excess of 15. Due to the width of the passband of the order-sorting filter, the F-P must be operated in 25th order (or less) leading to a resolving power in excess of 400.

5.3 Tenerife Experiences

The next few sections describe the use of the near-infrared F-P with the 60" Infrared Flux Collector (IRFC) on Tenerife. The observing procedures are presented and then some astronomical results are discussed.

5.3.1 Observing Runs

The 10μm F-P has been taken to the IRFC on three separate occasions. During the first run (December 2-18, 1977), the weather closed in with rain, hail and snow and only six nights were at all useable. Of these three were of reasonable quality and were used for 10μm photometry to check out and evaluate the photometric system. Electronic and mechanical integration of the F-P with the telescope was carried out in this period but it was never possible to use the interferometer astronomically. The first week of the second observing trip (April 28-May 11, 1978) was devoted to 1-5μm observations of X-ray objects as part of a simultaneous multi-wavelength observing programme (Willis *et al.*, 1980; Treves *et al.*, 1980). The second week was shared between the F-P and a 10μm polarimeter

(Rosen, 1981); results from the interferometer's four nights on the telescope are described below. No liquid helium was delivered to the observatory until 22.00 hours on the last night of the third observing run (13-28 October 1978), and, thus, this trip was used for JHKLM observations of various objects, especially Nova Cygni 1978 (cf. Appendix B). However, the F-P was hurriedly put on the telescope on the last night and atmospheric scans - using the moon as a source - were made.

5.3.2 Observing procedures

The photometry system and observing procedures used for these 10μm observations are very similar to those described in Appendix B. The main difference is the use of a liquid helium dewar containing the WPSM photometer (cf. section 5.1.3) and a Low bolometer. Measurement of the load curve of the detector established that a bias voltage of 1½V across the bolometer and load resistor (7.6MΩ) would maximise the electrical responsivity at about $2\times10^{6}VW^{-1}$.

Each evening, at twilight, the dewar is topped up with cryogens. The resistance of the bolometer at 4.2K, when looking at a reflection of itself, is measured. The obtained value of 14.2kΩ was repeatable from night to night. The cryostat is then placed in the photometer cage (cf. figure B2) atop the adjustable dewar stand. Figure 5.21 is a photograph of the 10μm photometry dewar in position. Note that the F-P (bottom left hand corner) has not yet been moved from its test position in the photometry cage to its operational position underneath the cryostat. After the pressure above the liquid helium has been slowly reduced to about 4 torr, the bolometer resistance is repeatably about 2.4MΩ.

Next, the frequency and amplitude of the chopper have to be set. To reduce the effect of 1/f noise, it is desirable to work at high frequencies. But, since the response of the bolometer decreases with increasing frequency, a compromise has to be made. A frequency around 20 Hz is suitable because the bolometer test results show that its output at this frequency is 99% of that at d.c. The chopper is fine-tuned in frequency around 20 Hz until no chopper-induced microphonics are seen on the detector output. The chopper amplitude is then adjusted to give a movement of just over $\tilde{20}''$ on the sky, for a $\tilde{10}''$ beam. Next, the position of the dewar is altered until the 'offset' between the two infrared beams is minimised. Finally, the telescope is slewed to a bright star and focussed as described in section B.3.

Figure 5.21

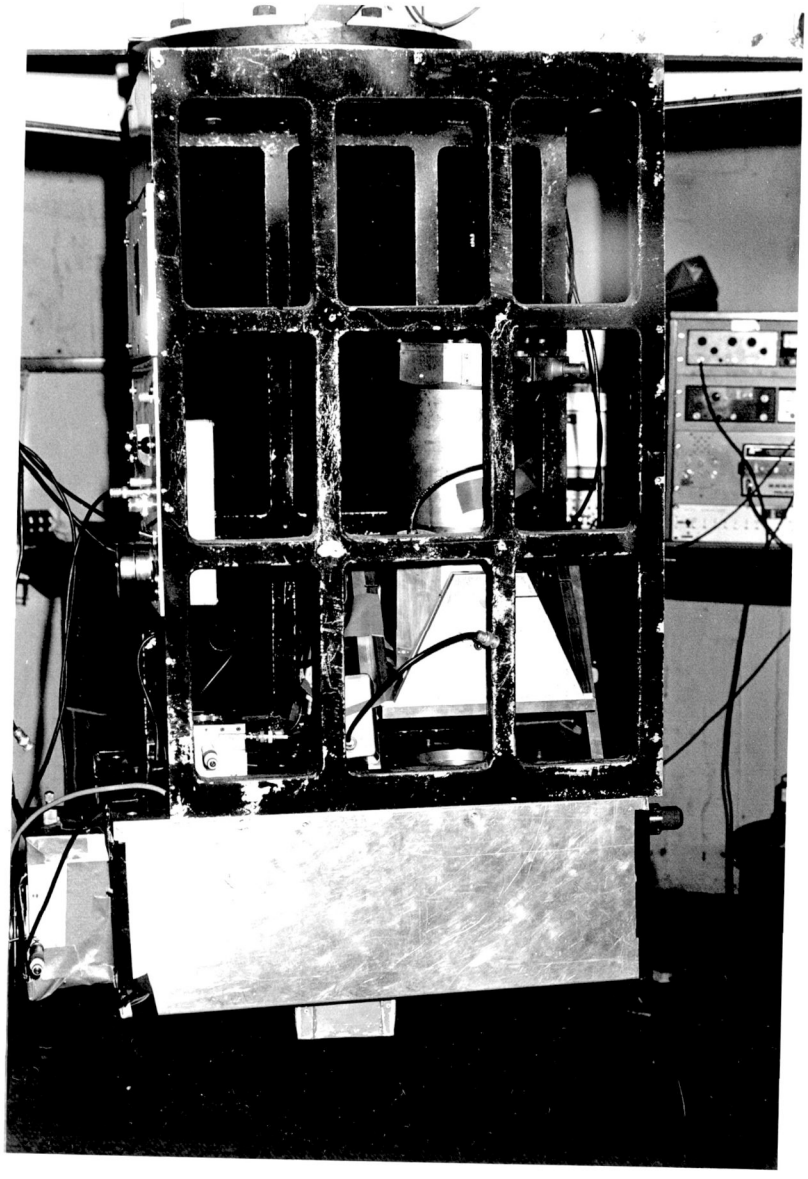

The I.R. Laboratory's Dewar on the IRFC.

A BASIC computer programme, written by N.L. Vine and modified by P.R. Jorden and D.L. Rosen (among others) is used to perform long integrations upon faint sources. Once the two infrared beams have been found, the object is centred up in one of them. The computer, through the CAMAC interface and a CAMAC analogue-to-digital converter, samples the phase-sensitively-detected bolometer output a certain (adjustable) number, n, of times at a certain (adjustable) frequency. Then, upon a computer command, the telescope is nodded i.e. the object moves into the second infrared beam. When the telescope has settled, the detector output is again sampled n times. After this, the IRFC is nodded back to the first beam and another n samples taken. The computer programme processes these three sets of data together and, having removed spikes and linear drifts, gives real-time signal-to-noise information. The nod cycle can be repeated as often as desired, usually being terminated when the signal-to-noise ratio has either built up to an acceptable level or shows no signs of so doing.

While working on very bright objects, it was found that the signal through the F-P could be increased by $\sim$ 25% by slightly refocussing the telescope. Thus, the telescope focus is always altered by a given amount when changing from photometry to spectroscopy. Also, as expected (cf. section 5.1.1), it was very difficult to find astronomical objects with the F-P in position. Therefore, the interferometer and the order-sorter are always removed from the telescope beam while searching for the source. They are only replaced after the object has been located in both infrared beams. A quick-release locating clamp was designed and used to re-position the F-P to within the tolerances quoted in section 5.2.4.

5.3.3 Noise and Sensitivity Checks

With the telescope looking at blank sky, the system noise is on average $\sim$ 40nV $Hz^{-\frac{1}{2}}$, of which 14nV $Hz^{-\frac{1}{2}}$ is due to the preamplifier, leaving an observed detector noise, e_o, of 37nV $Hz^{-\frac{1}{2}}$. When the shunting effect of the load resistor, R_L, is considered, the true detector noise, e_d, is given by,

$$e_d = \left[\frac{(R_L+R_d)^2}{R_L^2} e_o^2 - \frac{R_D^2}{R_L^2} \cdot e_L^2 \right]^{\frac{1}{2}} , \qquad 5.7$$

where R_d is the detector resistance and e_L, the Johnson noise voltage of the load resistor. For the above case, e_d = 48nV $Hz^{-\frac{1}{2}}$ which is three times higher than the Johnson noise expected from a 2.4MΩ resistor.

The noise does not change when the dewar window is blanked off, showing that the system is indeed detector and not background noise limited (cf. section 5.1.1). Consistent with this conclusion, no change in the noise is observed when the F-P is put into the beam.

To measure the sensitivity of the system, a noise run was made on blank sky and then photometry performed on the star, α Boo. The output filters of the phase-sensitive detector (psd) used have a roll-off of 6dB per octave. Thus, with the RC time constant of the psd set to 1s, the integration time is 2s and the noise bandwidth, $\frac{1}{4}$ Hz. The noise was observed for a time equal to 100τ; the maximum excursion corresponded to 90nV peak-to-peak at the detector, i.e. the 1σ noise was 18nV. Next, several nod cycles of photometry were done on α Boo; the signal at the detector for this star was 5.5μV. Thus, a signal-to-noise ratio of 290 was achieved in a post-detection bandwidth of 0.25 Hz. The CIT list gives the 10μm magnitude of α Boo as -3.25. Using the magnitude-flux calibration given by Thomas et al., (1973), the 10μm flux from this star was calculated to be 730 Jy. Thus, the sensitivity of the IC 10μm photometry system is 5 Jy $Hz^{-\frac{1}{2}}$.

5.3.4 Observations of Mars on 7/8 May 1978

The IRFC was set up as described above and the planet, Mars, was found. The F-P was optically aligned and put into the telescope beam. After refocussing and peaking up the signal, it was found that the F-P, without the order-sorting filter, had attenuated the signal by a factor of x30. This ratio was used to estimate the maximum transmission, $\mathcal{T}_M$, of the interferometer in this manner. The flux transmitted is roughly proportional to the spectral bandwidth of the system. Without the F-P, this is just the bandpass, dλ, of the Grubb Parsons filter in the cryostat (cf. section 5.1.3). With the F-P, it is approximately the product of the number, N, of F-P orders inside dλ and the width, δλ, of each F-P order. In the latter case, an additional factor of $\mathcal{T}_M$ must be included to allow for losses in the F-P. N is given by the ratio dλ/Δλ, where Δλ is the free spectral range of the F-P. Finally, the ratio of fluxes with and without the F-P is obtained by bringing together the above factors and using the definition of overall finesse, $\mathcal{F}_I$, to give,

$$\frac{\text{Signal with F-P}}{\text{Signal without F-P}} = \frac{\mathcal{T}_M}{\mathcal{T}_I} \quad . \qquad 5.8$$

The experimentally-determined ratio of 30, leads to a maximum transmission of 50% if an overall finesse of $\gtrsim$ 15 is assumed (cf. section 5.2.4). This value is slightly higher but, in view of the approximations made, not inconsistent with the > 30% expected from equation 5.6.

When the order-sorting filter was added to the optical train, the signal fell by a factor of x125. A reduction of about x80 can be accounted for by the following: x12 for only having one F-P passband and not many; x2 for the transmission of the order sorter; about x2½ because the F-P passband was not at the centre of that of the order sorter and about x1.3 for the variation in transmission with wavelength for the GP filter. Thus, a factor of about 1½ is left to be explained. This is thought to be due to the order sorter because a similar fraction was lost in an earlier run when comparing the signal through the GP filter with that through the GP and order-sorting filter.

Next, the F-P was calibrated in wavelength by plotting out the passband of the order sorter and looking for atmospheric absorption features. For simplicity, the instrument is operated in a "stop and integrate at a point" mode rather than continuously scanning and adding many scans. This means that the computer is used to do photometry at one point and after a reasonable signal-to-noise ratio has been achieved, the F-P is scanned about half a resolution element and photometry again performed. This was repeated about 25 times on Mars. The change in wavelength transmitted by the F-P from point to point can be calculated if the order and the change in plate spacing are known. The former is obtained from the absolute etalon gap and the latter measured in two independent ways. Firstly, the output of the capacitance micrometer is noted at each point and using previous optical measurements of the sensitivity (cf. section 5.2.2), the gap change is calculated. Secondly, the amount that the carriage is deflected from point to point is measured by reading the drive micrometer (cf. figure 5.2(a)) and using the previously measured demagnification at this setting, the change in etalon gap is again obtained.

The capacitance micrometer can be read to one more significant figure than the drive micrometer but it drifts slowly during the night. Thus,

the capacitance micrometer is used as the prime wavelength change indicator with the drive micrometer being used to correct - if necessary - for its drift. Figure 5.22(a) shows the measured spectrum of Mars as a plot of relative flux against change in wavelength from an arbitrary zero. The dotted region was under-sampled and thus nothing can be said about it. Figure 5.22(b) is the spectrum that is expected for a 225K black body observed through the earth's atmosphere and the Grubb Parsons' and order-sorting filters. The atmospheric transmission was obtained from Kyle and Goldman (1975). The four atmospheric features of interest in this region are detailed in table 5.2,

Table 5.2 - Atmospheric Features around 12.8μm

Feature	Wavenumber(cm^{-1})	Wavelength(μm)
1	775.5	12.895
2	777.0	12.870
3	779.0	12.832
4	784.4	12.749

On examination of figure 5.22(a) features 2, 3, and 4 can be clearly seen and an absolute wavelength scale can thus be placed on this spectrum. Feature 1 falls in the region were there is no data. A considerable amount of cross-checking is possible because three separate features have been identified and there are two independent measures of wavelength change. No discrepancies have been found.

To check on capacitance micrometer drift, the points on Mars were not sampled sequentially in wavelength. There were some changes of direction and a plot of drive micrometer reading versus capacitance micrometer output was prepared (figure 5.23). This is a single smooth curve to within the drive micrometer errors and thus shows that capacitance drift was insignificant during the Mars scans. The curavture is due to the non-linearity of the scanning motion as discussed in section 5.2.2. Figure 5.23 also shows the relationship between drive and capacitance micrometer readings for work on the HII region G29.9-0.0. This is a similar curve to that for Mars but is slightly displaced due to capacitance micrometer drift (cf. section 5.3.6).

The main achievements of the Mars observations were to estimate the peak transmission of the Fabry-Pérot Interferometer and to unambiguously calibrate it in wavelength.

Figure 5.22

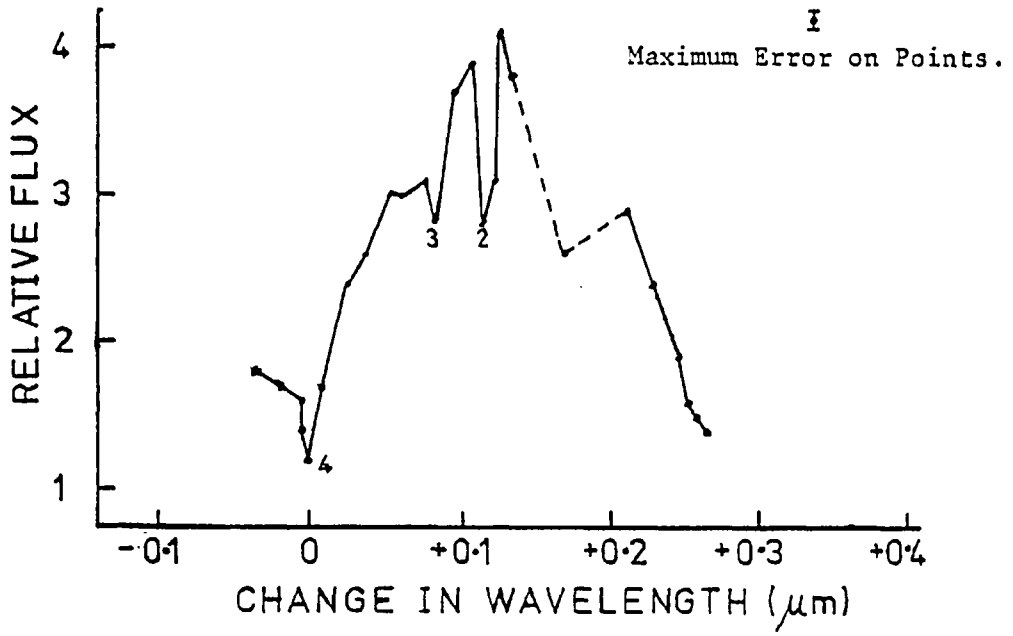

(a). Measured.

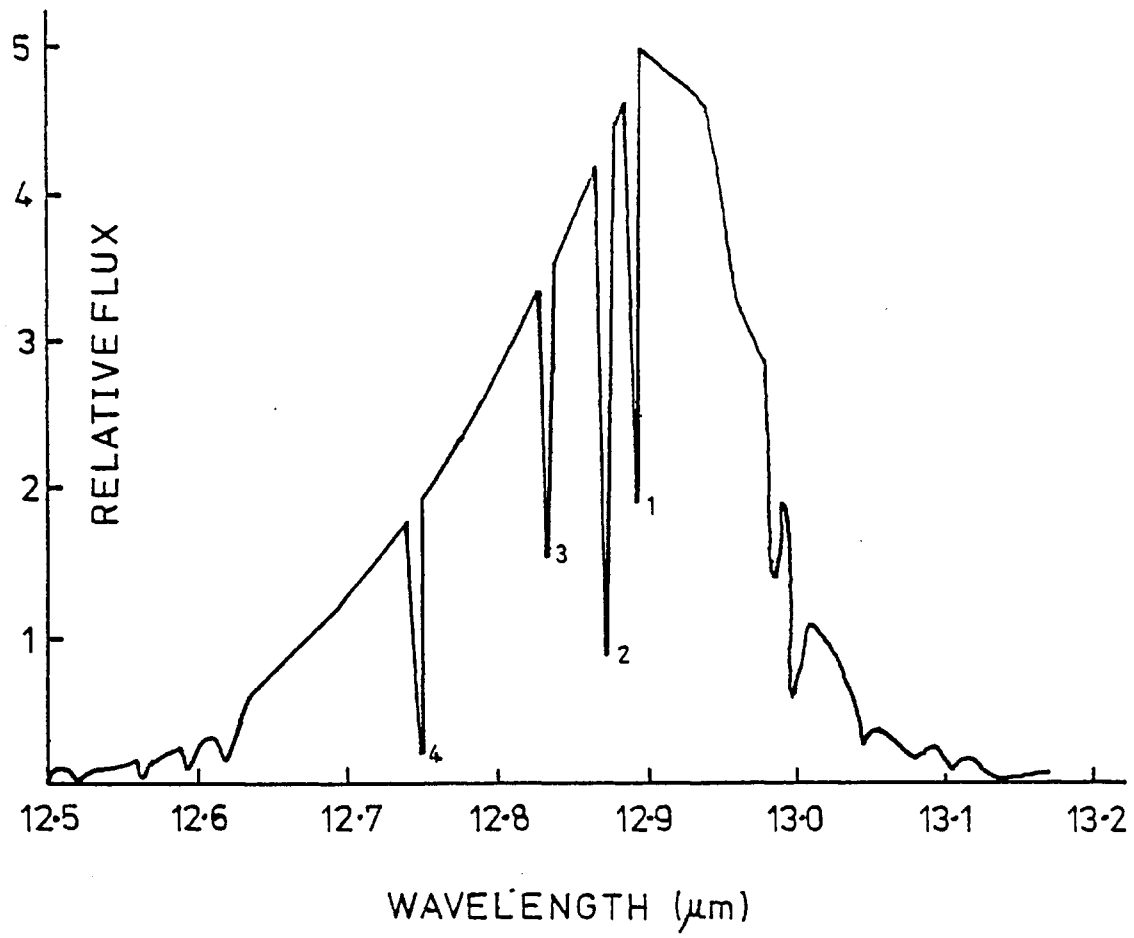

(b). Expected.

Spectra of Mars.

Figure 5.23

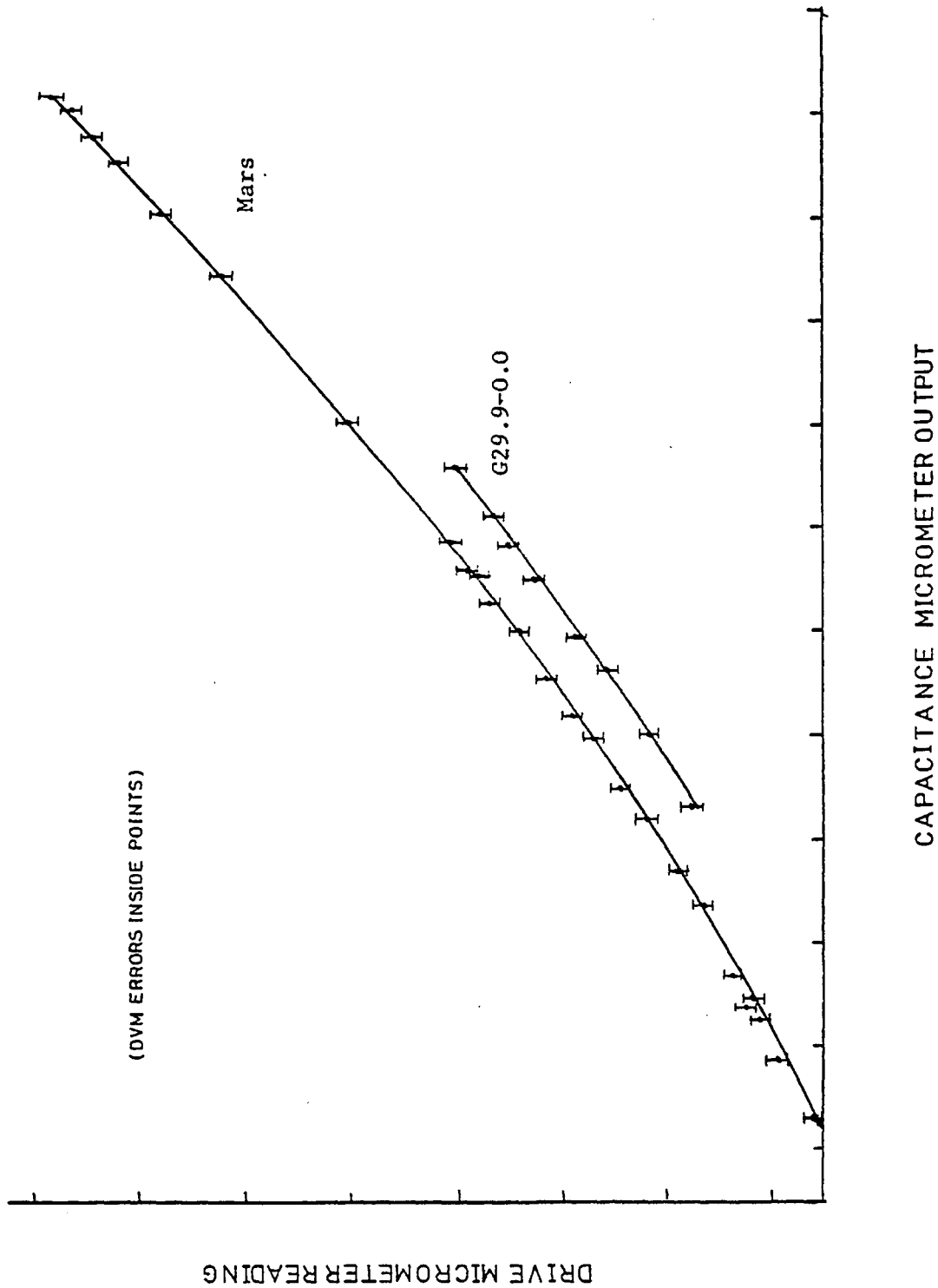

Relationship between Capacitance and Drive Micrometers for Mars and G29.9-0.0.

5.3.5 Observations of the Moon on 27/28 October 1978

During the October 1978 observing run, the F-P was only on the telescope for half a night; the only results of interest were some scans of the moon. Instead of the 'stop and integrate' mode used for the Mars work, the F-P was, in this case, continuously scanned at a very slow speed through several orders. The detector was chopped on and off the edge of the moon. The time constant of the psd was set to match the time taken to scan through one F-P resolution element. Figure 5.24 shows the results. The modulation is just under 80%, the deviation from 100% being caused by operating the F-P in too high an order and thus having two F-P passbands inside the order sorter profile at some times. The signal-to-noise ratio is not really high enough to identify features on the order-sorter's profile but it is certainly apparent that there are some repeatable absorption features. If peak D, the best of the four, is considered in the most favourable light possible, four putative features (see figure 5.24) are seen. The wavelengths of these can be estimated from the sensitivity of the capacitance micrometer, if the peak of the profile of the order sorter is used as a wavelength datum. The results are listed in table 5.3, together with the wavelengths of the atmospheric absorption features from Kyle and Goldman (1975).

Table 5.3 - Wavelengths of Tentative Absorption Features in Lunar Spectrum

Feature	Wavelength(μm)	Wavelength of Telluric Features(μm)	Difference
1	12.85	12.895	-0.05
2	12.81	12.870	-0.06
3	12.78	12.832	-0.05
4	12.72	12.749	-0.03

Thus, it is possible to identify the features in peak D with known atmospheric absorption lines. However, the data is so poor and the identification so tenuous that the conclusion must be only that it is not possible to rule out having detected telluric absorption features in the lunar spectrum.

5.3.6 Detection of the 12.8μm [NeII] line in G29.9-0.0 on 7/8 May 1978

After the F-P had been calibrated on Mars on the night of 7/8 May 1978, it was carefully removed from the beam. The HII region, G29.9-0.0

Figure 5.24

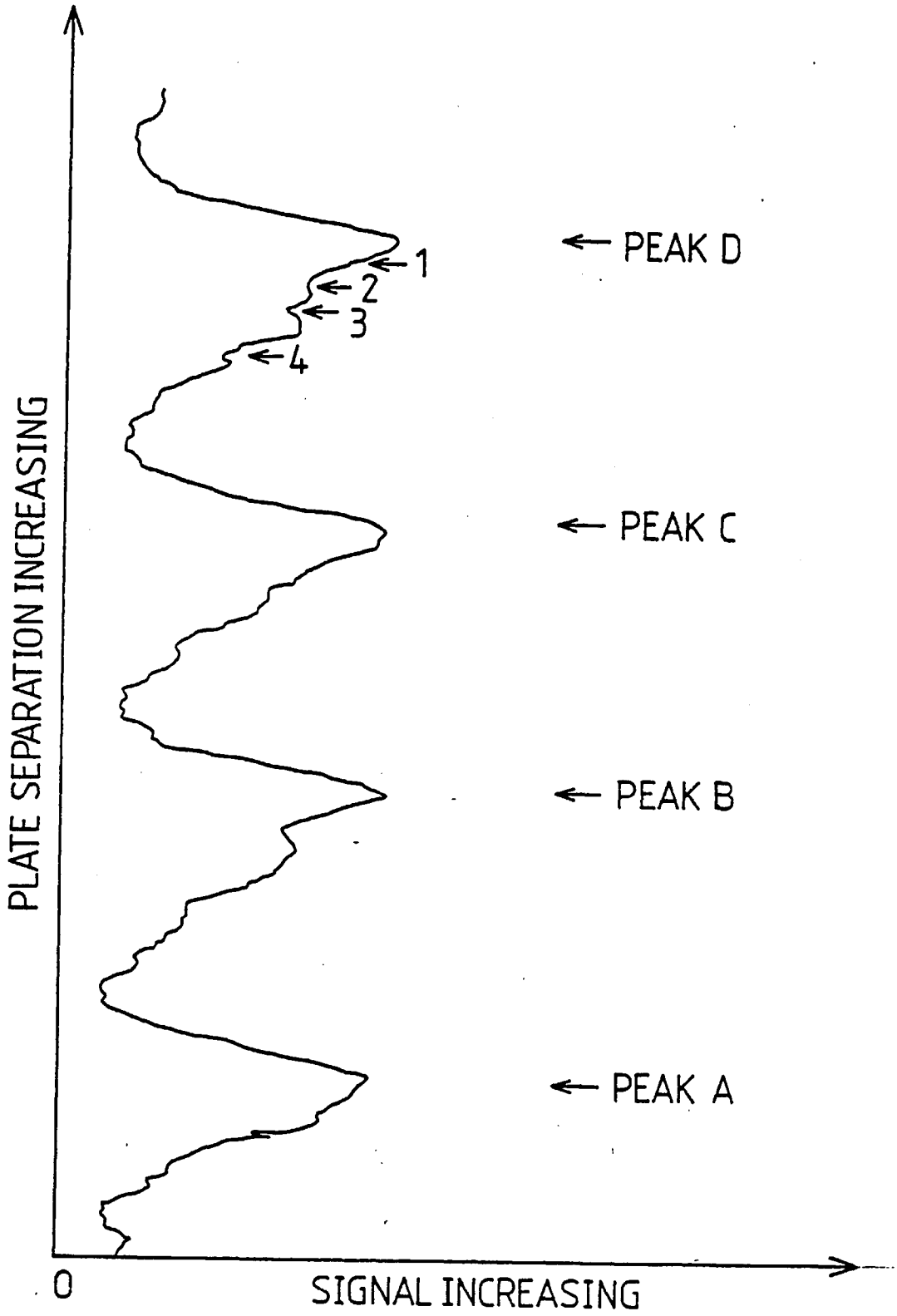

F-P Scans of Moon.

was then found before replacing the F-P. Next, photometry was performed at 8 points spaced around where the [NeII] line was expected. At each point, both the drive and capacitance micrometers were read. Figure 5.23 shows the relationship between these two quantities. To compensate for the obvious capacitance micrometer drift between the Mars and the HII region work, all the capacitance micrometer readings were corrected by the average distance between the two curves of figure 5.23 before being converted to wavelengths. The results are shown in figure 5.25. Each point represents, on average, 140 seconds of observation. In the resolution element around 12.82μm (recall that the F-P bandpass is $\sim$ 0.02μm), the signal-to-noise ratio built up steadily and reached 5 after 180 seconds observation. This is a detection of the 12.81μm [NeII] emission line.

The flux in this feature is now calculated. From the data points around the neon line, the continuum signal is around 4, thus the line signal is between 13 and 17 relative units. The signal from Mars, at the position of the line, is 915, after correcting for all gains. At the time of observation, the angular diameter of Mars was $6.5''$. If it is considered as a 225K black body, the flux through the F-P from Mars is 3.7×10^{-15} W cm^{-2}. Thus, the measured flux in the [NeII] line is $5\text{-}7\times10^{-17}$ W cm^{-2}. This is comparable but slightly less than that of $9\text{-}22\times10^{-17}$ W cm^{-2} reported by Soifer and Pipher (1975).

5.3.7 Other Observations and Conclusions

In the very limited time that the F-P was on the telescope, some other observations were attempted. An effort was made to find the passband of the order sorter using α Sco and a 3σ detection resulted. The galactic centre and IC418 were also searched for neon emission, but the former object was lost during the course of the observation and the data from the latter was scrambled through mis-setting of computer parameters and has not yet been unravelled.

The IRFC runs with the 10μm F-P have demonstrated that the design is adequate and that the instrument works well with a resolution of up to 600 and reasonable maximum transmission. Much experience was gained in the mechanics of operating a spectrometer at a telescope and the need for several design changes for the balloon instrument was clearly seen. The highlight of this part of the project was obviously the detection of [NeII] emission from G29.9-0.0.

Figure 5.25

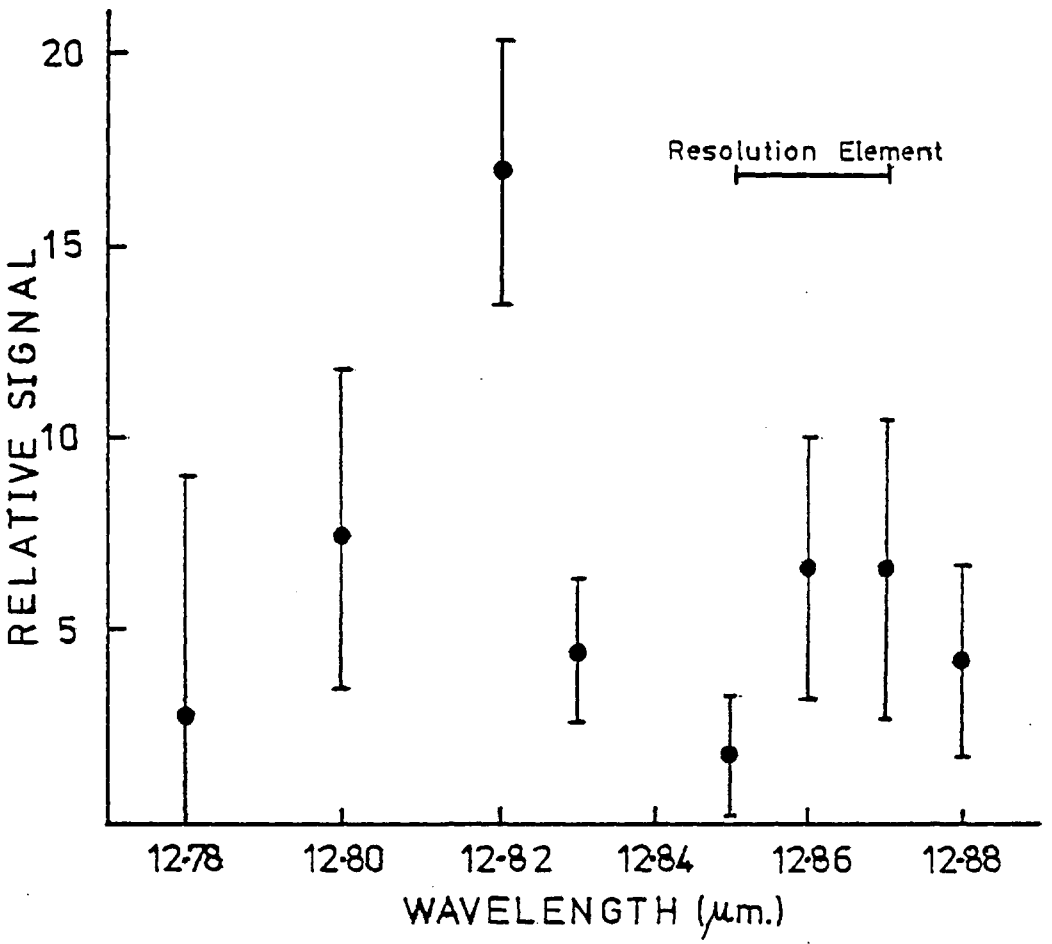

Spectrum of G29.9-0.0.

Chapter 6

Far-Infrared Fabry-Pérot Interferometer

The design details of a far-infrared Fabry-Pérot (F-P) Interferometer and its associated instrumentation are discussed in this chapter. Particular emphasis is placed upon the differences between this instrument and the 10μm F-P described in chapter five. Then, some techniques and various sub-system tests are detailed. Results from laboratory trials of the entire instrument are given together with comments upon their completeness. The chapter closes with details of the mechanical performance of the F-P during a balloon flight in 1979 December; failure of the stabilisation system during this flight precluded any optical trials of the instrument.

6.1 Design Details

Astronomical trials of the 10μm F-P had shown that the basic mechanical design, as outlined in section 4.5 and detailed in section 5.1.2, was sound. For the balloon-borne instrument, it was, thus, decided to retain this design but with two modifications. Firstly, the F-P would be cooled to liquid-nitrogen temperature and secondly, a new adjustment method for the plates would be adopted. It was obvious that due to the change in wavelength, an entirely new optical system would be needed and so the opportunity was taken to add a second detector, which would measure the continuum radiation from the astronomical object. This detector would be used initially to aid finding an object and then to guide on it. The problems of remote operation and scaling output parameters for the telemetry meant that the electronics needed rebuilding. Various other electronic modifications were also made; these and details of the mechanical and optical designs are discussed in the next three sections.

6.1.1 Mechanical Design

6.1.1.a Environmental Considerations

The overriding consideration in the decision whether to fly an ambient temperature or a cryogenically-cooled interferometer was the external environment. During the course of a balloon flight, this alters drastically. On the launch pad, the temperature and pressure are about 20°C and 760 torr respectively. The atmospheric temperature may fall to -70°C in

the tropopause and at float altitude (30 km) the conditions are likely to be -40°C and 8 torr. The near-infrared F-P took a considerable time to adjust to a temperature change (section 5.2.1) and its capacitance micrometer was sensitive to air currents (section 5.2.2). Because of these factors, it is desirable to provide a stable environment for the instrument. Examination of the physical dimensions involved showed that it was just possible to fit the F-P inside our IR Laboratories' HD-3 dewar without any major modifications to either. It is planned to cool the order-sorting optics to liquid-helium temperature and, therefore, the system is sufficiently narrow-banded to be limited by bolometer noise irrespective of the temperature of the interferometer. The trade-off is, thus, between the additional complexity of scanning a cryogenically-cooled interferometer and the advantages of a known and stable environment. The problems associated with scanning an instrument inside a dewar did not seem to be unsurmountable and so this approach was adopted.

6.1.1.b Drive Mechanism

The first difficult to be overcome with a cooled instrument was how to drive the F-P carriage sideways in order to scan the interferometer. Manufacturers of electric motors do not, in general, produce motors for operation below -55°C. This temperature limit is not due to technical problems for, while examining different electric motors, a very cheap one was totally immersed in liquid nitrogen and it continued to run, albeit a trifle jerkily. Despite this minor success, it was decided to avoid the field of cryogenic motors by using one at ambient temperature. Various methods of coupling its drive to the cooled instrument were then investigated. A liquid-helium-cooled polarimeter, developed in this laboratory by Rosen (1981), uses a magnetic coupling to transfer a rotating motion through the dewar wall. This technique was not used for the F-P because of doubts about its torque capability. Wilson seals were immediately ruled out because of the danger of the rubber bearings freezing at float temperatures. The problem was eventually solved by putting the motor inside the vacuum jacket of the dewar but thermally clamped to its outer case so that the motor remains at ambient temperature. This design is shown schematically in figure 6.1. The drive assembly (cf. section 5.1.2), consisting of the motor and gearbox, 1, the extendable coupling, 2, and the micrometer, 3, is contained in and attached to a dural extension, 4, to the dewar. A nylon rod, 5, firmly fixed to the micrometer spindle, is used for thermal insulation between the drive mechanism and the cooled

Figure 6.1

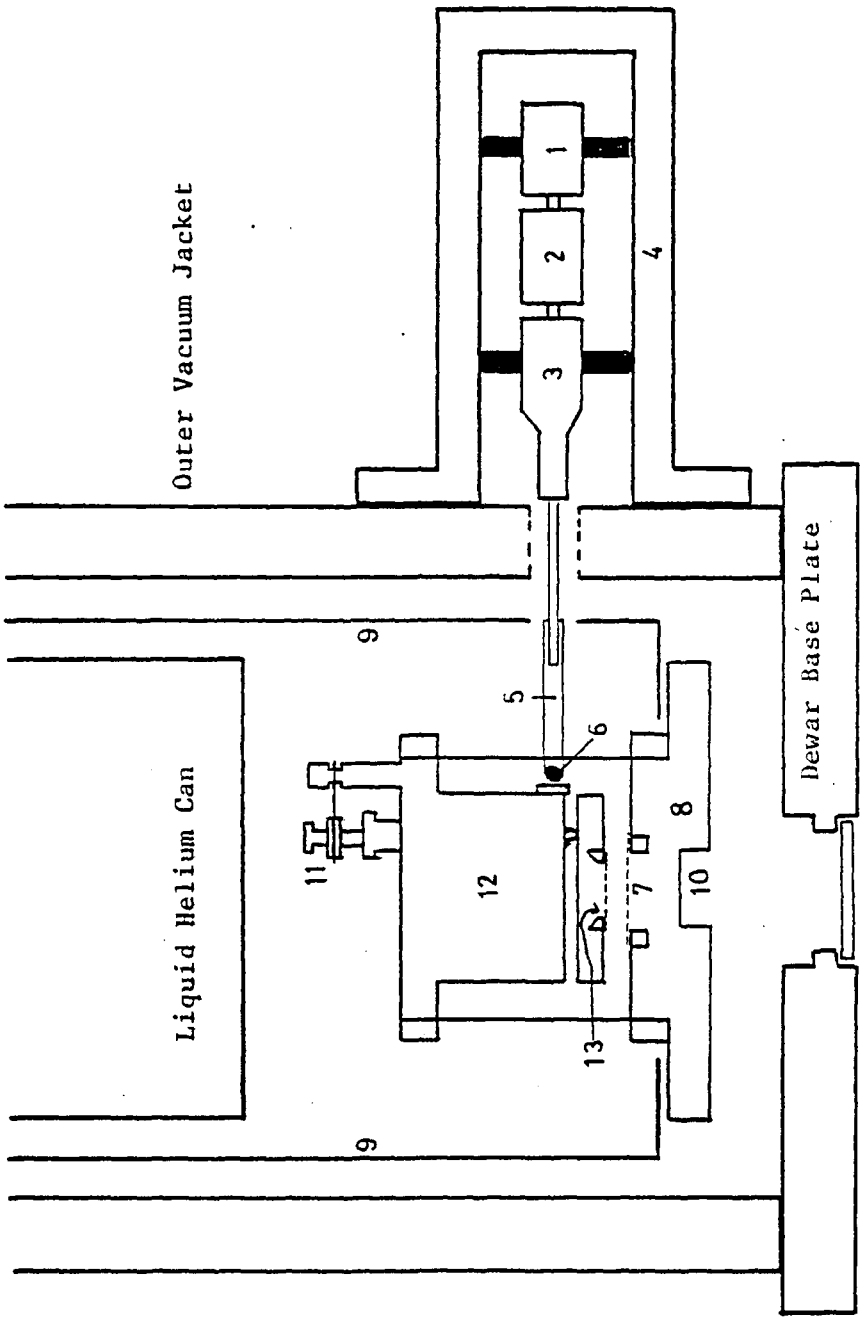

The Far-Infrared F-P inside the Dewar with Extension.

interferometer. A steel ball-bearing, 6, is let into the end of the nylon rod to reduce wear on the latter.

This drive method requires the interferometer to be operated at 77K rather than 1.8K for the following reason. When the F-P is at liquid-nitrogen temperature, the heat leak along the nylon rod boils off 7cc of liquid nitrogen during a 12-hour flight. However, if the instrument were to be at liquid-helium temperature, an additional 700cc of liquid helium, half the total dewar capacity, would be lost in 12 hours. This is clearly unacceptable.

6.1.1.c Adjustment Mechanism

The difficulty of adjusting the etalon parallelism with the ball-bearing/V-groove mechanism is discussed in section 5.2.1. Also, as seen in figure 5.3, the adjusting screws protrude from the sides of the base in the near-infrared design; inside the dewar, there is insufficient room for this. For these reasons, the V-groove mechanism was abandoned in favour of a differential screw design. Figure 6.2 shows the principle of the latter technique. A central screw, 1, bearing against the plate to be moved, passes through the centre of a second screw, 2, which in turn passes through the support, 3. The outer screw does not touch the plate. A locking device, 4, can be used to prevent the central screw, 1, from turning with respect to the support, 3. Suppose the central screw is unlocked and rotated. Friction prevents 2 from turning and thus the plate follows the motion of the coarse adjusting screw, 1. Consider what happens, now, if 1 is locked solid and 2 is rotated. Since 1 cannot rotate with respect to the support, the effect of advancing 2 is to retract 1 and, thus, for one revolution of the fine screw, 2, the plate moves a distance equal to the difference in pitch of 1 and 2. The sensitivity of this technique is obviously determined by the degree to which the two pitches can be matched. A practical consideration is that the major diameters of the chosen threads must be such that one screw is able to fit inside the other. A combination of a 2BA inner screw (pitch $\approx$ 31.8 thou) and an outer screw with a 5/16" Model Engineers' (ME) thread (pitch $\approx$ 31.3 thou) gives a practical minimum change in plate angle of $2''$ for the present F-P. This is less than the $1''$ sensitivity achieved with the V-grooves but this is not important because the far-infrared instrument is working at wavelengths which are 10 times longer. The same argument holds for the loss of sensitivity in the coarse adjustment (from 6BA to 2BA

Figure 6.2

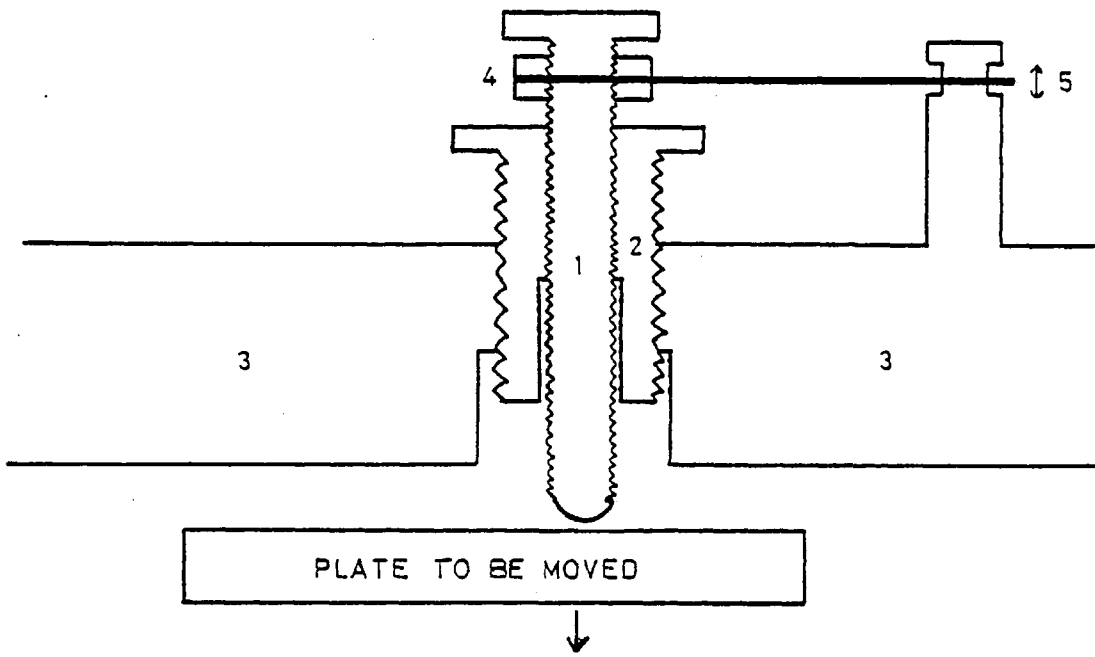

Differential Screw Mechanism.

screws). Two practical points must be made with regard to building differential screws. Firstly, all threads must be cut to high precision so that there is a minimum of play in the system. Unfortunately, over distances greater than $\sim \frac{3}{4}$", pitch errors build up and the screws are liable to seize. To avoid this, the female parts were only threaded along part of their length; the rest being a tight clearance for the screw (see figure 6.2). Secondly, when using the system in fine mode, the coarse screw must be able to move up and down with respect to the support. To allow this to happen, some vertical play, 5, must be left in the locking device.

6.1.1.d The Complete Instrument

Figure 6.1 also shows the complete instrument inside the dewar. The lower mirror, 7, is rigidly attached to the base, 8, which, to increase the thermal sinking of the F-P, is also the top cap of the liquid-nitrogen-cooled radiation shield, 9. Space, 10, is provided in the base for ancillary optics at 77K (cf. section 6.1.2.b). Three differential screws, 11 (only one shown), are spaced 120° apart in the F-P carriage, 12. They bear upon a dural plate holding the upper mirror, 13. The coarse adjustment screws protrude to within $\frac{1}{2}$" of the liquid-helium surface. A photograph of the F-P is shown in figure 6.3.

Since the F-P was a new instrument, it was decided not to devote an entire balloon flight to it but, rather, to fly it as part of a two-experiment payload. Thus, dewars for both the F-P and a two-colour photometer (Joseph et al., 1977) have to be accommodated on the L-shaped equipment flange, 1, behind the primary mirror (figure 6.4). The side-entry photometry dewar, 2, is on the optical axis, while the bottom-entry F-P dewar, 3, is supported above the beam-line by a 'cake-stand', 4. A moveable mirror, 5, inside the cake stand, switches the telescope beam from one cryostat to the other. Both dewars are mounted on silicone rubber mats, 6, for electrical and vibrational insulation from the telescope structure. Figure 6.5 shows the two dewars and the IC telescope on the Appleton Laboratory Stabilised Balloon Platform in Texas in autumn 1979.

6.1.2 Optical Design

6.1.2.a The Etalon

Renk and Genzel (1962) first demonstrated that two-dimensional metal

Figure 6.3

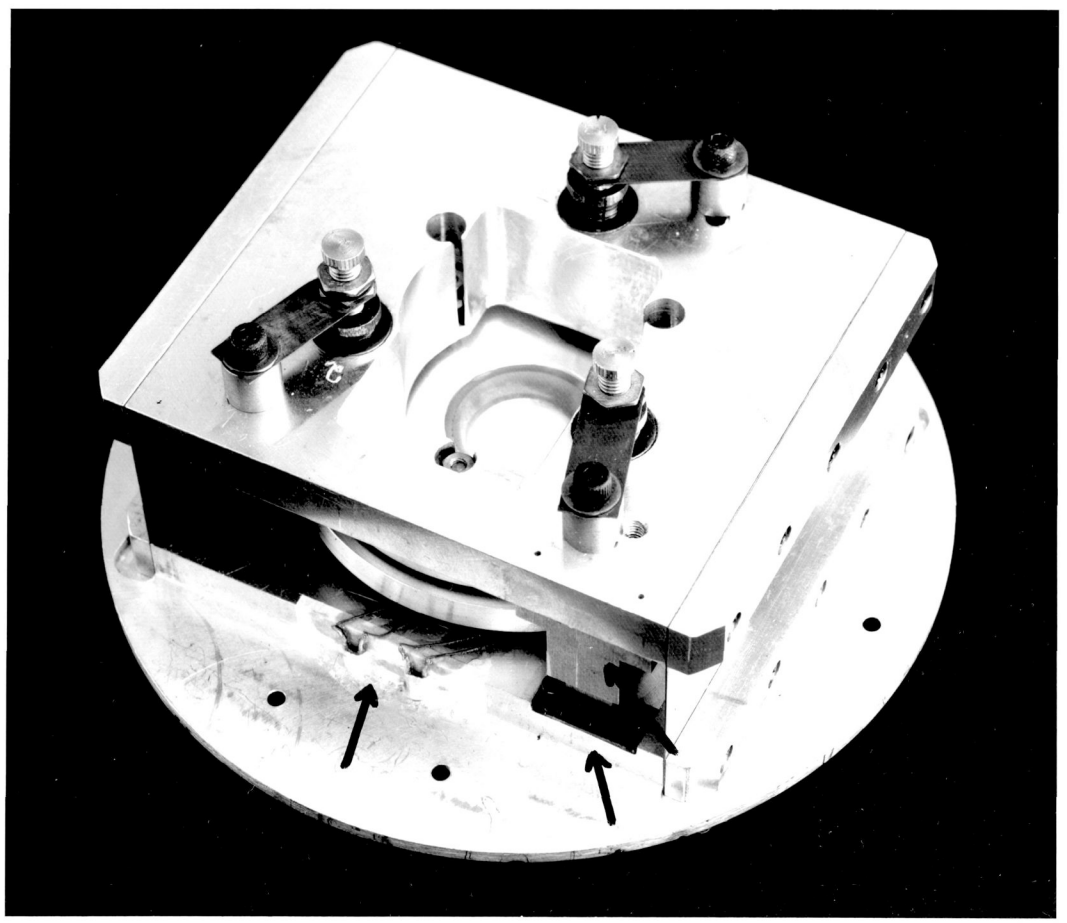

The Far-Infrared Fabry-Perot Interferometer.

Figure 6.4

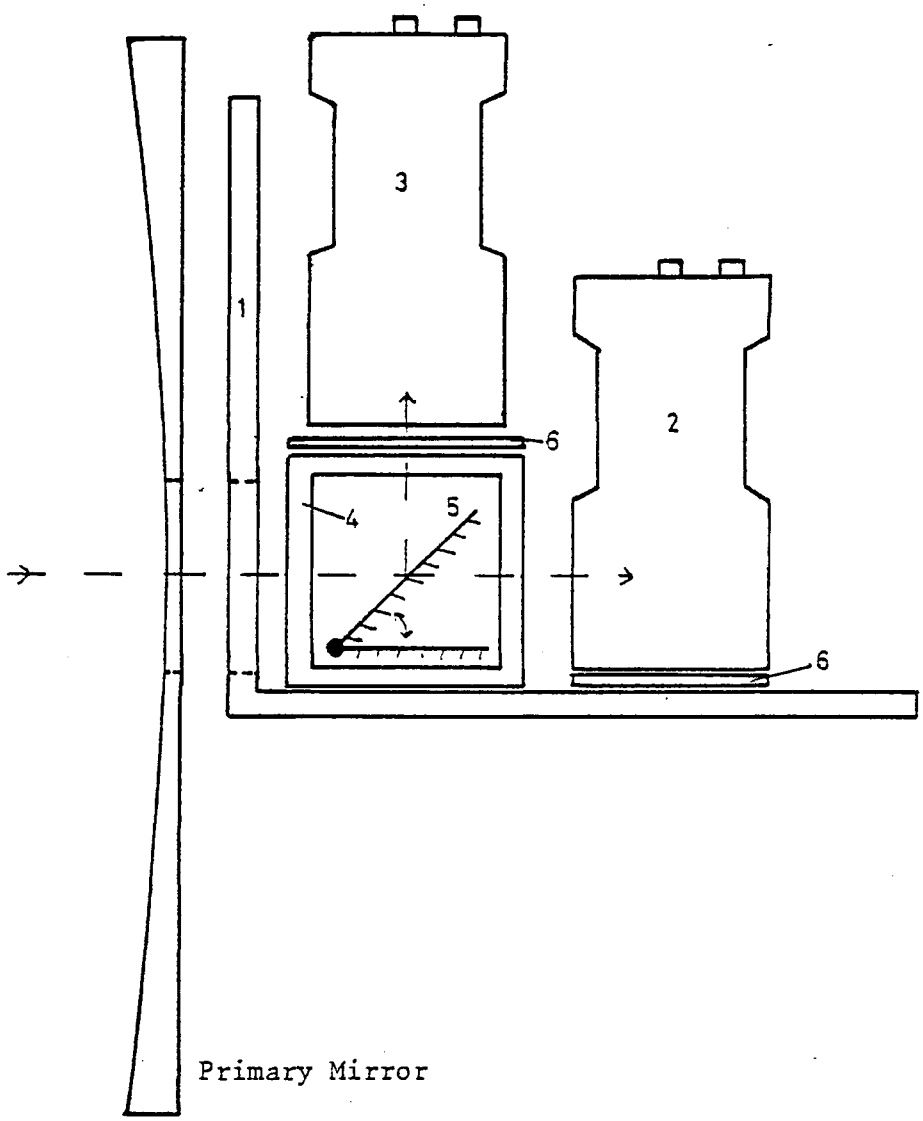

Two Dewar Configuration for IC Telescope.

Figure 6.5

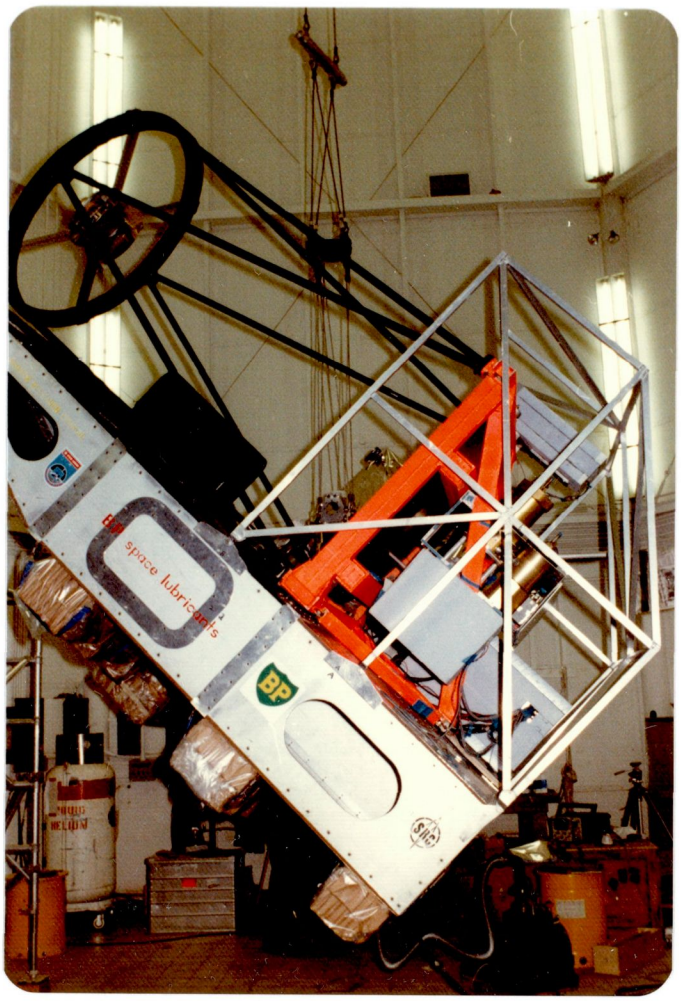

Two Dewars and Telescope in Position on
the Stabilised Balloon Platform.

mesh (figure 6.6(a)) could be used for far-infrared F-P mirrors. For this application, the important characteristic of these meshes or grids is that, when the wavelength, λ, of the illuminating radiation is such that,

$$\lambda/g \gtrsim 4 \quad , \qquad 6.1$$

where g is the grid periodicity, their reflectivity, R, is very high and only varies slowly with λ. These are almost the ideal properties for F-P mirrors.

The variation of the reflectivity and transmittance, T, with λ/g has been investigated by many authors. Vogel and Genzel (1964) find that, for normal incidence, R and T are independent of the polarisation of the incident radiation. Some of their results are shown in figure 6.6(b); note that the grids are only useable for F-P work well beyond the resonance at $\lambda/g \sim 1.1$. Lecullier and Chanin (1976) investigated the variation of R with larger values of λ/g for meshes with different periodicities. Their results, reproduced in figure 6.6(c), confirm the usefulness of these grids for far-infrared F-P's.

Free-standing electroformed metal mesh is commercially available from various companies, e.g. EMI Electron Tube Division, Hayes, Middlesex, and Buckbee-Mears Company, Saint Paul, Minnesota, USA. Due to the ready availability of this so-called 'inductive' mesh, it is used for the F-P. Once the desired reflectivity and the wavelength of operation have been specified, it is only a question of examining the R v. λ/g curves to determine the correct grid for a given F-P application. Measurements on various meshes are presented in section 6.2.2.c. The choice of grid for the IC-F-P was based upon these data.

The importance of keeping the absorption, A, in an F-P mirror to a minimum was stressed in section 4.3.2. For metal meshes, the absorption depends on a/g but is expected to be about 1% (Renk and Genzel, 1962). However, this variation is of academic interest only, since, for a given g, commercial meshes are, at present, only available at one value of a/g.

6.1.2.b Auxiliary Filtering

The second stage in the optical design was the choice of auxiliary

Figure 6.6

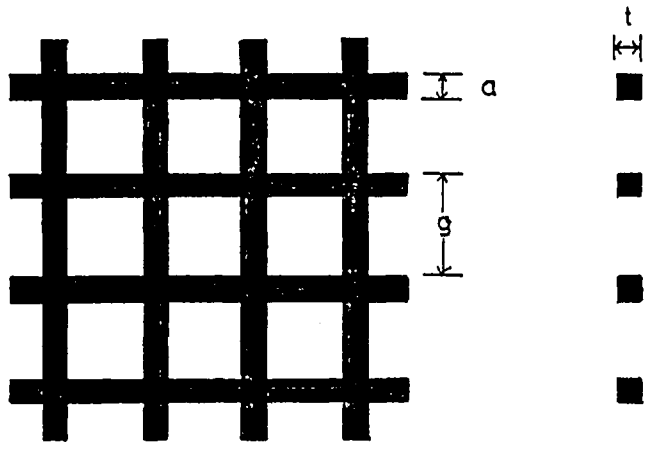

(a). Description.

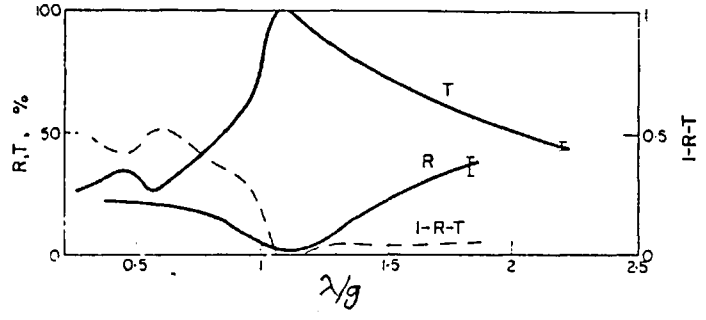

(b). Reflection and Transmission at Normal Incidence.
(From Vogel and Genzel, 1964).

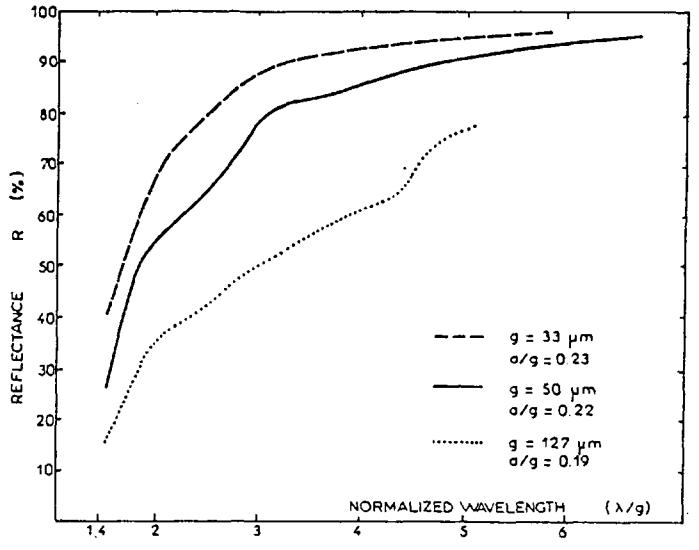

(c). Variation of Reflectivity with λ/g.
(From Lecullier and Chanin, 1976).

Properties of Metal Mesh.

filtering. The bandwidth of the order-sorting filters must be less than the free spectral range, $\Delta\lambda$, of the F-P in order to avoid spectral ambiguity. To specify $\Delta\lambda$, it is necessary to know the order of interference, n, in which the F-P is operating (equation 4.9). This, in turn, is governed by the desired resolution and the expected overall instrumental finesse (equation 4.12). There is insufficient room inside the dewar for collimating optics, as well as the F-P and photometer, and so, once again, the resolution of the instrument is limited by being used in a converging beam. The IC telescope has a focal ratio of f/7. Thus by equations 4.12 and 4.15, the maximum resolution attainable is around 400. This is adequate to detect the 88μm [OIII] line for it was found by Ward et al. (1975) with a resolution of 70. By knowing the desired resolution and estimating the defect and reflective finesses, n was calculated using an iterative process. (Iteration is necessary since n couples into equation 4.12 both directly and also through the aperture finesse.) It was decided to operate in approximately 15th order; this, with an expected finesse of $\sim$ 20, gives a resolving power of 300. Under these conditions, the bandwidth of the instrument is 0.3μm, the plate separation is $\sim$ 0.7mm and the free spectral range is 6μm. Thus, the auxiliary filtering must isolate a spectral bandpass of less than 6μm centred on 88.4μm or, to put it another way, the resolving power of the order-sorter must be 15.

It is difficult to construct a fully blocked single filter with a resolution of 15 in the far-infrared region and so a two-part system was adopted. There is insufficient space within the dewar for a prism or grating post-disperser. Thus a low-resolution fixed-gap F-P is used to isolate a passband of 6μm. The order-sorting for the second F-P is achieved with restrahlung reflections. Using data from Strong et al. (1938) and from Harshaw Optical Crystals (from Rofin Ltd, Egham, Surrey) various combinations of transmissions through and reflections off restrahlung crystals were examined before it was decided to follow Wijnbergen et al. (1972) and use reflections off potassium iodide. Hadni et al. (1968) measured the reflectivity of this crystal at 4.2K and from their data, it was calculated that two reflections would isolate a wavelength range from 70μm - 95μm with a small long wavelength leak (see figure 6.7).

The design of the order-sorting F-P bears closer examination. To achieve low resolution it is possible to use either low order or low finesse. However, if the finesse is low, there is inter-order leakage

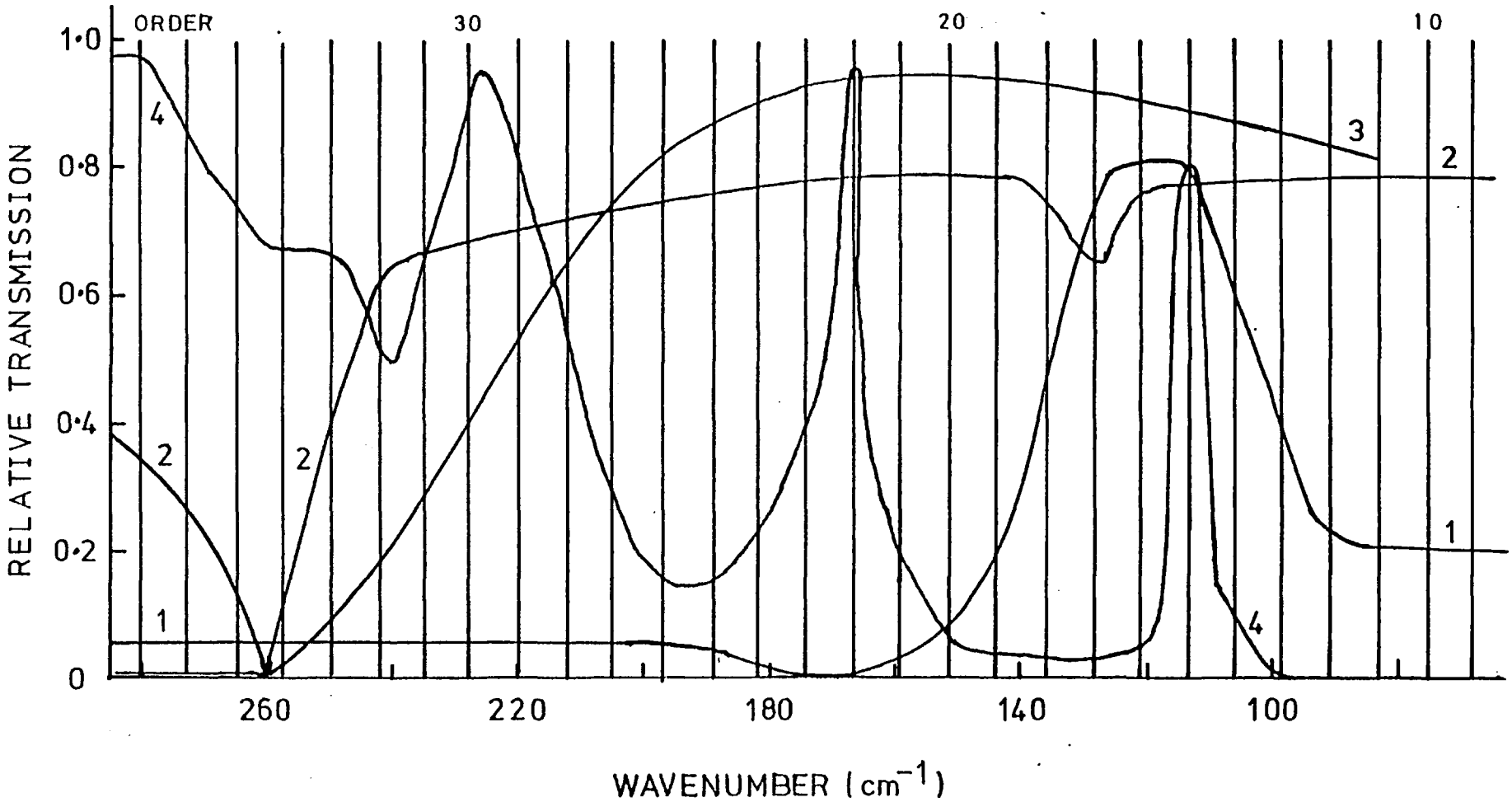

Figure 6.7

1. Potassium Iodide. 2. Crystal Quartz Lens. 3. Diamond-Dusted Calcium Fluoride. 4. Order-Sorting F-P.

(cf. figure 4.2(b)). Thus the F-P must be operated in low (i.e. first or second) order. A fixed-gap F-P may be made either by holding two metal meshes apart with a spacer (air-gap F-P) or by depositing meshes on both sides of a thin wafer of e.g. quartz (solid F-P). The former technique is used because it is much easier to alter the thickness of a spacer rather than that of a solid F-P in order to move the transmission band to the desired wavelength, λ_{max}. This ease is important because calculations using equation 4.8 and phase changes from Lecullier and Chanin (1976) had shown that to achieve transmission at the desired wavelength, the gap had to be set to within 1/20 thou. The phase changes are somewhat uncertain and, thus, the best way of measuring the gap is optically. It was envisaged that tuning the F-P to λ_{max} would be a repetitive process and, hence, the interest in easy alteration of the gap. The spacer is a piece of copper shim stock, etched to the desired thickness. It is clamped in place between the polished flats of the metal-mesh support rings (cf. section 6.2.2.a). Once again, considerations of available space dictated the choice of a clamped spacer rather than the free-floating ones used by Lecullier and Chanin (1976).

As mentioned in section 4.1, it is vital to have adequate short-wavelength rejection. A 1mm-thick piece of calcium fluoride, covered with diamond dust, is used to scatter wavelengths shorter than 40μm out of the beam. This filter is antireflection-coated for 88μm and since it is located in the base of the F-P (cf. section 6.1.1.c), it is cooled to 77K. Further short-wavelength blocking is provided by black polyethylene and to some degree by the crystal quartz Fabry lens. The relative transmissions of all these filters are shown in figure 6.7. Note that the transmission of the main F-P is shown schematically as a set of delta functions whereas, that for the order-sorting F-P was calculated in detail from the Airy function using wavelength-dependent reflectivities and phase shifts from Lecullier and Chanin (1976). Use of the order-sorting F-P in 1st order obviates the problem of the long wavelength leak discussed earlier.

A useful consequence of using restrahlung reflections is that it is very straightforward to incorporate a second or "guiding" detector into the system. This is done because experience with the near-infrared F-P in Tenerife has shown that it is very difficult to find objects due to the narrowness of the instrument's bandpass (cf. section 5.3.2). Calculations for the far-infrared show that an object even as bright as M17 is only

just detectable immediately through an F-P and so, some finding system is obviously needed. Potassium iodide has a strong reflection band at 70μm - 95μm, but outside this range it transmits (Daneu et al., 1978). Thus, a detector, placed behind the first potassium iodide crystal, receives radiation in the 40μm - 70μm band. The two detectors are arranged so that both view the same astronomical object and thus finding and guiding is accomplished using the second detector.

6.1.2.c The Two-Channel Photometer

The last stage in the optical design of the far-infrared F-P was the photometer. The design of this is subject to the constraints that it must both contain two detectors and the auxiliary filtering and also be compact enough to leave sufficient space in the dewar for the F-P. Other design philosophies were firstly, to minimise the number of interfaces between components in order to improve thermal sinking of the photometer, and secondly, to minimise the number of components that have to be aligned with respect to the optical axis. Originally, it was hoped that the order-sorting F-P could be placed only in front of the main or F-P detector. However, this proved to be impossible and so it had to be positioned in front of both bolometers. The effect of this upon the signal reaching the guide detector is discussed in a later paragraph.

The complete photometer is shown diagrammatically in figure 6.8. The main body, 1, of the photometer is circular and hollow and is attached to the liquid-helium-cooled cold surface. The two potassium iodide mirrors, 2 and 3, rest against two lapped faces of an accurately machined "extension", 4, to the main photometer body. This extension ensures that the mirrors are parallel to each other and at 45° to the optical axis. Good thermal contact between the potassium iodide crystals and the photometer is achieved by using spring washers inside the two lids, 5 and 6, which hold the mirrors in position. The order-sorting F-P, consisting of two stretched metal meshes, 7 and 8, and a copper spacer, 9, is contained inside the forward stop, 10. This assembly is also attached to the photometer extension 4. This size of the forward stop is discussed in a later paragraph. By machining the photometer and its extension out of the same piece of metal, the number of interfaces between the cold surface and the order-sorting F-P was reduced to only three, thereby improving the thermal contact between the two items. Figure 6.9 is a photograph of the photometer with the forward stop and the two lids removed. The three slots

Figure 6.8

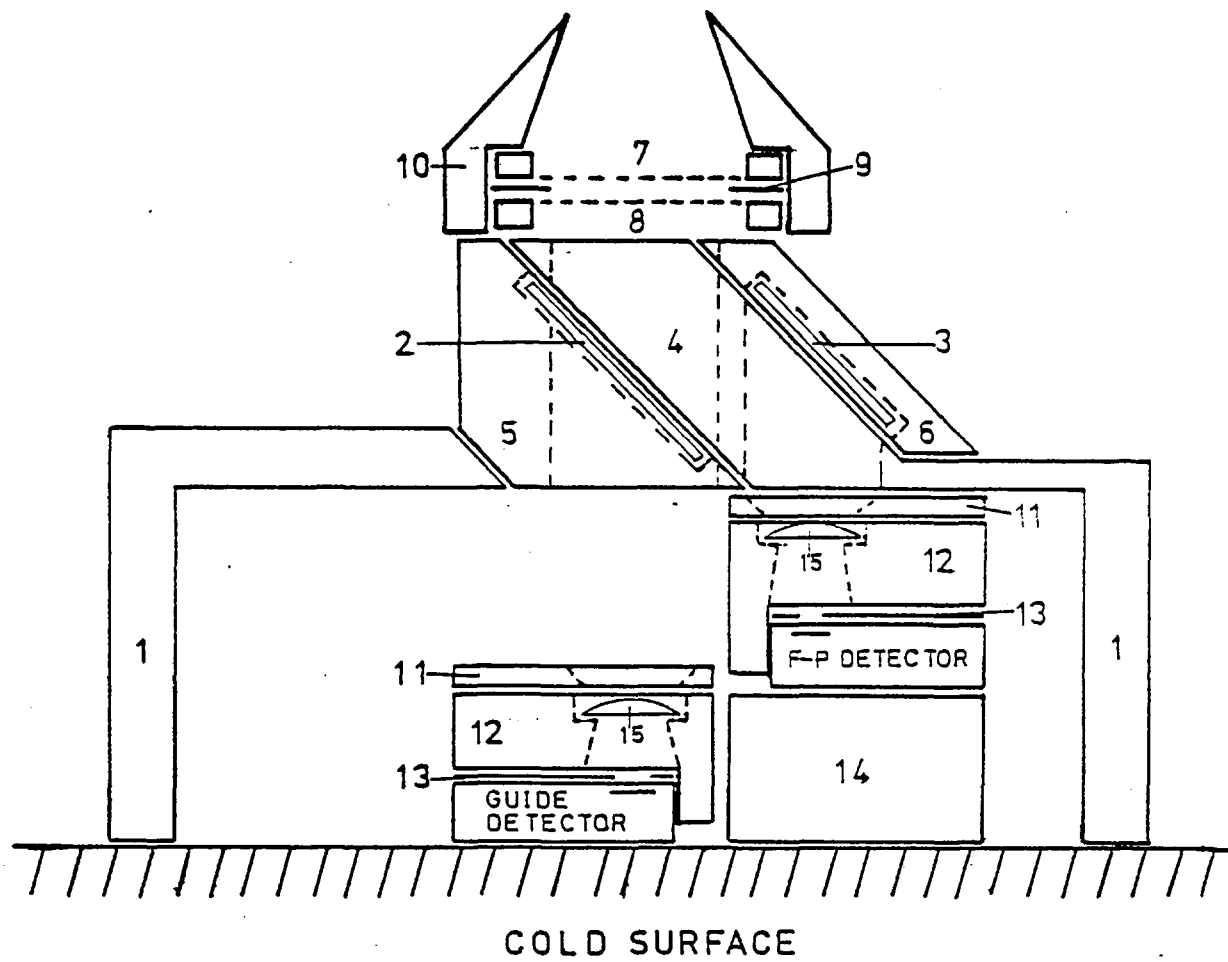

The Two-Channel Photometer.

Figure 6.9

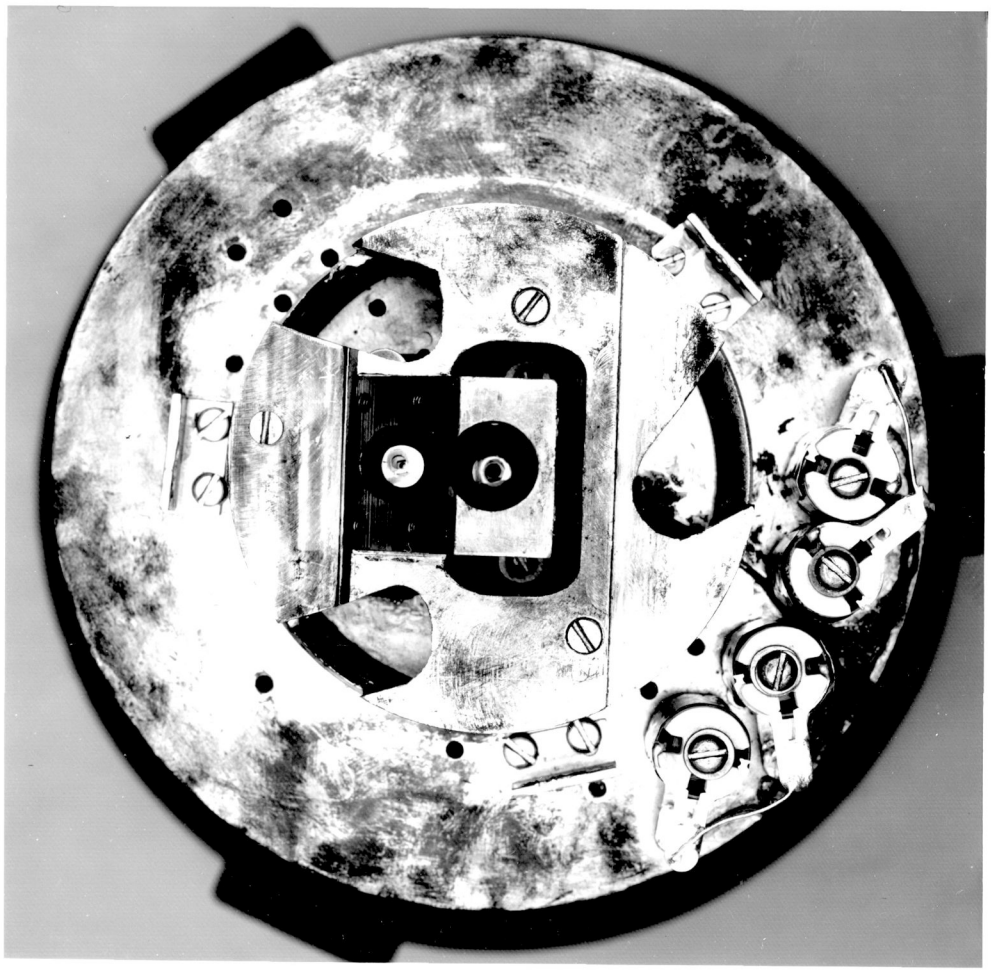

The Photometer in Position on the Cold Surface.

seen in the picture are needed to accommodate the differential screws of the F-P. All components of the photometer described so far are aligned to within workshop tolerances and thus no further adjustments are needed.

The two detector assemblies (F-P and guide) are contained inside the hollow body of the photometer. Each assembly consists of a field stop, 11, a Fabry lens holder, 12, a detector stop, 13, and a gallium-doped germanium Low bolometer. These four components are held together by four bolts running from the field stop into tapped holes in the detector mount, and are thus located with respect to each other to within machine shop errors. The field stops define a $\sim 3'$ field of view on the sky and must be at the telescope focus. Because of the extra path length between the potassium iodide mirrors, the F-P detector assembly has to be raised above the cold surface by a metal block, 14, in order that its field stop may be at the focus of the telescope. Good thermal contact between the crystal quartz Fabry lenses, 15, and their holders is maintained with spring washers (not shown in figure 6.8). The detector stop is a three thou-thick piece of copper shim stick. The size of the aperture in the detector stop and also the Fabry lens design are discussed later in this section. By keeping the detector assemblies separate from the photometer one interface has been eliminated at the cost of having to align the three units. To facilitate alignment, each detector assembly has some freedom of movement upon the cold surface. The final alignment is checked using a travelling microscope. Throughout the photometer, all bores are tapered, where possible, in order to minimise the amount of scattered light reaching the detectors. Figure 6.10 shows the two detector assemblies in position on the helium surface. Also visible are the four wirewound 3.8MΩ load resistors, two for each bolometer.

All metal parts of the photometer are made of oxygen-free high-conductivity copper because of its high thermal conductivity. Every surface which 'sees' objects whose temperature is above that of liquid helium is polished and gold-plated to reduce its emissivity. Surfaces inside the photometer were sandblasted and painted with 'Nextel' - an infrared black - to reduce scattered light.

Many aspects of the optical design were dictated by the space available. The severity of the problem is highlighted by the size of the clearances in the final design. For example, the tip of the forward stop is within 3mm of the upper metal mesh, and the clearance between the facing surfaces of the liquid-nitrogen-cooled F-P and the liquid-helium-cooled

Figure 6.10

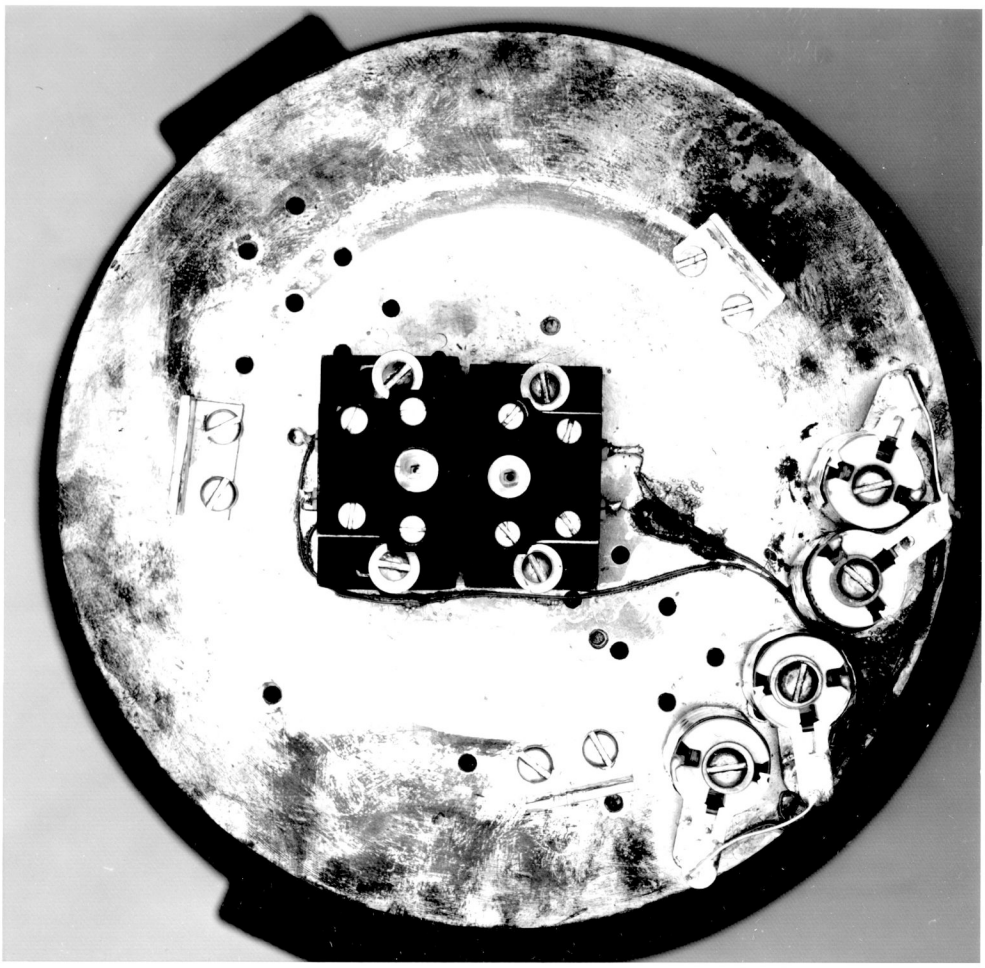

The Detector Assemblies in Position on the Cold Surface.

photometer is merely 1½mm. As the F-P is scanned, the carriage moves sideways and thus there is a danger of the forward stop touching the support ring for the metal mesh, thereby "shorting" helium temperatures to nitrogen. To alleviate this problem, the inner edge of the support ring is bevelled (cf. figure 6.3). In short, all necessary components are contained in the HD-3 dewar, but it is a very tight squeeze.

The purpose of a Fabry lens is to eliminate the effect of the variation of detector sensitivity with position upon the detector. (Its effect upon the photometer beam is discussed later.) The Fabry lens achieves its aim by re-imaging the telescope primary mirror onto the detector. To put this more physically, it ensures that every point in the field of view of the telescope illuminates all of the detector. The design of the Fabry lenses for this photometer is now elaborated upon. Consider a plaino-convex lens of radius of curvature, r, thickness, t, and made of material of refractive index, μ. A ray incident upon it at a height y above and at an angle α to the optical axis, will cross the axis a distance d behind the lens (figure 6.11(a)). Simple trigonometry and Snell's law permit d to be expressed as a function of these five variables,

$$d = \frac{\left[y-(t-r+\sqrt{r^2-y^2})\tan\{\sin^{-1}(y/r)-\sin^{-1}[1/n(\sin^{-1}(y/r)-\alpha)]\}\right]}{\left[\tan(\sin^{-1}(n\sin\{\sin^{-1}(y/r)-\sin^{-1}[1/n\sin(\sin^{-1}(y/r)-\alpha)]\}))\right]} . \quad 6.2$$

Equation 6.2 was evaluated for a crystal quartz lens for a range of values of y and α consistent with a $3'$ field of view and an f/7 telescope. Numerical values for r and t were chosen on the basis of available lens grinding tools. The refractive index of quartz at 1.6K as a function of wavelength is given by Alvarez, Jennings and Moorwood (1975). The results were plotted out and at 88μm, the circle of least confusion was found to be 1.1mm in diameter and to be 5.45mm behind the lens. Thus the aperture in the F-P detector stop (cf. figure 6.8) is 1.3mm in diameter to allow for a slight misalignment and the length of the Fabry lens holder is 5.45mm. For the guide detector, equation 6.2 was evaluated for wavelengths between 40μm and 70μm and the corresponding numbers were 1.7mm and 4.6mm. The large diameter of the spot is embarrassing because the only detector available for the guide detector is an old one, with a sensitive area only 1mm x 1mm. The guide detector stop has an aperture of 1.7mm, i.e. larger than the detector, and it is hoped that the integrating cavity behind the bolometer will trap some of the radiation that misses the detector.

Figure 6.11

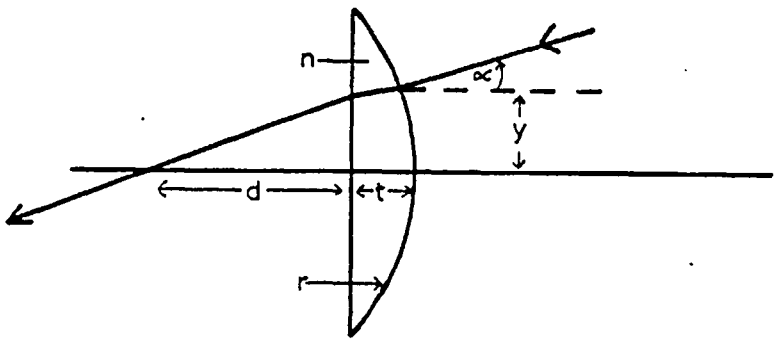

(a). Fabry Lens Design.

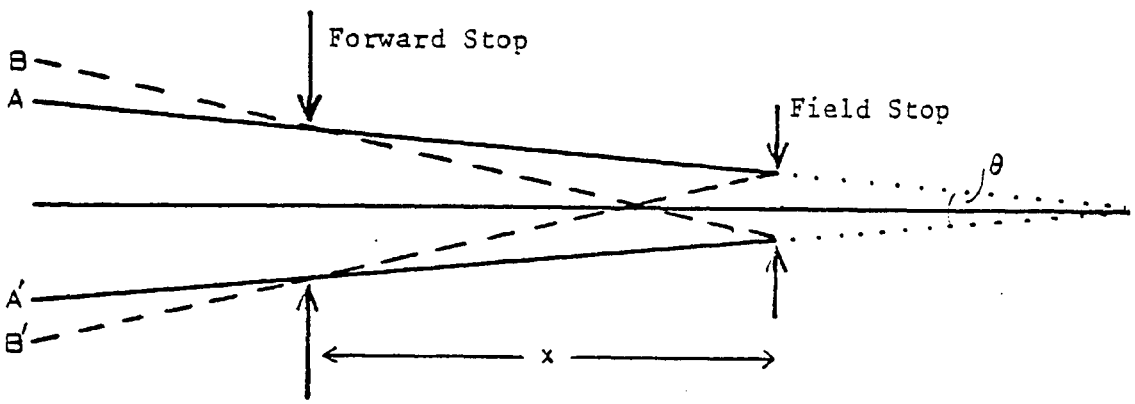

(b). Penumbra.

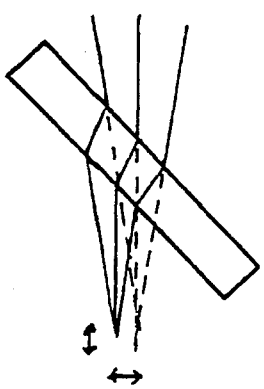

(c). Defocussing and Displacement by Potassium Iodide.

Optical Design Considerations.

One of the most important facets of infrared telescope and instrument design is to keep warm objects out of the detector's field of view. The diameter of the forward stop (cf. figure 6.8) is calculated so that it, in conjunction with the field stop, defines a cone of light (AA' in figure 6.11(b)), whose angle θ is matched to the convergence angle of the telescope beam. However, as shown by rays B and B', objects outside this cone can still illuminate part of the field stop. The region between the rays A and B is referred to as the penumbral region. In theory, there is no problem here because a perfect Fabry lens images the penumbra into an annulus around the detector stop aperture and no penumbral energy reaches the bolometer. In the real world, misalignments, aberrations in the lens, diffraction and scattering ensure that the detector does see objects outside its main beam. The size of the penumbra is reduced as the distance, x, between the forward and field stops is increased. The presence of the F-P and the size of the dewar limit the maximum value of x; with the current optical arrangement, it is not possible to get all the penumbra through the Cassegrain hole in the primary mirror to view cold, low-emissivity sky. An annulus, approximately $\frac{1}{4}$" in width, of the back of the primary mirror is seen by the detector. This problem is not at all serious for this application because of the liquid-helium-cooled narrow-band optics but may cause difficulties if wider-bandwidth work is undertaken.

Another optical worry is the exact position of the guide detector with respect to that of the F-P. As shown in figure 6.11(c), transmission through the potassium iodide crystal causes a displacement and a defocussing of the beam. The sizes of these effects were calculated to be $\sim \frac{1}{2}$mm each and due allowance was made, when the photometer was constructed.

The efficiency of the filtering system was estimated using realistic numbers. It is expected that the overall transmission of the optics to the F-P detector will be $\sim$ 25%. In its stop bands, only one part in 10^6 of the 10μm - 40μm radiation will get through and only 1 in 10^4 for 40 - 50μm. An unfortunate consequence of having to put the guide detector behind both the main and order-sorting F-P's is that it is only expected to receive about 4% of the total radiation in the 40μm - 70μm band. In view of the available time and space, it was decided to accept this state of affairs for the guide detector and to see if it were useable.

6.1.3 Electrical Design

The electronics for the far-infrared F-P was designed and built by Mr J. Allen, as part of his overall responsibility for the electronics of the IC balloon payload, It is briefly described here for completeness. The main contribution of the author to this work was to suggest the use of the metal mesh etalon, itself, as the gap-sensing capacitor.

6.1.3.a Telecommand and Telemetry System

The National Scientific Balloon Facility in Palestine, Texas provides a communications system between the base and the balloon as part of their service to experimenters. There are two ways of sending a command to the payload, either by a DATAWORD or by a DISCRETE command. The IC payload uses 8 bits of the 16 bit dataword and decodes these into a 4 bit address and 4 data bits. These uniquely identify a particular action. There are about 48 discrete commands available. Each of these actuates a momentary switch closure on board. The F-P electronics are housed in a separate box to the main electronics and thus, to avoid having to build another decoding system, it was decided to use discrete commands to control the interferometer. Data may be transferred from the balloon payload to the ground station in either analogue or digital form. There are about 15 frequency-modulated (FM) channels, with bandwidths ranging from 5 Hz to 50 kHz, for transmitting analogue information to the ground. However, not all of these are available to the experimenter. The highest bandwidth channel is used to carry digital data in 'pulse code modulated' (PCM) form. Signals presented to either an FM/FM channel or to the PCM must be in the range 0-5V. Thus if a signal is likely to go both positive and negative, it must be biassed and scaled so that its range is $\pm 2\frac{1}{2}$V.

6.1.3.b Signal Processing

The on-board detector signal processing is very simple. The preamplifiers (cf. section 5.1.4) for the two detectors are mounted directly on the side of the dewar and are allowed to cool to ambient temperature. However, the bias and power batteries for the preamplifiers are thermally insulated and provided with a passive source of heat (cf. section 6.3.4). The output from each of the preamplifiers passes through a switchable gain amplifier before being transmitted to the ground via one of the FM/FM channels. The gain of the amplifier can be switched from x1 to x10 and

back by toggling a discrete command, which opens and closes TTL switches on board through a J-K flip-flop. The last stage of the amplifier adds in an offset of 2½V so that zero output from the detector is mid-range for the telemetry. On the ground, the signal is both tape-recorded and fed into an Ithaco lock-in amplifier. The output from this is displayed on a strip chart.

6.1.3.c Controlling the F-P

Four discrete commands, START, STOP, FORWARD, REVERSE, are used to control the electric motor, which scans the F-P. A series of latching relays is used to 'remember' the command after the momentary switch closure. Experience with the near-infrared F-P (cf. section 5.3.4) had shown that it was wise to monitor the lateral motion of the F-P carriage. Thus, a magnet was firmly attached to the carriage and a 'Magneto-Resistive Differential Sensor' (MRD) to the base. These are marked in figure 6.3. The output from the MRD is proportional to the movement of the carriage. The MRD signal, after suitable scaling, is transmitted down both an analogue channel and also the PCM. It is displayed alongside the two detector signals on the ground on a multi-channel strip chart.

Two discrete commands are used to control the motor for moving the beam switching mirror (cf. section 6.1.1.d). Microswitches, located at the mirror end stops, automatically stop the motor when the mirror is in position. The status of all switchable functions is continually monitored. By examination of which bits are set in one PCM word, it is possible to see if, e.g., the beam-switching mirror is up or down, or whether the switchable gain is set to x1 or x10.

6.1.3.d Gap Sensing

Capacitance micrometry (cf. section 5.1.4) is once again used to measure the changes in etalon gap. The metal meshes which form the etalon are mounted upon non-conducting support rings to permit them to be used as the capacitor for the gap-sensing electronics. The upper mesh (cf. figure 6.1) is smaller than the lower to minimise edge effects as the F-P is scanned. Electrical connection to the grids is made via constantan wire affixed with conducting epoxy. To avoid thermal drift, the reference and balance capacitors are attached to the interferometer (cf. figure 6.3) and are thus kept at a constant temperature. The transformer used for the capacitance micrometer for the 10μm F-P consumes too much power to be used

in a balloon flight and so a completely solid state system was developed. A 16 kHz fairly pure sine wave is obtained by dividing down and integrating the output from a 4 MHz crystal oscillator. This sine wave is used as one of the bridge drives. The other is obtained by inverting part of the former. The two drives are servo-stabilised in both amplitude and phase. Balance control is achieved by feeding a 'false' error signal into the servo loop. To minimise sensitivity to pick-up and microphonics, the output stages of the bridge drives use operational amplifiers with very low output impedances. Despite this, it is still necessary to secure the bridge drive and return cables very firmly and also to encapsulate the connectors in araldite to avoid microphony. The signal from the F-P capacitor is amplified and then the capacitative, C, and resistive, R, components are extracted by on-board phase-sensitive detectors, using phase-shifted reference signals derived from the bridge drive. Another phase-sensitive detector monitors the amplitude, A, of the bridge drive. After suitable scaling, the C output is transmitted down an FM/FM channel, while the A and R outputs come down the PCM. On the ground, A and R pass through digital-to-analogue converters and are then, with C, displayed on the same strip chart as the MRD and detector outputs.

6.2 Sub-System Tests

Most of the components of the far-infrared F-P/two channel photometer system were tested independently of the complete instrument. These trials are discussed in the next three sections, under the general headings of mechanical, optical and electrical. Included in the optical section is a description of the technique used to stretch the electroformed metal mesh over support rings.

6.2.1 Mechanical Trials

6.2.1.a Differential Screw Adjustment Mechanism

The differential screw adjustment mechanism was tested optically to determine its sensitivity and stability. The metal mesh etalon was removed and a mirror was placed in the position of the upper mesh. A He-Ne laser beam was reflected off this mirror and the deflection of the laser spot observed as the differential screw was used. Due to the close mechanical tolerances on the threads, the fine adjusting screws are very stiff. Although it is possible to turn them by hand, use of a small spanner is

preferable. A change in the angle of the mirror of $\sim 6''$ (equivalent to a parallelism finesse of 65 at 100μm wavelength for this F-P) is easily attainable; finer adjustments are possible with smaller rotations of the screw. The adjustment is slightly non-linear, e.g. 60% of the motion occurs during the first half-revolution of the screw and the remaining 40% during the second. This is probably due to thread errors in the screws. In order to check the stability of this mechanism, a pair of semi-reflecting optical flats was used in place of the metal mesh etalon. These were aligned parallel using the differential screws and viewing visible light fringes (cf. section 5.2.1). The alignment is not disturbed when the instrument is moved, picked up or tilted. Vigorous shaking shifts the fringe pattern by about one quarter of a visible fringe, an amount which is negligible at 100μm. Sharp taps to the carriage and base have no effect but knocking the adjusting screws themselves causes mis-alignments of up to 3 fringes ($\equiv \mathcal{F}_d \sim 70$ at 100μm). Thus the sensitivity and stability of the differential screw adjustment mechanism are easily adequate.

6.2.1.b Drive Assembly

The operation of the drive assembly (cf. section 6.1.1) was checked at low temperatures and pressures. To avoid the possibility of freezing, the micrometer, motor and gearbox are all run without lubricants, i.e. dry. The micrometer is degreased by washing it in trichloroethylene, while the motor and gearbox are supplied dry by the manufacturers (Portescap(UK) Ltd.). Low temperature lubricants are not used because of fears that they might poison the dewar vacuum. When degreased, the micrometer is prone to rust and is, therefore, always kept in a vacuum or a dry atmosphere. The entire drive assembly was left in a small environmental chamber at a temperature of $-50^{\circ}C$ for several hours. No damage was sustained and the system still operated. The same results were obtained when the drive mechanism was run at a pressure of ~ 1 torr.

6.2.1.c Mechanical Resonances

On a balloon payload, it is necessary to keep a close watch on possible mechanical resonances. The F-P is a spring system (cf. the tertiary chopper of Appendix A) and thus has a natural frequency, f_o. This was evaluated by clamping the F-P to a solid surface, and then displacing and releasing the carriage so that it oscillated. These oscillations were monitored using a magnet and MRD. The resonant frequency is 35 Hz and the Q of the F-P is around 35. Resonant systems tend to deflect under

their own weight. A rule of thumb is that this deflection, at maximum, in inches is given by $10/f_o^2$. For the F-P, the deflection is 0.2mm and thus the top carriage must always be deflected (or pre-tensioned) by at least this amount to avoid effects due to changing orientation.

6.2.1.d Parallelism of the Photometer

It is important that both the F-P and guide detectors (cf. figure 6.8) look at the same piece of sky. This depends both on the positions of the detectors and also on the parallelism of the two potassium iodide mirrors. The former is adjustable; the latter was checked by directing a He-Ne laser beam into the top of the photometer and measuring the angular separation of the two emergent beams. For this test, the crystal mirrors were replaced by semi-silvered glass flats. After removing all the burrs on the photometer, lapping the faces of the photometer extensions and chamfering the edges of the mirrors, the angular deviation of the two beams was found to be less than $\sim 2'$. This figure remained unchanged as the photometer was subjected to mechanical shock. This leads to a miniscule shift in the field of view of the second detector and is therefore sufficient.

6.2.1.e Mechanical Modifications

During early tests of the F-P at liquid-nitrogen temperature, the nitrogen hold-time of the dewar was very poor, about 20 minutes. No vacuum leak could be found so it was assumed that the instrument was outgassing severely. This could be either due to material adsorbed onto the metal surfaces or to air, trapped somewhere inside the F-P, slowly leaking out. To solve the latter problem, the interferometer was examined in minute detail and every putative air pocket was provided with an escape hole, e.g. every screw going into a blind hole was hollowed out. These precautions reduced the problem but did not solve it. After the system had been under vacuum for some time, the outgassing decreased and the cryo-pumping action of the liquid helium improved the vacuum sufficiently to retain the cryogens.

The drive assembly showed two problems while undergoing tests. Firstly, there were 'glitches' in the scan motion, during which the scan rate slowed and the motor current soared. This difficulty was traced to non-concentricity in the extendable coupling and was solved by increasing the mechanical clearances therein. Secondly, the various

screws holding the component parts of the drive mechanism together showed a tendency to work loose. They are now held in position with 'Loctite 601'. This appears to have no detrimental effect on the vacuum in the cryostat.

6.2.2 Optical Trials

6.2.2.a Mesh Stretching Technique

The technique used to tightly stretch the metal mesh over the support rings is now described. The electroformed grids are packed flat by the manufacturers between two sheets of plastic. If these are removed, the mesh (especially if made by Buckbee-Mears) tends to curl up and stick together, and it is almost impossible to flatten it again. Thus, the grids must always be held down in some manner. In order to produce a mounted mesh with a clear aperture of 20mm, a piece 40mm x 40mm must be cut from the main sheet. Two squares of thin plastic (approx. 40mm square, with the corners snipped off) are very carefully inserted between the mesh and the large plastic sheets, see figure 6.12(a). The mesh contained between the two small pieces of plastic sheeting is then cut free, while care is taken not to allow the remaining mesh to curl up. The small piece of mesh is then positioned over a 30mm diameter aperture in the centre of a 5" square of $\frac{1}{8}$" dural plate. Two of the corners of the grid are superglued to the metal and then the lower plastic sheet is removed. The mesh is tensioned by pulling gently on the other two corners before they, too, are glued down. At this stage, no large wrinkes should be visible in the portion of the mesh over the central hole.

After removing the second sheet of plastic, the dural plate and mesh are placed under an infrared lamp, see figure 6.12(b), for about 10 - 15 minutes. A dilute solution of General Electric 7031 varnish in alcohol is used to further secure the mesh to the dural plate. It is applied on the slightly rounded end of a stick, e.g. a biro cap, with a stroking motion, directed radially outwards from the centre of the grid. Thus, each stroke tensions the mesh slightly more and, since the varnish dries on contact with the hot plate, the mesh is prevented from relaxing. This process is repeated until the entire grid, apart from that part over the hole, is covered in varnish. By this time, the mesh should be flat, although it does not matter if it is still slightly slack. The grid and plate are left under the lamp for another 10 or so minutes to

Figure 6.12

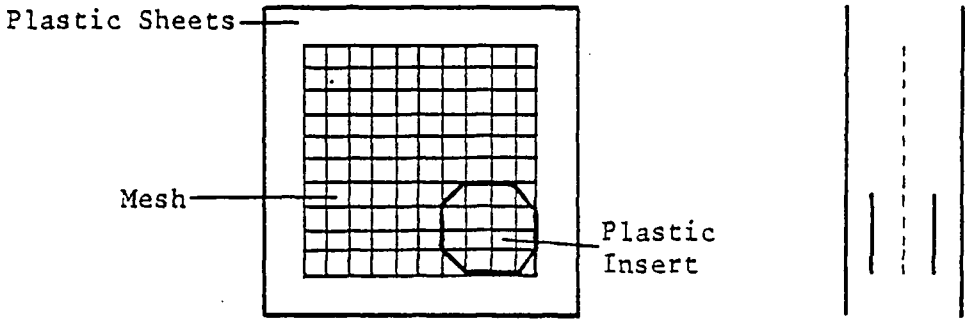

(a). Plastic Inserts.

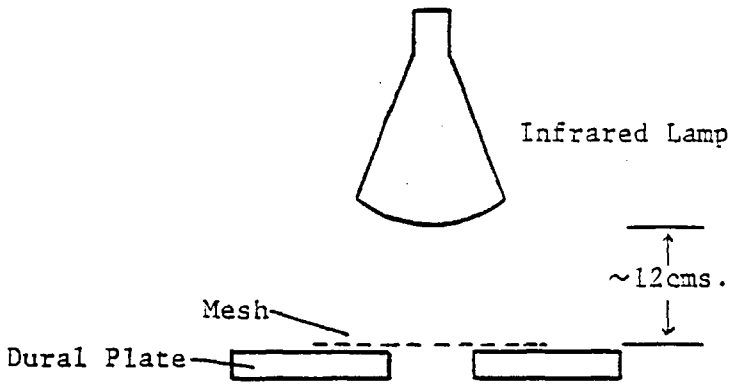

(b). Infrared Lamp.

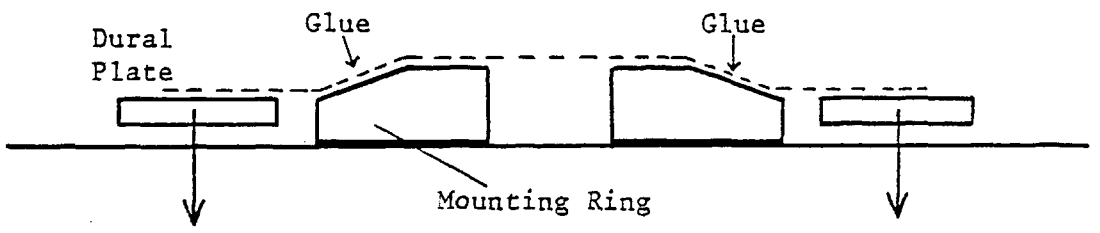

(c). Stretching over Mounting Ring.

Mesh Stretching Techniques.

allow the varnish to harden fully.

The mesh support ring is slightly thicker than the dural plate and its outer diameter is such that it passes freely through the aperture in the plate. The upper face of the ring is lapped and polished flat and its outer edge is bevelled. When the varnish is dry, the infrared lamp is turned off. The mesh cools more quickly than the plate and its contraction pulls it taut. The plate is then carefully lowered onto the mesh support ring so that the grid itself rests on the polished face of the ring. Due to the difference in thickness of the ring and plate, the weight of the dural plate is now tensioning the mesh over the ring (figure 6.12(c)). Dilute GE varnish is then dripped through the mesh onto the bevelled edge of the ring to glue the two together. When all the rim has been coated in varnish, the mesh is covered with an inverted petri dish to exclude dust. The varnish is allowed to dry overnight. The next day, the mounted mesh is cut free from the plate with a scalpel. Throughout the entire process, great care must be taken to keep all items used clean and free from dust. Using the above technique, both copper and nickel electroformed meshes, ranging from 500 lines per inch to 3000 ℓ.p.i., have been successfully mounted upon rings made of steel, brass, tufnol and glass.

6.2.2.b Flatness and Temperature Testing of Grids

The flatness of some of the mounted grids was measured using a Twyman-Green Interferometer. This was only possible for the fine grids (e.g. 3000 ℓ.p.i.) because the optical reflectivity of the coarser meshes (e.g. 500 ℓ.p.i.) is far too small to form fringes. Even the fringes formed by the 3000 ℓ.p.i. grid have such poor contrast that they are very difficult to see, let alone photograph. These fringes show that the central $^2/_3$" of the grid has a defect finesse in excess of 100 at 100μm.

The behaviour of the mounted meshes on cooling to 77K was investigated. If they are thermally shocked, the grids have a tendency to split. This problem is overcome if the meshes are slowly cooled to liquid-nitrogen temperatures over a period of a minute or so. The grids mounted on steel rings become slack when cooled. At first sight, this is a surprising result since the coefficient of linear expansion is smaller for steel than for nickel, the material of which the grids are made. The solution to this apparent riddle is that the nickel meshes

are electroformed; this process causes the grids to have different properties to those of the bulk metal (G. Chanin, private communication). Meshes mounted on pyrex glass rings remain taut at 77K. Thus, glass rings are used for the meshes of both the main and order-sorting F-P's. These rings also provide the necessary electrical insulation for the meshes of the main F-P (cf. section 6.1.3.d).

6.2.2.c Transmittance and Reflectance of Grids

The transmittance and reflectance of various mounted meshes was measured by Mr R. Chater of the Analytical Services Laboratory at IC using a Fourier Transform Spectrometer (FTS). First, a spectrum is taken with a sample in the beam and then, after the sample has been removed, a background spectrum is obtained. The ratio of the two gives the absolute transmittance or reflectance of the sample. The results obtained for the transmission through 500 ℓ.p.i., 750 ℓ.p.i. and 1000 ℓ.p.i. grids are given in figure 6.13 together with limited data for 1500 ℓp.i. and 3000 ℓ.p.i. grids. In each case, the maximum transmission occurs at $\lambda/g \sim 1.2$ as expected (cf. figure 6.6(b)).

Measurements of transmission are much easier to make with the FTS than those of reflection. Mr Chater made up a jig to allow measurement of the reflectance of samples at near normal incidence. However, this unit blocks a large part of the beam and thus only a small fraction of the incident radiation reaches the detector. This increases the noise in the reflection measurements and reduces their accuracy to ±5-10% compared with a few per cent for the transmission case. Some smoothed results are shown in figure 6.14. As expected, the reflectivity of the finer meshes 'flattens' out at shorter wavelengths than that for the coarser grids. The problem of the accuracy of the results is demonstrated by the 1000 ℓ.p.i. mesh appearing to have higher reflectivity than those with 1500 ℓp.i. or 3000 ℓ.p.i. A further problem is that because of the way electroformed metal mesh is made, it has both a dull and a shiny side. Whenever an attempt was made to measure the reflection from the shiny side, spurious reflectivities, consistently greater than unity, were obtained. It is possible that short-wave specular reflection and/or diffraction are causing this effect. The author started investigating this problem but was unable to finish due to lack of time.

On the basis of the transmission measurements, the 1000 ℓ.p.i. meshes were selected for the main F-P etalon. At 88μm, their trans-

Figure 6.13

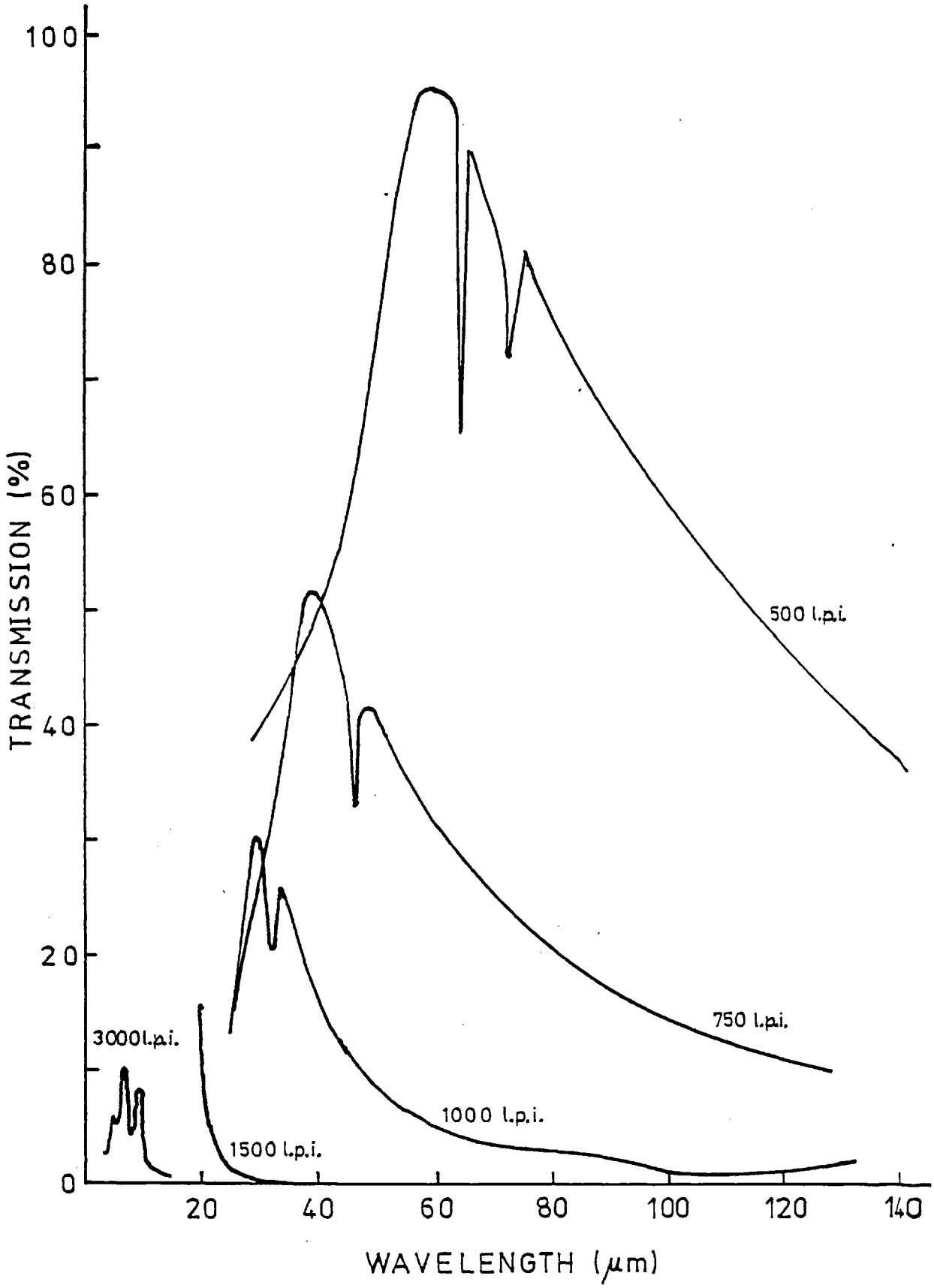

Transmittance of Various Meshes.

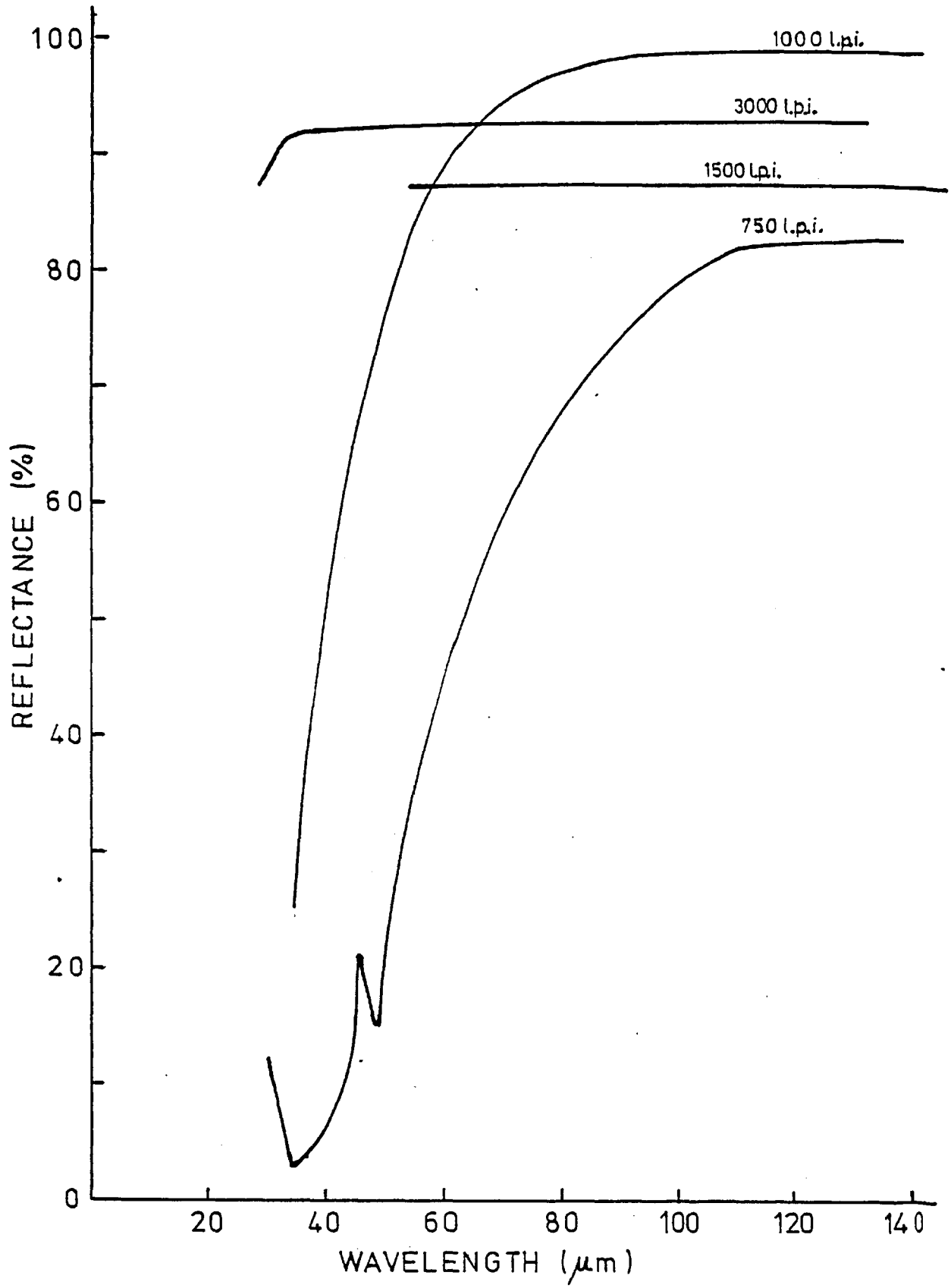

Reflectance of Various Meshes.

mission is 3% or 4% and assuming an absorption of 1%, this leads to a reflective finesse in excess of 60. This is rather higher than would be liked but is useable. The 500 ℓ.p.i. meshes were chosen for use in the order-sorting F-P.

6.2.2.d Grid Alignment Techniques

Three separate techniques for aligning the two metal meshes parallel were tried. One was unuseable, one worked and the third shows promise for future use but needs further investigation. Firstly, a 'Mini-Dekkor' was used. This is an autocollimator which projects a set of cross-wires and images the returned cross-wires onto a graticule graduated, according to the particular model, in either arc minutes or arc seconds. This method failed because of the low optical reflectivity of the meshes. The second technique is to set the meshes parallel to within 5 thou using feeler gauges and then to shine a He-Ne laser at near normal incidence onto the grids. A bright reflection diffraction pattern is seen from the mesh nearest the laser. A faint reflection diffraction pattern is also seen from the other mesh, even though this is confused by the two transmissions through the first grid. However, it is easy, in a darkened room, to identify the central order of the pattern from the second mesh and to adjust the parallelism of the grids until the two central orders are superposed. To achieve a parallelism finesse of 30, the faint spot must be placed upon the bright one to within $\frac{1}{2}$mm for an optical lever arm of 2m. This is possible even though the inherent divergence of the laser beam has broadened the spot to 2mm at this distance. It is important to work as close to normal incidence as possible to ensure greatest accuracy in the grid alignment. This method works well and is usually used. However, a third technique was briefly investigated and shows promise. This involves expanding the laser beam using a lens, so that it illuminates the entire mesh. The reflected patch shows a fringe pattern, and minimising the number of fringes seen corresponds to maximising the parallelism of the grids. However, some rough tests seemed to indicate that the number of fringes visible also depended on the orientation of the F-P. Thus, this technique, despite its high sensitivity, was not used extensively. Further investigation of the nature (e.g. Twyman-Green, Fabry-Pérot, Moiré, etc.) of these fringes is necessary before this interferometric alignment technique may be used with confidence.

6.2.2.e Scan Parallelism

The parallelism of the motion of the F-P during the course of a scan was measured by observing the two reflected diffraction patterns (see above) from a laser and looking for relative motion between them. The accuracy of this method only allows the placing of a lower limit of 20 on the parallelism finesse. To investigate the change in parallelism with cooling, the black polythene and calcium fluoride (cf. section 6.1.2.b) filters were removed and the white polythene dewar window replaced with a piece of glass. The cryostat was evacuated and filled with liquid nitrogen. Once again, the meshes were illuminated with a laser and the positions of all the reflected spots marked on a sheet of graph paper. The cryogen was allowed to evaporate and the dewar to warm up, before the new positions of the spots were marked. There is a distinct movement but it is uncertain whether this is due to changes in parallelism or to gross mechanical movements. A much more careful check on this aspect of the instrument is needed.

6.2.2.f Bandpass of Auxiliary Filtering

The Fourier Transform Spectrometer was used to measure the wavelength response of the auxiliary filtering (cf. section 6.1.2.b) at cryogenic temperatures. Figure 6.15 shows the normalised results from these runs, which were made without the order-sorting F-P. The expected long-wave leak to the F-P detector is clearly visible at about 5% of the peak transmission but the short-wavelength radiation seems adequately blocked. The bandpass for the guide detector only extends from 44μm to 55μm rather than to about 70μm as had been hoped. This, together with having to put the order-sorting F-P in its beam, severely limits the usefulness of the guide detector.

6.2.2.g The Order-Sorter

Figures 6.16 and 6.17 show the transmission spectra of two order-sorting F-P's made from 500 ℓ.p.i. mesh and having spacers of nominal thickness 76μm and 50μm respectively. As expected, the transmission peaks of the etalon with the thinner spacer are shifted to shorter wavelengths. The general shape of the curves agrees well with that predicted (cf. figure 6.7). These curves are repeatable, i.e. if an etalon is taken apart and then rebuilt, the 'before' and 'after' spectra are almost identical. Note also, that there is some transmission at short

Figure 6.15

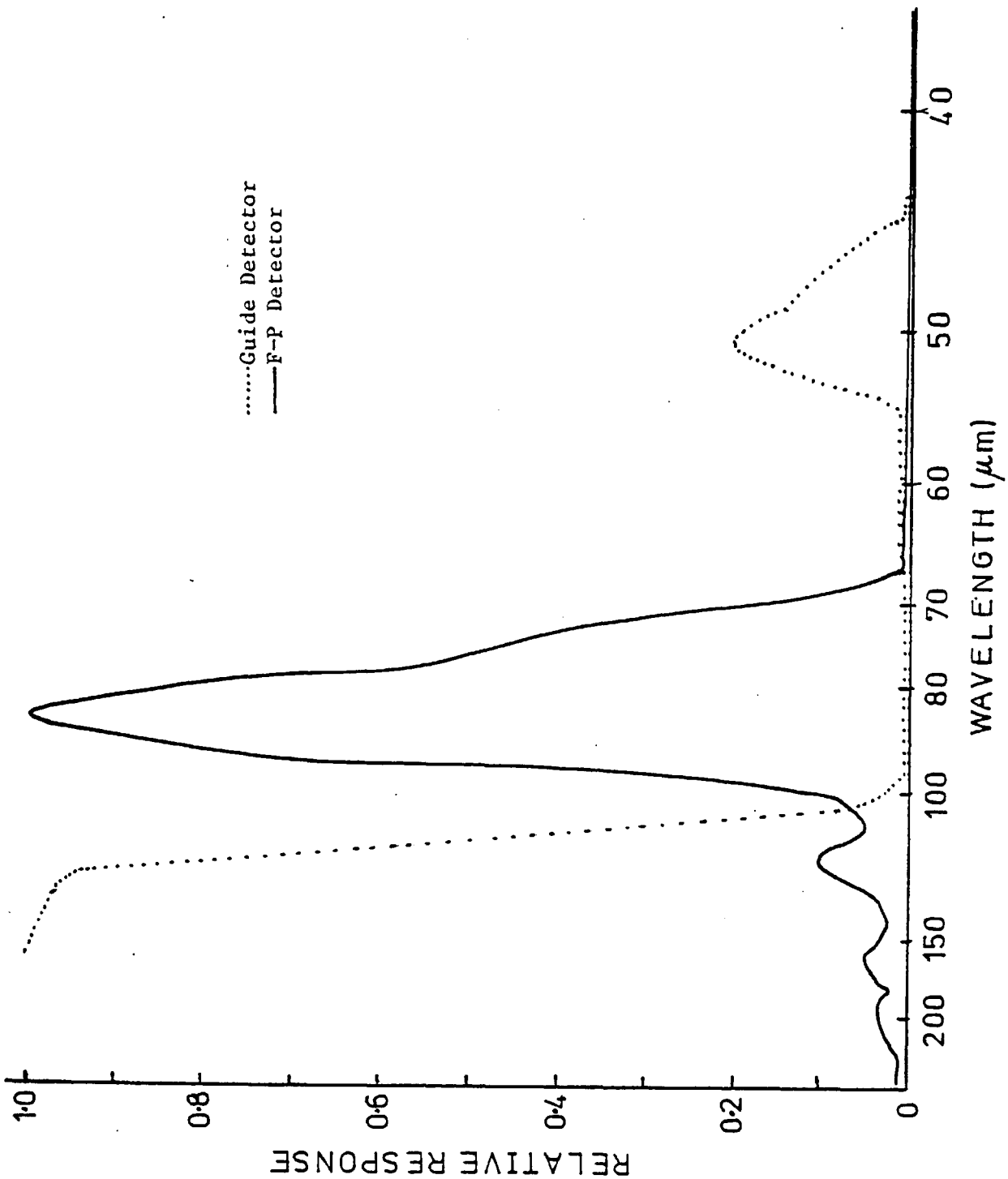

Bandpass of Auxiliary Filtering.

Figure 6.16

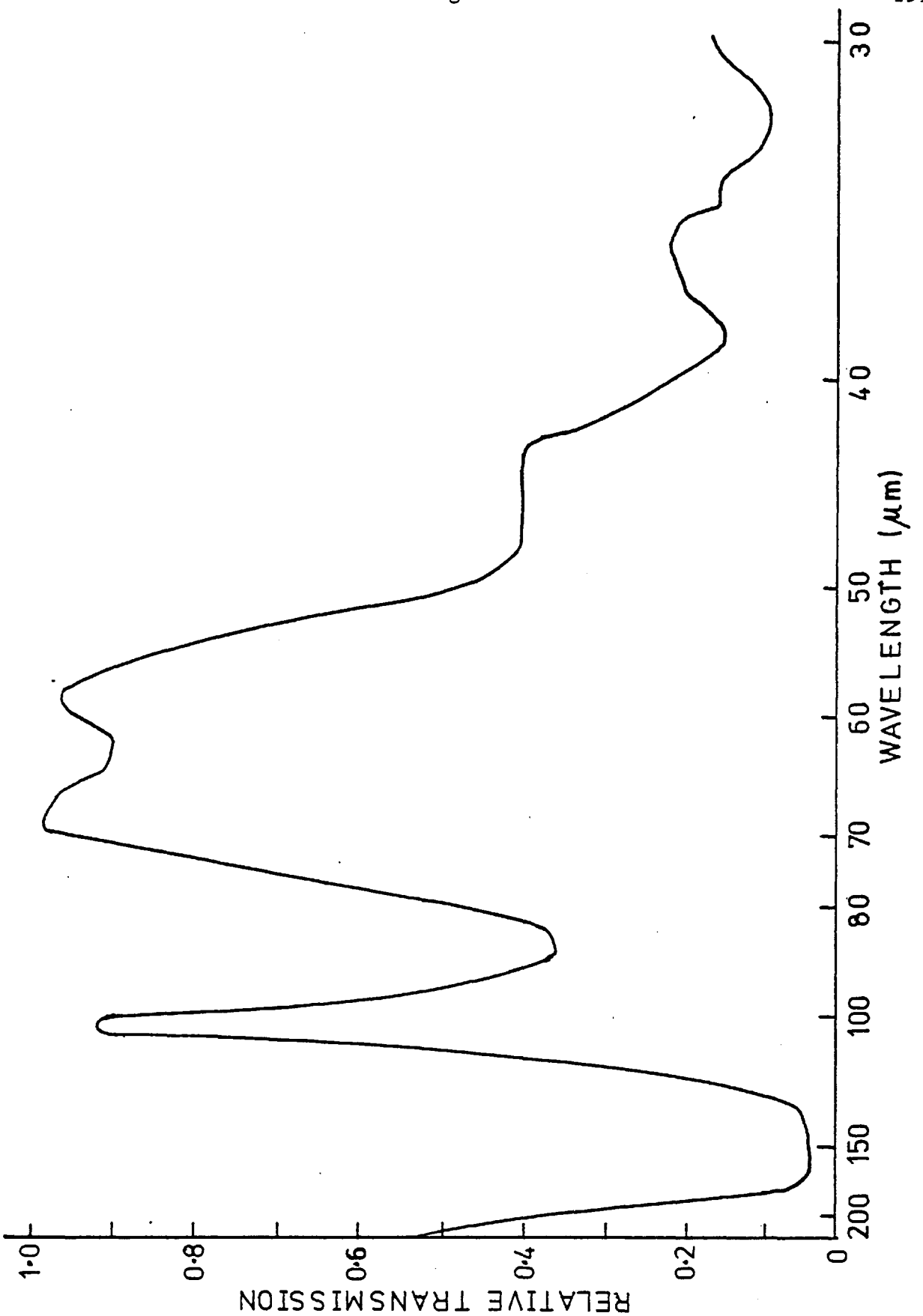

Transmission Spectrum of Order-Sorting Filter I.

Figure 6.17

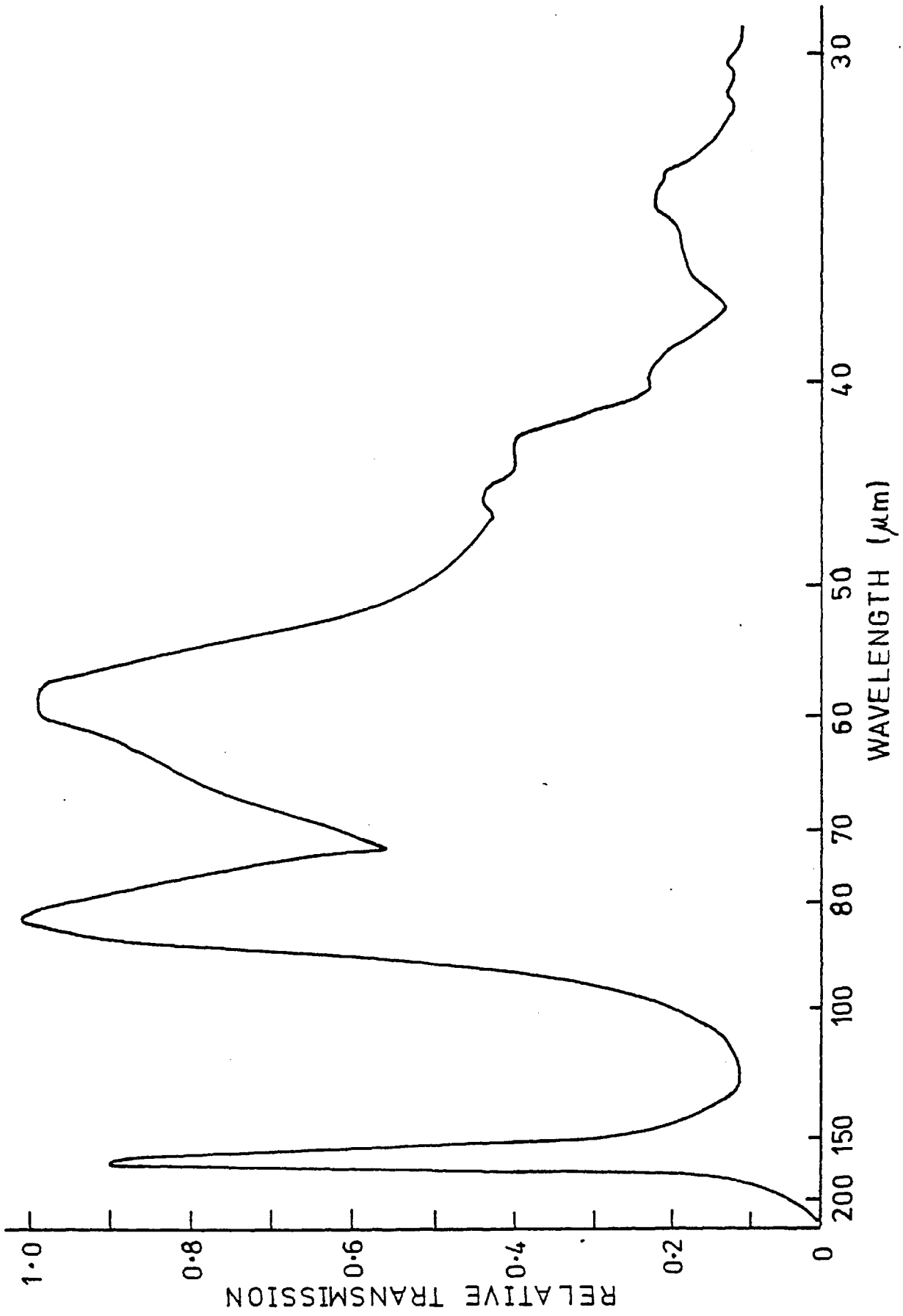

Transmission Spectrum of Order-Sorting Filter II.

wavelengths; this is needed for the guide detector.

Apart from these general points, the spectra are very difficult to interpret. Columns 1 and 2 of table 6.1 give the order of interference and its wavelength for the curves shown in figures 6.16 and 6.17. Column 3 gives the calculated gap (using equation 4.8) assuming zero phase change on reflection. The results from this are fairly consistent from order to order. For each etalon, the gap calculated in this manner is about 30μm greater than the nominal value of the spacer. This increase in gap can be explained either by burrs on the spacer or by some of the GE varnish used to glue the mesh onto the bevelled edge of the support ring having spread onto the polished flat. This interpretation of the order/wavelength data is unsatisfactory because firstly, a non-zero phase shift on reflection is expected and secondly, two identical but distinct etalons give nearly identical spectra. It is very difficult to believe that either the burrs or stray varnish would be the same in two different cases.

If the data is interpreted in terms of non-zero phase shifts, assuming that the physical gap is the nominal spacer value, then the phase shifts given in column 4 of table 6.1 are obtained. This explanation is also suspect both because of the values of the phase shifts themselves and also because they disagree totally with results quoted by Lecullier and Chanin (1976). Their phase shifts are listed in column 6. A third approach is to adopt the phase shifts of Lecullier and Chanin (1976) and solve equation 4.8 for d using the measured values of n and λ. These results are given in column 7 and once again, they are internally inconsistent. Due to lack of time, this problem was not pursued further. The nominal 75μm spacer was etched away in ferric chloride solution until, by trial and error, the 2nd order peak occurred at 84μm. This was the etalon flown.

From figures 6.16 and 6.17, it is obvious that the finesse is poor, around 4. This is due to two effects, firstly, the parallelism of these etalons was not good and secondly, the beam of the spectrometer is f/1.7 thus leading to an aperture finesse (in 2nd order) of 12 (equa-(equation 4.15). The parallelism finesse of the flight etalon was measured by the second of the techniques described above and was found to be 13. The overall finesse of this etalon, when measured by the FTS, was 7. Thus, when in the f/7 beam of the IC telescope, the flight

Table 6.1

(a) 500 ℓ.p.i. Mesh with Nominal 76μm Spacer.

n	λ(μm)	d(μm, if ϕ=0)	ϕ(if d=76μm)	λ/g	[a]ϕ ⇒	d(μm)
1	∿215	107	-0.92	4.2	0.83π	197
2	105	105	-1.74	2.1	0.68π	141
3	68	102	-2.40	1.3	[b]0.58π	122
4	60	120	-4.61	1.2	[b]0.55π	137

(b) 500 ℓ.p.i. Mesh with Nominal 50μm Spacer.

n	λ(μm)	d(μm, if ϕ=0)	ϕ(if d=50μm)	λ/g	[a]ϕ ⇒	d(μm)
1	164	82	-1.22	3.2	0.80π	148
2	82	82	-2.45	1.6	[b]0.61π	107
3	58	87	-4.01	1.1	[b]0.53π	102

Notes

a. From Lecullier and Chanin (1976).
b. Data uncertain due to proximity to grid resonance.

etalon is expected to have a finesse in excesss of 9 and thus a passband less than 5μm. However, there is a long wavelength leak from the 1st order and some short wavelength leakage between 2nd and 3rd orders.

In summary on the order-sorting F-P, the amount of time and effort needed to tune an F-P to 88μm in 1st order was seriously underestimated. Consequently, it was necessary to fly a 'leaky' 2nd order filter with the [OIII] line only just in the wing of the passband. Much development work, including full testing at liquid helium temperatures, is still needed.

6.2.3 Electrical Trials

The viability of using the metal mesh etalon was investigated using a test ring. No problems were found and so development of the flight system went ahead. Operation of the capacitance micrometer in a vacuum presented no difficulties.bar an apparent gap change as the system was evacuated. The mechanical and electronic precision of the interferometer were sufficient for the F-P to be scanned in steps of less than one spectral resolution element. The speed of the scanning motor as a function of applied voltage was measured (cf. section 6.3.2). Other electrical tests, mainly on the entire system, are described in section 6.3.

6.3 F-P system tests

An account of the testing done on the complete system is now given. Firstly, some results from an ambient-temperature metal-mesh F-P working at wavelengths between 30μm and 50μm are presented. Then, the setting up procedures for the liquid-nitrogen-cooled model are explained before the results from laboratory tests are discussed. Lastly, the runs made in a thermal vacuum chamber are described.

6.3.1 Warm 30μm - 50μm F-P Tests

The aim of these tests was to check very quickly and easily the feasibility of using metal meshes for Fabry-Pérot etalons. The 30μm - 50μm wavelength range was chosen because a grating spectrometer was available for this range. The zinc selenide plates were removed from the near-infrared F-P and replaced by two 3000 ℓ.p.i. metal meshes. These meshes were aligned parallel to each other by the second of the three techniques of section 6.2.2.d. The gap between them was measured

to be about 230μm using a travelling microscope and focussing on each mesh in turn. Then, the F-P was placed inside the sample chamber of the grating spectrometer, which was then purged with dry air. When the system had settled, the grating spectrometer was scanned from 285cm^{-1}(35μm) to 200cm^{-1}(50μm). Figure 6.18 is typical of the results that were obtained. The rising baseline is an instrumental effect, possibly either due to the very low signal level in the system or because this wavelength region is at the very end of the range of the grating instrument. However, three or maybe four peaks may be seen above the baseline. To improve the signal to noise ratio, the rising baseline was manually subtracted off six separate traces and the results then added to give figure 6.19. This clearly shows transmission peaks at about 204cm^{-1}, 223cm^{-1}, and 246cm^{-1} and probably another at around 268cm^{-1}, with a free spectral range, $\Delta\bar{\nu}$, of roughly 21cm^{-1}. Since the etalon gap is known (see above) it is possible to calculate both the expected free spectral range (equation 4.9) and the positions of the transmission maxima (equation 4.8). The calculated $\Delta\bar{\nu}$ of 22cm^{-1} is consistent with the experimental data. Transmission in the 9th, 10th, 11th and 12th orders is expected to occur at wavenumbers of 196cm^{-1}, 217cm^{-1}, 239cm^{-1} and 261cm^{-1} respectively, which are very close to the experimentally-determined values.

Once again, the finesse of the instrument appears low because of the degrading effect of the convergent spectrometer beam. The conclusion from this test is that transmission in four orders has been seen and thus, a metal mesh F-P is a viable proposition.

6.3.2 Setting up Procedures

The assembly of the complete instrument is now described. All components are carefully cleaned with alcohol and acetone. Firstly, the F-P must be assembled. The mounted meshes are glued into the F-P base and upper plate holder using GE varnish; the electrical leads to the grids are secured to the F-P surfaces, again with varnish. The MRD and its magnet are attached to the F-P base and carriage respectively. After the upper mesh holder has been fixed to the F-P carriage, the latter is placed in position above the base upon the springs. Once again, equality of free spring length is assured by the use of dural parallels (section 5.2.1). The F-P gap is set to the desired value using the coarse adjusting screws and a travelling microscope. The etalon is then aligned parallel using the fine adjustment screws and a

Figure 6.18

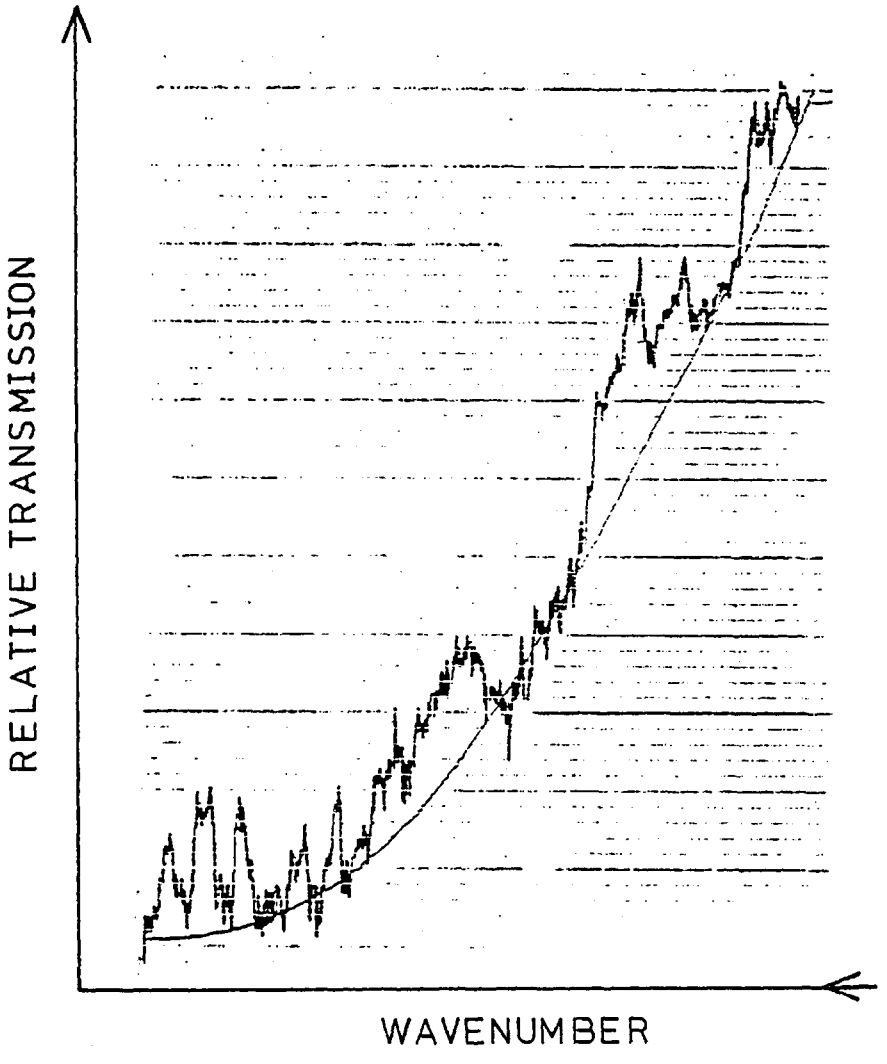

Raw 30μm-50μm F-P Transmission Spectrum.

Figure 6.19

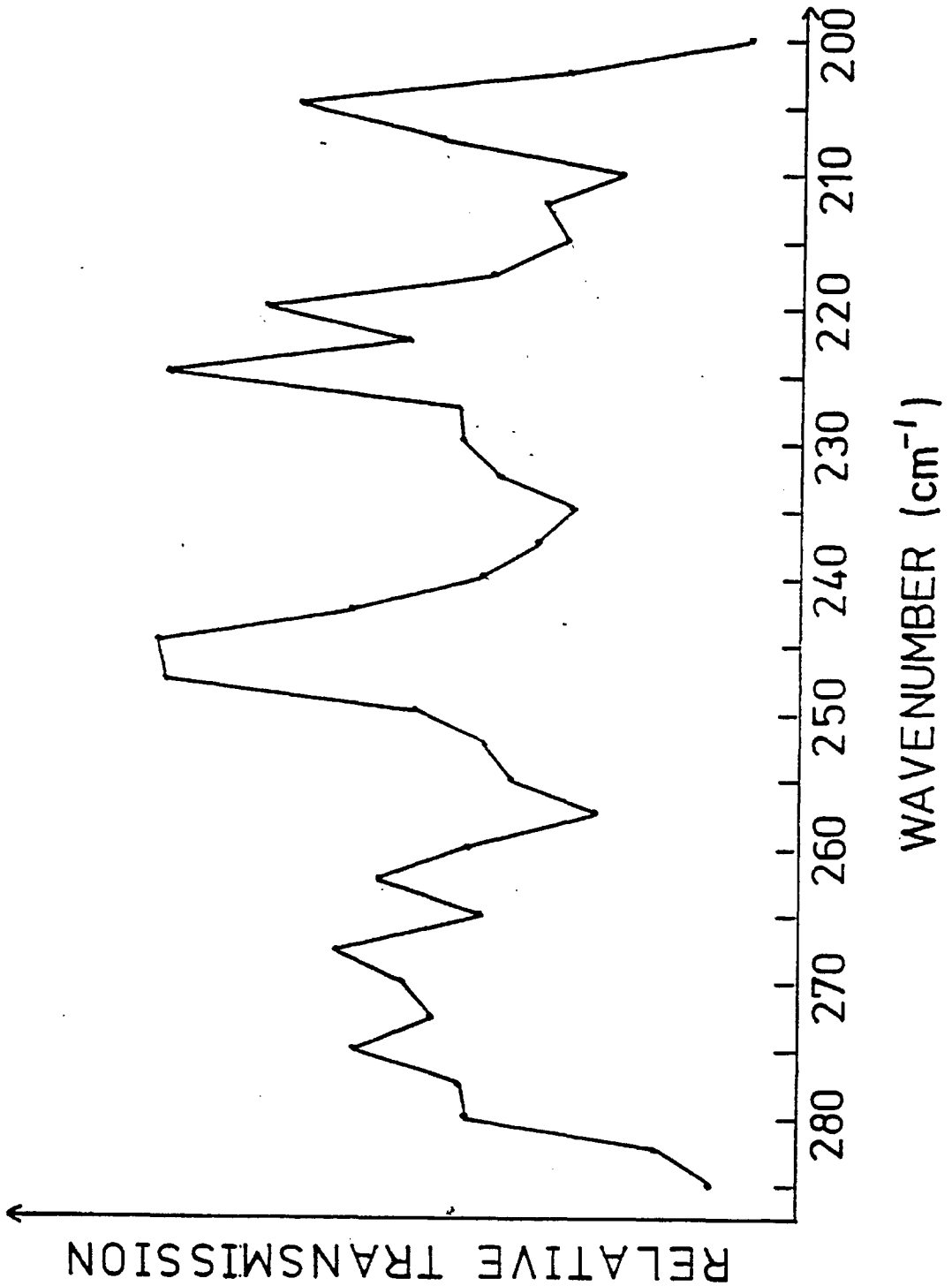

'Summed' 30 m-50 m F-P Transmission Spectrum.

laser (cf. section 6.2.2.d). A capacitance bridge is used to measure the capacitance between the F-P meshes. Two sub-miniature plate ceramic capacitors (from Radio Spares) of this value are glued to the F-P base to act as reference and balance capacitors (cf. section 5.1.4). The MRD and all the capacitors are wired up using constantan wire. These leads are varnished in place on the F-P and their free ends taken out through the base of the interferometer.

Now, the photometer must be constructed. The two detector assemblies are built and placed upon the cold surface of the dewar. Their relative positions are checked using a travelling microscope; the guide detector is placed on the axis of the cryostat. The constantan leads for the detectors and load resistors are secured to the cold surface with GE varnish. Next, the photometer body is positioned over the detectors, once again using the travelling microscope to ensure that it is in the correct position. The spring washers and potassium iodide mirrors are placed inside their 'lids' and these are then attached to the photometer. Potassium iodide is hygroscopic and therefore, during this stage, plastic gloves must be worn and care must be taken not to breathe on the crystals. The order-sorting F-P is assembled inside the forward stop and its parallelism checked. When this is satisfactory, the forward stop is screwed into position on the photometer, and the parallelism of the order-sorter is re-measured. The liquid-nitrogen-cooled radiation shield is then replaced. This is positioned very carefully so that it is concentric with the helium cold surface.

At this point, the parallelism of the F-P is rechecked, before it is inverted and very gently lowered into place on the nitrogen shield. The adjusting screws must not be knocked on the photometer as they pass through it into position. If the alignment of the F-P has not been disturbed by this manoeuvre, the electrical leads are glued into place along the top and side of the radiation shield. Next, the outer vacuum jacket of the dewar is replaced. The electrical leads are taken through this and checked for continuity and shorts. The calcium fluoride scatter filter is put into its place in the F-P base and covered with a piece of black polyethylene. The drive assembly has previously been built inside the dewar extension and this is now affixed to the cryostat. The power leads for the motor are secured to the inside of the dewar vacuum jacket, thus ensuring that they remain at ambient temperature. Electrical connections are made to the motor, MRD and capacitors through

a 10-way connector, and to the detectors through a separate 6-way connector. The constantan leads are now soldered to these. If all the electrical connections are satisfactory, the dewar base is replaced and the cryostat is ready to be evacuated. Throughout the entire assembly process, every screw, as soon as it has been finally adjusted, is glued in position using GE varnish.

The dewar is now evacuated and once the pressure is low enough, it is removed from the pump and filled with cryogens. Experience shows that it is best to pre-cool the dewar with liquid nitrogen for at least two hours before filling with liquid helium. After the system has settled, the F-P motor is activated and the F-P scanned 'out', i.e. in the direction of increasing etalon gap, until the MRD and capacitance micrometer (CM) show that there is no further F-P carriage movement. This means that the drive micrometer has retracted sufficiently for the nylon micrometer extension to have come out of contact with the F-P, i.e. the F-P is in an undeflected position. The motor is then reversed until the MRD just shows movement. This zero-deflection position gives a datum for the gap-sensing electronics. Initial calibration for the MRD and CM is obtained by timing the motor as it scans from the zero datum. From section 6.2.3, the time taken for the motor to make one revolution is known. The pitch of the micrometer is 0.5mm. Thus the distance that the F-P carriage has moved sideways can be calculated from the time taken to get there and hence, the MRD is calibrated. It is now easy to make a preliminary calibration of the CM for knowing the sideways motion, the change in plate separation can be calculated using the demagnification data of section 5.2.1. Wavelength calibration and more accurate calibration of the MRD and CM is hoped to be achieved by observation of atmospheric absorption lines in flight.

It is vital not to scan the F-P more than 2½mm from the zero-deflection position. If this is done, the liquid-helium-cooled forward stop comes into contact with the liquid-nitrogen-cooled F-P, thereby causing a thermal short. A microswitch ought to be fitted to the interferometer to stop the scanning motor automatically when it reaches this point.

6.3.3 Laboratory Tests

The far-infrared F-P was tested to some degree in the laboratory. This section presents the results of these trials under three general

headings, performance of gap-sensing electronics, detector tests, and signal tests.

During the laboratory tests of the entire system, the performance of the electronics for sensing the etalon gap and the motion of the F-P carriage was evaluated to some extent. After the dewar had been filled with liquid helium and had settled, the MRD was set up as described in section 6.3.2. The gains of the MRD electronics were set so that at zero deflection, the output was 0.5V and at 2mm deflection, 4.5V. The capacitance micrometer (CM) electronics' gains and offsets were adjusted so that its output remained between 0V and 5V as the F-P was scanned full range. The variation of MRD and CM outputs with the position of the F-P carriage was investigated. As expected, the MRD output is linear with carriage position while the CM appears to become more sensitive as the deflection increases (see CM output on figures 6.25 - 6.27). This is due to the changing demagnification.

The sensitivity (cf. section 5.2.2) of the CM at a particular displacement is found from the gradient of the CM curve at that point, using the appropriate demagnification factor from figure 5.12. It is planned to operate the F-P around a deflection of 1.5mm. The CM sensitivity, here, is 15mV/μm and the laboratory noise is less than 1mV peak to peak. Thus, in the laboratory, a change in etalon gap of $^1/_{30}$th of an F-P resolution element can be seen. However, in flight, noise in the telemetry prevents the CM output being read to better than 10-20mV. Thus, assuming worst case telemetry noise, the ground electronics can detect a change in gap of half a resolution element. This is just adequate. The CM output drifted by one resolution element in 18 hours.

The change (if any) of MRD and CM sensitivity, as they are cooled from room temperature to 77K, is not directly relevant to this work, because they are calibrated when cold. However, the sensitivity of the MRD appears unaltered by cooling while the CM may become slightly more sensitive. There is also a change in offset for the CM, presumably due to a change in value of the reference capacitor.

Standard performance checks are always made on the detectors before proceeding further. The dewar entrance window is covered with silver foil and the resistances of the bolometers at 4.2K measured. These are about 8.6kΩ (F-P detector) and 10.1kΩ (guide detector) and do not alter from run to run. (If the dewar is left to stand, it retains its liquid

helium for 21 hours). The pressure above the liquid helium is now slowly reduced to a few torr in order to cool the bolometers to their operating temperature. The variation of detector resistance with pressure during pump-down is always repeatable. Typical values for the pumped-down resistances are 4.2MΩ (guide) and 2.0MΩ (F-P). Noise measurements show that the guide detector is substantially noisier than the other, $\sim$ 65nV $Hz^{-\frac{1}{2}}$ compared to $\sim$ 30nV $Hz^{-\frac{1}{2}}$ at a frequency of about 8½Hz. The detector noise does not alter either when the scan motor is running or when the 16kHz signal to the metal meshes is switched on and off. The F-P bolometer is very microphonic. It has a resonant frequency of around 300Hz and, if the dewar is jolted, the oscillations take $\sim$ 15 seconds to die away. Load curves for each detector, with a 7.6MΩ load resistor, show that the optimum bias voltage is 1V. At this point, the electrical responsivity of the F-P detector is 2×10^{6} V W^{-1} and that of the guide detector, 6×10^{6} V W^{-1}.

For the signal tests, the dewar is supported on a metal framework above a 45° mirror, in a similar manner to that shown in figure 5.18. When the silver paper is removed from the cryostat window, both detectors respond to the movement of warm objects in their field of view. However, it is disappointing that the F-P detector is the more sensitive of the two to this crude test, because the guide detector ought to receive the bulk of the radiation from an object slightly above room temperature. No change in signal level is seen as the 16 kHz oscillator driving the F-P capacitor is switched on and off.

The interferometer was next used to map out the profile of the order-sorter. The dewar was set up as in figure 5.18 to look at a chopped black body. The F-P was scanned from nearly zero deflection (≡ MRD output of 0.5V) to maximum deflection (≡ MRD output of 5V) and then back to zero. The output from the F-P detector is shown in figure 6.20. Two orders of the interferometer have been scanned through the order-sorter profile. The peaks are repeatable in terms of the MRD output (numbers on right of figure 6.20). Due to the 'leakage' in the order-sorter, the depth of modulation is only $\sim$ 65%. The switching transients seen as the motor is started and stopped originate in the latching relays. The non-linearity of the change in etalon gap (cf. section 5.2.1) is clearly shown in figure 6.20. Near zero deflection, the demagnification of the F-P carriage motion is large and hence, the etalon gap only changes slowly with deflection of the carriage, thus

Figure 6.20

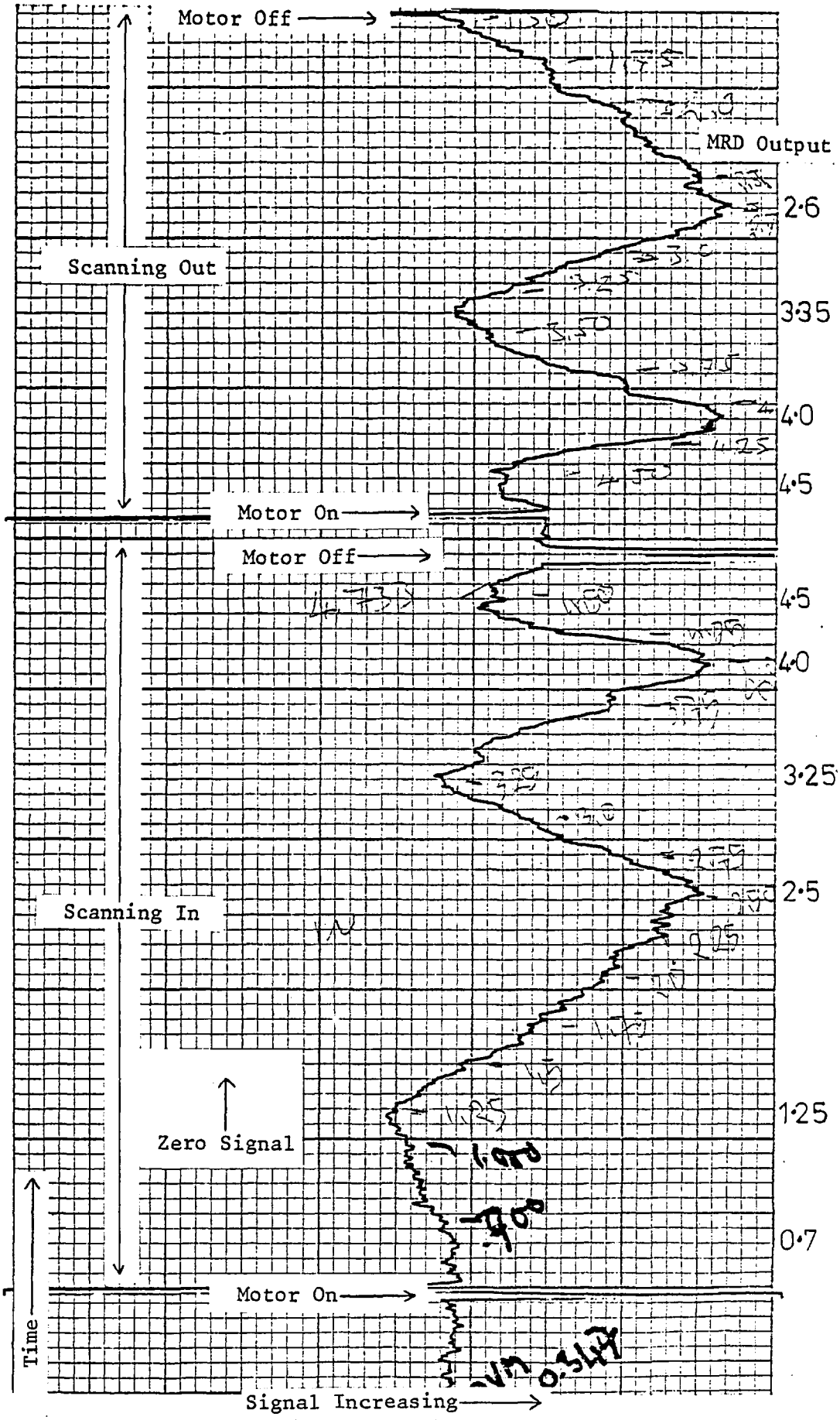

Output of F-P Detector as Interferometer is Scanned.

leading to a broad shape for the first pass through the order-sorter. At higher deflections, the change in etalon spacing per unit deflection of the F-P carriage is larger and thus, the second order-sorter profile appears narrower. The effect upon the guide detector of scanning the F-P back and forth across its range is shown in figure 6.21. No F-P orders are seen, but there are some features larger than noise which may be genuine. To check that the peaks seen in figure 6.20 were genuine F-P effects, the silver foil was replaced over the dewar window and the F-P, once again, scanned over its entire range. Nothing above the noise level was seen.

6.3.4 Thermal Vacuum Tests

The behaviour of the complete F-P system in an environment similar to that encountered during a balloon flight was investigated by placing both the dewar and the F-P electronics in a small thermal vacuum chamber at NSBF, Palestine, Texas. Both were prepared as if for flight. The dural box, containing the electronics, is insulated with a 2" thick layer of styrofoam, and also holds two water-filled bottles. As the water freezes, it gives up its latent heat of fusion, which is used to warm the electronics. The dewar has a check valve fitted to the exit port of the liquid-nitrogen can to keep the pressure therein at approximately one atmosphere in order to prevent the nitrogen freezing. A standard safety valve is fitted to the liquid-helium reservoir for pressure relief in the event of a freeze-up. As mentioned in section 6.1.3.b, the pre-amplifier, attached to the side of the dewar, is allowed to cool freely but the bias and power batteries for it are well insulated and provided with thermal ballast.

A realistic pressure-temperature profile was not followed when using the chamber, because at pressures below $\sim$ 40mb, the cooling is very slow. Thus, the pressure was usually reduced from atmospheric to 40mb over the course of an hour of so and held there for two to three hours to get the dewar and electronics cold. Then, the chamber was pumped down to $\sim$ 20mb and the contents left to 'soak' at low temperatures for up to 12 hours. The detectors and gap-sensing electronics were continually monitored on strip charts; every half hour, the F-P motor was energised and the interferometer scanned over its full range. A thermocouple was taped onto the outer casing of the dewar to measure its temperature.

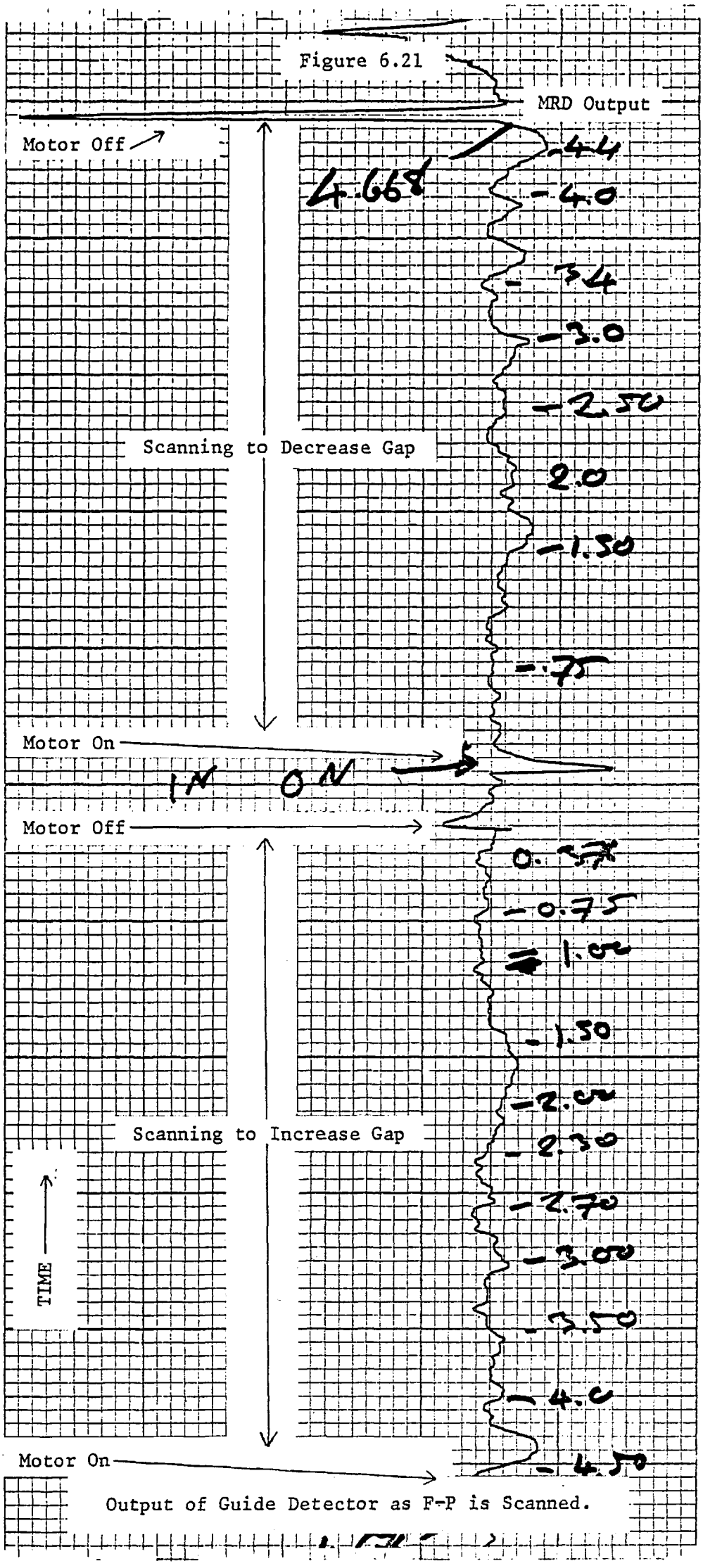
Figure 6.21
MRD Output
Motor Off
4.668
-4.4
-4.0
-3.4
-3.0
-2.50
2.0
-1.50
-.75
Scanning to Decrease Gap
Motor On
IN ON
Motor Off
0.75
-0.75
-1.50
-2.30
-2.70
-3.50
-4.0
-4.50
Scanning to Increase Gap
TIME
Motor On
Output of Guide Detector as F-P is Scanned.

With the exception of the F-P scanning motor, the results from the thermal vacuum run were very encouraging. Everything else worked: the dewar retained its vacuum after 9 hours below -30°C; the detectors showed signs of life, i.e. microphonics at the expected pressure; the electronics continued to function; the preamplifier batteries had only cooled to -4°C after 12 hours of cooling; the pumped liquid helium hold-time was in excess of 17 hours; and the pressure relief valve on the liquid-helium can also worked. The problem with the motor was that as it cooled the scan became rougher, i.e. jerkier. This was noticed by the detectors, for their noise increased dramatically when the motor was running. When cold, the motor needed a current of 45mA to restart and about 25mA to run, compared to about 5mA drawn when at room temperature. Thus the motor obviously stiffens up when cold and overcoming this resistance presumably leads to the vibration noticed by the detectors. Twelve hours after the start of the thermal vacuum run, a direct short between the motor drive and earth occurred.

The dewar was warmed up and stripped down. The fault lay in the motor itself. However, this was not thought to be a design problem because, to prevent air pockets being trapped inside the motor casing, a cap had been removed from the latter. This cap also provided additional support for the motor armature, and its removal could allow the armature enough freedom to vibrate. Therefore, the motor was replaced with a spare, with end cap, and a second thermal vacuum test performed. This motor also showed increased current demand when cold and a jerky scan, but was still working perfectly after twelve hours. After the dewar had been brought back to room temperature, the motor began not to re-start after stopping unless tapped. This problem slowly became worse, Eventually, even after the motor had been tapped into motion, there was still no movement of the F-P carriage.

When the motor was removed from the dewar, the entire drive assembly was seized up. The gearbox had been stripped and the motor, itself, still only restarted after tapping. Apparently the motor fault was caused by trying to drive the seized micrometer rather than by cooling. It was, therefore, decided to put the last motor into the dewar and to fly it. The F-P would be scanned every 30 minutes in flight to keep the motor 'loose'.

6.4 Balloon Flight 1186-P

The far-infrared F-P was part of the Imperial College infrared payload on balloon flight number 1186-P, launched at 17.45 CST on 9th December 1979 from Palestine, Texas. In the next few paragraphs, details of the complete payload are given, followed by a brief history of the flight, before the performance of the F-P is discussed.

The IC part of the payload consisted of the 41" telescope and two-colour photometer (Joseph et al., 1977) together with the F-P and a new secondary mirror chopper. The experiment was flown upon the Appleton Laboratory's Mark I Stabilised Balloon Platform, SBP (Chaloner, Farman and Hardie, 1979). The SBP is stabilised in three-axes and is designed to carry experiments weighing up to 500kg. The design pointing accuracy is better than one arc minute and a blind offsetting capability of similar accuracy over 5^{o} is specified.

Both the IC and AL groups arrived in Texas in early October and began preparing the payload. By the start of December, the SBP was deemed to be ready for flight. The control equipment for both the experiment and the platform was housed in a specially-converted container, the inside of which is shown in figure 6.22. A dummy run to the launch pad was carried out on 6/12/79 and much valuable experience gained. The weather then closed in for two days.

On the 9th, the weather forecast was good. The two dewars were filled with liquid helium at 10 o'clock and a series of pre-determined electrical and mechanical checks undertaken. For the F-P these included checking the position, alignment and security of the dewar on the telescope; measuring the resistances of the detectors; checking the signal lines by measuring the preamplifier noise; and scanning the F-P back and forth across its entire range. These tests, where possible, were done from the control trailer. The weather briefing at 11.00 confirmed that launch would be possible and that the estimated time at 100,000 feet would be $6\frac{1}{2}$ - 8 hours.

Just after lunch, when all checks were complete, the platform was picked up by the launch vehicle, 'Tiny Tim', and taken out to the launch pad, see figure 6.23(a). The liquid nitrogen in the dewars was topped up at 15.30 and the liquid helium levels checked. Another complete set of checks was made on the launch pad. In general, these were similar to

Figure 6.22

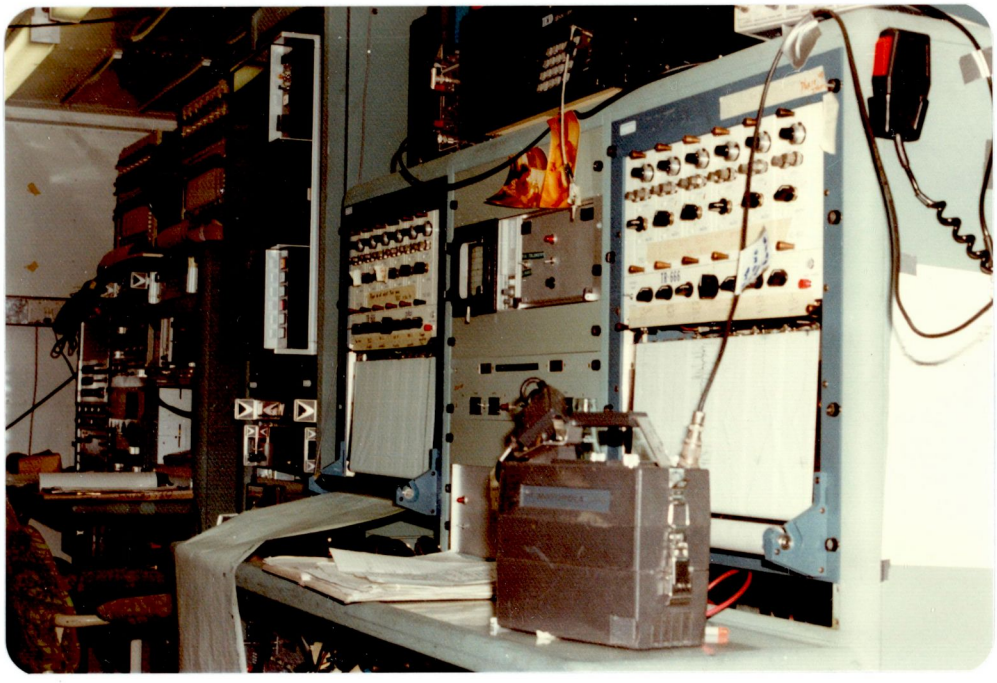

Interior of Control Trailer.

(a). Just Arrived on Launch Pad.

(b). Ready for Launch.

SBP on Launch Truck.

those that had been done before the payload left the staging building. When all tests had been satisfactorily completed, the liquid-nitrogen check valve and the liquid-helium pressure relief valve were fitted. The experiment was then ready for launch, and inflation of the balloon began. There was a brief delay while NSBF remedied some telemetry faults. Thus, the payload was still on the launch pad as dusk fell, see figure 6.23(b). (Also visible on this photograph is the planet Venus, directly above Tim.) Eventually, the experiment was launched smoothly at 17.45 CST.

The platform was switched on at an altitude of 20mb and it operated successfully. At 19.42 a bright guide star, Zeta Ori, was acquired and the platform locked onto this. Several platform control problems became apparent at this point and these led to temporary loss of the guide star. After Zeta Ori had been re-acquired the platform was offset to look for the first infrared calibration object, NGC 2024. It was necessary to use this HII region for calibration since there were no planets visible until Mars and Jupiter rose at about 3.00 am. A coarse raster search was undertaken for NGC 2024 and it appeared in both photometer channels. However, before the fine raster was completed, control of the platform was lost and never fully regained. In fact, control became progressively more difficult. By 23.00 hours, the platform was hard up against the roll stop and could not be moved from there. Some limited control was still available in azimuth and, using this, attempts were made to scan the telescope across the moon in order to gather some data on the optical performance of the F-P in flight. However, this proved impossible because the elevation angle of the platform was both unknown and uncontrollable. At 2.30 the platform was put into 'stow' position and powered down. Telemetry was lost at about 03.15. The descent was normal and the platform landed safely, albeit 40 feet up a tree, near Starkville, Mississippi (figure 6.24). The NSBF recovery team managed to bring the platform back to ground level without any damage and returned it to Palestine within five days. The IC experiment was undamaged, except for the photometry dewar, the contents of which were destroyed by an explosion, presumably following a liquid-helium freeze-up.

Because of the almost total failure of the AL SBP, very little information was gathered about the performance of the F-P. On the launch pad, the preamplifier noise for each detector was measured

Figure 6.24

SBP after Landing.

through the telemetry and found to be about 10nV $Hz^{-\frac{1}{2}}$, as expected. Figure 6.25 shows the CM, MRD and capacitance micrometer R outputs just before and during launch, and also the first scan of the F-P. It is seen that the interferometer was unaffected by any jolts at launch, and that the scan is smooth. The F-P was scanned back and forth every half hour as planned and never showed any problems. At float, with the F-P motor not running, the noise of the F-P detector was about 120nV $Hz^{-\frac{1}{2}}$ and that of the guide detector around 70nV $Hz^{-\frac{1}{2}}$, i.e. the F-P detector noise was a factor of 4 up on laboratory noise, while the noise in the other detector was much the same. Both detectors noticed the motor running; their noise increases by a factor of x10 in this case (cf. indicated portions of figures 6.26 and 6.27). This obviously rules out use of the F-P in continuous scan mode; it must be stepped and then stopped for integration on a source. As the flight proceeded, the scan as measured by the CM appeared to become rougher, see figure 6.26. However, this was not shown by the MRD and later in the flight (figure 6.27) the CM seemed cleaner. A likely explanation for this is that as the motor drives, it vibrates the dewar. This leads to microphony in the CM cables, causing the irregularities seen. Later, in the flight, the cables have stiffened due to the cold and so do not move as the dewar vibrates. Therefore, the scan now appears less rough. The scan also became slower during the course of the flight, presumably due to the motor stiffening. However, the motor worked perfectly throughout the flight and even, now, shows no sign of any fault. Thus the conclusion must be that other factors (cf. section 6.3.4) than the cold were responsible for the failure of the first two motors.

6.5 Conclusions

A far-infrared liquid-nitrogen-cooled F-P for operation at a wavelength of 88μm has been designed and built. Preliminary testing has been done and the results are encouraging. In order to fully evaluate this instrument, two main areas need attention. These are firstly, the order-sorter, which must be tuned to the correct wavelength with high enough finesse and tested at liquid-helium temperatures, and secondly, the main F-P, whose resolution and transmission must be measured. The mechanical performance during a balloon flight is adequate although an improved cold-running motor is desirable. Some possible design improvements are suggested in chapter 7.

Figure 6.25

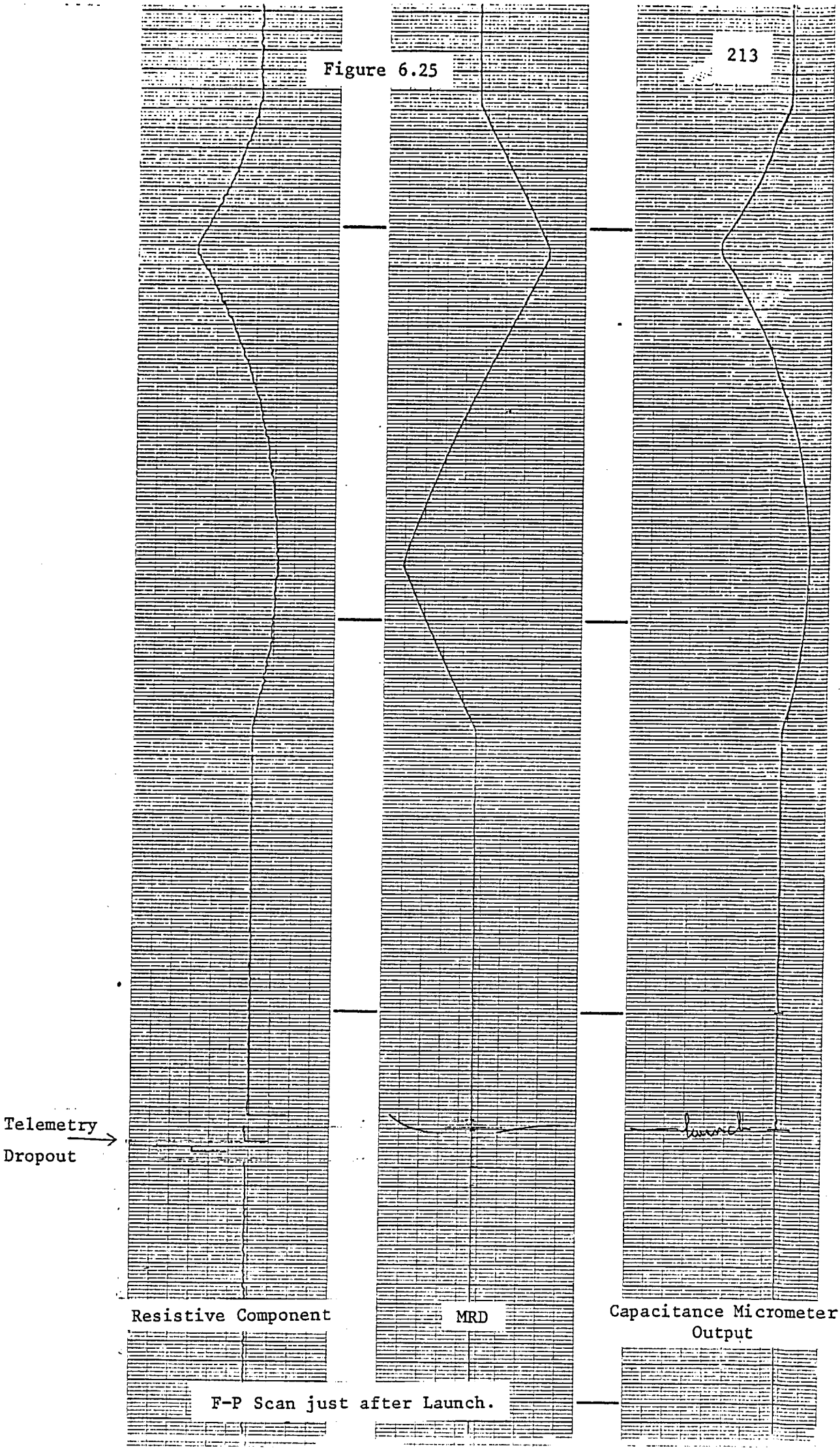
Telemetry
Dropout
Resistive Component
MRD
Capacitance Micrometer
Output
F-P Scan just after Launch.

Figure 6.26

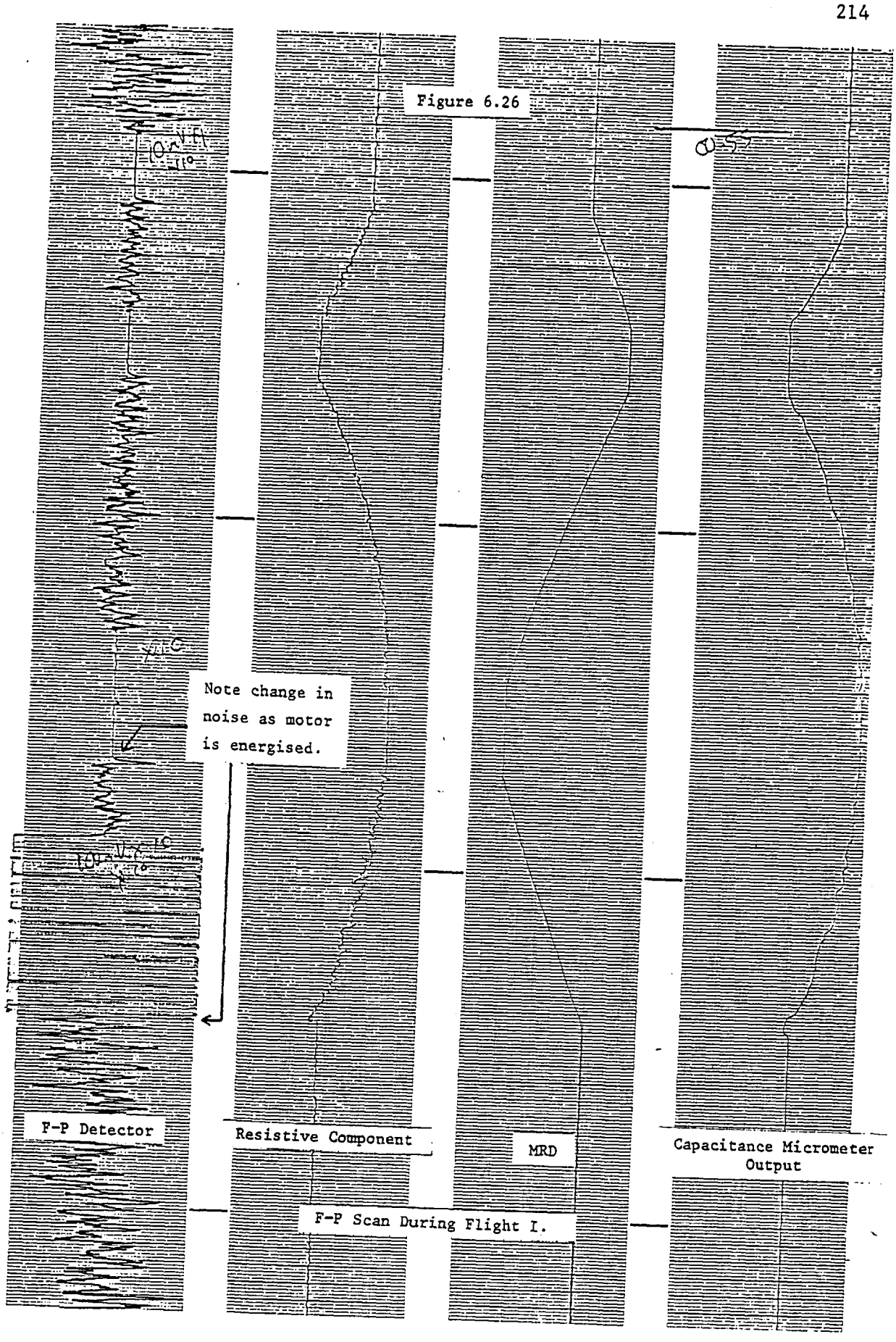
Note change in noise as motor is energised.
F-P Detector
Resistive Component
MRD
Capacitance Micrometer Output
F-P Scan During Flight I.

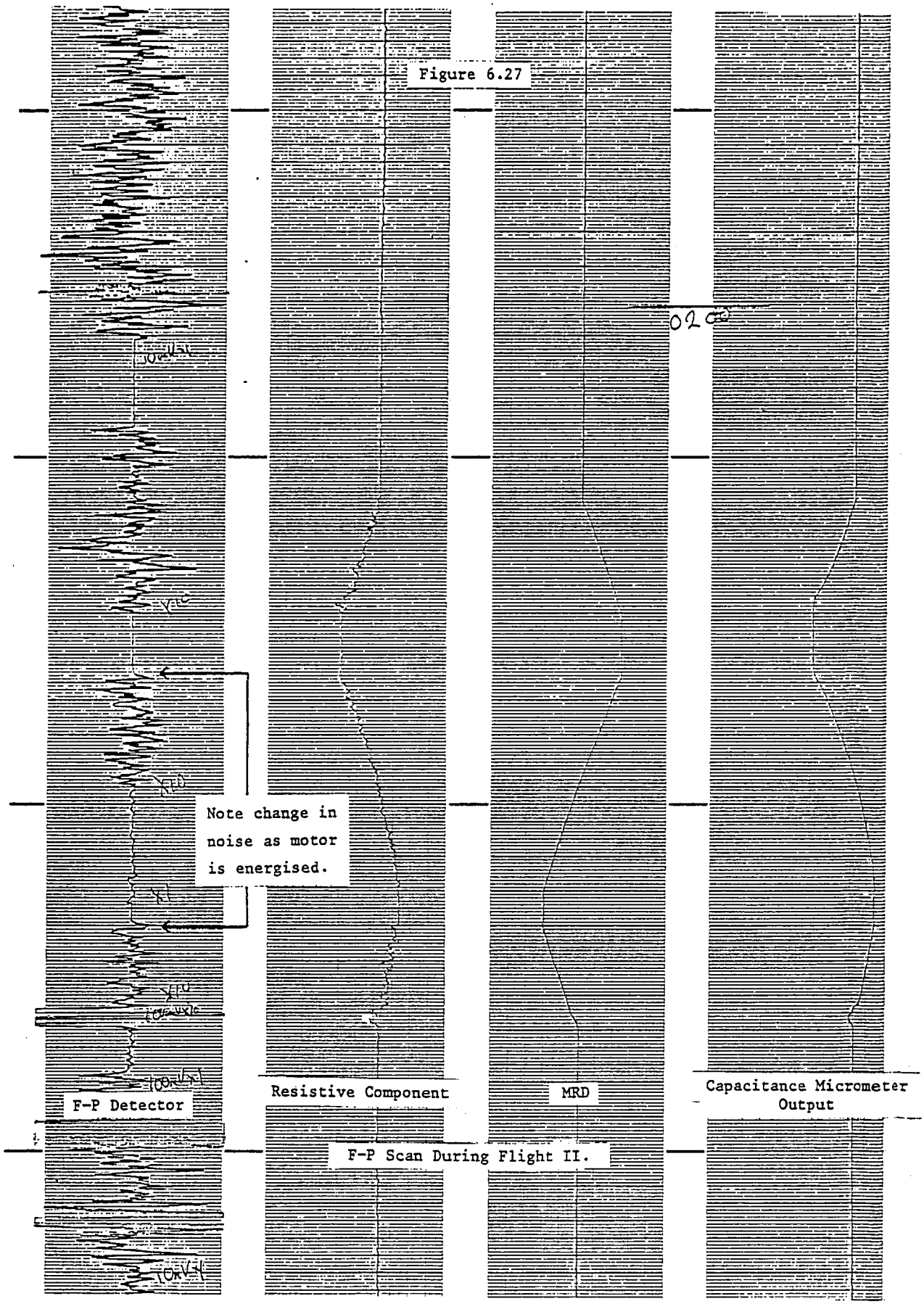

Figure 6.27

F-P Scan During Flight II.

Chapter 7

Summary, Conclusions and Recommendations

This thesis began by considering the astrophysical justification for infrared line astronomy. It was shown that infrared line emission is expected from both the hot and cold parts of the interstellar medium and that detection of infrared lines allows determination of the physical conditions in these regions. The advantages of infrared lines over their optical and radio counterparts were briefly reviewed. In conclusion, it was stated that the applicability of infrared recombination, atomic and ionic fine structure, and of molecular vibrational-rotational and pure-rotational line studies ranged, in space, from our galaxy to extragalactic sources, and in time, from the present back to the birth of the universe.

The achievements of infrared line astronomy to date were summarised. Most of the work has been on fine structure lines, but in the last year the first detections of molecules in the far-infrared have been made. Fine structure studies have progressed beyond merely reporting line intensities; sources are being mapped in infrared forbidden line emission and accurate ionic abundances and electron number densities are being calculated. Five years ago, at the start of the work described in this thesis, far-infrared line astronomy was a virtually unknown area. Today, its viability has been conclusively proven. The entire field is opening up and a period of rapid development is about to be witnessed.

Chapter one concluded with an account of the development of infrared astronomy. The perennial problems of the subject were a lack of sensitive detectors and an excess of atmospheric absorption. In chapter two, the latter point was addressed by calculations of theoretical transmission and emission spectra of the terrestrial atmosphere at high resolving powers. A very simple one-layer, constant-temperature, constant-pressure atmospheric model was adopted. Molecular abundances were culled from the literature. Spectra were calculated for the residual atmosphere above three different balloon altitudes around the wavelengths of nine interesting astrophysical lines. The results showed firstly, that the atmosphere did not rule out detection of any of these lines and secondly, that the atmospheric emission, in general, decreased by a factor of x10 between altitudes of 30 km. and 40 km.

Comparison of the transmission spectra of chapter two with those obtained by other authors using more sophisticated models showed that, although the results are similar, the latter have lower transmission at the centres of the absorption features. Further work is necessary to determine the cause of this discrepancy. Possibilities include the molecular abundances adopted and the very simple nature of the model. Thus, the author recommends investigation of firstly, the sensitivity of the transmission to molecular abundances and secondly, the effects of replacing the Lorentz with a Voigt line profile.

The method used to calculate the emissivity of the atmosphere makes the emission spectra very dependent upon the accuracy of the model. In addition, the use of a constant temperature for the atmosphere is a worse approximation for emission rather than transmission spectra. Thus, the emission spectra must be critically examined. It is suggested that the model be re-run for wavelength regions where there is experimental data (e.g. Baluteau et al., 1977) and the two sets of results be compared.

In chapter three, several lines were chosen as candidates for study in the Imperial College Line Astronomy Programme. For the near-infrared instrument, the 12.8μm [NeII] line was selected in preference to the other two bright 10μm fine structure lines because of its proximity to the 12.3μm molecular hydrogen line. For the far-infrared lines, some theoretical work on estimating line intensities was examined. The later predictions were lower than the earlier and closer to the measured values. No molecular lines had been detected at this time and thus, no direct information was available on the reliability of the estimates. For a first flight with a new instrument, it is desirable to be searching for a line that is known to be present and therefore, it was decided not to look for a molecular line. Predictions of fine structure line intensities for HII regions and Planetary Nebulae were then examined in more detail, and the former seemed brighter than the latter. Eventually, it was decided to look for 88μm [OIII] emission from HII regions because this line is strong, very free from atmospheric confusion and technically feasible with the proposed instrumentation. For future work, however, molecular lines must be re-examined. The recently-detected molecules have very bright transitions and, in addition, are species that were not considered by the author in chapter three.

The rationale for choosing a Fabry-Pérot Spectrometer (F-P), with

which to attempt balloon-borne detections of far-infrared emission lines, was given in chapter four. After comparing and contrasting different spectroscopic techniques, the choice lay between the Michelson and Fabry-Pérot Interferometers. Both have a large resolution-luminosity product and the former can have a multiplex advantage. However, this was not considered sufficient to outweigh the disadvantages of the Michelson, namely, increased size and complexity and thus, it was decided to build a Fabry-Pérot Interferometer.

The standard theory of the F-P, complete with wavelength-dependent phase shifts, was presented before design criteria were discussed. A brief survey of previous F-P designs illustrated the wide diversity of approach. The chapter concluded with a brief description of the general design of the IC F-P. A novel form of a spring hinge arrangement is used with the gap being monitored by capacitance micrometry.

Design details specific to the near-infrared F-P were discussed at the start of chapter five. Most of the components of the interferometer were tested individually and all performed satisfactorily. Infrared tests of the entire instrument showed that it was working as a Fabry-Pérot with reasonable transmission and a finesse in excess of 15, compared to the expected value of around 20. The resolving power is limited to about 400 by the need to work in 25th order or less because of the order sorter. The F-P was taken to the 60" telescope on Tenerife on three occasions. Telluric absorption features were found and identified in spectra of Mars and the Moon. The 12.8μm [NeII] emission line from G29.9-0.0 was detected. It has, thus, been conclusively shown that this instrument is both ready and able to be used for astronomy.

However well an instrument is working, there are always further tests and modifications that can be made. This paragraph describes one measurement and one alteration that must, in the opinion of the author, be carried out before taking the F-P on another observing trip. Firstly, an obvious omission from the laboratory trials is a measurement of the instrumental profile of the F-P. The ideal way to obtain this information is to scan a laser line. However, this is difficult because of the shortage of suitable lasers in the wavelength region. The 10.6μm CO_2 laser is a possibility but, as shown in figure 5.15, the reflectivity of the F-P plates has fallen substantially by this wavelength. In the next few years, solid state diode lasers for the 10μm wavelength region may become generally available but until then, perhaps the most practical method of

measuring the instrumental profile of the F-P is to use a 'high' resolution grating spectrometer. The drawback of these instruments, as has been seen, is that the beam through the sample chamber is usually highly convergent. This degrades the apparent resolution of the F-P through its effect on the overall finesse. Nevertheless, it should not be too much of a problem to equip the grating instrument with ancillary optics so that a beam of any desired f/number may be passed through the interferometer. It is strongly recommended that this be done and the profile of the F-P be measured. Secondly, at present, the 'drift' in the capacitance micrometer is corrected by cross-calibration against the position of the drive micrometer. This is very inconvenient as reading the drive micrometer involves climbing onto the telescope as it is tracking a source. A magneto-resistive device, as used for the far-infrared instrument, should be installed on the 10μm version, and be used to cross-check the capacitance micrometer.

The next two paragraphs suggest firstly, some modifications to the current instrument and secondly, a few ideas for a completely rebuilt system. The next stage in the development of the present near-infrared F-P system is to improve its sensitivity and resolution. The former is now limited by the bolometer and the latter by the bandwidth of the order-sorting filter. A new 10μm photometer, incorporating a Si:As photoconductive detector, is under development in the laboratory. This system promises to be background noise limited even at very narrow spectral bandwidths and thus is ideal for use with the F-P. However, to take full advantage of the new detector, the photon shot noise from the interferometer and its ancillary optics must be reduced as much as possible. This may be done by cooling some or all of the components. If just the order-sorter were to be cooled to 77K, then a gain in sensitivity of x30 is expected by using the photoconductor. Unfortunately, cooling the order-sorting filter to liquid-nitrogen temperature shifts its passband towards shorter wavelengths by between 1% and 3% and might, therefore, make it unuseable for the neon line. If this is the case and a new order-sorting filter is needed, the opportunity ought to be taken to buy one with a narrower bandpass and, thereby, improve the resolving power of the system. The resolution of the F-P is limited to 1500 because it is operating in the converging telescope beam. It is possible to make a multi-layer, dielectric-coated interference filter at these wavelengths with a bandwidth narrow enough to allow the interferometer to be operated in high enough order to reach this value. Thus, by merely cooling a new

order-sorting filter and using a photoconductive detector, the sensitivity of the system can be increased by x30 and the resolution improvedto the maximum achievable in the present set-up.

If the entire system were to be rebuilt, it is envisaged that the telescope beam would be collimated for passage through the F-P to enable higher resolving powers to be reached. Depending on the chosen order sorter and photon shot noise considerations, the entire F-P may have to be cooled. Experience with the far-infrared F-P has shown that it is possible to operate a cryogenically-cooled F-P and, also, van der Wal and Slingerland (1979) have shown that dielectric-coated zinc selenide plates are useable at liquid nitrogen temperatures. It is recommended that a second or "finding and guiding" detector be added to the system. The order-sorting filter could be used as a dichroic, transmitting a very narrow spectral band to the F-P detector and reflecting the rest of the 10μm - 13μm (or even 1μm - 5μm!) radiation to the second detector.

Chapter six began with a detailed description of the design of a liquid-nitrogen-cooled far-infrared Fabry-Perot Interferometer, placing particular emphasis upon the differences between it and the 10μm instrument. The interferometer uses stretched, electroformed metal mesh for the etalon mirrors, which are also the capacitor for the gap-sensing electronics. A fixed-gap low-order F-P is the order-sorting filter. Additional filtering is provided by restrahlung reflections off potassium iodide crystals, which are housed in a new two-channel photometer. The second channel is used for a guide detector. The results of laboratory tests on the F-P and its sub-systems were discussed with close attention to their completeness. To the limit of the testing, the instrument was shown to be working well. During a balloon flight in 1979 December, the mechanical performance of the interferometer was adequate. Platform stabilisation problems prevented any optical testing of the F-P during the flight.

The far-infrared F-P has not yet been fully evaluated in the laboratory. This paragraph outlines some of the important tests that remain to be made. The interferometric alignment technique of section 6.2.2.d must be examined in detail to determine its reliability and accuracy. The parallelism of the etalon meshes needs to be measured, firstly as the F-P is cooled from room temperature to 77K and secondly, as the instrument is scanned. Most important of all, the resolution (and transmission)

of the interferometer are, at present, unknown. There are some far-infrared laser lines, e.g. Methyl alcohol at 119μm, across which the F-P could be scanned in order to determine its instrumental profile. However, if no laser is easily available, the far-infrared Fourier Transform Spectrometer (FTS) in the Analytical Services Laboratory at Imperial College could be used. Once again, auxiliary optics would be needed to overcome the problem of the converging beam. It would also be interesting to measure the performance of the F-P as a function of the periodicity of the grids used for the etalon. Lastly, but not least, the order-sorting F-P must be tuned to the correct wavelength and have its performance checked at liquid-helium temperatures. No doubt, this can also be done with the FTS and its ancillary optics.

From the experiences to date with the F-P, the need for several modifications has been seen. The guide detector appears to be receiving very little signal. This is due to two factors. Firstly, it is a very small detector and is over-filled by the Fabry lens and secondly, the four meshes of the F-P and order-sorter attenuate the radiation reaching the guide detector. In the absence of a larger detector, a simple solution to the first problem is to re-design the Fabry lens. The second problem is much more difficult to overcome because there is not enough room inside the present dewar to move either the F-P or the order-sorter or both out of the beam of the guide detector. Thus, it is desireable to consider moving to a bigger cryostat. If this is done, two further alterations ought to be made. Firstly, collimating optics should be added; this will improve both the resolution and the transmission of the F-P. Secondly, the parallelism adjusting screws, at present, face the liquid-helium surface. This means that the entire F-P has to be removed from the cryostat in order to align the grids parallel to each other. Operation of the instrument would be greatly simplified if it were to be 'inverted' so that the differential screws are accessible when the F-P is in position inside the dewar.

Looking further forward to possible future developments, several other points deserve mentioning. The sensitivity of the system will be increased when the Low bolometers, currently used, are replaced by gallium-doped germanium photoconductive detectors. The Imperial College Balloon Astronomy Group have recently purchased one of the latter, and laboratory testing of it will shortly be started. For wavelength calibration of the F-P in flight, a gas cell and a black body (cf. Storey, Watson and Townes, 1980) ought to be added to the payload. A flip-in mirror would allow the

F-P to view the black body through an absorption cell, containing a gas with absorption lines at known wavelengths.

The next point concerns the metal grids themselves. Chanin (private communication, 1979) says that metal mesh F-P's will be limited in resolution by the intrinsic irregularities of the grids themselves. He measures the thickness variation of the meshes as about 40%-50% of the mean thickness. Rousseau and Setton (1978) solve a similar problem by embedding metal grids in epoxy cement, polishing them flat and then dissolving away the glue. However, their grids are coarser and thicker than those used in this work and the polishing technique may not be applicable to the thinner grids. Another method of improving the flatness of the reflecting surfaces is to deposit a mesh onto an optically flat substrate. The author has briefly experimented in this field, using two different techniques. In each case an electroformed grid was used as a mask. The first technique was to deposit common salt onto the substrate through the mesh and then remove the mesh before depositing aluminium. When the substrate was washed in water, the aluminium on top of the salt came away, leaving the image of the original mesh. Figure 7.1(a) is a photograph of a 30 ℓ.p.i. grid deposited this way. The results are impressive but the presence of some little fillets of metal in the corners of the apertures shows that this technique is not useable for very fine grids. Thus, a second technique, using standard photo-lithographic methods, was tried. Figure 7.1(b) shows a 1000 ℓ.p.i. aluminium mesh deposited on crystal quartz in this way. These grids look very promising and it is strongly recommended that they be tried in an F-P as soon as possible.

Another possible future development would be to observe several lines simultaneously. The telescope beam could be passed through the main scanning F-P and then split up into different wavebands by restrahlung reflections (or other means, e.g. possibly the single mesh narrow-bandpass filters of Sakai and Yoshida, 1978). Each channel would contain an order-sorting F-P tuned to a particular line, and its own detector. An arrangement such as this would make extremely efficient use of observing time. This is essential for a balloon flight.

Infrared line astronomy is still a very new area of research but the wealth of information contained in these lines is certain to ensure continued growth of both interest and effort. It is hoped that the instrumental base, laid in this thesis, will contribute, in a small way, to

Figure 7.1

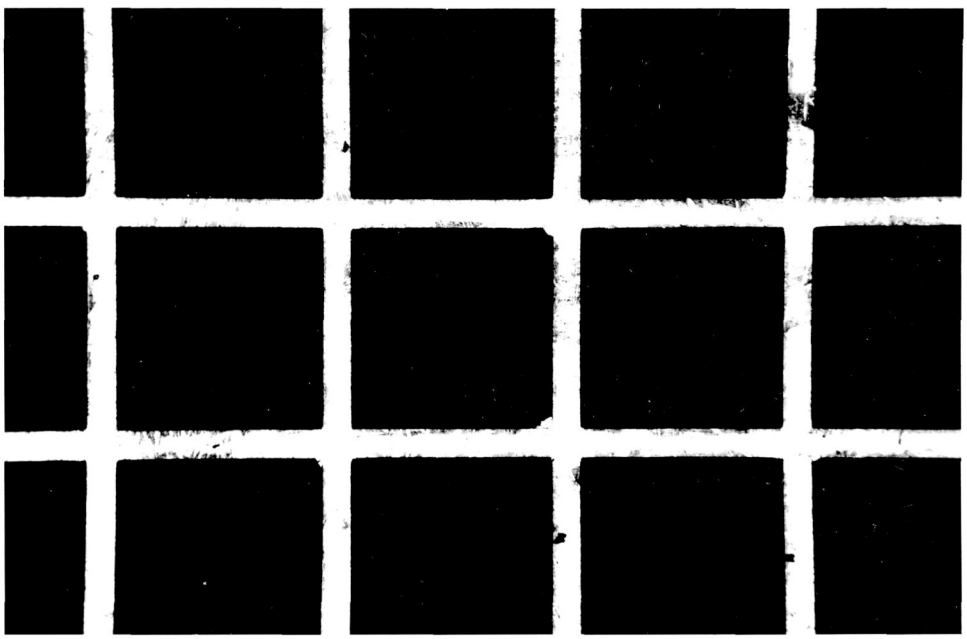

(a). 30 l.p.i. Using 'Salt' Technique.
(Prepared with the assistance of Mr. R.W. Airey).

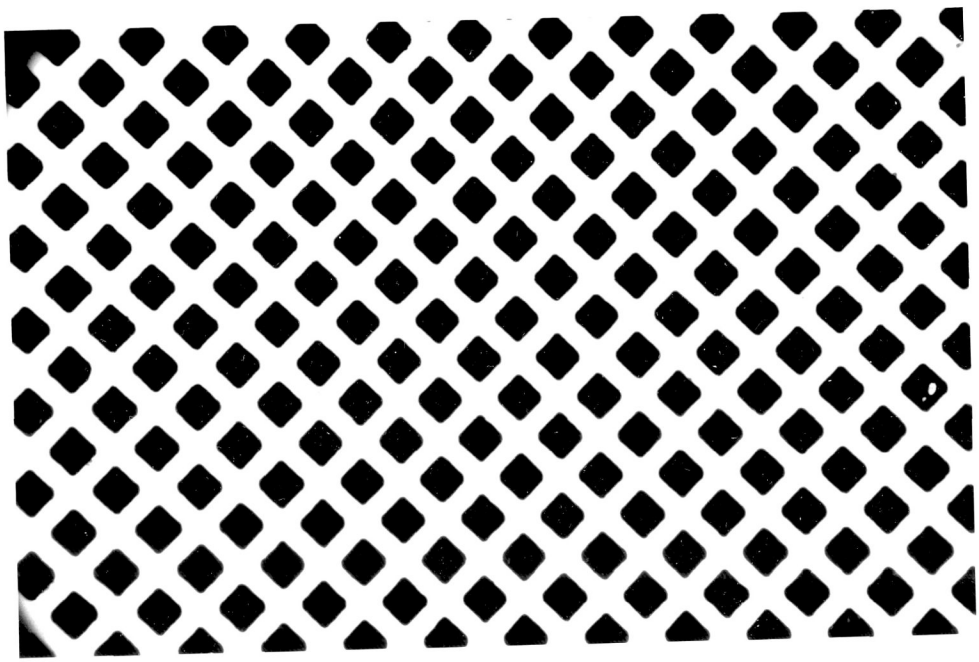

(b). 1000 l.p.i. Using Photolithographic Technique.
(Prepared by Dr. M.J.Lee).

Deposited Grids.

this process. The pioneering phase of astronomical infrared line studies is nearly over and the subject is rapidly becoming an established and productive branch of modern astrophysics.

THE END

References

Ackerman, M. & Muller, C., 1972. Proc. Joint Meeting of Amer.Geophys. Union and the Am.Meteorol.Soc. Aug.15-17. p.12-1.

Aitken, D.K. & Jones, B., 1973. Ap.J., 184, 127.

Allen, C.W., 1976. Astrophysical Quantities, 3rd Edition, Reprinted with Corrections, The Athlone Press, London.

Allen, D.A., 1975. Infrared, The New Astronomy, Keith Reid Ltd., Devon.

Alvarez, J.A., Jennings, R.E. & Moorwood, A.F.M., 1975. IR Phys., 15, 45.

Anderegg, M., Moorwood, A.F.M., Salinari, P., Furniss, I., Jennings, R.E., King, K.J., Towlson, W.A. & Venis, T.E., 1980. Astron.Astrophys., 82, 86.

Atherton, P.D., Hicks, T.R., Reay, N.K. & Wells, M., 1978. Proc. 4th Int. Coll.Astrophys., Trieste, 1978. p.573.

Andriesse, C.D., de Vries, J.S. & van der Waal, P.B., 1979. IR Phys., 19, 375.

Aumann, H.H., Gillespie, C.M. & Low, F.J., 1969. Ap.J., 157, L69.

Auth, D.C., 1969. Appl.Opt., 8, 1125.

Baluteau, J.P., Bussoletti, E., Anderegg, M., Moorwood, A.F.M. & Coron, N., 1976. Ap.J., 210, L45.

Baluteau, J.P., Marten, A., Bussoletti, E., Anderegg, M., Beckman, J.E., Moorwood, A.F.M. & Coron, N., 1977. IR Phys., 17, 283.

Baluteau, J.P., Moorwood, A.F.M., Biraud, Y., Coron, N., Anderegg, M. & Fitton, B., 1980. submitted to Ap.J.

Beck, S.C., Lacy, J.H., Baas, F. & Townes, C.H., 1978. Ap.J., 226, 545.

Beck, S.C., Lacy, J.H. & Geballe, T.R., 1979. Ap.J., 231, 28.

Beck, S.C., Lacy, J.H. & Geballe, T.R., 1979. Ap.J., 234, L213.

Beckwith, S., Persson, S.E. & Gatley, I., 1978a. Ap.J., 219, L33.

Beckwith, S., Persson, S.E., Neugebauer, G. & Becklin, E.E., 1978. Ap.J., 223, 464.

Beer, R., 1966. Nature, 209, 1226.

Beer, R. & Ring, J., 1961. IR Phys., 1, 94.

Bradley, D.J., 1962. J.Sci.Inst., 39, 41.

Bregman, J.D., 1978. P.A.S.P., 90, 548.

Burbidge, G.R., Gould, R.J. & Pottasch, S.R., 1963. Ap.J., 138, 945.

Bussoletti, E. & Stasinska, G., 1975. Astron.Astrophys., 39, 177.

Cameron, R.M., Bader, M. & Mobley, R.E., 1971. Appl.Opt., 10, 2011.

Campbell, M.F., 1979. SPIE, 172, Instrumentation in Astronomy III, 159.

Carruthers, G., 1970. Ap.J., 161, L81.

Chabbal, R., 1953. J.Rech.CNRS(Paris), 24, 138.

Chabbal, R., 1958. J.Phys.Rad., 19, 295.

Chabbal, R. & Soulet, M., 1958. J.Phys.Rad., 19, 274.

Chaloner, C.P., Farman, M.E. & Hardie, A.L., 1979. 8th IFAC Symp., Oxford. entitled, Automatic Control in Space.

Chanin, G. & Lecullier, J.C., 1978. IR Phys., 18, 589.

Churchwell, E., Mezger, P.G. & Huchtmeier, W., 1974. Astron.Astrophys., 32, 283.

Clarke, J.H.R., Norman, M.A. & Borsay, F.L., 1975. J.Phys.E., 8, 144.

Cosmovici, C.B., Inguscio, M., Strafella, F. & Strumia, F., 1979. Astro. Sp.Sci., 60, 475.

Cosmovici, C.B., Strafella, F. & Dirscherl, R., 1980. Ap.J., 236, 498.

Dain, F.W., Gull, G.E., Melnick, G., Harwit, M. & Ward, D.B., 1978. Ap.J., 221, L17.

Dalgarno, A., de Jong, T., Oppenheimer, M. & Black, J.H., 1974. Ap.J., 192, L37.

Dalgarno, A. & Wright, E.L., 1972. Ap.J., 174, L49.

Daneu, V., Maxson, C., Peres, G., Serio, S. & Vaiana, G., 1978. Proc. of NATO Advanced Study Institute, Erice, Sicily. Series C, vol.38, p.335. Dordrecht.

Delmer, T.N., Gould, R.J. & Ramsay, W., 1967. Ap.J., 149, 495.

Drapatz, S., 1980. 5th ESA Symp. on European Rocket & Balloon Programmes and Related Research. ESA SP-152.

Drapatz, S. & Michel, K.W., 1974. Astron.Astrophys. 36, 211.

Eddy, J.A., Lena, P.J. & MacQueen, R.M., 1969. Solar Phys., 10, 330.

Ehhalt, D.H., 1974. Can.J.Chem., 52, 1510.

Eisberg, R.M., 1961. Fundamentals of Modern Physics, J.Wiley & Sons Ltd.

Erickson, E.F., Caroff, L.J., Simpson, J.P., Strecker, D.W. & Goorvitch, D., 1977. Ap.J., 216, 404.

Fabry, C. & Pérot, A., 1899. Annal.Chim.Phys., 16, 115.

Farmer, C.B., 1974. Can.J.Chem., 52, 1544.

Fazio, G.G., Kleinmann, D.E., Noyes, R.W., Wright, E.L., Zeilik, M. & Low, F.J., 1974. Proc. 8th Eslab Symp. ed. A.F.M. Moorwood. ESRO SP-105, p.79.

Fellgett, P.B., 1951. M.N.R.A.S., 111, 537.

Fellgett, P.B., 1951. Ph.D.Thesis, Univ. of Cambridge.

Flower, D.R., 1968. Astrophys.Lett., 2, 205.

Flower, D.R., 1969. M.N.R.A.S., 146, 171.

Flower, D.R., 1970. M.N.R.A.S., 147, 245.

Forrest, W.J., McCarthy, J.F. and Houck, J.R., 1980. Ap.J., in press.

Friedlander, M.W., Goebel, J.H. & Joseph, R.D., 1974. Ap.J., 194, L5.

Furniss, I., Jennings, R.E. & Moorwood, A.F.M., 1972. Ap.J., 176, L105.

Gautier, T.N., Fink, U., Treffers, R.P. & Larson, H.P., 1976. Ap.J., 207, L129.

Geake, J.E., Ring, J. & Woolf, N.J., 1959. M.N.R.A.S., 119, 616.

Geake, J.E. & Wilcock, W.L, 1957. M.N.R.A.S, 117, 380.

Geballe, T.R. & Rank, D.M., 1973. Ap.J., 182, L113.

Gillett, F.C., Kleinmann, D.E., Wright, E.L. & Capps, R.W., 1975. Ap.J., 198, L65.

Gillett, F.C., Merrill, K.M. & Stein, W.A., 1972. Ap.J. 172, 367.

Gillett, F.C. & Stein, W.A., 1969. Ap.J., 155, L97.

Goldman, A., Murcray, D.G., Murcray, F.H. & Williams, W.J., 1973. J.Opt.Soc., 63, 843.

Goldman, A., Murcray, D.G., Murcray, F.H., Williams, W.J., Kyle, T.G. & Brooks, J.N., 1970. J.Opt.Soc., 60, 1466.

Greenberg, L.T., Dyal, P. & Geballe, T.R., 1977. Ap.J., 213, L71.

Greenler, R.G., 1958. J.Phys.Rad., 19, 375.

Hadni, A., 1967. Essentials of Modern Physics Applied to the Study of the Infrared. Pergamon Press.

Hadni, A., Claudel, J., Morlot, G. & Strimer,P., 1968. Appl.Opt., 7, 161.

Harper, D.A. & Low, F.J., 1973. Ap.J., 182, L89.

Harries, J.E., 1973. Nature, 241, 515.

Harwit, M., 1973. Astrophysical Concepts. J.Wiley & Sons.

Herschel, W., 1800. Phil.Trans.Roy.Soc.London, 90, 255, 284, 293, 437.

Herzberg, G., 1971. The Spectra and Structure of Simple Free Radicals. An Introduction to Molecular Spectroscopy. Cornell University Press.

Hicks, T.R., Reay, N.K. & Scaddan, R.J., 1974. J.Phys.E., 7, 27.

Hill, J.K. & Hollenbach, D.J., 1978. Ap.J., 225, 390.

Hoffmann, W.F. & Frederick, C.L., 1969. Ap.J., 155, L9.

Hoffmann, W.F., Frederick, C.L. & Emery, R.J., 1971a. Ap.J., 164, L23.

Hoffmann, W.F., Frederick, C.L. & Emery, R.J., 1971b. Ap.J., 170, L89.

Hoffmann, W.F., Woolf, N.J. & Frederick, C.L., 1967. Science, 157, 187.

Hoffmann, R., Drapatz, S. & Michel, K.W., 1977. IR Phys., 17, 451.

Holtz, J.Z., Geballe, T.R. & Rank, D.M., 1971. Ap.J., 164, L29.

Houck, J.R., Soifer, B.T., Harwit, M. & Pipher, J.L., 1972. Ap.J., 178, L29.

Houck, J.R. & Ward, D.B., 1979. P.A.S.P., 91, 140.

Jacquinot, P., 1954. J.Opt.Soc.Am., 44, 761.

Jacquinot, P., 1960. Rep.Prog.Phys., 23, 267.

Johnson, H.L., 1962. Ap.J., 135, 69.

Johnson, H.L., 1964. Ap.J., 139, 1022.

Johnson, H.L., Low, F.J. & Steinmetz, D., 1965. Ap.J., 142, 808.

Johnson, H.L. & Mitchell, R.I., 1963. Ap.J., 138, 303.

de Jong, T., 1974. Centre for Astrophysics, p.print no.253.

Jones, R.V., 1951. J.Sci.Instr., 28, 38.

Jones, R.V., 1962. J.Sci.Instr., 39, 193.

Jones, R.V. & Richards, J.C.S., 1973. J.Phys.E:Sci.Inst., 6, 589.

Jones, R.V. & Young, I.R., 1956. J.Sci.Instr., 33, 11.

Joseph, R.D., Allen, J., Meikle, W.P.S., Sugden, K.C., Kessler, M.F., Rosen, D.L. & Masson, G., 1977. Opt.Eng., 16, 558.

Joyce, R.R., Gezari, D.Y., Scoville, N.Z. & Furenlid, I., 1978. Ap.J., 219, L29.

Joyce, R.R., Gezari, D.Y. & Simon, M., 1972. Ap.J., 171, L67.

Kuhn, H.G., 1962. Atomic Spectra, Longmans, London.

Kyle, T.G. & Goldman, A., 1975. Atlas of Computed Infrared Atmospheric Absorption Spectra. NCAR-TN/STR-112.

Lecullier, J.C. & Chanin, G., 1976. IR Phys., 16, 273.

Lester, D.F., Dinerstein, H.L. & Rank, D.M., 1979. Ap.J., 232, 139.

Lindsay, S.M. & Shepherd, I.W., 1977. J.Phys.E., 10, 150.

Longhurst, R.S., 1967. Geometrical and Physical Optics, Longmans.

Low, F.J., 1961. J.Opt.Soc.Am., 51, 1300..

Low, F.J. & Aumann, H.H., 1970. Ap.J., 162, L79.

Low, F.J. Aumann, H.H. & Gillespie, C.M., 1970. Astronautics & Aeronautics, 7, 26.

Low, F.J. & Rieke, G.H., 1974. Methods of Experimental Physics, vol.12A, ch.9. The Instrumentation and Techniques of Infrared Photometry. ed. N. Carleton, Academic Press, London.

Low, F.J., Rieke, G.H. & Armstrong, K.R., 1973. Ap.J., 183, L105.

Lowe, R.P. & McKinnon, D., 1972. Can.J.Phys., 50, 60.

McCarthy, J.F., Forrest, W.J. & Houck, J.R., 1979. Ap.J., 231, 711.

McClatchey, R.A., Benedict, W.S., Clough, S.A., Burch, D.E., Calfee, R.F., Fox, K., Rothman, L.S. & Garing, J.S., 1973. AFCRL Atmospheric Absorption Line Parameters Compilation. AFCRL-TR-73-0096.

McKellar, A., 1941. Publ.Dominion Astrophys.Observ., Victoria, BC. No.15, 7, 251.

Martin, D.H. & Puplett, E., 1969. IR Phys., 10, 105.

Mather, J.C., Richards, P.L. & Woody, D.P., 1974. IEEE Trans.Microwave Theory Tech., 22, 1046.

Melnick, G., Gull, G.E. & Harwit, M., 1979a. Ap.J., 227, L29.

Melnick, G., Gull, G.E. & Harwit, M., 1979b. Ap.J., 227, L35.

Melnick, G., Gull, G.E., Harwit, M. & Ward, D.B., 1978. Ap.J., 222, L137.

Melnick, G., Russell, R.W., Gull, G.E. & Harwit, M., 1980. B.A.A.S., 11, 627.

Moorwood, A.F.M., Baluteau, J.P., Anderegg, M., Coron, N. & Biraud, Y., 1978. Ap.J., 224, 101.

Moorwood, A.F.M., Baluteau, J.P., Anderegg, M., Coron, N, Biraud, Y. & Fitton, B., 1980. Ap.J., 238, 565.

Moorwood, A.F.M., Salinari, P., Furniss, I., Jennings, R.E. & King, K.J., 1980b. submitted to Astron.Astrophys.

Murray, B.C. & Wildey, R.L., 1963. Ap.J., 137, 692.

Osterbrock, D.E., 1974. Astrophysics of Gaseous Nebulae, W.H. Freeman.

Petrosian, V., 1970. Ap.J., 159, 833.

Pettit, E. & Nicholson, S.B., 1930. Ap.J., 71, 102.

Pipher, J.L., Sharpless, S., Savedoff, M.P., Krassner, J., Varlese, S., Soifer, B.T. & Zeilik, M., 1977. Astron.Astrophys., 59, 215.

Pottasch, S.R., 1968. Bull.Astr.Inst.Neth., 19, 469.

Pottasch, S.R., 1973. Astron.Astrophys., 24, 305.

Ramsay, J.V., 1962. Appl.Opt., 1, 411.

Renk, K.F. & Genzel, L., 1962. Appl.Opt., 1, 643.

Richards, P.L., 1964. J.Opt.Soc.Am., 54, 1474.

Robson, E.I., Vickers, D.G., Huizinga, J.S., Beckman, J.E. & Clegg, P.E., 1974. Nature, 251, 591.

Roche, A.E., 1976. SPIE, 95, Modern Utilisation of IR Tech. II, p.196.

Roig, J., 1958. J.Phys.Rad., 19, 284.

Rosen, D.L., 1981. Ph.D.Thesis, London University, in preparation.

Rousseau, B. & Setton, R., 1978. Rev.Sci.Instrum., 49, 335.

Roychoudhuri, C. & Hercher, M., 1977. Appl.Opt., 16, 2514.

Russell, R.W., Melnick, G., Gull, G.E. & Harwit, M., 1980. Ap.J., 240, L99.

Sakai, K. & Yoshida, T., 1978. IR Phys., 18, 137.

Schild, R.E., 1977. Astron.J., 82, 337.

Schütz, K., Junge, C., Beck, R. & Albrecht, B., 1970. J.Geophys.Res., 75, 2230.

Selby, M.J., Jorden, P.R. & MacGregor, A.D., 1976. IR Phys., 16, 317.

Shepherd, G.G., 1960. Can.J.Phys., 38, 1560.

Simpson, J.P., 1973. P.A.S.P., 85, 479.

Simpson, J.P., 1975. Astron.Astrophys., 39, 43.

Slater, P.N., Betz, H.T. & Henderson, G., 1965. Jap.J.Appl.Phys., 4, Supp.I, 440.

Smith, R.A. Jones, F.E. & Chasmar, R.P., 1968. The Detection and Measurement of Infrared Radiation, 2nd Edition, Clarendon Press, Oxford.

Smyth, C. Piazzi, 1859. Phil.Trans.Roy.Soc.Lon., 148, 465.

Soifer, B.T. & Pipher, J.L., 1975. Ap.J., 199, 663.

Storey, J.W.V., Watson, D.M. & Townes, C.H., 1979. Ap.J., 233, 109.

Storey, J.W.V., Watson, D.M. & Townes, C.H., 1980. Int.J.IR.Mm.Waves, 1, 15.

Storey, J.W.V., Watson, D.M. & Townes, C.H., 1980a. submitted to Ap.J.

Strong, J., Neher, H.V., Whitford, A.E., Cartwright, C.H. & Hayward, R., 1938. Procedures in Experimental Physics, Prentice-Hall, New York.

Sugden, K.C., 1978. Ph.D. Thesis, London University.

Tai, M.H. & Harwit, M., 1976. Appl.Opt., 15, 2664.

Telesco, C.M. & Harper, D.A., 1977. Ap.J., 211, 475.

Telesco, C.M., Harper, D.A. & Loewenstein, R.F., 1976. Ap.J., 203, L53.

Terhune, R.W. & Peters, C.W., 1961. J.Opt.Soc.Am., 51, 530.

Thomas, J.A., Hyland, A.R. & Robinson, G., 1973. M.N.R.A.S., 165, 201.

Thompson, R.I., Lebofsky, M.J. & Rieke, G.H., 1978. Ap.J., 222, L49.

Thorne, A.P., 1974. Spectrophysics, Chapman & Hall & Science Paperbacks.

Traub, W.A. & Stier, M.T., 1976. Appl.Opt., 15, 364.

Treffers, R.R., 1977. Appl.Opt., 16, 3103.

Treves, A., Chiappetti, L., Tanzi, E.G., Tarenghi, M., Gursky, H., Dupree, A.K., Hartmann, L.W., Raymond, J., Davis, R.J., Black, J., Matilsky, T.A., Vanden Bout, P., Sanner, F., Pollard, G., Sanford, P.W., Joseph, R.D. & Meikle, W.P.S., 1980. Ap.J., in press.

U.S. Standard Atmosphere, 1962. U.S. Government Printing Office, Washington DC.

U.S. Standard Atmosphere Supplements, 1966. U.S. Government Printing Office, Washington DC.

Vogel, P. & Genzel, L., 1964. IR Phys., 4, 257.

van der Waal, P.B. & Slingerland, J., 1979. Appl.Opt., 18, 641.

Ward, D.B., Dennison, B., Gull, G. & Harwit, M., 1975. Ap.J., 202, L31.

Watson, D.M. & Storey, J.W.V., 1980. Int.J.IR.Mm.Waves, in press.

Watson, D.M., Storey, J.W.V., Townes, C.H. & Haller, E.E., 1980b. Ap.J. preprint.

Watson, D.M., Storey, J.W.V., Townes, C.H. & Haller, E.E., 1980c. In preparation.

Watson, D.M., Storey, J.W.V., Townes, C.H., Haller, E.E. & Hansen, W.L., 1980a. Ap.J. preprint.

Werner, M.W., Becklin, E.E., Gatley, I., Ellis, M.J., Hyland, A.R., Robinson, G. & Thomas, J.A., 1978. M.N.R.A.S., 184, 365.

Wesselink, A.J., 1948. Bull.Astron.Inst.Netherlands, 10, 351.

Wijnbergen, J., Moolenaar, W. & de Groot, G., 1972. Infrared Detection

Techniques for Space Research, ed. Manno, V. & Ring, J., D. Reidel Publishing Co.

Williamson, K.D., Blair, A.G., Catlin, L.L., Hiebert, R.D., Loyd, E.G. & Romero, H.V, 1973. Nature Physical Science, 241, 79.

Willis, A.J., Wilson, R., Vanden Bout, P., Sanner, F., Black, J., Davis, R.J., Dupree, A.K., Gursky, H., Hartmann, L., Raymond, J., Matilsky, T., Burger, M., de Loore, C., van Dessel, E.L., Whitelock, P., Menzies, J., Meikle, W.P.S., Joseph, R.D., Sandford, P., Pollard, G. & Sandford, M.C.M., 1980. Ap.J., 237, 596.

Willner, S.P., 1977. Ap.J., 214, 706.

Willner, S.P., Soifer, B.T., Russell, R.W., Joyce, R.R. & Gillett, F.C., 1977. Ap.J., 217, L121.

Wollman, E.R., Geballe, T.R., Lacy, J.H., Townes, C.H. & Rank, D.M., 1976. Ap.J., 205, L5.

Wollman, E.R., Geballe, T.R., Lacy, J.H., Townes, C.H. & Rank, D.M., 1977. Ap.J., 218, L103.

Woody, D.P. & Richards, P.L., 1979. Phys.Rev.Lett., 42, 925.

Yen, V.L., 1969. Optical Spectra, 3, no.3, 78.

Zeilik, M., 1977. Ap.J., 218, 118.

Appendix A

Tertiary Mirror Chopper

The development and test programme of a focal-plane chopper for the IC balloon telescope is described in this appendix.

A.1 Introduction

Chopping may be accomplished in many different ways. Two methods were considered in some detail for the IC Telescope. Firstly, the secondary mirror may be rocked to-and-fro and secondly, an additional mirror in the focal plane may be moved. Although it requires a third mirror, tertiary chopping was eventually chosen in preference to wobbling the large (13.6 diameter) and heavy (6 kg) secondary mirror. To minimise the movement of the telescope beam across the primary mirror, parallel, rather than angular motion of the chopper flat is used, even though this causes some defocussingin the focal plane. In addition to the normal chopper design criteria of amplitude (and frequency) stability and freedom from microphony, a balloon instrument must have exceptional reliability, low power consumption and be undisturbed by changes in ambient temperature and pressure. After consideration of several other ideas, an electro-mechanically-resonant design, based upon a parallel spring movement, was adopted. This design is outlined in the following two sections.

A.2 Parallel Spring Movements

A parallel spring movement (figure A.1(a) consists of two identical, flat, rectangular springs, A and A^1, held parallel to each other and clamped to opposite sides of two rectangular blocks, B and P. If the base, B, is secured, the application of a force, F, to the platform, P, causes the latter to move sideways, whilst remaining parallel to B, (see figure A.1(b)(i)). It should be noted that the motion, although parallel, is not rectilinear because P drops towards B. Measurements of the parallelism of the motion of this and similar arrangements are reported by Jones (1951). In addition to the desired S-bending of the springs, there may also be some cantilevering, (figure A.1(b)(ii)), which can be minimised (Jones and Young, 1956) by driving at the centre of the free length of the springs (figure A.1(b)(iii)). The same authors also discuss design and constructional criteria for maximising the parallelism of the motion.

Figure A.1

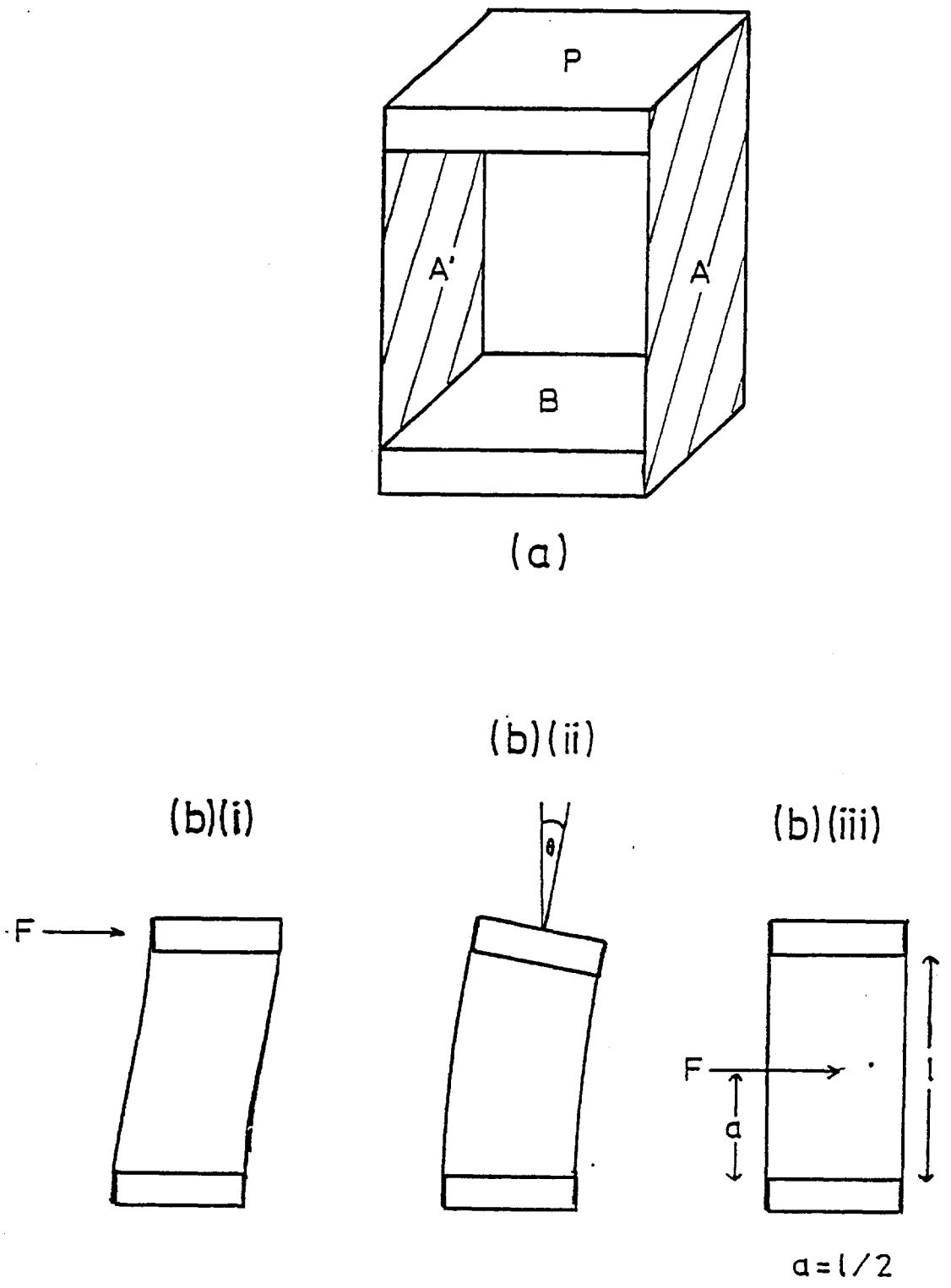

Parallel Spring Movements.

A.3 Design of Tertiary Chopper

To make the most efficient use of observing time, two detectors are used and the celestial source is chopped from one to the other. Behind the primary mirror, the beam is turned through 90^{o} into the dewar with the flat tertiary chopper mirror. To achieve the desired chop, it is necessary to move the flat nearly 5mm along its axis while keeping it parallel to its original position. This is accomplished using the design shown in figure A.2 (taken from Joseph et al, 1977, cf. Appendix C).

In order to reduce the vibration transferred to the telescope structure (microphonics), momentum must be conserved internally. In the y-direction (figure A.2), this is done by driving two identical mirror carriages against each other in antiphase. Due to the non-rectilinearity of the device, the platforms also move in the x-direction. However, this motion is very small compared to that in the other direction and so no attempt is made to balance the chopper in this plane. The mirrors used are diamond-turned aluminium (Heliotrope Ltd.) with a thin gold coating. They are kinematically mounted in their weight-relieved cells. The system is made electromechanically resonant by using a drive signal derived from the motion of one of the carriages. This movement is monitored by a magnet, fixed to the mirror cell, moving across a magneto-resistive sensor. The electronics were designed and built by Mr J. Allen and are shown in block diagrammatic form in figure A.3. The coil and drive magnet are both mounted on rigid extensions to the mirror carriages, so that the force acts at the centre of the springs, thereby maximising the parallelism of the motion.

A.4 Performance Trials

The natural frequency, f_o, of the mirror assemblies was adjusted semi-empirically to the desired range of 10 Hz - 20 Hz by altering the thickness, t, of the springs. This is not a particularly sensitive method because f_o is a strong function of t ($f_o \propto t^{3/2}$) and also shim stock only comes in standard gauges. For fine frequency tuning, additional mass is added to the carriage. This adjustment is not easy because the resonant frequency is not only sensitive to the total mass but also to its distribution.

The major problem with the chopper was that changes in either

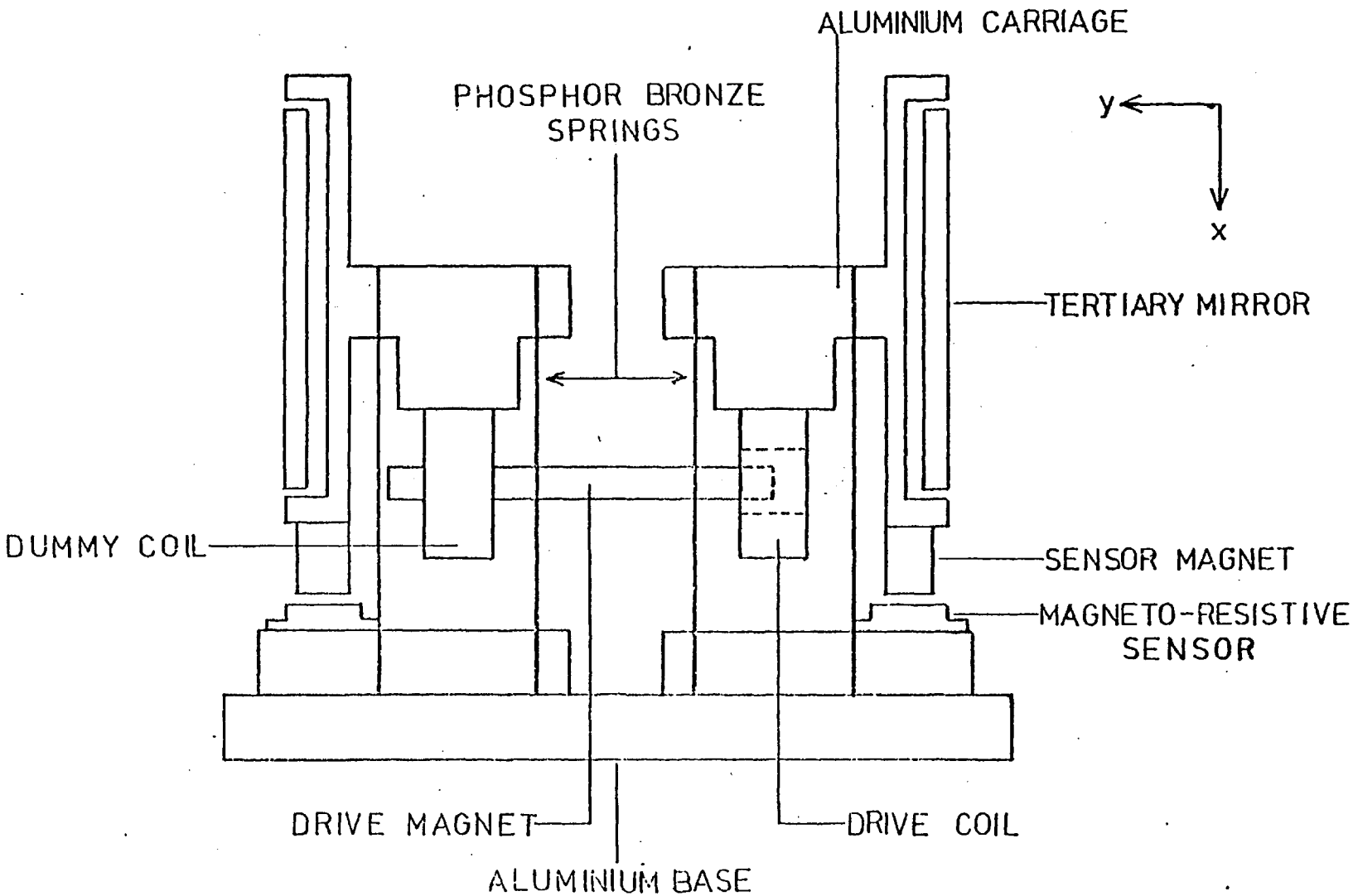

The Tertiary Chopper.

Figure A.2

Figure A.3

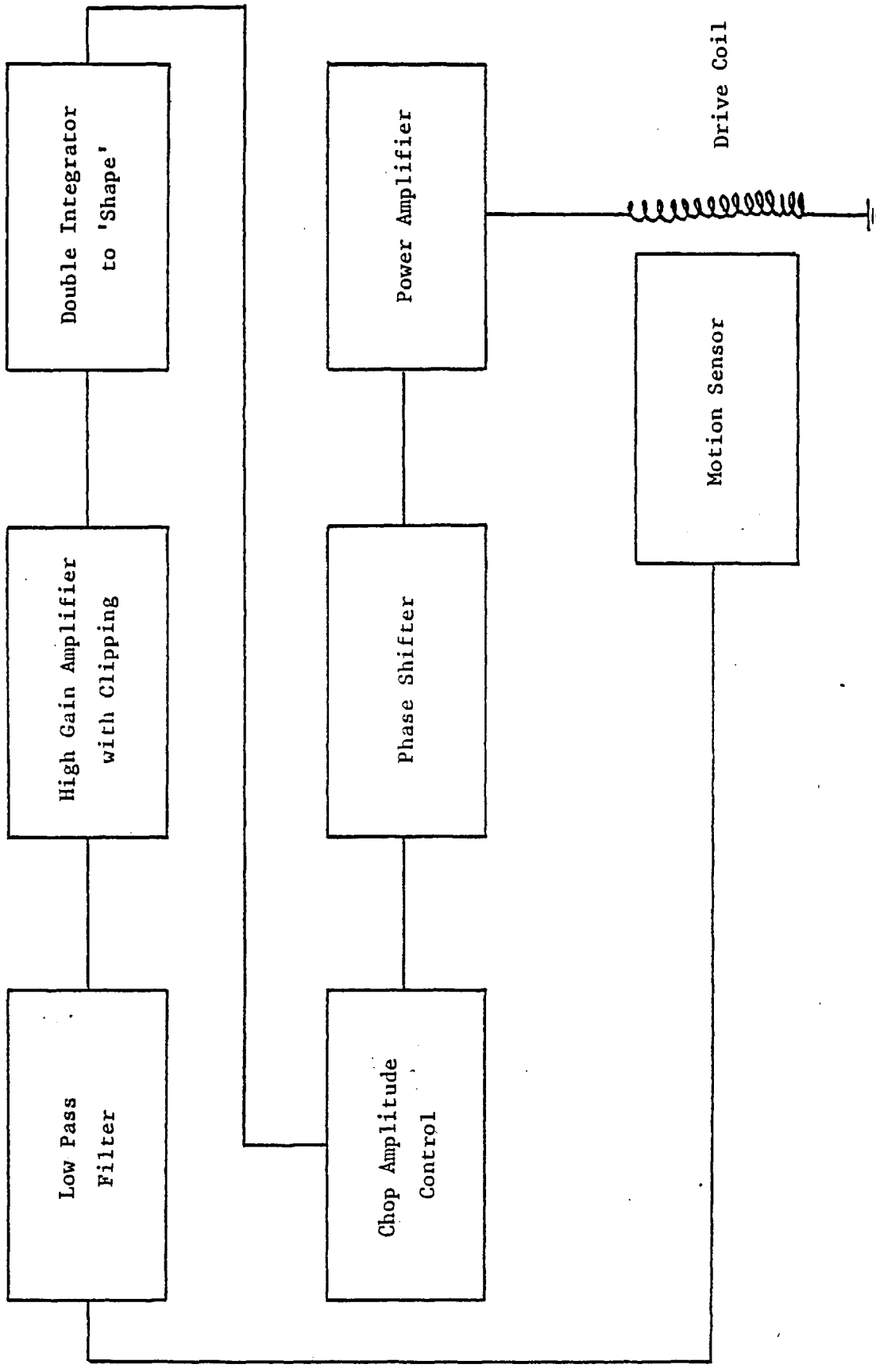

Block Diagram of Tertiary Chopper Electronics.

orientation or coupling to its surroundings could cause the two carriages, whose amplitudes had previously been stable and equal, to go into either a beating or a stable-but-unequal amplitude mode. This was assumed to be caused by variations in the 'amount' and phase of the energy being coupled from one carriage to the other; the carriages having different resonant frequencies and Q-curves sharp enough to permit the system to operate on either peak or to beat between them. Accurate measurements of the individual natural frequencies and of the Q for the phosphor-bronze springs showed that the resonant frequencies were separated by more than the FWHM of the Q-curve. Two approaches were used to improve the chopper performance. Firstly, attempts were made to reduce Q and secondly, different couplings between the two carriage-spring assemblies were tried.

To attempt to widen the resonance curves, springs of materials with higher damping capacities were used. The results of this are as follows: Phosphor bronze, Q $\sim$ 330, Mild steel, $\sim$ 180; Aluminium, $\sim$ 100. However, the aluminium springs fatigue and break after 2 hrs - 4 hrs of operation. The mild steel springs also suffer from fatigue and, in addition, show no improvement in amplitude stability over the phosphor bronze ones. Thus, it was decided to retain the latter and to investigate dissipative methods of spoiling Q. Frictional damping - with a lever spring on one carriage, pressing down on a pad on the other - reduces the sensitivity to beating but does not eliminate the problem. It also leads to long-term amplitude fluctuations due to uneven wear in the pad. The Q of the system can be reduced to 200 by using electrical damping. In summary, methods of spoiling Q do not solve the problem and so the second approach was adopted.

On a totally empirical basis, many different mechanical arrangements were tried in order to control the coupling between the two carriages. The best results occur when the chopper is clamped at the centre of its base between two pieces of silicone rubber and the entire assembly insulated from the telescope structure with another piece of rubber. With this configuration, the amplitude is stable to one part in 300 and although there are still changes in amplitude with orientation, it was decided to fly the chopper in this form with no damping. Figure A.4 shows the chopper in position alongside the dewar.

Other mechanical trials of the chopper include parallelism checks, together with vacuum and thermal runs. The parallelism of the motion is

Figure A.4

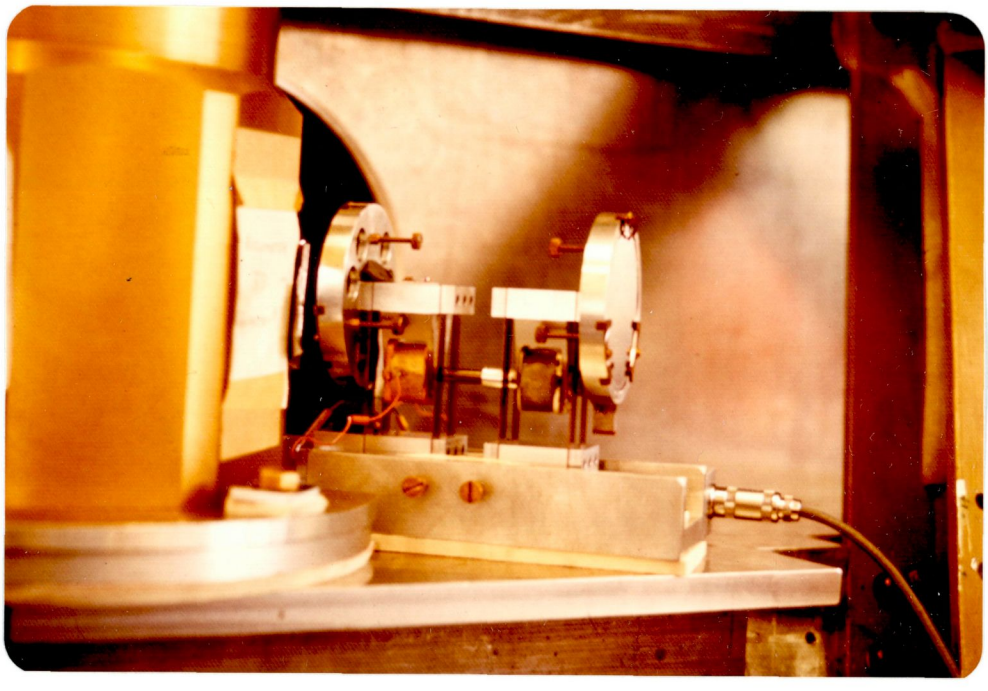

The Tertiary Chopper and Dewar Ready for Flight.

adequate; the tilt is less than $10''$ for a chop amplitude of $3'$. Vacuum tests show that the frequency change is less than 1% for a drop in pressure from 760 torr to 2 torr. In thermal tests between $-70^{o}C$ and $+20^{o}C$, the change in frequency was < 3% and the total change in Q was about 10%. The change in Q shows no systematic trend with temperature and so it is likely that this is due to other effects e.g. varying amounts of ice on the chopper etc.

The figure of the aluminium mirrors was investigated by the author with a Twyman-Green Interferometer. This work is reported in detail in Sugden (1978). All of the mirrors have a saddle-shaped surface. The best has a centre-to-edge flatness error of about 1μm. An interference microscope was used to examine the surface microstructure. Turning marks show up as thin lines across the main fringes and are about $\lambda_{vis}/20$ wide.

A.5 Conclusions

The abject failure of the Marconi Stabilised Balloon Platform in two flights in 1976 prevented full flight trials of the chopper. Nevertheless, the available data show adequate performance to the limit of the testing (Joseph et al, 1977; Sugden, 1978).

The chopper has two major disadvantages, which are common to all resonant systems. Firstly, it suffers a static deflection under its own weight. This deflection alters with telescope elevation and roll, thus causing a slow change in instrumental offset. To eliminate the effect of elevation upon static deflection requires only a small design change, namely, rotating the chopper through 45^{o} so that its direction of vibration is parallel to the elevation axis. The chopper mirror would also have to be turned through 45^{o} with respect to the direction of motion. Static deflection may be entirely prevented by coupling the carriages together and driving against a fixed point. Secondly, the amplitude of the oscillation is very easily perturbed. These amplitude fluctuations cause changes in the chopped offset, which increases the system noise. A technique has been developed for another resonant chopper (Rosen, 1981), that reduces this noise to below detector noise, by monitoring the amplitude fluctuations and adding them in anti-phase to the signal.

To conclude, it has been shown that with a quiet and stable balloon platform and the use of the above bucking system, the tertiary mirror chopper is useable for the IC photometry programme.

A.6 Postscript

A secondary mirror chopper was built for the second flight campaign in 1979. This was done for the following reasons. Firstly, two dewars were to be flown and it is not easy to fit two cryostats, a beam-switching mirror and a tertiary chopper behind the primary mirror. Secondly, the instrumentation for a third campaign may include a polarimeter, and this cannot tolerate reflections off plane surfaces. Thirdly, a secondary mirror chopper does not defocus across a chop.

A.7 References

Jones, R.V., 1951. J. Sci. Instr., 28, 38.

Jones, R.V. & Young, I.R., 1956. J. Sci. Instr., 33, 11.

Joseph, R.D., Allen, J., Meikle, W.P.S., Sugden, K.C., Kessler, M.F., Rosen, D.L. & Masson, G., 1977. Opt. Eng., 16, 558.

Rosen, D.L., 1981. Ph.D. Thesis, London University, in preparation.

Sugden, K.C., 1978. Ph.D. Thesis, London University.

Appendix B

J H K L M Observations of Nova Cygni 1978

This appendix presents some 1μm - 5μm spectrophotometric observations of Nova Cygni 1978 that were made in the period 16-28 October 1978. The instrumentation, observational procedure and data reduction are described and the results are briefly discussed. Further interpretative work on this data and the more extensive observations reported by Gehrz et al. (1980a) is still in progress.

B.1 Introduction

As mentioned in section 5.3.1, no liquid helium was delivered to the Infrared Flux Collector (IRFC) in Tenerife until the last night of the October 1978 observing trip. Thus, it was impossible to carry out any of the planned 10μm programmes and so observations were made between 1μm and 5μm using a liquid-nitrogen-cooled photovoltaic detector belonging to Dr M.J. Selby and resident in Tenerife.

All necessary finding charts for Nova Cygni 1978 were prepared before leaving London because it was planned to observe the early spectral development of the nova with the 10μm F-P. The interest in this nova arose from the suggestion by Ferland and Shields (1978) that the weak 10μm excess in the late development of Nova Cygni 1975 (Ennis et al., 1977) might be due to fine structure [NeII] emission.

B.2 Instrumentation

The Cabezon Observatory of the University of La Laguna, Tenerife is at an altitude of 2400m and a position of $28^{o}17'32''$ latitude and $1^{h}05^{m}48^{s}.1$ longitude. The IRFC is the largest telescope on the site and, for these observations, the f/13.6 Cassegrain focus was used. A cast aluminium cage is attached underneath the primary mirror. The telescope beam is turned through 180^{o} by a two-mirror chopper (a modified version of that described by Jorden et al., 1976), mounted on the base of the cage, and channeled into a bottom-entry cryostat (figure B.1). The liquid-nitrogen dewar contains an Indium Antimonide photovoltaic detector with two switchable load resistors and a filter wheel containing five filters and a blank. Table B.1 lists the passbands of these filters.

Figure B.1

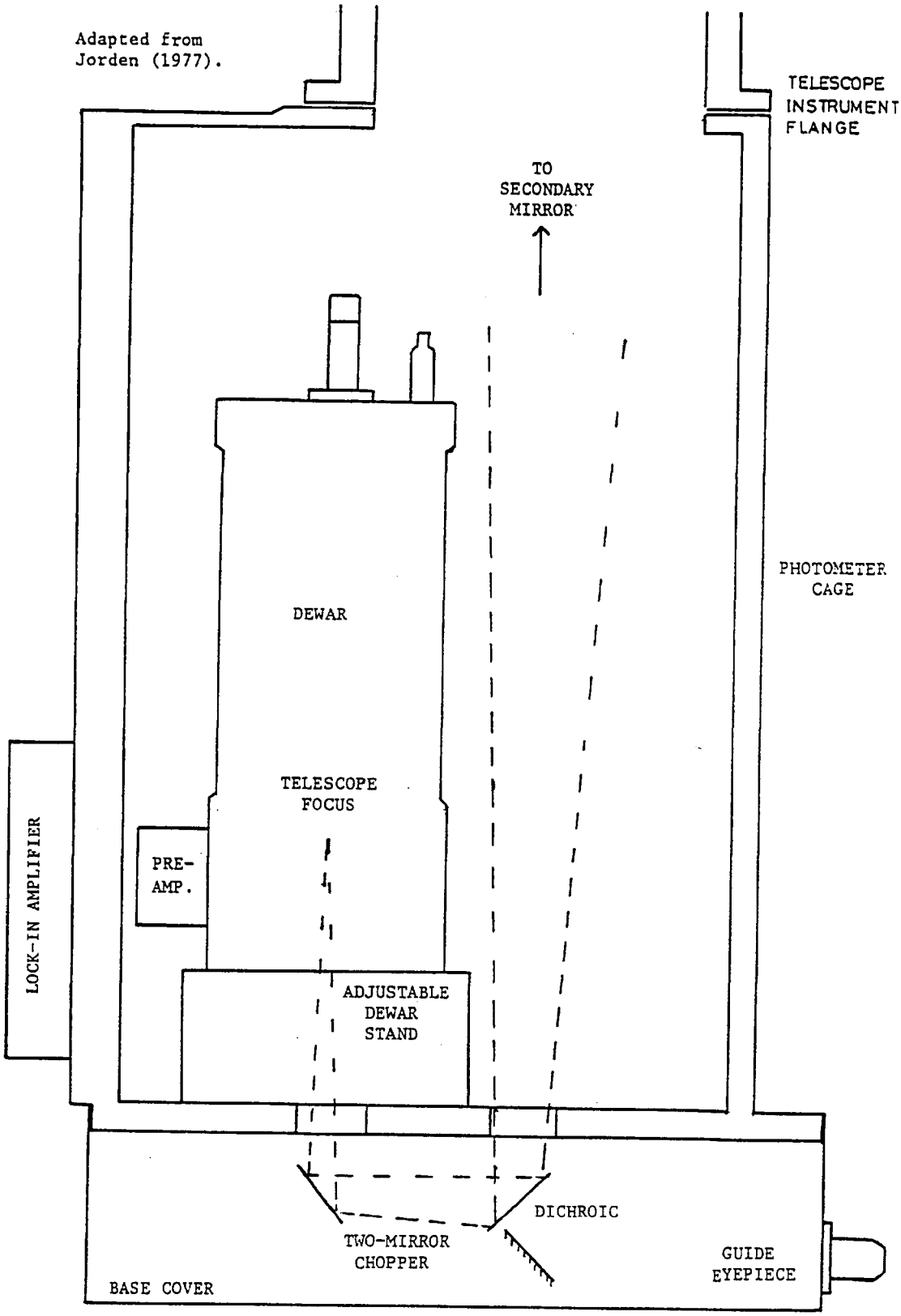

Tenerife Photometry Set-Up.

Table B.1

Filter	Effective Wavelength(μm)	Bandwidth (μm)	Apparent Magnitude σ Cyg	β And	[c]Infrared Colour Excess $(E_{V-X})/(E_{V-B})$	Flux(Jy) $0^m.0$ Star
J	1.2	0.2	[a]3.86	[a]-0.93	2.30	[e]1780
H	1.6	0.3	[a]3.82	[a]-1.73	2.6	[e]1080
K	2.2	0.4	[a]3.78	[a]-1.87	2.78	[d]649
L	3.8	0.7	[b]3.65	[b]-2.04	2.91	[e]245
M	4.9	0.6	[b]3.57	[b]-1.73	2.95	[e]155

Notes

a. Standard values.
b. Interpolated from standard values.
c. Johnson (1968).
d. Thomas et al. (1973).
e. Interpolated from Thomas et al. (1973).

A beam size of $\sim 15''$ was chosen for this work. The signal from the detector passes through a preamplifier (gain x1000), mounted on the side of the dewar and into an Ithaco lock-in amplifier, attached to the photometer cage. The phase-sensitively-detected output is taken off the telescope through a buffer with a gain of x2 and is then displayed on a chart recorder and also presented to a NOVA minicomputer through a CAMAC analogue-to-digital converter. A standard photometry programme numerically integrates over many nod cycles and provides real-time signal-to-noise information. A dichroic mirror in the chopper (cf. figure B.1) diverts the optical radiation to an eyepiece for guiding. Two auxiliary telescopes are provided for finding, a 4" refractor with a $2\frac{1}{2}^{o}$ field of view and a 10" reflector with a $\sim 15'$ field of view.

B.3 Observational Procedures

Standard setting-up procedures are used. The dewar is topped up with liquid nitrogen before the InSb detector is hypersensitised by J-flashing. The impedance and noise of the detector are checked, once the bias has been set. Next, the telescope is focussed by scanning across a small source and adjusting the position of the secondary mirror until the signal is at maximum and the beam profile has steep sides and a flat top. The frequency and amplitude of the chopper are set and the positions of the infrared beams with respect to the visible image in the guide eyepiece carefully noted. Next, the two finding telescopes are aligned with the IRFC.

The nova was found by manually slewing the telescope to roughly the position of σ Cygni. When this star had been found, it was centred up in the field of view of the IRFC and the telescope position readouts were reset to the correct values. Then the IRFC was moved to the position of an SAO star near to the nova. The 4" telescope was used to identify the star field and the SAO star was centred up. Then, after the position readouts had been corrected, the telescope was offset to the nova position and the guiding controls used to place the nova in the centre of one of the infrared beams.

Observations of Nova Cygni 1978 were only possible on six nights between 16th and 28th October and, on some of these nights, conditions were far from ideal. The data obtained on the first and third nights are particularly poor and are not used in any of the analysis. The usual sequence of events was a calibration run on the nearby star,

σ Cygni at all wavelengths, a study run on the nova and then another calibration run on σ Cyg. However on the 19th/20th, β Andromeda was used for calibration. On the last night, σ Cyg was the calibration object but two observations of η Cyg were used for the atmospheric extinction correction (see below).

B.4 Data Reduction

Both the output from the computer and the deflections on the chart record are proportional to the energy, L, from either the object or the calibration source. Thus, if the apparent magnitude, m_c, of the latter is known, then the apparent magnitude of the object, m_o, can be found from,

$$m_o = m_c + 2.5 \log (L_c/L_o). \qquad \text{B.1}$$

The magnitudes of σ Cyg and β And in the IC passbands (table B.1) were obtained by interpolation from a list of the apparent magnitudes of standard stars at certain wavelengths.

Once the magnitude of the nova has been found from equation B.1, two corrections must be applied. This first is to take account of atmospheric extinction. The two observations of the calibration star are taken at different air masses and so the extinction, in magnitudes per air mass, may be evaluated. Table B.2 lists the observed magnitudes, corrected for atmospheric extinction, of the nova for six nights. The errors quoted are the random errors in the sampling. The nova magnitudes are probably slightly more uncertain due to the variability of the extinction. This was observed to vary by up to a factor of 2 over periods of 5 hours and thus makes the corrections equally uncertain. However, this is not a serious problem because the corrections to be applied are only a few hundredths of a magnitude owing to the proximity on the sky of the nova and calibration star. No account was taken of the variation of effective wavelength of the filter with the temperature of the object as this is a small effect. The data obtained from the chart record and from the computer output were reduced independently to provide a cross-check. In all cases, the final magnitudes agreed to better than 0.3%; the smaller of the two was used for subsequent calculations.

Table B.2

DATE	DAYS PAST MAXIMUM	MAGNITUDE AT DIFFERENT WAVELENGTHS J	H	K	L	M	λ_m (μm)	T_c (K)	S_{υ_m}(Jy)	INTEGRATED IR FLUX (ergs s^{-1} cm^{-2})
Oct 16/17	35.4	7.32±0.01	7.15±0.01	6.17±0.02	4.28±0.04	3.45±0.27	-	-	-	-
Oct 19/20	38.5	7.08±0.05	6.86±0.01	5.63±0.06	3.67±0.16	2.93±0.30	4.8	1062	9.2	9.3×10^{-9}
Oct 22/23	41.4	7.38±0.05	7.55±0.06	5.78±0.04	3.73±0.08	2.97±0.22	-	-	-	-
Oct 24/25	43.4	7.48±0.01	6.71±0.01	5.41±0.01	3.31±0.01	2.72±0.23	4.87	1047	13.0	13.0×10^{-9}
Oct 26/27	45.4	7.53±0.01	6.75±0.01	5.32±0.01	3.19±0.05	2.64±0.08	4.95	1030	14.3	14.0×10^{-9}
Oct 27/28	46.4	7.61±0.01	6.80±0.01	5.40±0.01	3.19±0.05	2.53±0.33	5.05	1010	15.3	14.7×10^{-9}

The second correction is necessitated by the presence of interstellar dust. This both weakens and reddens starlight. The value of the ratio, R, of the total extinction in magnitudes in the V-photometric band (A_V) to the selective absorption or colour excess ($E_{B-V} = A_B - A_V$) has been the subject of considerable debate. Johnson (1968), among others, maintains that R depends on galactic longitude and lies between 3 and 6. However, many other authors (e.g. Schultz and Wiener, 1975 and references therein) conclude that a mean reddening law exists for all directions in the galaxy. A value for R of 2.98 (Nandy et al., 1975) has been adopted for this work. W.P.S. Meikle (private communication, 1979) produced a weighted mean for infrared colour excess ratios from the recent literature. For most wavebands, these are very similar to those obtained from Van der Hulst curve no.15 (Johnson, 1968) and so the latter were used (column 6 of table B.1).

The dereddened nova magnitudes were converted to fluxes using the data of Thomas et al. (1973) for the flux from a $0^m.0$ star (table B.1). A Rayleigh-Jeans spectrum, equated to the flux density at J, was subtracted from the raw nova spectrum. (This is further discussed later.) Black body curves were fitted by eye to the resulting spectrum as shown in figure B.2. The quality of the fit was not significantly altered as the data was processed for values of E_{B-V} from 0.3 to 1.2. Thus $E_{B-V} = 0.4$ (Slovak and Vogt, 1979) was adopted for all further analysis. A colour temperature, T_c, was obtained from the black body curves by reading off the wavelength, λ_m, of the peak and using,

$$T_c = 5100 \; / \; \lambda_m(\mu m) \; . \qquad \text{B.2}$$

The temperatures, thus deduced, are listed in table B.2.

There are two ways in which the total infrared flux, F_{ir}, at the earth may be found. The first is by numerical evaluation of the area under the fitted black body curve. Secondly, the infrared optical depth may be assumed to be constant with wavelength, and using $F_{\upsilon_m} = 5.956 \times 10^{-16} T_c^{\,3}$ ergs $cm^{-2} K^{-3}$ (Allen, 1976), where F_{υ_m} is the flux at the maximum of the black body curve, the total infrared flux may be calculated from,

$$F_{ir} = 9.52 \times 10^{-13} \; T_c \; S_{\upsilon_m} \text{ ergs } s^{-1} \text{ cm}^{-2} \qquad \text{B.3}$$

Figure B.2

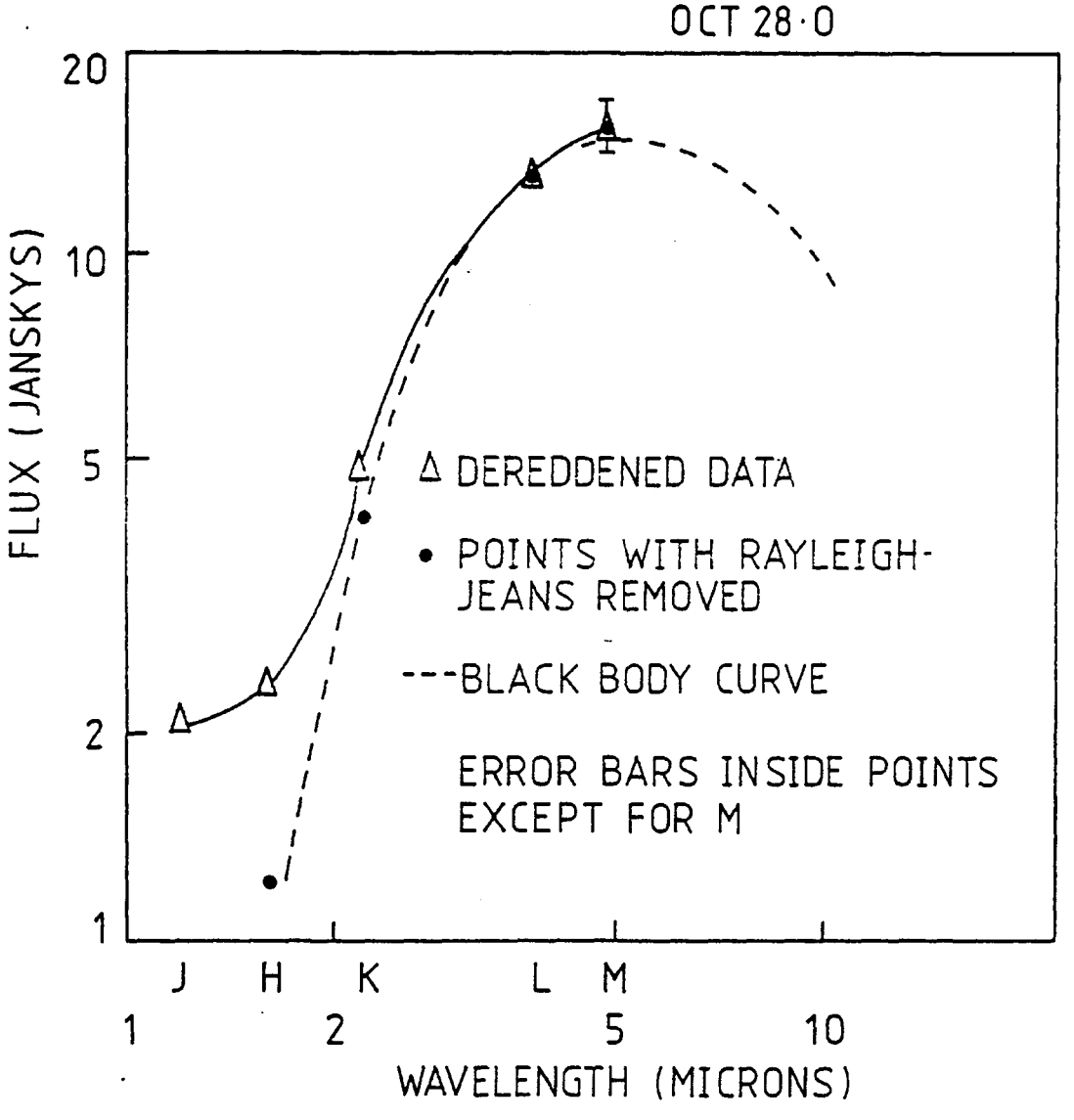

Typical Black Body Fit.

where S_{υ_m} is the observed flux density (in Janskys) at the black body maximum. The latter method was generally used, although it was checked by the former in some cases. Table B.2 gives the integrated infrared flux from the nova for four nights.

B.5 Interpretation

The infrared observations of Nova Serpentis 1970 by Geisel, Kleinmann and Low (1970) provided a new insight into the energetics of classical novae and their post-maximum evolution. These observations showed that dust grains may condense out of the expanding nova ejecta and grow until they absorb most of the radiation emitted by the nova, reradiating it in the infrared.

There have been extensive infrared observations of three other novae since Nova Serpentis 1970. The slow Nova Vulpeculae 1976 exhibited dust formation similar to Nova Serpentis 1970 (Ney and Hatfield, 1978), as did Nova Serpentis, 1978 (Gehrz *et al.*, 1980b), but in the fast Nova Cygni 1975 no substantial dust formation phase ever appeared (Ennis *et al.*, 1977). Nova Cygni 1978 was a fast nova (time to fall two magnitudes $\sim$ 12 days) and so it should be an interesting test case for theories of dust grain formation in novae.

Figure B.3 shows some IC data together with infrared observations reported by Gehrz *et al.* (1978), for two nights earlier in the post-maximum period, and still earlier observations by Phillips *et al.* (1979). Taken together, the infrared data show the declining Rayleigh-Jeans tail of the emission from the nova photosphere (cf. Bath and Shaviv 1976) until about day 25 when thermal emission from the dust emerges. (It was assumed that most of the flux at J was from the photosphere and so a Rayleigh-Jeans spectrum, fitted to the J flux density, was subtracted off the IC data before the black body curve was fitted.)

The infrared observations during days 25-46 post-maximum exhibit three striking features: 1) The spectra in the 1-5μm region conform very precisely to black-body spectra, as figure B.2 shows. 2) The corresponding black-body temperatures of these spectra decrease during this time, with $T(t) \propto t^{-\frac{1}{2}}$, as is evident in figure B.4. Data for two nights from Gehrz *et al.* (1978) is included in this plot and in the rest of the calculations. 3) While the temperature drops, the integrated infrared luminosity rises by nearly a factor of ten in 20 days, approx-

Figure B.3

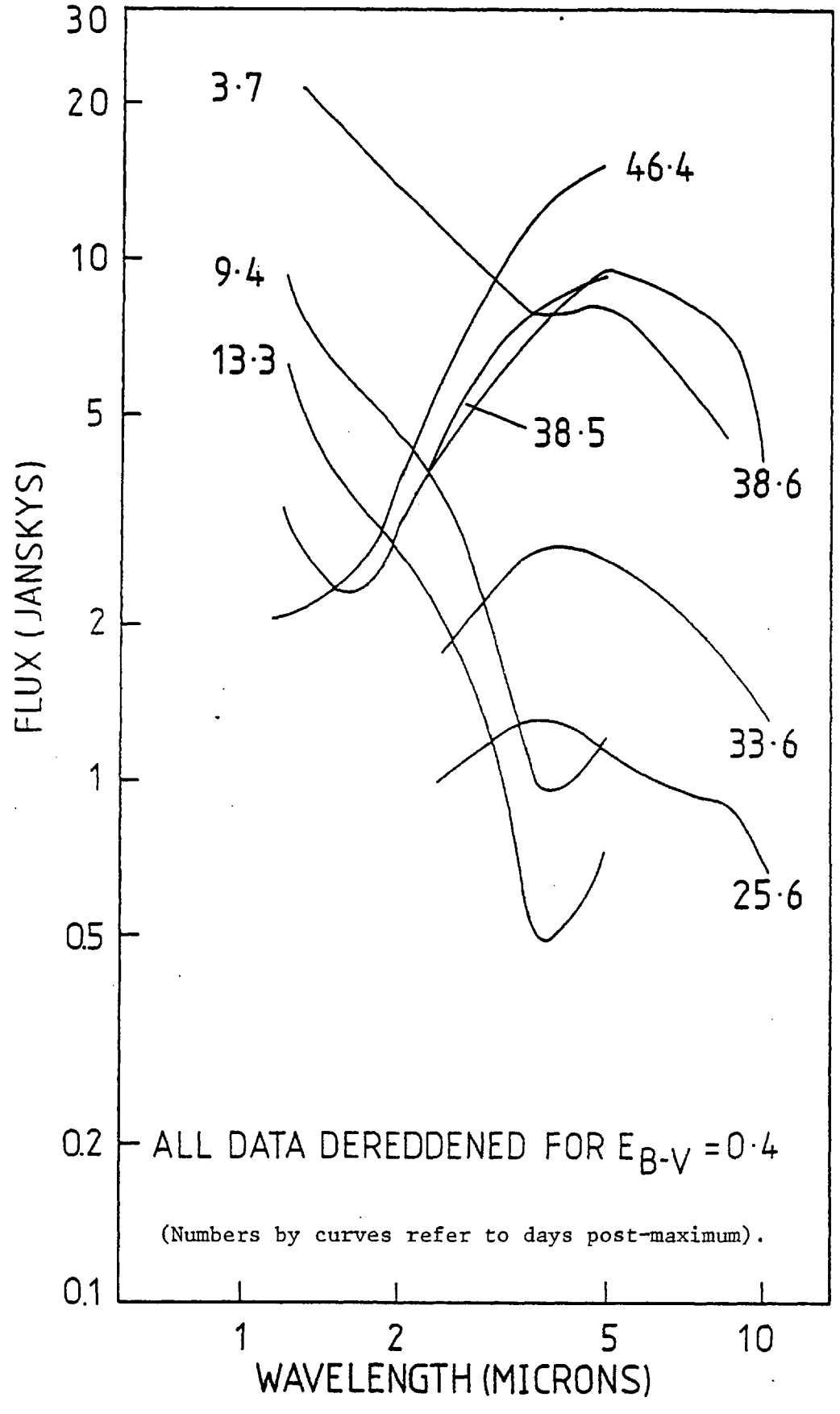

Spectral Development of Nova Cygni 1978.

Figure B.4

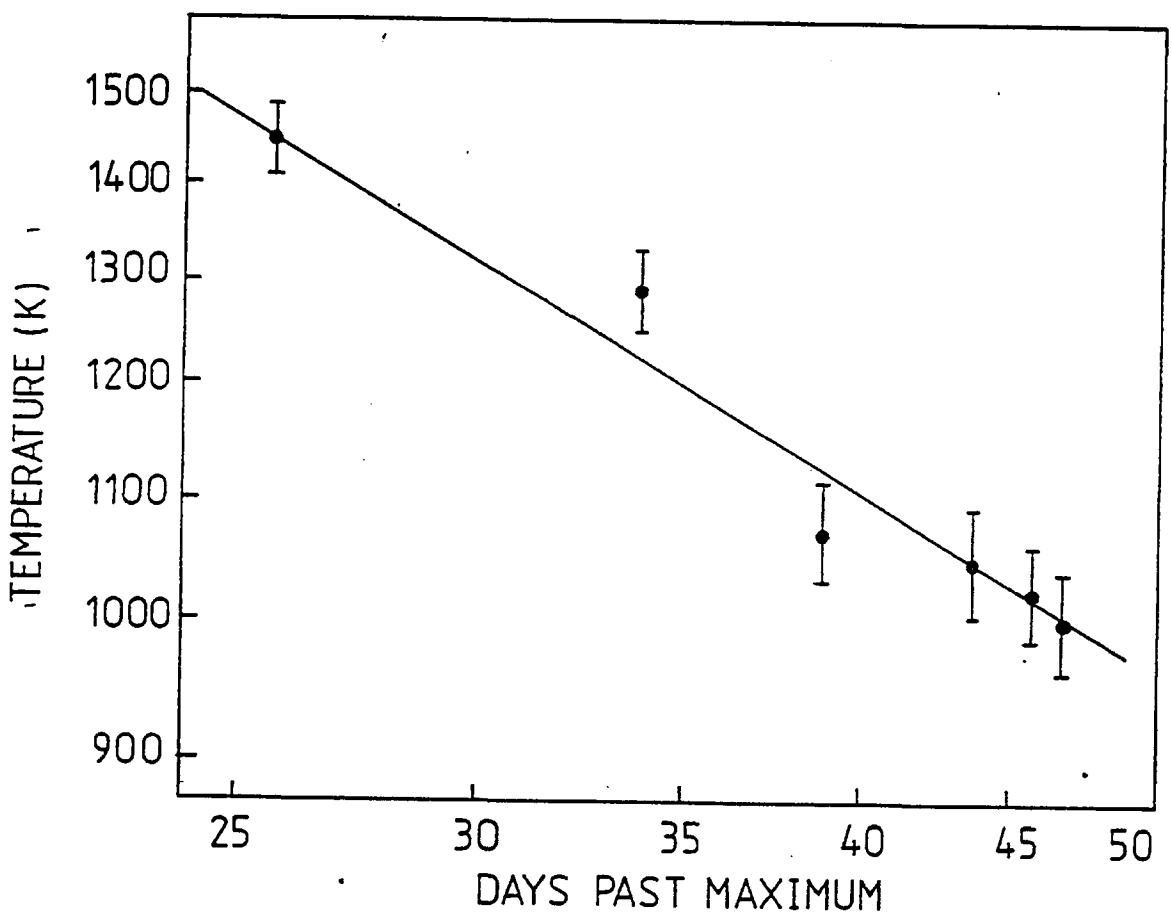

Dust Cooling Rate.

imately linearly with time. These features are generally characteristic of those novae which develop an infrared excess due to dust emission. Two questions about the physics producing these features are immediately apparent and their answers permit a model for the nova dust cloud to be chosen.

Firstly, the spectra are Planckian. Thus either the grains must be large, with the grain radius of the order of the infrared wavelength, or the dust cloud must be optically thick. Otherwise the Planck spectrum will be modified by a wavelength-dependent emissivity $\varepsilon(\lambda) \propto \lambda^{-\alpha}$ with $1 \lesssim \alpha \lesssim 2$. Such an emissivity would detectably distort the spectra of figure B.2, even with $\alpha = 1$. The dust cloud is certainly not optically thick in the infrared during this period, for it is still quite transparent at wavelengths 10 times smaller, in the visible. Thus the dust grains must be large enough for the Mie absorption efficiency, Q_{abs}, to have saturated at $\lambda \sim 5\mu m$. $Q_{abs} \gtrsim 1$ when the parameter $x = 2\pi a/\lambda$ is 2-4, which suggests a grain radius $a \lesssim 2\mu m$ from the time dust emission was first detected on day 25. Thus the nova dust grains must be an order of magnitude larger than the grains responsible for visible extinction in the general interstellar medium. This requirement has not generally been understood in interpretations of the infrared emission from novae, and grain sizes typical of the interstellar medium have usually been assumed for the nova dust grains.

Secondly, the infrared luminosity rises as the temperature falls. The temperature, T, of a dust grain a distance R from the nova photosphere (cf. Bath and Shaviv, 1976) is determined by equilibrium between absorbed ultraviolet and emitted infrared radiation and is given by,

$$T^4 = \frac{L_*}{16\pi \sigma R^2} \quad , \qquad \text{B.4}$$

where L_* is the luminosity of the nova photosphere and σ is the Stefan-Boltzman constant. In equation B.4, the Planck mean absorption,

$$\langle Q \rangle = \frac{\int_0^\infty Q_{abs} B_\upsilon(T) d\upsilon}{\int_0^\infty B_\upsilon(T)\, d\upsilon} \quad , \qquad \text{B.5}$$

where $B_\upsilon(T)$ is the Planck function, has been assumed to be equal to unity

both in the ultraviolet and in the infrared because the dust grains are large (cf. Gilman, 1974). If the luminosity of the nova is assumed to be constant (cf. Gallagher and Code, 1974), then the temperature of a dust grain only drops because it is further away from the nova photosphere. The infrared luminosity of the dust cloud is,

$$L_{ir} = 4\pi a^2 \sigma T^4 N \quad , \qquad \text{B.6}$$

where N is the total number of radiating dust grains in the cloud. Obviously the infrared luminosity can rise while the temperature falls only if there is an increase in number and/or radius of the grains.

There are two models for the formation and evolution of nova dust clouds in the literature. Following the suggestion of Geisel et al. (1970) that dust grains condense out in an expanding shell of material ejected in the nova outburst, Clayton and Wickramasinghe (1976) worked out a quantitative model. A second, rather different model, has been proposed by Bode and Evans (1979 and 1980). They postulate a shell of small dust grains around the nova before its outburst. These grains absorb larger fractions of the radiation from the nova photosphere as its radius shrinks and its spectrum hardens and reradiates it in the infrared.

These infrared results for Nova Cyg 1978 can be used to discriminate between these models. First of all, the Bode and Evans model seems to founder on its requirement for small grains, with a $\hat{<}$ 0.1μm. With larger grains the model does not provide the required increase in infrared luminosity as the photospheric spectrum shifts toward the ultraviolet. Secondly, it is difficult to see how this static grain model can provide increasing infrared luminosity while the dust temperature falls. Even allowing for the light travel time delay (the dust shell is imagined to be tens of light days across) the constant nova bolometric luminosity requires that during the rise in the infrared light curve the dust temperature be constant or increasing; it cannot appear to cool while the infrared luminosity increases, as is observed. Finally, if the light travel time delay is important (i.e. if the shell were this large), then it is difficult to imagine the infrared emission following a black-body spectrum (and, indeed, Bode and Evans (1979) point this out). Thus it appears that these infrared observations

exclude the Bode and Evans (1979 and 1980) model.

The expanding shell model of Clayton and Wickramasinghe (1976), on the other hand, seems to agree nicely with the features discussed above. If the shell thickness is small compared to R, then all the dust will radiate at the same temperature and the infrared spectrum will be Planckian at all times. If the shell expands at constant velocity, then equation B.4 gives $T(t) \propto t^{-\frac{1}{2}}$, which is very close to the cooling rate observed.

B.6 Conclusions

JHKLM photometry of Nova Cygni 1978 has been obtained during the post-maximum period when its infrared emission rose dramatically as dust grains formed in the expanding shell of ejected material. The dust shell is optically thin in the infrared and the dust grains are an order of magnitude larger than those responsible for the general interstellar extinction in the visible.

B.7 References

Allen, C.W., 1976. Astrophysical Quantities, 3rd Edition, Reprinted with Corrections, the Athlone Press, London.

Bath, G.T. & Shaviv, G., 1976. M.N.R.A.S., 175, 305.

Bode, H.F. & Evans, A., 1979. Astron.Astrophys., 73, 113.

Bode, H.F. & Evans, A., 1980. Astron.Astrophys., in press.

Clayton, D.D. & Wickramasinghe, N.C., 1976. Astrophys.Sp.Sci., 42, 463.

Ennis, D., Becklin, E.E., Beckwith, S., Elian, J., Gatley, I., Matthews, K., Neugebauer, G. & Willner, S.P., 1977. Ap.J., 214, 478.

Ferland, G.J. & Shields, G.A., 1978. Ap.J., 224, L15.

Gallagher, J.S. & Code, A.D., 1974. Ap.J., 189, 303.

Gehrz, R.D., Grasdalen, G.L., Hackwell, J.A. & Ney, E.P., 1978. IAU Circ. 3296.

Gehrz, R.D., Grasdalen, G.L., Hackwell, J.A. & Ney, E.P., 1980b. Ap.J., 191, 675.

Gehrz, R.D., Hackwell, J.A., Grasdalen, G.L., Ney, E.P., Neugebauer, G. & Sellgren, K., 1980a. Ap.J., 239, 570.

Geisel, S.L., Kleinmann, D.E. & Low, F.J., 1970. Ap.J., 161, L101.

Gilman, R.C., 1974. Ap.J.Supp., 28, 397.

Johnson, H.L., 1968. Ch.5 in 'Stars and Stellar Systems', vol.8,

Ed. B.M. Midhurst, the University of Chicago Press.

Jorden, P.R., Long, J.F., MacGregor, A.D. & Selby, M.J., 1976. Astron. Astrophys., 49, 421.

Nandy, K., Thompson, G.I., Jamar, C., Monfils, A. & Wilson, R., 1975. Astron.Astrophys. 44, 195.

Ney, E.P. & Hatfield, B.F., 1978. Ap.J., 219, L111.

Phillips, J.P., Selby, M.J., Wade, R. & Sanchez Magro C., 1979. M.N.R.A.S., 187, 45p.

Schultz, G.V. & Wiemar, W., 1975. Astron.Astrophys., 43, 133.

Slovak, M.H. & Vogt, S.A., 1979. Nature, 277, 114.

Thomas, J.A., Hyland, A.R. & Robinson, G., 1973. M.N.R.A.S., 165, 201.

Appendix C

Publications

During my time as a research student, I was co-author of the following two publications.

The Imperial College 41-Inch Telescope for Far-Infrared Balloon Astronomy

R. D. Joseph, J. Allen, W. P. S. Meikle, K. C. Sugden,
M. F. Kessler, D. L. Rosen, G. Masson

Astronomy Group
The Blackett Laboratory, Imperial College
London SW7, England

Abstract

We have developed a 41-inch balloon telescope for far-infrared astronomical observations. It is constructed entirely of aluminum alloy, including the optics, and incorporates several novel features. Two composite bolometers, operated at 1.7°K, with adjacent fields of view on the sky, allow us to carry out two-color photometry in the wavelength ranges 40-80 μm and 80-400 μm.

The far-infrared payload flies on a stabilized balloon platform developed in the U.K. as a national facility by the Science Research Council. The maiden flight of both systems was launched in 1976 November. Despite problems with the stabilization system which prevented releasing the telescope from its stow position, we were able to scan a number of far-infrared sources. In-flight calibration, based on detections of both Venus and Saturn, indicates that the far-infrared noise-equivalent flux density* (areance) was ∿ 130 Jy $Hz^{-1/2}$ for the short wavelength channel and ∿ 500 Jy $Hz^{-1/2}$ for the long wavelength channel.

I. Introduction

The opacity of the earth's atmosphere effectively prohibits ground-based astronomical observations throughout the five octaves of the electro-magnetic spectrum that comprise the far infrared (25 μm to 1 mm wavelength). Except for two rather poor transmission windows at ∿ 35 μm and ∿ 350 μm, observations must be made from platforms above most of the atmosphere. Large scientific balloons provide one attractive platform of this kind, and several far-infrared balloon telescopes have been flown, ranging from the pioneering 1" telescope of Woolf *et al.* (1969)[5] to the 40" Smithsonian-Harvard-Arizona telescope described by Fazio *et al.* (1974).[1] At Imperial College (London) we have developed a new 41" balloon telescope, and the associated payload, for far-infrared astronomy. The telescope is designed to fly on a stabilized balloon platform developed in the U.K. by the Science Research Council. In the following we will describe the main features of the infrared astronomy payload, and report on the preliminary analysis of its performance on the first two flights.

II. Instrumentation

Telescope Design

The mechanical configuration of the f/7 Cassegrain telescope is shown in Figure 1. The 41" diameter primary mirror has a spherical figure and a focal ratio of f/2.9. The secondary mirror is also spherical, and has a diameter of 13.6". A flat tertiary mirror behind the primary deflects the beam through 90° into the

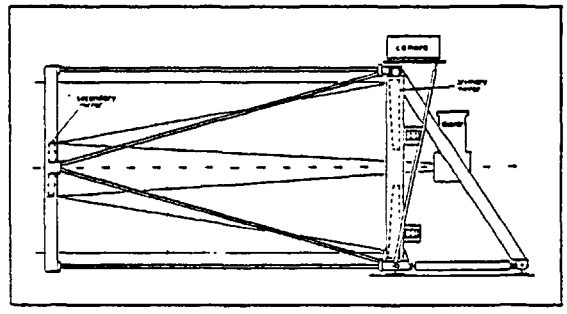

Figure 1. Layout of the 41-inch Cassegrain telescope.

detectors. All three mirrors are made of aluminum alloy and are gold-coated. The secondary and tertiary mirrors were both machined using diamond-turning techniques, whereas the final figuring and polishing of the primary was done by conventional methods after depositing a hard nickel alloy on the machined surface. All the mirrors were optically tested to confirm that they were figured to better than 4 μm.

The telescope is an open structure made of aluminum alloy, and uses conventional Serrurier trusses. The primary mirror cell is constructed of hollow rectangular section tubing. The mirror, which weighs 105 kg, is kinematically mounted inside the cell using orthogonal radial and axial supports. All six supports are shock-mounted and pre-tensioned to prevent movement of the mirror under its own weight as the telescope is tipped to various attitudes. The telescope attaches to the balloon platform by a three-point kinematic mount using commercially-available rod-end bearings. The total weight of the telescope, including the optics, is 215 kg.

The telescope design incorporates several noteworthy features. First, there is negligible thermal focal shift. When the mirrors and telescope structure undergo a temperature change δT, the focal length, F, of the telescope changes by $\delta F = F(\alpha_s - \alpha_m)\delta T$, where α_s and α_m are the thermal expansion coefficients of the structure and mirror materials respectively. For a typical balloon flight, δT is ∿ 80°K, which, with glass optics, would produce a focal shift of ∿ 14 mm. But by using aluminum optics, with thermal coefficient matched to that of the telescope structure, there is no thermal focal shift. This in turn permits mounting the secondary mirror without an active focusing mechanism requiring adjustment by telecommand during flight. This makes the telescope more simple and reliable in operation, and allows a much lighter secondary ring assembly. The trusses supporting the secondary ring can then be lighter and still maintain alignment of the two mirrors as the telescope orientation is

*See explanatory note in Guest Editorial.

IR-102 received June 6, 1977.

altered. Further, the use of aluminum rather than glass optics offers a factor of ~ 10 more resistance to permanent damage resulting from impact shock after parachute descent. Finally, the factor of 200 in the thermal conductivity of aluminum compared to glass means that thermal gradients across the aluminum mirrors will be much smaller, thereby minimizing thermally-induced aberrations.

Another feature of the telescope is the use of only spherical optics, with attendant figuring economies. The spherical aberration was calculated for a range of telescope parameters, and by the appropriate choice of mirror focal ratios it is possible to keep the spherical aberration less than the diffraction limit in the far infrared, to keep the telescope to a reasonable size, and to achieve a plate scale consistent with both the diffraction limit and the linear size of sensitive helium-cooled bolometers. The telescope is about 2 m in length, is diffraction-limited at ~ 70 μm, and has a plate scale of 30 arcsec mm^{-1}.

A final point concerns the thermal hygiene of the telescope, the *sine qua non* in achievement of the best far-infrared sensitivity. The entrance pupil of the telescope is fixed by the secondary mirror, which is slightly undersized compared to the aperture of the primary. This ensures that the detector field of view does not extend beyond the rim of the primary at either extreme of the chop cycle. A central hole in the secondary mirror, matching the shadowing of the secondary on the primary, guarantees that the detector does not see radiation emitted by the instrumentation behind the Cassegrain hole in the primary. The four vanes supporting the secondary mirror are very thin, 0.8 mm. Thus the detectors see about as little thermal emission from the telescope as the Cassegrain configuration allows.

Detectors and Infrared Filters

Since the large radiant background from the telescope demands that some form of spatial filtering (chopping) be performed so that faint astronomical sources can be discriminated against this background, observing time is used most efficiently if two detectors are placed in the focal plane with adjacent fields of view on the sky. It is then possible to chop so that the source is viewed by one detector while the other views the adjacent comparison field. Both detectors are composite germanium-silicon bolometers mounted in simple integrating cavities. They are operated at a temperature of 1.7°K by venting the liquid helium (LHe) to the ambient atmosphere. A 1 mm cold stop, just in front of each detector, is at the focus of an f/1 crystal quartz Fabry lens which images the primary mirror onto the cold stop. At the lenses are field stops which restrict the angular field of view on the sky to 3 arcminutes. In front of the field stops are helium-cooled filters which give the detectors effective bandwidths of 40 - 80 μm, and 80 - 400 μm, as shown in Figure 2.

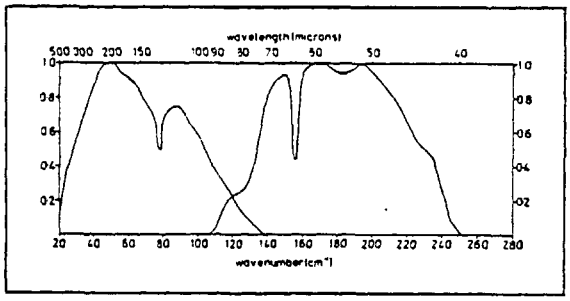

Figure 2. Relative spectral response of the two detector-filter combinations.

Both filters include diamond dust scattering layers on CaF_2 for short-wavelength blocking. The long-wavelength cutoff at 80 μ is provided by a thin 0.3 mm slice of KRS-5, while the cut-on at this wavelength for the other detector is due to KCl. There is additional short wavelength blocking provided by a diamond dust layer on crystal quartz at 77°K. The dewar vacuum window is made of high density polyethylene.

It is important to keep the angular field of view of the detectors as small as possible, consistent with filling the solid angle subtended by the secondary mirror, and this requires that the cold stop in front of each detector be positioned very precisely with respect to the field stop at the Fabry lenses. The mounting for these elements is designed so that the relative positions of the stops are determined to better than 0.05 mm.

The entire detector-filter assembly was enclosed in a LHe-cooled copper shield in order to keep radiation-driven thermal drops and drifts to a minimum. Initial beam-pattern measurements showed that considerable scattered radiation could reach the detectors, but by sand-blasting the inside of the shield and then painting it with a good optical black this stray radiation was greatly reduced. The measured beam pattern was then well-matched to the convergence angle from the secondary mirror.

For reasons both of thermal stability and LHe perdurance we chose to use a LN_2-shielded dewar. Thermal vacuum tests confirm that with Butyl rubber O-rings the dewar vacuum remains intact at the low temperature encountered at balloon float altitudes. Similar tests show a reduction by half in the LHe perdurance when the LN_2 reservoir is vented to the atmosphere, allowing the nitrogen to solidify, despite the fact that the LN_2 reservoir is filled with copper gauze to maintain good thermal contact with the shield when the LN_2 freezes. The dewar was therefore flown with a simple check valve on the LN_2 vent to maintain the vapor pressure over the LN_2 at about one atmosphere.

Chopper

Rather than rocking the comparatively large and heavy secondary mirror, a parallel-motion, focal plane chopper was chosen, in order to reduce problems with microphonic noise, amplitude stability, and drive power required. The chopper is designed to conserve momentum internally as it oscillates, thereby minimizing the generation of microphonic noise which can seriously degrade the noise performance of the detectors. To accomplish this, duplicate mirror carriages are mounted on parallel springs, as shown in Figure 3. The carriages are electromagnetically driven against each other using an amplified and phase-shifted

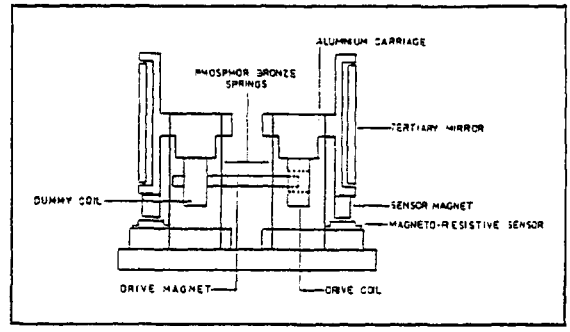

Figure 3. The focal-plane chopper.

signal derived from the motion of one of the carriages. Thus the system is electromechanically resonant, and requires very little drive power. Its amplitude stability, as measured by thermal vacuum tests in the laboratory, was more than adequate, as was its performance in long-term room-temperature runs. Its major disadvantage is the static deflection under its own weight, due to change of attitude, that is a feature of such resonant systems. This results in a small drift of the offset due to chopped instru-

mental radiation as the telescope changes attitude.

Star-Field Camera

For precise post-flight determination of the celestial coordinates of the field observed by the telescope at any time, a 16 mm pulse camera is mounted on the instrument flange of the telescope. It is aligned with the telescope axis, and is capable of taking up to 4000 star-field photographs during the flight. The field-of-view is 1.5° x 2.7°, and the scale is 11.5 mm^{-1}. The camera may be operated in either a manual mode, in which the shutter is both opened and closed by a discrete telecommand from the ground, or in an automatic mode, in which pictures are taken at regular intervals which may be varied from 1 to 16 seconds by the appropriate digital telecommand word. A frame number is written both on each frame of the film and in the main data format, so that there is unambiguous correlation between the star field photographs and the rest of the experimental data. The film we use is Kodak 2475 high-speed recording emulsion. In ground tests, trails of 9^m stars were easily observable.

On-Board Signal Processing

A block diagram of the on-board electronics system is shown in Figure 4. Each signal channel consists of a conventional phase-

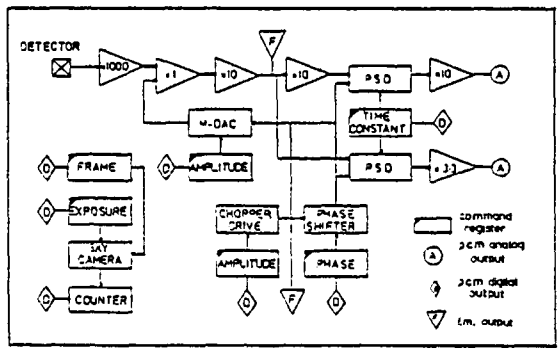

Figure 4. Block diagram of the on-board electronic signal-handling system.

sensitive detector (PSD) with telecommandable phase shifts and integration time constants. Two PSD channels for each detector, with gains differing by a factor of 30, permit linear readout over a dynamic range extending from detector noise to the signal levels expected for planets. One novel feature is the scheme for cancelling the component of signal due to chopped instrumental radiation. This signal can be several orders of magnitude larger than that due to detector noise, and it is virtually impossible to determine its magnitude, or even its phase, before flight. Since we are using a sinusoidal chopping waveform, the detector signals are approximately sinusoidal as well, but shifted somewhat in phase relative to the chopper waveform due to the finite response time of the bolometers. The reference signal derived from the chopper is phase-shifted by telecommand and routed to a multiplying digital-to-analog converter (MDAC), in parallel with the PSDs, and the 10-bit MDAC performs as a digitally-controlled attenuator, adjusted by telecommand from the ground. The attenuated reference signal from the MDAC is then fed to one input of a differential amplifier, while the preamp signal goes to the other input. The MDAC attenuation is commanded from the ground to a value such that the output of the differential amplifier is nearly zero when the telescope is not pointed at a celestial infrared source. By bucking out the instrumental offset signal at this point, extended dynamic range is achieved for the downstream electronics.

Battery power is provided by a rechargeable pack of sealed Ni-Cd batteries with 300 W-hr capacity. There is no active heating for the electronics box; all circuits are designed to operate to specification below $-20^\circ C$, and are kept above this temperature by 1 kW-hr of energy released by 10 kg of water stored inside the insulated electronics box.

Telemetry of scientific and payload housekeeping data is done using the PCM system provided by the National Scientific Balloon Facility (NSBF). Nine digital and fourteen analog data words are telemetered at a rate of 10 kbits sec^{-1}. To provide a measure of redundancy in case of disaster, the analog detector and chopper signals are also telemetered directly to ground via the FM/FM telemetry system. Telecommand requirements include seven discrete and eleven digital functions, and the telecommand equipment used is also that provided by NSBF.

Stabilized Balloon Platform

The Imperial College payload is flown on a stabilized balloon platform designed and built by GEC Marconi Electronics Ltd. for the U.K. Science Research Council, and operated by a team from the SRC's Appleton Laboratory. A preliminary description of the overall design concept and performance specifications of the platform has been given by J. How (1974),[3] and the prototype platform differs from this design only in one or two respects. The approach taken is to stabilize the entire gondola in three axes – azimuth, elevation, and roll – about a central gimbal-torque-motor cluster which is suspended from the balloon. The reaction mass against which the platform is driven in azimuth is the balloon itself.

There are two guidance modes. In the degree mode, position information is derived from magnetometers for the azimuth loop and from accelerometers for the roll and elevation loops. In the arcminute mode, position information comes from a star-sensor which has a stellar magnitude limit of $+5^m$. In both modes rate information is derived from a three-axis gyro package. The star-sensor can be offset $\pm 5^\circ$ both in elevation and in cross-elevation to permit acquisition and tracking by the telescope of fields which have no suitable guide stars. A TV camera which gives a 10° star field picture is also provided to aid acquisition of the desired guide star.

In pre-flight ground tests, the platform pointing and stability were generally up to the design specifications:

Degree Mode

Roll and Elevation:	Offset	<	40 arcmin
	Drift	<	6 arcmin hr^{-1}
	Noise	<	1 arcmin RMS
Azimuth:	Offset	<	1.6°
	Noise	<	1 arcmin RMS

Arcminute Mode

Lateral Axis:	Offset	<	20 arcsec
	Drift	<	1 arcmin hr^{-1}
	Noise	<	10 arcsec RMS
Twist Axis:	Offset	<	62 arcmin
	Drift	<	15 arcmin hr^{-1}
	Noise	<	5.5 arcmin RMS

A major modification to the design described by How (1974)[3] is the scheme for handling out-of-balance torques. An auto-balancing system was devised which pumps fluid between tanks located at the ends of the roll and elevations axes, and this replaces the cross-slide mechanism which How described. The system pumps fluid to readjust the weight distribution about the roll and elevation axes whenever the torque demand exceeds about 2 Nt-m. The gondola is stowed for launch and parachute descent by pumping extra fluid into the forward and right-hand tanks, thereby parking the platform against the stops, normally at -5° in elevation and $+5^\circ$ in roll.

Total payload weight below the parachute is about 2800

pounds. Its dimensions are 10 ft x 15 ft x 9 ft high. Figure 5 shows a picture of the gondola on the launch pad just before the second flight.

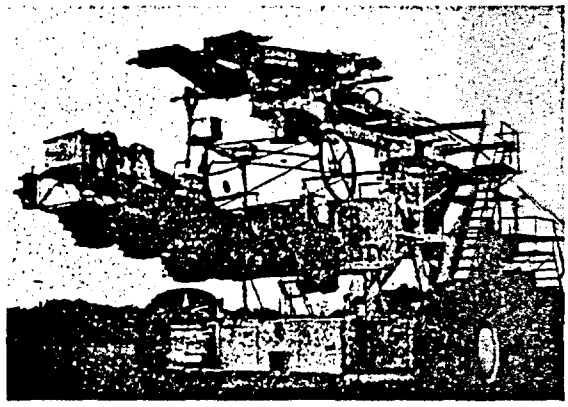

Figure 5. Gondola suspended from the launch truck just before the second flight.

III. Flight Performance

The first flight of this payload was launched on 29 November 1976. With a 4.3 Mft^3 balloon the telescope reached an altitude of 100,000 ft. Unfortunately, we were unable to unstow the payload in roll due to a problem with the auto-balancing system. However, despite a large frictional force against the roll stop we were able to point the telescope at elevations above -5°, and scan it in azimuth in an attempt to detect bright sources. Although the scan was at the rather fast degree mode slew rate of about 1° sec^{-1}, we detected Saturn easily, and the data indicate that the infrared system was working well. Parachute impact was near Selma, Alabama in a pine forest, and in spite of the fact that the gondola did not land on the crush pads, the infrared system suffered almost no damage. Only two vanes of the secondary mirror spider were broken, and the entire infrared telescope system was checked out and ready for reflight within five days. The stabilization system experienced somewhat more damage, and in particular the elevation axis gimbal was slightly sprung. However, the entire payload was repaired and tracking stars from the suspension on the ground within about 10 days after the recovery.

The second flight was launched on 16 December 1976, but we were unable to unstow the gondola from its park position on the forward elevation stop. However, following the first flight the stop had been rebuilt at +5°, so it was possible to attempt to observe sources rising or setting at +5° elevation. To do this, we carried out a raster scan using the sidereal motion of the sky, by scanning the telescope in azimuth about the position in which the putative source would be rising or setting. In this way we were able to detect both Venus and Saturn, and thereby calibrate the far-infrared sensitivity.

Parachute impact on this flight was in open ground, and the payload suffered very little damage, aside from slightly bent telescope trusses and some breaks in the protective structure underneath the telescope. In particular, the telescope, optics, LHe dewar, chopper, star-field camera, and electronics were all undamaged and ready for reflight.

Far-Infrared System Performance

Analysis of the flight data is still under way, but preliminary assessment of the overall performance of the payload indicates that there were no failures in the infrared system during either flight. We have calibrated the in-flight optical efficiency of the entire infrared detection system using the observations of Saturn and Venus. The adopted temperature of Venus was 240°K (Wright, 1976),[6] and that of Saturn plus its projected rings (taken to be optically thick) was 88°K (Rieke, 1975;[3] Fazio *et al.*, 1976 (flight 2);[2] Wright, 1976).[6] These give peak-to-peak signals at the detectors, per Jansky of source flux density at the telescope, of 0.8 nV Jy^{-1} in the 40-80 μm band, and 0.2 nV Jy^{-1} in the 80-400 μm band.

For both detectors the minimum noise during the flights was within 20% of the levels measured in the laboratory under simulated flight conditions, *viz.* ∿ 40 nV (RMS) $Hz^{-½}$, although this value was exceeded by several times when the platform underwent oscillation due to problems with the stabilization system. The source flux density that results in an RMS detector signal equal to the RMS detector noise is the noise-equivalent flux density (NEFD), and it can be found by substituting the flight data given above in the expression

$$\text{NEFD} \simeq \frac{1}{D} \frac{\text{detector noise (Volts RMS Hz}^{-½})}{\text{detector response (Volts P-P/Jy)}}$$

The duty factor, D, is ½ for a square-wave modulated signal; in our case $D \simeq 0.4$. (It is not always clear in the literature whether this factor has been included in the measured (or calculated) NEFD reported for infrared astronomical observations.) From the data for these flights we find:

$$\text{NEFD (40-80 } \mu\text{m)} \simeq 130 \text{ Jy Hz}^{-½}$$
$$\text{NEFD (80-400 } \mu\text{m)} \simeq 500 \text{ Jy Hz}^{-½}.$$

The offset signal produced by chopped instrumental radiation is always a problem besetting infrared observations, not only because it can saturate the signal processing chain at some crucial point, but also because small fluctuations in its amplitude can easily become the dominant noise source that limits sensitivity. In flight the offset signal was about 350 times the RMS noise (in a 1 Hz bandwidth) for the short wavelength detector and about 90 times the RMS noise for the long wavelength detector. To cancel out this signal required less than 10% of the dynamic range available in the electronic compensation scheme described above. The amplitude stability of the chopper was sufficiently good that we did not experience noise due to fluctuations in the radiant background on the detectors from variations in the amplitude of the chopper throw, except for periods when the gondola suffered severe suspension train oscillations.

Star-field photographs were taken mostly with 3 sec and 6 sec exposures throughout the flights, and despite the rather fast angular scan rates we had to employ, traces for 8^m stars are identified on these pictures without difficulty.

During the second flight we were able to scan several possible far-infrared sources in our observing list when they were rising or setting at +5° elevation, and between these times we scanned the galactic plane. Analysis of this data is still under way.

In addition to two-color photometry, future flights of this payload will include far-infrared polarimetry and emission-line observations with a Fabry-Perot interferometer.

Acknowledgments

We are grateful for the support we have received from many sources in developing and flying this payload. Chris Chaloner, Neil Urquhart, and Graham Luscombe of the SRC Appleton Laboratory, and Paul Cope, from GEC Marconi Electronics Ltd., expended really heroic efforts in preparing the SRC stabilized platform for its first flights. Among our colleagues at Imperial College, John Long, Bill Stannard, Roy Barr, and Jack Crabtree were especially helpful with the solution of various mechanical problems, Charles Wynne gave expert advice on the optical calculations, Dick Chater of the Analytical Services Laboratory

provided efficient assistance with the spectral calibration of the detectors and filters, and we would like to thank Jim Ring for his interest and encouragement in the I.C. balloon astronomy program. It is always a pleasure to acknowledge the superb ballooning support, and hospitality, provided by the National Scientific Balloon Facility in Palestine, Texas. And finally, we wish to thank the U.K. Science Research Council for its continuing financial support of this entire project. J.A. and W.P.S.M. are SRC Research Assistants, and M.F.K., D.L.R. and K.C.S. hold SRC Research Studentships.

References

1. Fazio, G. G., Kleinmann, D. E., Noyes, R. W., Wright, E. L., and Low, F. J. 1974, *Proc. Symposium on Telescope Systems for Balloon-Borne Research*, NASA Ames Research Center, California, NASA TM-X-62,397, p. 38.
2. Fazio, G. G., Traub, W. A., Wright, E. L., Low, F. J., and Trafton, L. 1976, Ap.J., *209*, 633.
3. How, J. 1974, *Proc. Symposium on Telescope Systems for Balloon-Borne Research*, NASA Ames Research Center, California, NASA TM-X-62,397, p. 284.
4. Rieke, G. H. 1975, Icarus, *26*, 37.
5. Woolf, N. J., Hoffmann, W. F., Frederick, C. L., and Low, F. J. 1969, Phil. Tran. Roy. Soc., *264*, 263.
6. Wright, E. L. 1976, Ap.J., *210*, 250.

Infrared Physics, Vol. 18, pp. 627–628
0020-0891/78/1201-0627$02.00/0

A SCANNING FABRY–PEROT INTERFEROMETER FOR FAR-INFRARED BALLOON ASTRONOMY

M. F. KESSLER, R. D. JOSEPH and J. ALLEN
Astronomy Group, Blackett Laboratory, Imperial College, London SW7 2BZ, U.K.

Abstract—Design and performance details of a scanning Fabry–Perot interferometer developed for far-infrared balloon astronomy are presented. Scanning is achieved mechanically by a parallel spring arrangement and plate spacing is measured by capacitance micrometry.

We have developed a scanning Fabry–Perot interferometer for astronomical use with the Imperial College 41 in. balloon telescope.[1] The instrument is scanned mechanically by varying the plate spacing using a parallel strip spring arrangement,[2] shown in Fig. 1, to maintain alignment. When the upper carriage of this movement is displaced to the left in the figure, there is a corresponding demagnified vertical movement. With the plane of our interferometer etalon parallel to the drive direction, the demagnified movement permits use of an ordinary micrometer for scanning. We drive at the centre of the spring to reduce non-parallel movement caused by cantilevering. Coarse gap and tilt adjustment are carried out using three screws bearing on the upper mirror holder, whereas the fine adjustment is achieved by moving ball bearings along tapered glass V-blocks attached to the underside of the lower plate holder.

The mirror spacing is measured by capacitance micrometry based upon the techniques described by Jones and Richards.[3] The capacitor pads are $\sim 1\ \text{cm}^2$ gold-coated glass pillars standing on the mirror holders. The lower pad is the larger of the two to reduce edge effects which would otherwise result from lateral displacement of the top carriage. To measure the change in the etalon gap, the capacitance of these pads is compared to that of a reference capacitor of similar design but optically contacted. The absolute gap is determined with a travelling microscope focusing on each mirror in turn.

The mirrors are made from commercially available[4] electroformed metal mesh stretched tightly over lapped metal rings. The mounted meshes have a defect finesse in excess of 100 at 100 μm wavelength over their central 2/3 in.

The design allows for easy interchange of etalons. By replacing the wire mesh etalon with one made of dielectric coated zinc selenide plates, the instrument becomes useable for astronomy in the 10 μm atmospheric window. The performance of the scanning system was checked using visible light and semi-transparent gold-coated zinc selenide plates. These indicate that the interferometer remains in alignment to one visible light fringe over 40 visible orders. The peak-to-peak noise in the whole system is 0.02 μm with an average drift of 0.02 μm/hr. The upper carriage was given a small displacement

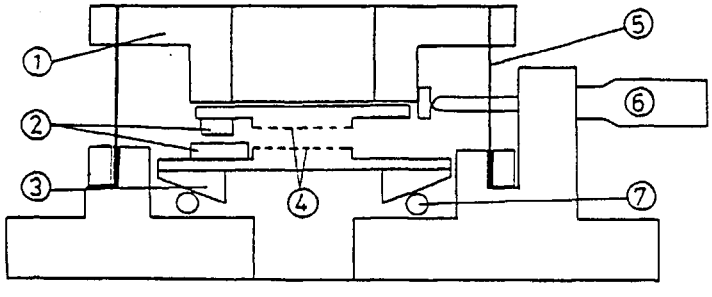

Fig. 1. Scanning Fabry–Perot interferometer. (1) Upper carriage. (2) Capacitor pads. (3) Tapered glass V-blocks. (4) Metal meshes. (5) Phosphor bronze springs. (6) Drive micrometer. (7) Ball bearing.

to pretension it against the micrometer and the arrangement was stable against tilt to 0.001 μm/deg over angles from $-40°$ to $+40°$ in all directions from horizontal.

Acknowledgements—We wish to thank Dr J. J. Wijnbergen, Paul Atherton and Richard Chater for advice and help, and the Science Research Council for financial support for our balloon astronomy programme. MFK holds an SRC studentship and JA an SRC Research Assistantship.

REFERENCES

1. JOSEPH, R. D., J. ALLEN, W. P. S. MEIKLE, K. C. SUGDEN, M. F. KESSLER, D. L. ROSEN & G. MASSON, *Opt. Eng.* **16**, 558 (1977).
2. JONES, R. V., *J. scient. Instr.* **28**, 38 (1951).
3. JONES, R. V. & J. C. S. RICHARDS, *J. Phys.* E: *Sci. Instr.* **6**, 589 (1973).
4. EMI Electron Tube Division, Hayes, Middlesex.